Master's thesis

NTNU
Norwegian University of Science and Technology
Faculty of Engineering
Department of Marine Technology

Stian Næss Boge
Daniel Wergeland Ekerhovd

A Hydro-Aerodynamic Analysis of a Floating Offshore Wind Turbine to Assist in Floater Selection

Master's thesis in Marine Technology
Supervisor: Marilena Greco
Co-supervisor: Finn-Christian W. Hanssen
June 2022

NTNU
Norwegian University of
Science and Technology

Stian Næss Boge
Daniel Wergeland Ekerhovd

A Hydro-Aerodynamic Analysis of a Floating Offshore Wind Turbine to Assist in Floater Selection

Master's thesis in Marine Technology
Supervisor: Marilena Greco
Co-supervisor: Finn-Christian W. Hanssen
June 2022

Norwegian University of Science and Technology
Faculty of Engineering
Department of Marine Technology

NTNU
Norwegian University of
Science and Technology

Preface

The presented master's thesis is performed at the Department of Marine Technology at NTNU and written as part of the specialization in hydrodynamics during the spring of 2022. The master's thesis is mainly based on numerical studies on floating offshore wind turbines and is written in cooperation and guidance by SEMAR AS.

A project thesis was carried out in the fall of 2021 as a preliminary study for the master's thesis. The project thesis's main objective was to perform a literature study on the state-of- the-art numerical tools, development of floating offshore wind turbines and relevant sites for Norwegian floating offshore wind turbine development. This thesis on the other hand, only consider literature and theory related to the objective. Some sections were taken directly from the project thesis, but this is emphasised at the relevant sections.

Department of Marine Technology, NTNU

Trondheim, 10th June 2022

Stian Næss Boge

Daniel Wergeland Ekerhovd

Acknowledgment

Firstly, we would like to express our sincere gratitude to our supervisor Professor Marilena Greco for her guidance and expertise throughout the project and master's thesis. She has been a valuable resource in assisting with several aspects such as discussions of results, work progress and problem-solving during our weekly meetings throughout the thesis. We have really appreciated her genuine interest and commitment to the thesis, which has made it more motivating for us.

Secondly, we would like to thank Finn-Christian Hansen and Mohd Atif Siddiqui from SEMAR AS for providing guidance and sharing relevant knowledge from the industry. Additionally, we would like to thank them for helping us identify the master's thesis scope.

We would also like to thank all the other professors at the institute who have helped us by giving advice and making recommendations during the thesis.

NTNU Trondheim
Norwegian University of Science and Technology
Faculty of Engineering Science and Technology
Department of MarineTechnology

MASTER THESIS IN MARINE TECHNOLOGY

Spring 2022

FOR

Daniel W. Ekerhovd, Stian Boge

A hydro-aerodynamic analysis of a Floating Offshore wind turbine to assist in floater selection

(En hydroaerodynamisk analyse av en flytende offshore vindturbin for å hjelpe til med flytevalg)

Various types of floaters have been proposed to support floating offshore wind turbines (FOWTs). Semi-submersibles (semi-subs), tension leg platforms and spar platforms are the most common concepts currently in operation or consideration. Each concept is associated with some inherent advantages and disadvantages and there are several aspects that affect the choice of the type and specific design of the platform, among them minimizing the wave-induced motions, the mooring-system footprint, and the costs. It is important to analyse the behaviour of floater designs for FOWTs to predict operational parameters correctly. In this framework, the floater response and the wind turbine's performance are coupled, and it is necessary to perform a coupled aero-hydrodynamic analysis of the platform including the loading from the turbine.

The present study aims to implement a systematic procedure for a dedicated comparison of two different floaters proposed for FOWTs and accounting for these coupling mechanisms. In the project thesis, the candidates examined the state-of-the art on the topic, selected the wind turbine, two semi-submersibles (OO-Star and INO WINDMOOR) to be considered as potential floaters and proposed a scaling-up strategy for one of them (OO-Star) to be suitable for the wind turbine (12MW). They selected the site ("Utsira Nord") for the two FOWTs and collected environmental data; they also examined different state-of-the-art prediction tools as candidates for the comparative analyses of the two FOWT concepts. Finally, they performed preliminary study on numerical convergence and compared frequency-domain predictions for hydrodynamic coefficients, excitation loads and rigid-motion RAOs against available data for both floaters.

Objective

The master thesis has the overall target to provide insights on the influence of semi-submersible features on the operation and extreme-weather behaviour of a selected wind turbine. The two floaters selected in the project will be comparatively examined using an available state-of-the-art prediction tool. Examples of aspects and response variables that could be relevant for this analysis are platform natural periods, features of critical phenomena (e.g., resonances and instabilities), platform motions (including second-order slow-drift contributions), fairlead and mooring tensions, influence of floaters on performance of the wind turbine.

The work should be carried out in steps as follows; some include part of the work done in the project thesis so to make the MSc thesis a stand-alone document:

1. Provide the background motivation and the state-of-the-art relevant for this topic, describe available prediction tools for studying the behaviour at sea of FOWTs with emphasis on the tool chosen for this analysis. Provide the information on the selected site and related environmental conditions. Base this on the material collected in the project work and complement it when needed.
2. Provide the frequency-domain analyses, including first- and second-order load effects, for the two floaters to be used with the same wind turbine, and include proper numerical convergence of the results.
3. Based on the studies in step 1, select the environmental conditions to carry on statistical analyses of operational and extreme conditions for the two FOWTs. Moreover, model a proper mooring-line system and the dry part of the platforms and related loads.
4. Perform statistical analyses of the two platforms in operational conditions when including linear and second-order hydrodynamic loads, with the turbine in operational and parked conditions in order to investigate the turbine influence on the floater, and examine relevant response variables for the two platforms. Perform a similar analysis considering extreme conditions.
5. Assess how to discretize wave scatter diagram and determine corresponding representative wind conditions for fatigue analysis. Using the established environmental conditions, examine fatigue for tower, fairlead, and mooring lines of the two FOWTs.
6. Draw the conclusions from the studies and discuss possible further research steps.

The work may show to be more extensive than anticipated. Some topics may therefore be left out after discussion with the supervisor without any negative influence on the grading.

The candidates should in their report give a personal contribution to the solution of the problem formulated in this text. All assumptions and conclusions must be supported by mathematical models and/or references to physical effects in a logical manner.

The candidates should apply all available sources to find relevant literature and information on the actual problem.

The thesis should be organised in a rational manner to give a clear presentation of the work in terms of exposition of results, assessments, and conclusions. It is important that the text is well written and that tables and figures are used to support the verbal presentation. The thesis should be complete, but still as short as possible. In particular, the text should be brief and to the point, with a clear language. Telegraphic language should be avoided.

The thesis must contain the following elements: the text defining the scope (i.e. this text), preface (outlining project-work steps and acknowledgements), abstract (providing the summary), table of contents, main body of thesis, conclusions with recommendations for further work, list of symbols and acronyms, references and (optional) appendices. All figures, tables and equations shall be numerated.

The supervisor may require that the candidates, in an early stage of the work, present a written plan for the completion of the work. The plan should include budget for the use of computer and laboratory resources that will be charged to the department. Overruns shall be reported to the supervisor.

From the thesis it should be possible to identify the work carried out by the candidate and what has been found in the available literature. It is important to give references to the original source for theories and experimental results.

Supervisor : Marilena Greco
Co-supervisor : Finn-Christian W. Hanssen
Co-supervisor : Mohd Atif Siddiqui

Submitted : January 15th 2022
Deadline : June 11th 2022

Marilena Greco
Supervisor

Abstract

Various types of floaters have been proposed to support floating offshore wind turbines. The bulk of market activity is in semi-submersibles, where each concept is associated with inherent advantages and disadvantages with respect to the design. This thesis aims to perform a fully coupled time-domain dynamic analysis for two different floater designs in operational and extreme environmental conditions and compare their response features and challenges. Two different second-order hydrodynamic load models were applied in the analysis to investigate the applicability of Newman's approximation compared to a full quadratic transfer function (QTF).

The two selected floaters, INO WINDMOOR and OO-Star, were modelled in GenieE, hydrodynamically analysed in HydroD and lastly imported to SIMA for the fully coupled time-domain analysis. The OO-Star floater was originally designed to support a 10 MW turbine but was, in this thesis, upscaled in order to support a 12 MW turbine. In HydroD, a first and second-order frequency domain analysis was performed with outputs consisting of hydrodynamic coefficients, excitation forces, RAOs, mean drift forces, and QTFs.

The numerical models were successfully verified through the results obtained from the hydrodynamic frequency domain analysis from HydroD and the free decay test performed in SIMA. Added mass and damping coefficients, RAOs, the mean drift force, natural periods and the QTFs were used for the verification. A constant wind test was conducted to ensure that the performance of the wind turbine was correct.

The Utsira Nord area was considered a suitable location due to its high wind speed potential and low distance from the coast. The environmental conditions from this area were obtained and used to define the design load cases for the time-domain analyses. Joint distribution models of wind and waves were used to establish the environmental conditions.

Newman's approximation underestimates the surge, heave, and pitch resonant response compared to the analyses with a full QTF. However, this had a negligible effect on the total response of the two FWTs. Therefore, it was concluded that Newman's approximation is applicable in surge, heave and pitch.
The INO WINDMOOR experiences the largest dynamic motions in heave while the OO-Star experiences the largest dynamic motions in surge. The dynamic pitch motion is not consistently larger for either model. The tower on the OO-Star FWT is generally subjected to lower axial loads and bending moments for both operational and extreme conditions. The mooring lines of INO WINDMOOR are subjected to larger tension than the OO-Star, which is due to the larger pretension of the mooring line system for the INO WINDMOOR. Concerning the electrical power output, the INO WINDMOOR is advantageous, however, the differences are quite small between the FWTs. In general, the fatigue damage at the tower, fairlead and different mooring lines segments are more significant for the INO WINDMOOR than the OO-Star.

Sammendrag

Ulike typer fundamenter er foreslått til flytende vindturbiner. Hovedtyngden av markedsaktiviteten er "Semi-submersible" fundamenter, hvor hvert konsept har sine fordeler og ulemper med hensyn til designet. Denne oppgaven tar sikte på å utføre en fullstendig koblet dynamisk analyse for to forskjellige fundamenter under operasjonelle og ekstreme sjøtilstander og sammenligne deres respons og utfordringer. To forskjellige andre-ordens hydrodynamiske lastmodeller ble brukt i analysen for å undersøke anvendeligheten av "Newman's approximation" sammenlignet med en full "quadratic transfer function" (QTF).

De to utvalgte flytefundamentene, INO WINDMOOR og OO-Star, ble modellert i GenieE, hydrodynamisk analysert i HydroD og til slutt importert til SIMA for en fullstendig koblet tidsdomeneanalyse. OO-Star fundamentet ble opprinnelig designet for å støtte en 10 MW turbin, men ble i denne oppgaven oppskalert for å støtte en 12 MW turbin. I HydroD ble det utført en første- og andreordens frekvensdomeneanalyse med resultater bestående av hydrodynamiske koeffisienter, RAO-er, eksitasjonskrefter, "mean drift"-krefter og QTF-er.

De numeriske modellene ble verifisert gjennom resultatene oppnådd fra den hydrodynamiske frekvensdomeneanalysen fra HydroD og "free decay"-testen utført i SIMA. "Added mass" og dempnings koeffisienter, RAO-er, "mean drift"-krefter, naturlige perioder og QTF-er ble brukt for verifiseringen. Det ble også utført en vindtest med konstant vind for å sikre at vindturbinen opererte slik den skulle.

Området Utsira Nord ble ansett som et egnet sted på grunn av det høye vindpotensialet og den lave avstanden fra kysten. Miljøforholdene fra dette området ble innhentet og brukt til å definere lasttilstandene for tidsdomeneanalysene. Simultanfordelinger av vind og bølger ble brukt for å etablere lasttilstandene.

"Newman's approximation" underestimerer jag, hiv og trim-responsen ved resonans sammenlignet med analysene utført med full QTF. Dette hadde imidlertid liten effekt på den totale responsen til de to flytende vindturbinene. Derfor ble det konkludert med at "Newman's approximation" er anvendelig i jag, hiv og trim.
INO WINDMOOR opplever de største dynamiske bevegelsene i hiv, mens OO-Star opplever de største dynamiske bevegelsene i jag. Den dynamiske trim responsen er ikke konsekvent større for noen av modellene. Tårnet på toppen av OO-Star flyteren utsettes generelt for lavere aksiale belastninger og bøyemomenter for både operasjonelle og ekstreme forhold. Fortøyningslinene til INO WINDMOOR utsettes for større spenninger enn OO-Star, noe som skyldes en større forspenning av fortøyningslinesystemet til INO WINDMOOR. Når det gjelder den elektriske effekten, er INO WINDMOOR fordelaktig, men forskjellene er ganske små mellom fundamentene.

Generelt er utmattelsesskadene i tårnet, festepunktet til forankringslinene og de forskjellige segmentene i fortøyningslinene mer betydelig for INO WINDMOOR enn OO-Star fundamentet.

Table of Contents

List of Figures

List of Tables

Nomenclature

Abbreviations

BC	Boundary Condition
BEM	Blade Element Momentum
BVP	Boundary Value Problem
COG	Center Of Gravity
DLC	Design Load Case
DLF	Dynamic Load Factor
DLL	Dynamic Link Library
DOF	Degree of Freedom
FE	Finite Element
FEM	Finite Element Method
FOWT	Floating Offshore Wind Turbine
FWT	Floating Wind Turbine
GDW	Generalized Dynamic Wake
HAWC2	Horizontal Axis Wind turbine simulation Code 2
IEA	International Energy Agency
JONSWAP	Joint North Sea Wave Project
KC	Keulegan Carpenter
MBL	Minimum Breaking Load
MBS	Multi-Body System
ML	Mooring Line
MPM	Most Probable Maximum
MSL	Mean Sea Level
MW, GW	Mega Watt, Giga Watt
NORA10	Norwegian Reanalysis 10 km
NREL	National Renewable Energy Laboratory
NTM	Normal Turbulence Model
PM	Pierson-Moskowitz
QTF	Quadratic Transfer Function
RAO	Response Amplitude Operator
SCF	Stress Concentration Factor
SIMO	Simulation Of Marine Operations
TLP	Tension-Leg Platfrom
WADAM	Wave Analysis by Diffraction and Morison Theory

Greek letters

α	Shape parameter
β	Wave heading angle, frequency ratio, scale parameter
ϵ	Phase angle
$\eta, \dot{\eta}, \ddot{\eta}$	Body motion, velocity and acceleration
Γ	Gamma function
γ	Peak shape parameter
λ	Wave length, tip speed ratio
λ_r	Local tip speed ratio
∇	Displaced volume
Ω	Angular rotor velocity
ω	Wave frequency, angular velocity
ω_p	Angular spectral peak frequency
Φ	Gradient of the velocity potential
ϕ	Velocity potential
ψ	Speed profile parameter
ρ	Density
σ	Spectral width parameter, axial stress
σ^2	Variance
σ_s	Solidity ratio
τ	Time lag integration variable
θ	Angle
ξ	Damping ratio
ζ	Free surface condition
ζ_a	Wave amplitude

Latin letters

$\mathbf{A}$	Added mass matrix
$\mathbf{B}$	Damping matrix
$\mathbf{C}$	Restoring matrix
$\mathbf{F}$	Force vector
$\mathbf{M}$	Inertia matrix
$\mathbf{X}$	Motion vector
A	Cross-sectional area
a	Axial induction factor
a'	Angular induction factor

A_γ	Normalization factor
a_D	Intercept parameter
B	Number of blades
C^D	Specified discrete damping matrix
C^H	Hydrodynamic damping matrix
C^S	Internal structural damping
C_D	Drag coefficient
C_L	Lift coefficient
C_M	Inertia coefficient
C_n	Normal coefficient
C_P	Power coefficient
C_T	Thrust coefficient
D	Diameter, accumulated fatigue damage
d_0	Reference depth
D_1	Linear damping matrix
D_2	Quadratic damping matrix
E	Energy
F	Force
f	Force vector, probability density
g	Gravity constant
h	Water depth
H_s	Significant wave height
K	Hydrostatic stiffness
k	Wave number, Thickness exponent
L	Lift force
l	Tangential vector
m	Slope parameter, mass
M^F	Mass matrix accounting for internal fluid flow
M^H	Hydrodynamic mass matrix
M^S	Structural mass
M_y, M_z	Flapwise and edgewise bending moment
N	Predicted number of cycles to failure
N_x	Axial force
P	Power
P_0	Load

p_o	Atmospheric pressure
Q	Torque
$r, \dot{r}, \ddot{r}$	Structural displacement, velocity and acceleration vectors
R	Radius
R^D	Damping vector
R^E	External force vector
R^I	Inertia vector
R^S	Internal structural reaction force vector
r_g	Radius of gyration
s, S	Geometrical scaling factors
S_ζ	Spectral density of wave elevation
T	Thrust, Tension
T_c	Cut-off time
T_p	Peak period
t_{ref}	Reference thickness
U_c	Current velocity
U_w	Wind speed
$U_{c,wind}$	Wind-generated current
V	Fluid velocity
$x, \dot{x}, \ddot{x}$	Position, velocity and acceleration

1 Introduction

1.1 Background

The impact of global warming is becoming severely apparent and requires urgent action. Today, fossil fuels still dominate the global energy system and account for more than 80% of the world's total energy supply (Tian et al., 2022). However, there is a convincing call to push for a green economy through the energy transition, where 90 % of the required carbon reduction can be achieved through renewable energy and efficiency measures within the energy sector (IRENA, 2022). Despite this, there is no hiding the fact that the COVID-19 pandemic has caused challenges to the energy industry, where many countries have prioritized health and medical attention, thus withdrawing funds from renewable energy projects (Tian et al., 2022). Additionally, in the midst of the Ukraine war, which requires an extraordinary mobilization of energy sources, the demand for the use of coal could increase even further. However, due to the Russian invasion of Ukraine, the European Commission has, through the REPowerEU Plan, decided to end the EU's dependence on Russian fossil fuels (Commission, 2022). Consequently, accelerating and up-scaling renewable energy sources to replace fossil fuels will be a part of the path to independence from Russian fossil fuels. Where according to DNV (2022), the Ukraine war, as COVID-19, will not derail Europe's energy transition.

Offshore wind turbines are today the most advanced technology among offshore renewable and have a significant potential to support the drive for a low carbon economy in Europe (Atcheson, 2016). As an effect of its offshore location and high energy output per square metre, this rapidly growing industry is a valuable option for providing electricity in a cost-effective manner (IRENA, 2019). In general, offshore wind turbines experience higher mean wind speeds than onshore, which is favourable for power production. However, the most common offshore wind turbines today are with bottom fixed foundations, which are restricted to water depths up to 60 m (IRENA, 2019). Floating offshore wind turbines (FOWTs), on the other hand, are not restricted to shallow water depths, and 80 % of the world's offshore wind resource potential lies in water deeper than 60 m (Lee and Zhao, 2021). The Norwegian government aims to take advantage of Norway's deep water coastline and has the ambition to launch a large-scale investment in offshore wind, where areas capable of 30 GW will be allocated by 2040 (Regjeringen.no, 2022). The majority of this investment will be in floating wind turbines. Today, the areas Utsira Nord and Sørlige Nordsjø II are open for offshore renewable's. However, the government aims to implement the next licensing round for offshore wind in new areas in 2025 (Havvind, 2022).

The trend for larger wind turbines introduces a necessity for further developing the floating foundations in today's industry. The challenges with FOWT arise with deeper waters and more extreme environmental conditions. This, in turn, affects the accessibility for maintenance purposes at the installation site. Various types of floaters have been proposed to support FOWTs, where the bulk of market activity is in semi-submersibles at present (Lee and Zhao, 2021). Each concept is associated with some inherent advantages and disadvantages concerning the design. Therefore, it is important to analyse the behaviour of the floater designs to predict operational parameters correctly. The present work will compare two different state-of-the-art semi-submersible floater concepts using numerical analysis.

1.2 Offshore Wind Energy Today

The world's first offshore wind farm Vindeby was built in Denmark in 1991 and consisted of eleven 450 kW turbines capable of extracting annual power equivalent to 2-3000 danish households (Ørsted, 2019). Figure 1.1 illustrate the offshore wind installations in 2020 and the offshore cumulative installation as of 2020. As seen from Figure 1.1, the offshore wind capacity has now passed 35.3 GW, representing 5% of the global cumulative wind capacity (Lee and Zhao, 2021). 2020 was the second-best year of all time in the offshore market, as 6.1 GW were commissioned worldwide.

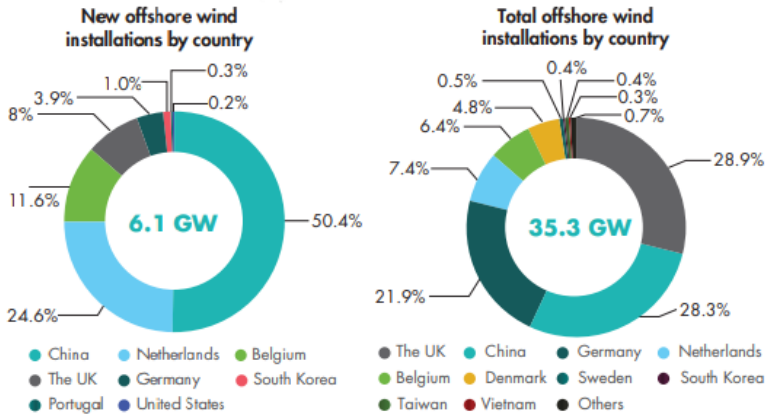

Figure 1.1: Offshore wind installations in 2020 and the cumulative installations as of 2020. (Lee and Zhao, 2021)

In 2009, Equinor installed the world's first megawatt scaled floating offshore wind turbine Hywind Demo outside the coast of Norway, utilizing a spar buoy as the floating foundation (Equinor, 2021a). Following the Hywind Demo, Principle Power installed the WindFloat 1 outside the coast of Portugal in 2011. The WindFloat 1 project consisted of a 2 MW turbine mounted on a semi-submersible floating structure. It was a full lifecycle demonstration of the features and benefits of the floating offshore wind turbine concept (4Coffshore, 2021). After five successful years of deployment, the WindFloat were decommissioned and towed back to port, where the structure was dissembled.

Outside Europe, the University of Maine deployed a 1:8 scale model of the 6 MW VolturnUS semi-submersible floating wind turbine (FWT) in 2013, making the VolturnUS the first FWT in the United States (Viselli et al., 2015). In Japan, a small scale experiment model (100 kW) was installed in 2012, providing the country with its first grid-connected FOWT facility. The demonstration model Sakiyama 2 MW FWT, using a steel hybrid spar buoy was deployed in 2013 and making it Japan's first commercial FOWT (CORPORATION, 2021).

Further, the developments of the floating offshore wind technology led to the world's first commercial offshore wind farm, Hywind Scotland, in 2017, consisting of five 6 MW turbines with a total installed capacity of 30 MW (Equinor, 2021b). New development of the WindFloat 1 led to the WindFloat Atlantic offshore wind farm being installed in 2019. The three turbines that make up the wind farm are mounted on semi-submersible floating platforms, with a total installed capacity of 25 MW. This made the WindFloat Atlantic the first commercial semi-submersible wind farm in the world with the largest turbine ever installed on a floating platform at the time (8.4 MW) (EDP, 2018). As of 2021, the world's largest floating offshore wind farm is the Kincardine project outside the coast of Scotland. Using the world's largest FWT, Vestas V164-9.5 MW provides a total installed capacity of 50 MW (Lee and Zhao, 2021).

Figure 1.2 and Figure 1.3 illustrate the global market outlook for offshore wind and the global market outlook for floating wind, respectively. The offshore market outlook predicts the total offshore wind capacity to reach 270 GW by 2030, where 30 % of this new volume will be installed in the first half of the decade (2021-2025) (Lee and Zhao, 2021). The majority of the installations will be built in the second half of this decade (2025-2030). During this decade, new installations outside of Europe, mainly in Asia, will lead to Europe losing its status as the largest regional offshore wind market by 2030. In the floating offshore wind market, 73 MW is in operation as of 2020, corresponding to only 0.1 % of the total installed wind capacity. However, it is predicted a total installed capacity of 16.5 GW by 2030, according to the Global Wind Energy Council (Lee and Zhao, 2021).

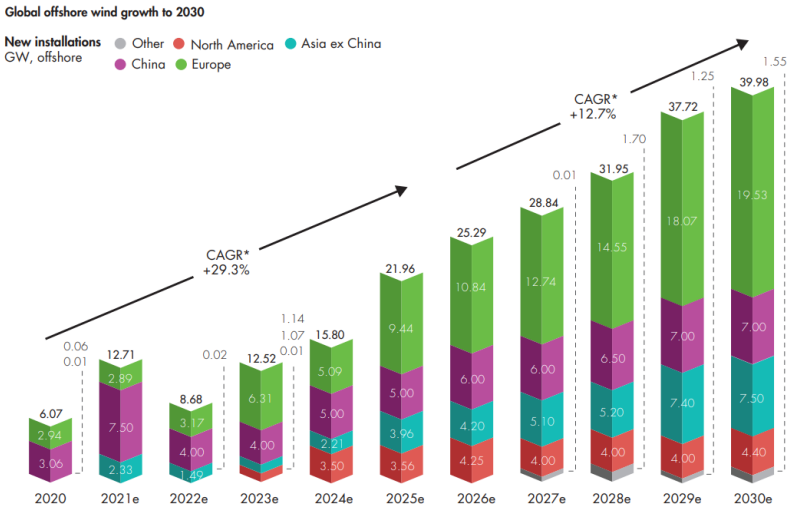

Figure 1.2: Global market outlook for offshore wind (Lee and Zhao, 2021).

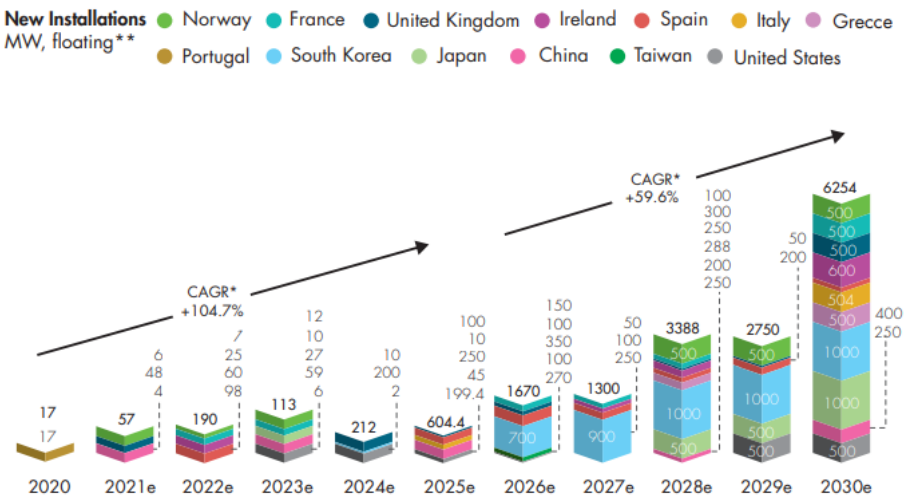

Figure 1.3: Market outlook for floating offshore wind (Lee and Zhao, 2021).

1.3 Summary of Preliminary Studies

A project thesis was carried out during the fall semester of 2021 as a preliminary study for the master's thesis. The project thesis's main objective was to perform a literature study and develop preliminary numerical models in the frequency-domain to prepare for the time-domain simulations. From the literature study, research on state-of-the-art industrial development for FOWT platforms and their targeted operation sites led to selecting two semi-submersible floating platform concepts and a relevant offshore site for Norwegian FOWT development, with water depths of approximately 280 m. Additionally, an extensive literature study on the current commercial/open-source prediction tools for FOWT was performed, resulting in selecting the prediction tool SIMA to be used in the time-domain analysis in the master's thesis.

The two selected semi-submersible platforms to investigate are the INO-WINDMOOR floater, jointly developed by Inocean and Equinor and the OO-Star Wind Floater developed by Dr.Tech. Olav Olsen AS. Following these two concepts, the corresponding articles (Souza et al., 2021) and by (Yu et al., 2018) given by SINTEF and LIFES50+, respectively, are used as a reference for the verification of the numerical models. In order to compare the two floaters, it was decided to upscale the OO-Star floater, which is designed to support a 10 MW turbine, to be capable of supporting

a 12 MW turbine, as the INO WINDMOOR is designed to support a 12 MW turbine. Hence, the WINDMOOR 12 MW turbine will be used on both platforms. The scaling parameter is based on the ratio of the turbine masses.

Both numerical models were modelled as finite element panel models with the DNV software GeniE, based on the dimension given in the reference articles. The frequency-domain hydrodynamic analyses were carried out in HydroD. For the discretization of the mesh, a convergence study was performed for both models, where two appropriate panel sizes for the respective models were selected for further analyses. Further, simplifications were implemented in HydroD, where both floaters were modelled without any influence of the mooring system and thus no additional stiffness for the horizontal motions. Additionally, in compliance with (Souza et al., 2021), an equivalent linear damping equal to 5% of the critical damping was implemented in heave, roll and pitch in order to account for viscous damping for both models.

The frequency-domain analyses showed satisfactory results for both models. Hydrodynamic coefficients such as added mass and wave-radiation damping and response amplitude operators (RAO) were used to verify the models against the reference articles. Table 1.1 presents the natural periods obtained from the frequency domain analysis in HydroD compared with the reference values.

Table 1.1: Natural periods obtained from the frequency domain analysis for the INO WINDMOOR and OO-Star during the project thesis.

	WINDMOOR		OO-Star	
	HydroD	Reference	HydroD	Reference
Heave	17 s	16.3 s	21 s	20.4 s
Roll	31 s	29.5 s	31.4 s	-
Pitch	31.2 s	31.4 s	31.4 s	31.25 s

As the verification of the numerical models developed in the project thesis showed satisfactory results, the numerical models were further implemented into the time-domain. The proceeding work to be done in the master's thesis was to design a mooring system corresponding to the water depth at the selected location of interest and identify and establish the environmental conditions at the site. Furthermore, a second-order frequency domain analysis is also needed to be performed in order to implement the full QTF in the time-domain.

1.4 Objectives of Master Thesis

The master thesis has the overall target to provide insights on the influence of semi-submersible features on the operation and extreme-weather behaviour of two selected wind turbine platforms. The two floaters selected in the project will be comparatively examined using an available state-of-the-art prediction tool chosen among those examined in the project work. Examples of aspects and response variables that could be relevant for this analysis are the FWTs natural periods, features of critical phenomena (e.g., resonances and instabilities), FWTs motions (including second-order slow-drift contributions), fairlead and mooring tensions, tower loads/moments and influence of floaters on the performance of the wind turbine.

1.5 Structure of Report

The structure of the report is listed as shown in the following.

- **Chapter 2** provides a literature study on state-of-the-art numerical prediction tools, on second-order wave effects on FWT's and on fatigue damage analysis.
- **Chapter 3** introduces the theory used in the numerical simulations and calculations in the master's thesis.
- **Chapter 4** gives an overview of the different floater types used for floating offshore wind turbines today, as well as an introduction of the two select floater types including system properties.
- **Chapter 5** presents a description of the selected site and procedure for establishment of environmental conditions used to define the design load cases. This chapter also describes an environmental lumping method for fatigue damage assessment and the corresponding load cases.
- **Chapter 6** describes the utilized software and methodology of the numerical modelling and design process.
- **Chapter 7** presents a numerical model verification study in both frequency and time domain.
- **Chapter 8** documents the results from the time-domain analysis for both floating wind turbines.
- **Chapter 9** provides the conclusions and suggestions for further work.

2 Literature Study

2.1 Numerical Modelling and Prediction Tools

This section presents the literature study on state-of-the-art numerical prediction tools for floating wind turbines. As the state-of-the-art prediction tools for floating wind turbines were discussed in the project thesis, some of the following paragraphs are taken from the project thesis with some alterations.

Floating offshore wind turbines are complex systems. Coupling effects between the turbine aero and hydrodynamics, structural dynamics and mooring line effects must be included in the analysis. Usually, the dynamic analysis of the floating substructure is performed in the frequency domain, obtaining the relevant hydrodynamic coefficients, while the coupled analysis is performed in the time-domain. A range of time-domain integrated aero-hydro-servo-elastic numerical tools is today available, capable of performing coupled analyses of a floating wind turbine (Borg and Bredmose, 2015). An overview of the industry's state-of-the-art numerical prediction tools for the design of FOWT is presented in Borg and Bredmose (2015), and a brief description of four of these are presented in the following.

OpenFAST is an open-source software package for simulating the coupled dynamic response of wind turbines developed by the National Renewable Energy Laboratory (NREL). The aerodynamic and hydrodynamic loads are calculated by the two modules, AeroDyn and HydroDyn, which are time-domain modules coupled in the OpenFAST multi-physics engineering tool to enable aero-hydro-servo-elastic simulation of offshore horizontal-axis wind turbines. (NREL, 2021). The hydrodynamic loads acting on a structure can be calculated with different approaches in HydroDyn: a potential-flow theory solution, a strip-theory solution, or a combination of the two (Laboratory, 2021). In AeroDyn, Blade Element Momentum Theory (BEM) is used. OpenFAST uses a combination of a modal and multi-body formulations when modelling the structural dynamics. The turbine blades and tower are modelled using a linear modal representation, assuming that the deflection is small. The blades and tower mode shapes are calculated using the finite element method. The floating platform is modelled as a 6DOF rigid body (Cordle and J. Jonkman, 2011). The mooring lines are modelled by using a quasi-static mooring system module to estimate the nonlinear restoring forces of the mooring lines.

HAWC2 is an aeroelastic code for calculating the response of wind turbines in the time domain (Kristiansen, 2021). The code is developed by the Aeroelastic Design Research Program at DTU Wind Energy. HAWC2 consists of different models that describe the environmental conditions, applied loads, structural dynamics and the control system. The environmental conditions models how the wind, waves and soil are expected to behave. The applied load models how the environmental conditions interact with the structure through hydrodynamic, aerodynamic and soil models. The aerodynamic forces on the rotor are calculated using BEM theory (Kristiansen, 2018). When calculating the hydrodynamic forces, the code is limited to Morison equation. The wave kinematics are not generated within the code but are provided externally through a defined DLL (dynamic link library) interface (Møller, 2018). The structural modelling in HAWC2 is based on a multi-body formulation using the floating frame of reference approach. This means that the turbine structure is subdivided into multiple bodies with its own coordinate system (Friis-Møller, 2021). The modelling of the mooring lines is done by external systems and is then coupled to HAWC2.

Orcaflex, developed by Orcina, performs global static and dynamic analysis of different offshore systems and finite element modelling of line structures. The hydrodynamic capabilities of Orcaflex can be coupled with a built-in aerodynamic turbine model, which makes Orcaflex capable of model fully-coupled dynamic analyses of floating offshore wind turbines. Orcaflex calculates the hydrodynamic loads by the use of Morison's equation as well as importing potential flow information from other software. The aerodynamic loading in OrcaFlex is calculated using BEM theory adopted from AeroDyn (Orcina, 2021c). The rigid bodies are modelled as OrcaFlex Vessels when diffraction effects tend to dominate, while if the rigid body is in the drag/inertia regime, it is modelled with OrcaFlex 6DOF Buoys (Orcina, 2021b). In Orcaflex, the finite element model of the mooring lines is modelled as Orcaflex Lines. Orcaflex lines are divided into a series of line

segments which are modelled by straight massless model segments with a node at each end of the line (Orcina, 2021a). The modelling of the mooring lines is done by external systems and is then coupled to HAWC2.

SIMA is an integrated prediction tool suited for marine operations and floating systems analysis. The SIMA workbench includes numerical codes developed at MARINTEK(now SINTEF Ocean), including SIMO and RIFLEX. SIMO is a general-purpose time-domain program for the modelling and simulation of offshore structures, while RIFLEX is a nonlinear finite element model code that models the static and dynamic analyses of slender marine structures, such as risers, mooring lines and wind turbine blades (Atcheson, 2016). SIMO and RIFLEX can be coupled to determine all of the hydrodynamic and structural options in order to model floating offshore wind turbines (Atcheson, 2016). SIMA is selected to be used in this master's thesis, therefore a more detailed description of SIMA and the time-domain solution of SIMO-RIFLEX is given in Section 3.6.

2.2 Second-Order Effects on FWTs

A literature study on the second-order effects on FWTs is conducted to highlight the differences in the floater response when using Newman's approximation in contrast to the full QTF to obtain the difference-frequency wave loads. The key findings from studies investigating the second-order wave-induced response will be presented in the following paragraphs.

Cao et al. (2020) investigated the second-order wave-induced response on a semi-submersible platform carrying the DTU 10 MW reference wind turbine under combined wind/wave conditions. The dynamic responses were calculated according to three models, labelled as "1st", "1st+Newman approximation" and "1st+full QTF". An aero-hydro-servo-elastic analysis was performed in FAST to analyse the integrated dynamic responses in the time-domain. Subsequently, the dynamic responses of the semi-submersible wind turbine considering the second-order loads using Newman's approximation and the full QTF were investigated, including motion response, tower-top shear force, fairlead tension and power production.
The average responses of the FWTs obtained using the three models are similar. The standard deviation of the low-frequency surge motion calculated by Newman's approximation is close to the values obtained using the full QTF. For the low-frequency pitch motion, the differences between Newman's approximation and full QTF is significant. The smaller the difference-frequency is, the more similar the low-frequency responses obtained by the two different models are. The wind loads significantly affect the mean values of the pitch motion, and the values are maximum under rated wind speed. Furthermore, it is seen that the wind loads do not evidently affect the wave-frequency response of the pitch motion. The standard deviation of the pitch motion in the low-frequency range exhibits a minimal value at the condition with rated speed. The wind loads are regarded as "aerodynamic damping" that weakens the amplitude of the pitch resonant response of the platform. In terms of the maximum and low-frequency responses of the fairlead tension, the accuracies of Newman's approximation and the full QTF method are almost identical. The power spectral density of the surge and pitch motion under irregular waves and steady wind at the rated speed are presented in Figure 2.1a and Figure 2.1b, respectively.

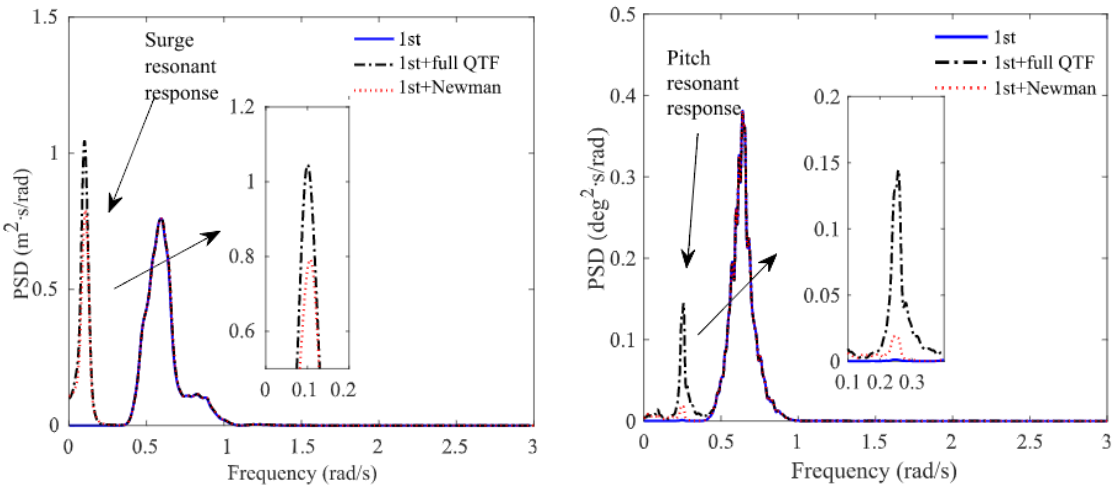

(a) (b)

Figure 2.1: Power spectral density of the surge and pitch motion (Cao et al., 2020).

Zhang et al. (2020) investigated the hydrodynamic effects on semi-submersible platforms supporting the NREL 5 MW turbine at different water depths addressing second-order hydrodynamic loads. The hydrodynamic models are developed using the ANSYS/AQWA tool with the panel model method. This paper focuses on the second-order hydrodynamic loading using Newman's approximation and the full QTF method. The second-order hydrodynamic loading loads and the resulting responses are compared with relevant loads, responses and induced motions in the frequency domain for three different water depths and for all three semi-submersible platforms. Regarding the dynamic motion response, the result shows that the difference-frequency wave force can excite resonance, especially for the pitch motion. The standard deviation values indicate that Newman's approximation underestimates the pitch motion compared to the full QTF method. The dynamic mooring tension response, mainly dominated by the surge resonant and wave frequency range responses, is more severe in the full QTF solution than Newman's approximation.

2.3 Fatigue Damage on FWTs

A literature study has been performed regarding the fatigue damage on the tower base and the mooring lines on FWTs. A short description of the most important findings is presented below.

The aim of the study was toinvestigate the necessary simulation duration, number of random realisations and bin sizes for the discretisation of the joint wind and wave distribution

Kvittem and Moan (2015) investigated simulation requirements for fatigue damage estimation, such as number of random realisations, simulation duration and bin sizes for the discretisation of the joint wind and wave distribution. The study deals with fatigue analysis for a semi-submersible supporting the NREL 5 MW turbine. One key objective was to investigate the necessary simulation length to capture the important effects of slowly varying loads. To evaluate if the most important wave periods are included in the total fatigue damage assessment, the fatigue damage estimate was compared for load cases with varying wave periods. The simulation tool used for the fatigue analysis was the SIMO-RIFLEX-AeroDyn from MARINTEK and CeSOS.
The study showed that the pitch motion of the platform and the blade passing frequency resonance in the tower were the most significant contributions to the fatigue damage in the tower. It is important to capture resonant responses when choosing load cases for fatigue analysis. To get a realistic fatigue damage estimation throughout the turbine's lifetime, choosing load cases that do not result in high fatigue damage is also important. The sensitivity to simulation length was investigated based on 3-h simulations with 10 seeds for each condition. By calculating the fatigue damage based on 10-min samples, the fatigue damage was underestimated by up to 10%. For 1-h samples, the fatigue damage was underestimated by 4% compared to the 3-h damage. The

simulations showed that the relative error for the fatigue damage estimate decreases with increasing simulation length. It was concluded that a 3-h realization gave a satisfactory fatigue damage estimate. The comparison of the load cases with varying wave periods showed that the fatigue damage increased with decreasing wave periods. Furthermore, it was found that the reduction of fatigue damage with increasing wave periods is quite linear.

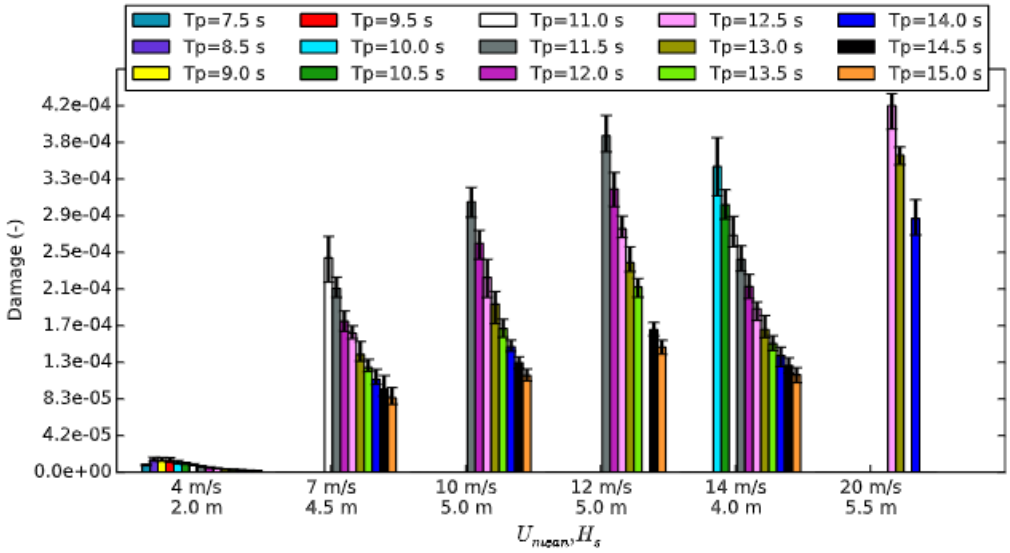

Figure 2.2: 3-h short term fatigue damage in the tower base for varying wave periods (Kvittem and Moan, 2015).

H. Li et al. (2017) performed a short-term fatigue analysis of a spar-type wind turbine tower with stochastic wind and wave loads. The nonlinear aero-hydro-servo-elastic tool FAST is used to calculate the axial force, fore-aft bending moment, and side-side bending at the tower base. Particular attention is given to the considerations of the effect of simulation length, wind-wave misalignment, wind only and wave only effect on fatigue damage.
The response of the axial stress with loading from wind and waves is dominated by the pitch resonant response, wave frequency response and the response corresponding to the first tower fore-aft natural frequency. The findings show that tower base's axial stress is affected separately and in a decoupled way from the wind and wave induced loads. Consequently, a sea state with higher wind speed will result in larger fatigue damage at the tower base. Furthermore, it is found that a 1-h simulation length is sufficient to give a satisfactory estimation of the fatigue damage. Due to the greater oscillation from the waves, the resulting fatigue damage from the waves is slightly larger than the fatigue damage induced by the wind loads under the specific environmental conditions used in the referred paper.

Xu et al. (2019) investigated the fatigue for the tower base, and mooring lines in operational conditions and the extreme values are predicted for critical responses in extreme conditions. The study considers a semi-submersible carrying a NREL 5 MW turbine. The fully coupled time-domain analysis is performed using HAWC2 with fully nonlinear wave kinematics in irregular stochastic waves.
The fatigue damage at the tower base is mainly dominated by the wind-induced response, additionally, the fatigue damage increases when the tower's natural mode is excited. The fatigue damage of the mooring line below rated wind speed is primarily governed by the wind. As the wind speed goes above rated wind speed, the contribution from the wave becomes more significant as the waves are more severe in these conditions. The fatigue damage of the mooring lines tends to increase with increasing wave height and decreasing wave periods. Furthermore, it has been found that an increase in the wind speed actually leads to a decrease in the fatigue damage of the mooring lines.

3 Theory

3.1 Hydrodynamic Theory

The following section gives a broad overview of the hydrodynamic theory used in HydroD and SIMA. In HydroD, the first-order potential theory is used to calculate first-order radiation and diffraction effects on large volume structures. First, the linear incident wave theory will be described, followed by a statistical description of waves and wave spectra. Thereafter, a description of the wave-body interaction problem and how Wave Analysis by Diffraction and Morison Theroy (Wadam) solves the wave-body interaction problem by the use of potential flow will be presented. Lastly an overview of the non-linear effects that has been accounted for in the numerical modelling is described. The hydrodynamic theory is in general based on the textbook *Sea Loads on Ships and Offshore Structures* (Faltinsen, 1993) and the compendium *Marine Dynamics* (Larsen, 2015).

3.1.1 Linear Wave Theory

As will be described in Section 5.1, the selected site is in deep water. In deep-water conditions, i.e. if $h/\lambda \geq 0.5$, with h the water depth and λ the wavelength, the linear regular wave solution is:

$$\phi(x, y, z, t) = \frac{g\zeta_a}{\omega} e^{kz} \cos(\omega t - kx) \tag{3.1}$$

$$\zeta(x, y, t) = \zeta_a \sin(\omega t - kx) \tag{3.2}$$

$$\omega^2 = gk \tag{3.3}$$

where ϕ is the first-order velocity potential, ζ is the first-order free surface elevation, ζ_a is the wave amplitude, g is the gravity acceleration, $\omega = 2\pi/T$ is the wave frequency, T is the wave period, and $k = 2\pi/\lambda$ is the wave number given by the linear wave dispersion relationship in Equation 3.3. The function $\sin(\omega t - kx)$ mathematically represents a sinusoidal wave propagating in positive x-direction and thus, the free surface is a sinusoidal wave with amplitude ζ_a.

3.1.2 Statistical Description of Waves

The linear surface process is constructed by a series of long crested waves, with different amplitudes, frequencies and phase-angles. By assuming that the waves are coming from the same direction, the surface process can be described as a sum of harmonic waves, given by:

$$\zeta(x, t) = \sum_{n=1}^{N} \zeta_{an} \cos\left(\omega_n t - k_n x + \epsilon_n\right) \tag{3.4}$$

where ζ_{an} is the wave amplitude, ω_n is wave frequency, t denotes the time and ϵ_n is the phase angle of the n^{th} wave component (Larsen, 2015).

The phase angle ϵ_n at time $t = 0$ is considered a stochastic variable and is assumed to be statistically independent and uniformly distributed between 0 and 2π. It is then common to assume that (Larsen, 2015):

- *The linear wave process is stationary, which means that the mean value and the variance of the process are constant within a short term interval (20 min-3 hours).*

- *The wave elevation is normally distributed with zero mean and with a standard deviation proportional to the significant wave height.*
- *The wave period is ergodic, which means that one time series is representative for the wave process.*

The wave amplitude ζ_{an} can be expressed in such a way that the area inside the frequency interval $\Delta\omega$ is equal to the energy of the wave components within this frequency interval, this is expressed as:

$$\frac{1}{2}\zeta_{an}^2 = S\left(\omega_n\right)\Delta\omega \tag{3.5}$$

By rearranging Equation 3.5, the wave amplitude can be expressed as:

$$\zeta_a = \sqrt{2S\left(\omega_n\right)\Delta\omega} \tag{3.6}$$

and by inserting this expression into Equation 3.2 the surface elevation can be described as:

$$\zeta(x,t) = \sum_{n=1}^{N} \sqrt{2S\left(\omega_n\right)\Delta\omega}\cos\left(\omega_n t - k_n x + \epsilon_n\right) \tag{3.7}$$

where $S(\omega)$ is denoted as the spectrum of $\zeta(x,t)$ and contains all the necessary information about the statistical properties of $\zeta(x,t)$.

By assuming that $N \to \infty$ such that $\Delta\omega \to 0$, the total amount of energy E in a sea state is given by:

$$\frac{E}{\rho g} = \frac{1}{2}\sum \zeta_{an}^2 = \int_0^\infty S(\omega)\mathrm{d}\omega \tag{3.8}$$

where ρ is the fluid density.

3.1.3 Wave Spectrum

The power spectral density is useful when considering the wave energy in a sea state and its distribution over different frequencies. Several power spectra density models exist, usually expressed in terms of sea state parameters such as the significant wave height H_s and spectral peak period T_p. The power spectral density models are often site-specific and based on data gathered for a specific location. The power spectral density models are often represented by one-peaked spectra for sea states dominated by wind-generated waves. In sea states dominated by swell in combination with wind-generated waves, a second peak may appear in the power spectral density model (DNV, 2018b).

According to DNV (2018b), for floating wind turbine structures, a two-peaked power spectrum model shall be used for the representation of the power spectral density. This is because floating wind turbine structures can be excited in heave, roll and pitch in the range of 20 to 25 seconds, which is associated with swell-dominated sea. This will not be included if only a wind-generated JONSWAP (Joint North Sea Wave Project) spectrum is utilized. However, for thesis work, a JONSWAP spectrum is assumed feasible.

The JONSWAP spectrum $S_j(\omega)$ is a modification of the Pierson-Moskowitz (PM) spectrum where it considers a developing sea state in a fetch limited situation (DNV, 2014). The JONSWAP spectrum is presented in Equation 3.9.

$$S_J(\omega) = A_\gamma S_{PM}(\omega)\gamma^{\exp\left(-0.5\left(\frac{\omega-\omega_p}{\sigma\omega_p}\right)^2\right)} \tag{3.9}$$

Where S_{PM} is the PM spectrum, γ is a non-dimensional peak shape parameter, σ is a spectral width parameter and A_γ = 1-0.287 ln(γ) is a normalization factor.

The PM spectrum, which is valid for fully developed sea states and unlimited fetch, is based on data from the North Atlantic and can be expressed as in Equation 3.10, in accordance with DNV (2014).

$$S_{PM}(\omega) = \frac{5}{16} \cdot H_S^2 \omega_p^4 \cdot \omega^{-5} \exp\left(-\frac{5}{4}\left(\frac{\omega}{\omega_p}\right)^{-4}\right) \tag{3.10}$$

Where $\omega_p = 2\pi/T_p$ denotes the angular spectral peak frequency.

The spectral width parameter is determined by the frequency as shown in Equation 3.11.

$$\sigma = \begin{cases} 0.07 & \text{for} \quad \omega \leq \omega_p \\ 0.09 & \text{for} \quad \omega > \omega_p \end{cases} \tag{3.11}$$

Based on experimental data, the average values for the JONSWAP spectrum are $\gamma = 3.3$, $\sigma_a = 0.07$ and $\sigma_b = 0.09$. The effect of the peak shape parameter is shown in Figure 3.1, whereas for $\gamma = 1$ the JONSWAP spectrum reduces to the PM spectrum.

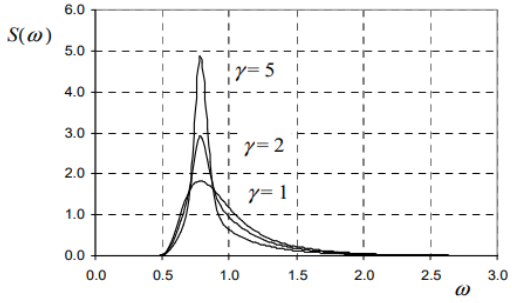

Figure 3.1: Effect of peak shape parameter γ (DNV, 2014).

The JONSWAP spectrum is regarded to be a reasonably good model for wind-generated sea states where the waves are in the region shown in Equation 3.12 (Larsen, 2015):

$$3.6 < T_p/\sqrt{H_s} < 5 \tag{3.12}$$

where the units of T_p and H_s are in seconds and meters, respectively. Should there be no particular values given for the peak shape parameter γ, the following values may be used as shown in Equation 3.13.

$$\begin{gathered} \gamma = 5 \text{ for } T_P/\sqrt{H_s} \leq 3.6 \\ \gamma = \exp\left(5.75 - 1.15\frac{T_p}{\sqrt{H_s}}\right) \text{ for } 3.6 < T_P/\sqrt{H_s} < 5 \\ \gamma = 1 \text{ for } 5 \leq T_P/\sqrt{H_s} \end{gathered} \tag{3.13}$$

3.1.4 Response in Regular Waves

By linearly superposing results from regular wave components, it is possible to obtain results in irregular seas. From a hydrodynamical point of view, it is sufficient to analyse the behaviour of a structure in incident regular sinusoidal waves with a small steepness. By assuming a steady-state condition, the linear dynamic loads and motions of the structure oscillate with the same frequency as the wave loads that excites the structure. Hydrodynamical problems in regular waves are commonly subdivided into two-sub-problems (Faltinsen, 1993):

A. The forces and moments on the body when the structure is restrained from oscillating and there are incident regular waves. The hydrodynamic loads are called wave excitation loads and composed of so-called Froude-Kriloff and diffraction forces and moments.

B. The forces and moment on the body when the structure is forced to oscillate with the wave excitation frequency in any rigid-body motion mode. There are no incident waves. The hydrodynamic loads are defined as added mass, damping and restoring terms.

Taking these two sub-problems into consideration, the equation of motion for steady-state sinusoidal motions can be written as shown in Equation 3.14. This formulation denotes the 6-DOF equation of motion for a rigid body.

$$\sum_{k=1}^{6} \left[\left(M_{jk} + A_{jk} \right) \ddot{\eta}_k + B_{jk} \dot{\eta}_k + C_{jk} \eta_k \right] = F_j e^{-i\omega t} \tag{3.14}$$

Where M_{jk}, A_{jk}, B_{jk} and C_{jk} the components of the generalized mass matrix, added mass, damping and stiffness matrix for the structure, respectively. $F_j e^{-i\omega t}$ represents the complex definition of the generalized excitation force component in direction, j. (Faltinsen, 1993).

3.1.5 Calculation of Wave Loads From Potential Theory

The theory in this section describes how Wadam calculates the first-order radiation and diffraction effects on large volume structures by the use of potential flow. The following theory is based on DNV (2017).

The assumption of potential flow allows defining the velocity flow as the gradient of the velocity potential Φ, as shown in Equation 3.15.

$$\nabla^2 \Phi = 0 \tag{3.15}$$

By the assumption of harmonic time dependence, the complex velocity potential ϕ is related to Φ by:

$$\Phi = \mathrm{Re}\left(\phi e^{i\omega t} \right) \tag{3.16}$$

where ω denotes the frequency of the incident wave, and t is the time. By expressing the associated boundary-value problem in terms of the complex velocity potential ϕ, all the complex quantities with the factor $\phi e^{i\omega t}$ apply. The combined linearized free-surface condition in its linearised form is expressed as:

$$\phi_z - k\phi = 0, \quad \text{on} \quad z = 0 \tag{3.17}$$

where $k = \omega^2/g$. The velocity potential of the incident wave is defined by:

$$\phi = \frac{g\zeta_a}{\omega} e^{i\omega t} \tag{3.18}$$

The velocity potential associated to the wave-body interaction problem satisfies four boundary conditions (BC): the deep-water conditions that the velocity potential and its gradient go to zero as $z \to \infty$, the body impermeability, free surface kinematics and the free surface dynamics. The free surface kinematic boundary condition requires a fluid particle on the free surface to stay on the free surface at all times. The dynamic boundary condition requires that the water pressure is equal to the constant atmospheric pressure p_0 on the free surface.

The total velocity potential ϕ, can be decomposed into the radiation and diffraction components by linearising the wave-body interaction problem as described in Section 3.1.4. Where the radiation problem denotes the sum of the potential from the forced oscillating body, and the diffraction problem denotes the sum of the incident wave potential ϕ_0 and the disturbance of the incident wave by the body ϕ_7.

$$\phi = \phi_R + \phi_D \tag{3.19}$$

$$\phi_R = i\omega \sum_{j=1}^{6} \xi_j \phi_j \tag{3.20}$$

$$\phi_D = \phi_0 + \phi_7 \tag{3.21}$$

The constant ξ_j donates the complex amplitudes of the body oscillations in its six rigid-body degrees of freedom.

The boundary conditions on the undisturbed mean position of the body are defined by:

$$\begin{aligned} \phi_{jn} &= n_j \\ \phi_{Dn} &= 0 \end{aligned} \tag{3.22}$$

where n_j is the generalized normal vector component in j-direction. From this, the equation of motion of a rigid floating body with 6-DOF in a regular wave can be expressed in the frequency domain as shown in Equation 3.23. The complex 6 by 1 motion vector $\mathbf{X}(\omega, \beta)$ can be found from the equation of motion, by applying Newton's law and including the added mass, damping and excitation force contributions acting on the panels (*SESAM USER MANUAL WADAM v8.1* 2010).

$$\left[-\omega^2(\mathbf{M} + \mathbf{A}(\omega)) + i\omega\left(\mathbf{B}(\omega)\right) + \mathbf{C}\right] \mathbf{X}(\omega, \beta) = \mathbf{F}(\omega, \beta) \tag{3.23}$$

Where $\mathbf{M}$ and $\mathbf{C}$ represent the 6 by 6 body inertia and hydrostatic restoring matrices, respectively. $\mathbf{A}(\omega)$ and $\mathbf{B}(\omega)$ represent the 6 by 6 frequency-dependent added mass and damping matrices, while $\mathbf{F}(\omega, \beta)$ is the 6 by 1 complex exciting force vector for frequency ω and incident wave heading angle β.

3.1.6 Frequency-Domain

In the frequency-domain approach, the steady-state response for each wave frequency is solved, which produces RAOs. The frequency-domain approach is based on the horizontal extent of the domain being infinite, and that the waves have been propagating since eternal time, there is, therefore, no transient phase. Solving the linearized boundary value problem (BVP) in the frequency domain requires just one computation per wave frequency.
From Equation 3.4, it is seen that the surface process is either a sine or cosine function with an amplitude, a wave frequency and a phase. When performing a frequency domain analysis, only these three parameters are needed to describe each quantity. The wave frequency ω is not changing for the different quantities, while the amplitudes and phases will differ. This means that for a

given wave frequency, it is the amplitude and phase for each of the quantities the linearized BVP is solved to find. The output from a frequency-domain solver like Wadam is a list of amplitudes and phases for each degree of motion for a given wave frequency and heading.

3.1.7 Non-Linear Effects

Mean Wave Drift Forces

According to Faltinsen (1993), the mean wave-drift forces in a potential flow model are "due to a structure's ability to cause waves". The mean drift forces are found by integrating the fluid pressure on the wetted-surface of the body. The drift forces have four contributions; the pressure from the relative vertical motion between the structure and the waves, the pressure drop because of the first-order velocity squared, the pressure from first-order pressure on a moving object due to first-order motions and lastly, the pressure from the product of the first-order initial forces and the first-order rigid rotations (Hanssen et al., 2013). Large relative motions between the structure and the fluid will cause large drift forces. Short waves that cause small relative motions will also contribute to the drift forces as the body diffracts the waves back into the incoming waves. In Wadam, the mean drift force is calculated by one of the following methods (*SESAM USER MANUAL WADAM v8.1* 2010):

- Momentum conservation in the three horizontal degrees of freedom
- Pressure integration in all the six degrees of freedom.

In this thesis, the mean wave force is calculated by both momentum conservation and direct pressure integration.
By using the conservation of momentum method, the horizontal force component in i direction averaged over one period of oscillation is found according to Equation 3.24 (Faltinsen, 1993):

$$\bar{F}_i = -\iint_{S_\infty} [pn_i + \rho V_i V_n]\, ds \tag{3.24}$$

where S_∞ is the time-dependent wetted-surface of a non-moving cylindrical control surface away from the body, p is the wave pressure acting on S_∞, ρ is the water density, V_i is the linear fluid velocity in direction i and V_n is the normal component of the fluid velocity on S_∞. Utilizing Equation 3.24, only the first-order velocity potential is necessary because the second-order velocity potential does not contribute to the mean wave force.

Using the direct pressure method, the mean drift force in regular waves is written as:

$$\bar{F}_i = \frac{\rho g \zeta_a^2}{2} \int_{L_1} \sin^2(\theta + \beta) n_i dl \quad i = 1, \ldots, 6 \tag{3.25}$$

where β is the wave propagation angle, n_i is the normal vector, l is the tangential vector and θ is the angle between the x-axis and the tangential vector.

Slowly Drift Motions

Slow-drift motions are resonance oscillations that are excited at frequencies that are low compared with the incoming-wave frequencies, which is due to nonlinear interactions in a steady-state condition. These slowly-varying motions are relevant for stationary structures that are moored or kept in position by a dynamic-positioning system (Greco, 2019). Slow-drift motions can not be caused by body interactions with one single regular wave, because a regular wave with frequency ω can only cause second-order effects connected to the mean drift force and a sum-frequency oscillation behaviour with frequency 2ω (Greco, 2019). The second-order frequency effect that is responsible for

the slow-drift motion of a body needs minimum two waves with different frequencies. The second-order velocity potential ϕ_2 contributes to the slow-drift loads, therefore, the first and second-order problems need to be solved in order to estimate these loads (Greco, 2019). A general formula for slow-drift loads in time domain $\boldsymbol{F}^{(2)}(t)$ can be formulated as given by Engebretsen et al. (2020):

$$\boldsymbol{F}^{(2)}(t) = \sum_{i=1}^{N}\sum_{j=1}^{N} \zeta_i^{(1)}\zeta_j^{(1)}[P_{ij}\cdot\cos\left((\omega_i-\omega_j)\,t+(\epsilon_i-\epsilon_j)\right)+Q_{ij}\cdot\sin\left((\omega_i-\omega_j)\,t+(\epsilon_i-\epsilon_j)\right)] \quad (3.26)$$

where $\zeta_i^{(1)}$ and $\zeta_j^{(1)}$ are the wave amplitudes, ω_i and ω_j are the wave frequencies, and ϵ_i and ϵ_j are the random phase angles. Further, $\boldsymbol{P_{ij}} = \boldsymbol{Re}(\boldsymbol{QTF}(\omega_i,\omega_j))$, and $\boldsymbol{Q_{ij}} = \boldsymbol{Im}(\boldsymbol{QTF}(\omega_i,\omega_j))$, are the real (in-phase) and imaginary (out-of-phase) part of the Quadratic Transfer Function (QTF), respectively. The low frequency force oscillates at the difference frequencies $\omega_i - \omega_j$.

For a given difference-frequency $\Delta\omega$, the second-order difference-frequency load spectral density in the frequency-domain can be written as (Engebretsen et al., 2020):

$$S_F(\Delta\omega) = 8\int_0^\infty S_\zeta(\omega+\Delta\omega)S_\zeta(\omega)|\boldsymbol{QTF}(\omega+\Delta\omega,\omega)|^2 d\omega \quad (3.27)$$

where S_ζ is the spectral density of the wave elevation and $S_\zeta(\omega+\Delta\omega)\cdot S_\zeta(\omega)$ represent the spectral density of the wave group. Lastly, the amplitude of the QTF, $|\boldsymbol{QTF}(\omega+\Delta\omega,\omega)|$ is further given as:

$$|\boldsymbol{QTF}(\omega+\Delta\omega,\omega)| = \sqrt{\boldsymbol{P}(\omega+\Delta\omega,\omega)^2+\boldsymbol{Q}(\omega+\Delta\omega,\omega)^2} \quad (3.28)$$

Figure 3.2, illustrates the amplitude of the QTF which can be represented as a square matrix. The color coding in the matrix, indicates that cells with the same color have the same difference frequency $\Delta\omega$. The diagonal of the matrix, highlighted in blue cells, is referred to as the *main diagonal* of the QTF. On the main diagonal the difference frequency $\Delta\omega = 0$, and thus corresponds to the mean-drift force.

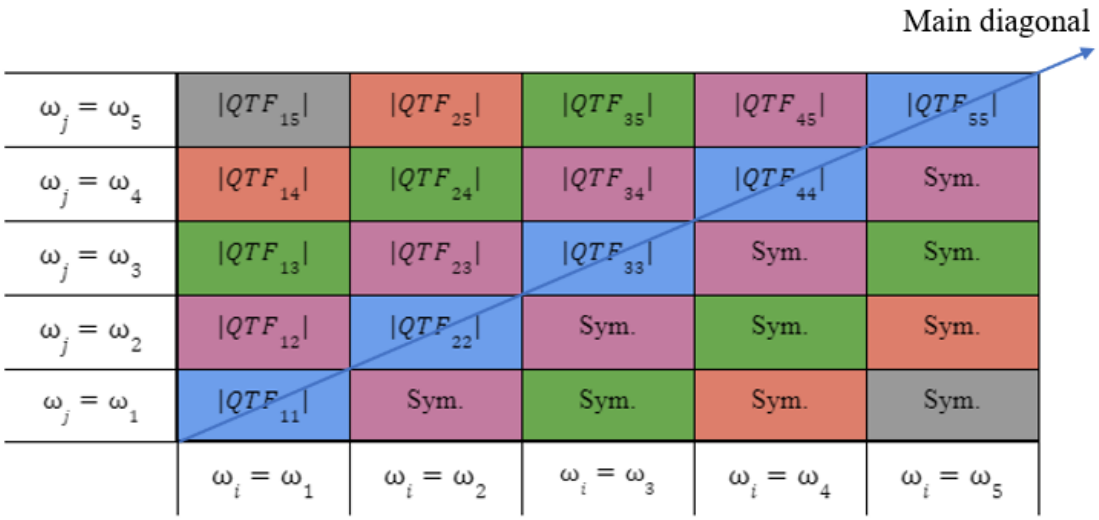

Figure 3.2: Illustration of example QTF matrix.

Newman's Approximation

From the mean drift force, Newman (1974) proposed an approximation of the full QTF, where only the values on the main diagonal are used to estimate the off-diagonal terms. Newman's approximation is given by different variations of formulations as seen in Hauteclocque et al. (2012) however, a general formulation of the approximation in the k - direction is given in Equation 3.29 as formulated by Nuno Fonseca (2018):

$$QTF_k(\omega_1, \omega_2) = 0.5\left[QTF_k(\omega_1, \omega_1) + QTF_k(\omega_2, \omega_2)\right] \tag{3.29}$$

where, ω_1 and ω_2 are frequencies of a pair of incident harmonic waves.

Using Newman's approximation does not provide an exact description of the full QTF. However, for small difference-frequency values $\omega_j - \omega_i$, which is close to the main diagonal where $\omega_j = \omega_i$, Newman's approximation is considered a good approximation. Small difference-frequency values indicate large periods of oscillation. This is relevant when the involved slow-drift motion natural period is large. Hence the application of Newman's approximation is best suited for horizontal motions of moored systems in deep waters and has, in general, been considered acceptable for such systems (DNV, 2010c). In the vertical plane, however, Newman's approximation is expected to underestimate the slow drift forces (DNV, 2010c).

Furthermore, the time-domain analysis using Newman's approximation becomes significantly more computationally efficient compared to the full QTF (Engebretsen et al., 2020).

Wave Viscous Drag Effects

The viscous effects become increasingly important for structures that experience sea states where the relation between the wavelength and the diameter of the structure is large (Faltinsen, 1993). The importance of viscous forces from waves is classified in Figure 3.3.

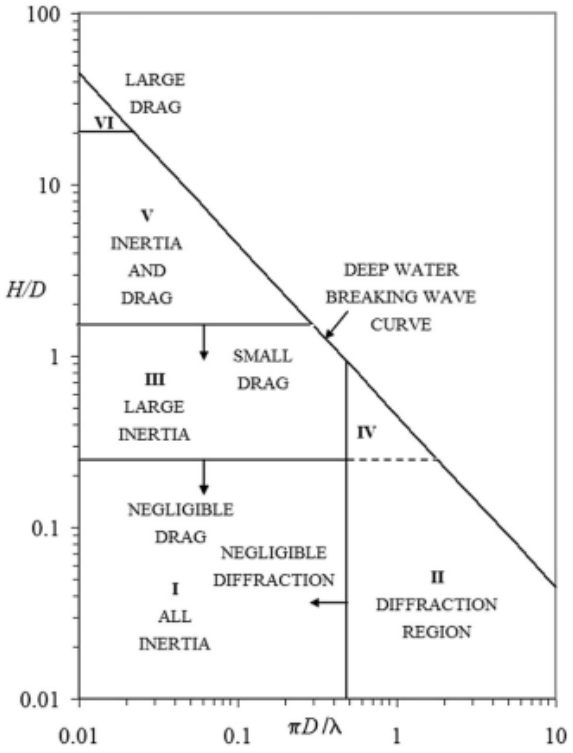

Figure 3.3: Different wave force regimes Chakrabarti (1987).

A prominent way of calculating wave loads on a cylindrical structure including the viscosity, is given by the Morison equation, which corresponds to a long-wave approximation. By superimposing the inertia force obtained from potential flow theory and the drag force obtained from the viscous flow on a cylindrical structure, the Morison equation for a moving object is described as (Bussemakers, 2020):

$$dF = \underbrace{A\rho C_M \frac{\partial u_1}{\partial t} dz - A\rho \left(C_M - 1\right) \ddot{\eta}_1 dz}_{\text{Inertia component}} + \underbrace{\frac{1}{2}\rho C_D D \left|u_1 - \dot{\eta}_1\right| \left(u_1 - \dot{\eta}_1\right) dz}_{\text{Drag component}} \tag{3.30}$$

where

- A is the cross-sectional area of a strip
- ρ is the water density
- $\frac{\partial u_1}{\partial t}$ is the flow acceleration
- C_m is the is the inertia coefficient
- $\ddot{\eta}_1$ is the body acceleration
- $\dot{\eta}_1$ is the body velocity
- u_1 is the flow velocity
- D is the diameter of the body

The inertia component partially depends on the body acceleration, and the drag component depends on the relative velocity between the flow and the body. The load is calculated per unit length along a slender structure, as the inertia component comes from the strip theory and the long-wave approximation applied to the potential solution on a cylinder.
The inertia component is not entirely dependent on the relative acceleration since the potential flow Froude-Kriloff contribution does not depend on the body acceleration. Therefore, the Morison equation is not able to account for hydrodynamic coupling effects obtained from the potential flow theory added mass matrix. Moreover, both the drag and added mass components in the Morison equation are independent of the frequency. It can further be observed that the second term in the inertia component is independent of the inertia coefficient. This is because radiation loads are included as the body is moving in the water (Bussemakers, 2020).

Current Viscous Loads

The current velocity can be decomposed into two components for offshore structures consisting of slender structural parts such as the columns and pontoons of a semi-submersible. One in the longitudinal direction and one in the cross-flow direction, as seen in Figure 3.4. As outlined by Faltinsen (1993), the mean force per unit length is given by:

$$F_D = \frac{\rho}{2} C_D D U_{c,N}^2 \tag{3.31}$$

$$F_L = \frac{\rho}{2} C_L D U_{c,N}^2 \tag{3.32}$$

where D is the diameter of the circular cylinder. F_D is the mean force in the cross-flow direction, the same direction as the cross-flow component $U_{c,N}$ of the current velocity. F_L is the mean force perpendicular to F_D. Lastly, C_D and C_L are the drag and lift coefficients, which are determined by empirical results (Faltinsen, 1993).

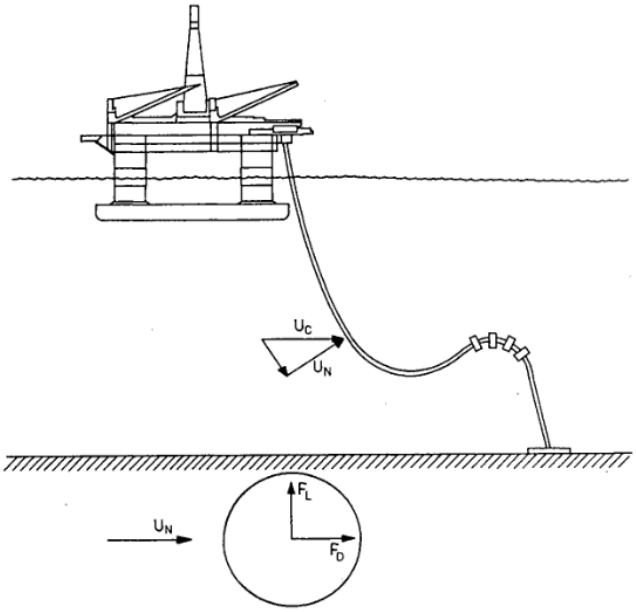

Figure 3.4: Current force components on a slender element (Faltinsen, 1993).

3.2 Dynamic Response for a One Degree of Freedom Linear System

The linear response of a one degree of freedom system in a sinusoidal load is described in this section to understand and interpret the behaviour at sea of the multi-degree of freedom system of the FWT. The theory is based on Larsen (2015).

For a damped system, the response of the system for a given load history $P(t)$ can be expressed in complex notation, by the assumption that the load is harmonic. This gives the equilibrium equation:

$$m\ddot{x} + c\dot{x} + kx = \mathbb{R}\mathrm{e}\left\{\tilde{P}e^{i(\omega t)}\right\} = P_0\cos(\omega t + \epsilon) \tag{3.33}$$

where only the real part of the load is of interest, indicated by $\mathbb{R}\mathrm{e}$. The maximum load P_0 is a real number, ω represents the angular frequency of the load and ϵ is the phase angle. The particular solution according to Equation 3.34 must be a harmonic function with the same frequency ω as the external load and can be written on the form:

$$u_P = \mathbb{R}\mathrm{e}\left\{\tilde{x}e^{i(\omega t)}\right\} \tag{3.34}$$

where $\tilde{x}$ is an unknown complex number. By inserting this into Equation 3.33 and solving for $\tilde{x}$, this gives the following expression as shown in Equation 3.35.

$$\tilde{x} = \frac{\tilde{P}}{-\omega^2 m + i\omega c + k} = \tilde{P}\frac{1}{k}\frac{1}{1-\beta^2 + 2\xi\beta i} \tag{3.35}$$

The particular solution is thus:

$$u_P = \mathbb{R}\left\{\tilde{x}e^{i(\omega t)}\right\} = |\tilde{x}|\cos(\omega t + \epsilon + \phi) \tag{3.36}$$

where

$$|\tilde{x}| = \frac{P_o}{k} \frac{1}{\sqrt{(1-\beta^2)^2 + (2\xi\beta)^2}} \tag{3.37}$$

$$\phi = \tan^{-1}\left(\frac{-2\xi\beta}{1-\beta^2}\right) \tag{3.38}$$

Here $\beta = \omega/\omega_0$ is the ratio between the load frequency and the undamped natural frequency, whereas ξ is the damping ratio. The amplitude of the response for the particular solution u_p is a product of the static response and a factor that reduces or enlarges the solution, depending on the damping and frequency ratio as seen in Equation 3.39:

$$\text{DLF} = \left|\frac{u_{\max}}{u_{st}}\right| = \frac{1}{\left[(1-\beta^2)^2 + (2\xi\beta)^2\right]^{\frac{1}{2}}} \tag{3.39}$$

For a 1DOF system, the dynamic response will be characterized by a dynamic load factor (DLF), and a phase angle ϕ between the load and response. The DLF denotes the ratio between the dynamic and static response for the relevant load.

Figure 3.5 displays the DLF and phase angle as a function of the frequency ratio β for given values of damping ratios ξ.

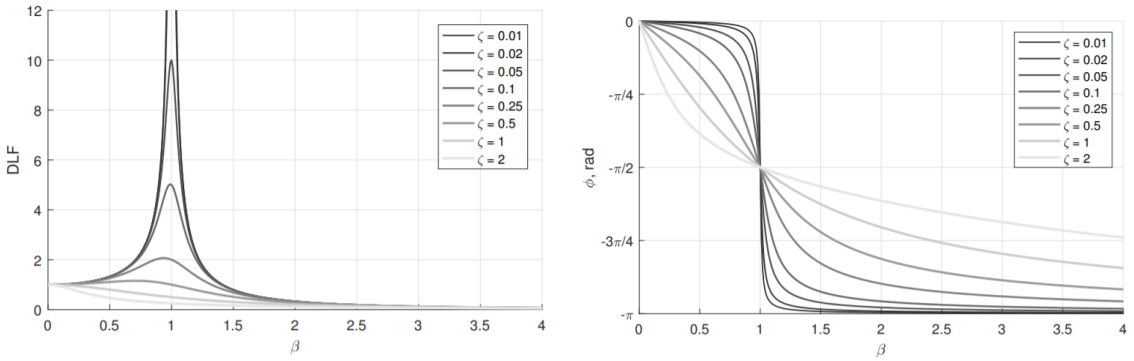

(a) (b)

Figure 3.5: DLF as a function of β for given values of ξ (a) and phase angle between the load and response as a function of β for given values of ξ (b) (Larsen, 2015).

The dynamic response is characterized by 3 different regions of the DLF as outlined by Larsen (2015):

- Stiffness dominated, where the load frequency is lower than the eigenfrequency, $\beta < 1$
- Resonance, where the load frequency is equal or close to the eigenfrequency, $\beta \approx 1$
- Inertia dominated, where the load frequency is higher than the eigenfrequency, $\beta > 1$

3.3 Aerodynamic Theory

This section will briefly describe the aerodynamic theory used in the time-domain simulations in SIMA.

3.3.1 1-D Momentum Theory for an Ideal Wind Turbine

A wind turbine is a device that extracts mechanical energy from the kinetic energy of the wind. To determine the thrust and power from an ideal turbine rotor, a simple model is used, where the turbine is represented by a uniform actuator disk creating a discontinuity of pressure in the rotor plane (Manwell et al., 2009). A boundary surface, which contains the affected air mass is represented as a control volume, where the control volume boundaries are the surface of a stream tube and two cross-sections of a stream tube (Manwell et al., 2009), as illustrated in Figure 3.6. This method is based on the following assumptions, as outlined by Manwell et al. (2009).

- Homogenous, incompressible, steady-state fluid flow.
- No frictional drag.
- An infinite number of blades.
- Uniform thrust over the disc or rotor area.
- Non-rotating wake.
- Pressure equal to ambient pressure far from the disk.

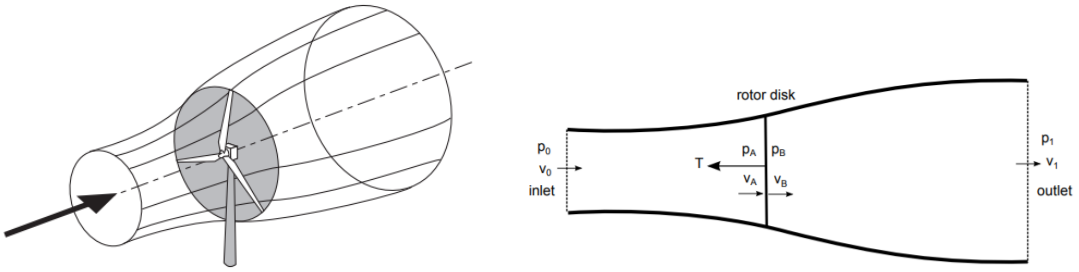

(a) (b)

Figure 3.6: Illustration of boundary surface (a) and actuator disk model of a wind turbine (b) (Bachynski, 2021a).

Through the One-Dimensional Momentum theory, the thrust force and power extracted by the wind can be expressed as given by Manwell et al. (2009):

$$T = \frac{1}{2}\rho_{air} A v_o^2 4a(1-a) \tag{3.40}$$

$$P = \frac{1}{2}\rho_{air} A v_o^3 4a(1-a)^2 \tag{3.41}$$

where ρ_{air} is the density of the air, A is the rotor disk area, v_o is the velocity of the incoming wind and a is the axial induction factor. The corresponding thrust and power coefficients representing the fraction of thrust on the turbine and power extracted by the rotor, are given by:

$$C_T = \frac{T}{\frac{1}{2}\rho_{air} {v_0}^2 A} \tag{3.42}$$

$$C_P = \frac{P}{\frac{1}{2}\rho_{air} v_0^3 A} \tag{3.43}$$

The axial induction factor is defined as the fractional decrease in wind velocity between the inlet v_o and the rotor plane v_A, as shown in Equation 3.44:

$$a = \frac{v_0 - v_A}{v_0} \tag{3.44}$$

The axial induction factor is restricted to be in the interval of [0, 0.5], where for values of $a > 0.5$ the flow stops behind the rotor and the simple theory is no longer applicable. The maximum value of the power coefficient C_P occurs when $a = \frac{1}{3}$, and is denoted as Betz limit, $C_P = \frac{16}{27}$, which applies for zero rotation (Manwell et al., 2009).

3.3.2 Ideal Turbine with Wake Rotation

The torque exerted by the blades causes the air to rotate in a direction opposite to that of the rotor, meaning that the air gains an angular momentum so that the air particles in the wake of the rotor disk will have a velocity component tangential to the rotation as well as an axial component (Tony Burton and Bossanyi, 2011). The effect of wake rotation in the one-dimensional momentum theory is disregarded, whereas for an ideal turbine that is rotating and giving kinetic energy to the wake, the hypothetical Betz limit cannot be achieved. The power coefficient for the full rotor is thus given as outlined by Manwell et al. (2009):

$$C_P = \frac{8}{\lambda^2} \int_0^{\lambda} a'(1-a)\lambda_r^3 d\lambda_r \tag{3.45}$$

where a' is the angular induction factor, λ is the tip speed ratio and λ_r is the local tip speed ratio.

The angular induction factor a' is given by:

$$a' = \frac{\omega}{2\Omega} \tag{3.46}$$

where ω is the angular velocity imparted to the free stream, whereas Ω is the angular velocity of the rotor.

The tip speed ratio λ is defined as the ratio between the blade tip speed and the free stream wind speed, where the local tip speed ratio λ_r denotes the ratio of the rotor speed at a given radius and the free stream wind speed.

$$\begin{aligned} \lambda &= \frac{\Omega R}{v_0} \\ \lambda_r &= \frac{\lambda r}{R} \end{aligned} \tag{3.47}$$

R is the radius of the rotor.

Accounting for the effect of wake rotation, the maximum power coefficient for an ideal horizontal axis wind turbine is hence a function of the tip speed ratio, as illustrated in Figure 3.7. For low tip speed ratios, the turbine uses some power from the wind to set the wind into a rotation, which gives a loss. However, the maximum power coefficient approaches the Betz limit for high tip speed ratios.

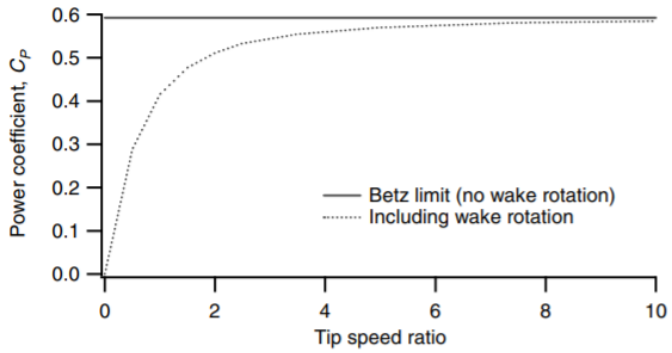

Figure 3.7: Theoretical maximum power coefficient as a function of tip speed ratio for an ideal horizontal axis wind turbine, with and without wake rotation (Manwell et al., 2009).

3.3.3 Blade Element/Momentum Theory

The blade element theory is based on the combination of an ideal turbine (the one-dimensional actuator disc model), including wake rotation and aerodynamic lift and drag on blade sections determined by the two-dimensional airfoil theory. The thrust and torque for an annular ring based on the momentum theory are expressed as (Bachynski, 2021a):

$$\mathrm{d}T = 4a(1-a)\frac{1}{2}\rho_{air}v_o^2 2\pi r \ \mathrm{d}r \tag{3.48}$$

$$\mathrm{d}Q = 4a'(1-a)\frac{1}{2}\rho_{air}v_0\Omega r^2 2\pi r \ \mathrm{d}r \tag{3.49}$$

Further, the thrust and torque can also be found by considering an airfoil section. Figure 3.8 illustrates an airfoil including the incoming wind v_0, the velocity of the blade due to the rotor rotation ωr, the induced axial velocity $a\omega r$, and the induced tangential velocity $a'\omega r$. The force components normal, and tangential to the rotor plane can be expressed based on the lift force L, drag force D and the angle of attack ϕ. From Figure 3.8 it is seen that the thrust and torque can be expressed as (Bachynski, 2021a):

$$dT = B(L\cos\phi + D\sin\phi)dr \tag{3.50}$$

$$dQ = Br(L\sin\phi - D\cos\phi)dr \tag{3.51}$$

where B is the number of blades.

The axial induction factor is then obtained by combining Equation 3.48 and 3.50, while the tangential induction factor is obtained by combining Equation 3.49 and 3.51. The axial and tangential induction factors are then expressed as (Bachynski, 2021a):

$$a = \frac{1}{\frac{4F\sin^2\phi}{\sigma_s C_n} + 1} \tag{3.52}$$

$$a' = \frac{1}{\frac{4\sin\phi\cos\phi}{\sigma_s C_t} + 1} \tag{3.53}$$

where $C_n = C_l\cos\phi + C_d\sin\phi$ is the normal coefficient, $C_t = C_l\sin\phi - C_d\cos\phi$ is the tangential coefficient and $\sigma_s = \frac{Bc}{2\pi r}$ is the solidity ratio.

The determination of the axial induction factor a and the tangential induction factor a' for each section is based on an iteration process, where the start values of the induction factors are guessed and thereafter used to calculate the angle of attack and consequently the lift and drag force. The induction factors are then updated using Equation 3.52 and 3.53 (Bachynski, 2021a).

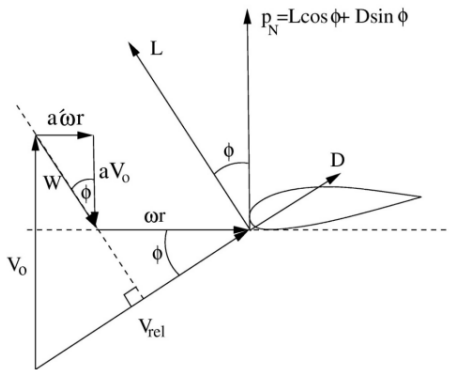

Figure 3.8: Airfoil section on the rotor plane (Bachynski, 2021d).

3.3.4 Corrections to BEM

The BEM theory requires some corrections due to simplifications imposed by the assumptions. This section will briefly describe these corrections and are based on the lecture notes from Bachynski (2021a).

Prandtl Correction

The air tends to flow around the blade tip from the lower to the upper side of the blade. This results in a lower aerodynamic force than one would otherwise have. To include this effect in the BEM theory, the Prandtl correction is used on the forces from the blade elements.

Glauert Correction

The BEM theory is not valid for induction factors $a > 0.5$ as the wind velocity in the far wake would then be negative. To avoid nonphysical flow in the far wake for high induction factors, the Glauert correction is used.

Dynamic Wake

In the BEM model, the induction factors will be updated immediately if there is a change in the incoming wind velocity, the blade pitch angle or the rotor speed. In reality, the flow can't catch up with up immediate changes. The dynamic wake effect is the time lag in the induced velocities due to the shedding and downstream convection of vorticity. Dynamic wake effects are most pronounced for rotors that are heavily loaded corresponding to high induction factors.

Dynamic Stall

The BEM method uses static lift and drag curves, and a single steady-state value of the force coefficients is given for each angle of attack. In practice, the blades will experience dynamic incoming wind, which may lead to sudden attachment and re-attachment of the flow. This may lead to large transient loads as the airfoil can experience a high lift coefficient after a sudden increase in the wind speed.

3.4 Stationkeeping Systems

Mooring systems are a crucial part of the stationkeeping system developed for floating structures in the offshore environment. From a marine operational point of view, an accurate position and motion control of floating structures is important. The mooring system generally consists of connectors, tensioning equipment, lines and anchors, where the ability to preserve a floating structure on station under various environmental conditions is the most vital requirement for a mooring system (Ma et al., 2019).

Mooring systems are often divided into two main categories; temporary and permanent mooring systems, which mainly are based on the duration of the offshore operation. A temporary mooring system has a stationkeeping duration from a few days up to several months, while a permanent mooring system can have a stationkeeping duration of several years up to several decades (Ma et al., 2019). For floating offshore wind turbines, a permanent mooring system is preferred as the expected lifetime of a FOWT is approximately 25 years.

In addition to the duration of the offshore operation, the mooring system can be grouped into catenary mooring systems and taut leg mooring systems depending on the profiles and configurations (Ma et al., 2019), as illustrated in Figure 3.9. The catenary mooring system, which is the most widely used system, has a part of the line laying on the seabed and uses the self-weight of the mooring line to apply restraining forces on the floating structure (Faltinsen, 1993). For the taut leg mooring system, on the other hand, the mooring lines are taut from the anchor at the seabed to the fairlead on the floater. In this system, no line is laying on the seabed, resulting in a smaller anchor footprint compared to a catenary system (Ma et al., 2019). In regards to the area of application, the catenary mooring system is most suitable for shallow to medium depth waters. In contrast, a taut leg mooring system is more suitable for deep or ultradeep waters.

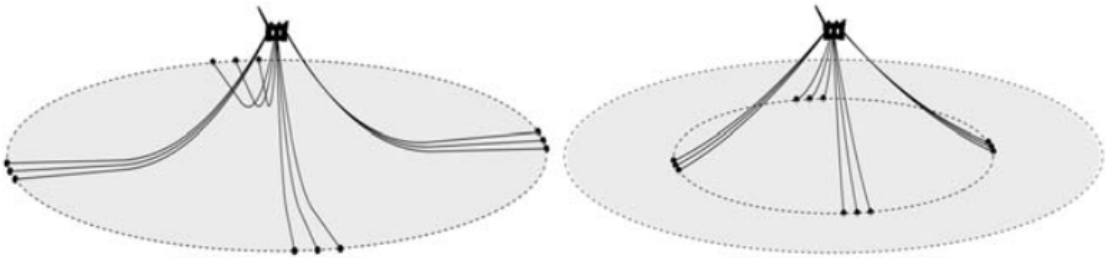

Figure 3.9: Catenary mooring system (left) and Taut leg mooring system (right) (Ma et al., 2019).

3.5 OO-Star Upscaling Procedure

This section describes the scaling laws used for the OO-Star floater upscaling procedure to enable the use of the same wind turbine for both selected floaters.

3.5.1 The Square-Cube Law

In a wind turbine system, the main value is in the energy it produces, which is proportional to the rotor's swept area and thus to the square of the diameter. The cost is related to the system's mass of material and is proportional to volume, hence diameter cubed. This relationship is referred to as the square-cube law, and it implies that when considering a single wind turbine system, the cost per unit capacity will increase linearly with the turbine scale (Jamieson, 2011).

3.5.2 Scaling Laws

There are different methods used for scaling floating offshore wind turbines today. In the present work, where only the semi-submersible floating platform is to be scaled, the scaling factor is used to scale the entire geometry. This ensures geometric self-similarity, as geometric similitude. In particular, geometric similitude requires that all dimensions are scaled with the same scaling factor (Davey et al., 2020). The scaling factor can be determined by one of the following methods as, according to Leimeister et al. (2016), there is no strict rule on what type of method to be used. If geometrical similarity is enforced, the power and weight, which are the main criteria used, is scaled according to $P \sim s^2$ and $m \sim s^3$, respectively, where s is the scaling factor (Sieros et al., 2012).

Power Scaling Rule

The geometrical scaling factor s, is determined by the power rating of new and initial turbine designs, utilizing the fact that the power is usually the predefined value of the desired upscaled turbine (Souza et al., 2021):

$$s = \sqrt{\frac{P_{new}}{P_{initial}}} \tag{3.54}$$

here P_{new} is the desired power rating of the upscaled wind turbine, and $P_{initial}$ is the initial power rating of the turbine.

Cube Root of the Ratio of Turbine Masses

The scale parameter S, is determined by taking the cube root of the ratio of the new and initial turbine masses (Kikuchi and Ishihara, 2019):

$$S = \sqrt[3]{\frac{M_{turbine}^{upscale}}{M_{turbine}^{original}}} \tag{3.55}$$

where $M_{turbine}^{upscale}$ is the mass of the new turbine mass, and $M_{turbine}^{original}$ is the mass of the original turbine that is to be upscaled.

3.6 Coupled Time-Domain Analysis

This section will briefly describe the coupling effects in a fully coupled time-domain analysis performed in SIMA. A more thorough review of the time-domain solution of SIMO-RIFLEX will be given in Section 3.7.

A floating wind turbine is subjected to response contributions from loads connected to the wind, waves and currents. Furthermore, the structural dynamics of the flexible slender elements of the turbine and the mooring lines will give a response contribution to the floating wind turbine. The interaction between these different response contributions leads to important coupling effects, which in this context are (Kvittem, 2014):

- Aerodynamic damping from the rotor on the floater motion
- The floater motions influence the wind forces
- The mean position of the floater influences the wind and mooring forces
- The dynamics of the floater are influenced by the mooring dynamics (inertia and damping)

In the coupled time-domain analysis, the rigid body and the flexible slender FE-elements are connected at common nodes. The motion equilibrium for the two systems is solved individually but simultaneously, exchanging external forces and displacements at every time step (MARINTEK and Veritas, 2010). Iteration is used at every time step to achieve motion equilibrium for both the flexible elements and the rigid body.

3.6.1 Non-Linear FEM

The system response of the FOWT is calculated including the interaction between the blade dynamics, mooring dynamics and the tower motions. The dynamics of these slender flexible elements are computed in RIFLEX by a non-linear finite element analysis (FEM). Non-linear FEM can handle the effect of large displacements, non-linear material behavior or changing boundary conditions (Kvittem, 2014). In a coupled analysis of a FOWT, the relevant non-linearities are connected to the geometric structural non-linearities, such as the effect of large displacements and quadratic load formulation in the thrust force from the turbine and the drag force on the slender elements.

3.7 Time-domain solution of SIMO-RIFLEX

This section will thoroughly review how the SIMO codes solve the equation of motion in the time domain by the convolution integral and which time integration methods are available in SIMO. Further, the dynamic time-domain solution strategy in RIFLEX will be described, together with the time integration methods available in RIFLEX. The theory described in this section is outlined according to the SIMO Theory Manual (SINTEF-Ocean, 2021b) and to the RIFLEX Theory Manual (SINTEF-Ocean, 2021a).

3.7.1 Time-Domain Dynamic Analysis - SIMO

The equation of motion that SIMO is trying to solve in the time domain is:

$$M\ddot{x} + C\dot{x} + D_1\dot{x} + D_2 f(\dot{x}) + K(x)x = q(t, x, \dot{x}) \tag{3.56}$$

where

M is the inertia load of the system

C is frequency-dependent potential damping matrix

D_1 is the linear damping matrix

D_2 is the quadratic damping matrix

f is a vector function where each element is given by $f_i = \dot{x}_i \left|\dot{x}_i\right|$

K is hydrostatic stiffness

q is the exciting force vector

x, $\dot{x}$, $\ddot{x}$ are the position, velocity and acceleration respectively

t is the simulation time

There are two different solution methods to solve the equation of motion above: solution by convolution integral and solution of separation of motions. The solution of separation of motions is an alternative to solving the whole differential Equation 3.56 in the time-domain by use of the retardation function. The motions are then separated into a high-frequency part and a low-frequency part. This solution will not be further described as the solution by convolution integral is the method that is used in the time-domain analysis performed in this master's thesis.

Solution by Convolution Integral

The default in SIMO is to solve Equation 3.56 by the convolution integral, the following section will give a review of how this is done.

Assuming that the equation of motion can be expressed as:

$$m + A(\omega)\ddot{x} + C(\omega)\dot{x} + Kx = f'(t) = q - D_2 f(\dot{x}) - D_1\dot{x} \tag{3.57}$$

where m is the body mass matrix and A is the frequency-dependent added mass.

Considering only the frequency-dependent coefficients, the equation of dynamic equilibrium can be written as:

$$A(\omega)\ddot{x} + C(\omega)\dot{x} = f(t) = f'(t) - Kx - m\ddot{x} \tag{3.58}$$

provided that the forces on the right side of the equation vary sinusoidally at one single frequency, ω.

By writing Equation 3.58 in the frequency domain and using the relations $A(\omega) = A_\infty + a(\omega)$ and $B(\omega)C_\infty + c(\omega)$ where A_∞ and $C_\infty = 0$, the equation of dynamic equilibrium can be written as:

$$-\omega^2 A_\infty X(\omega) + (i\omega a(\omega) + c(\omega))i\omega X(\omega) = F(\omega) \tag{3.59}$$

Taking the inverse Fourier transform of Equation 3.59 gives:

$$A_\infty \ddot{x}(t) + \int_0^t h(t-\tau)\dot{x}(\tau)\mathrm{d}\tau = f(t) \tag{3.60}$$

By substituting $f(t)$ from Equation 3.58 and $f'(t)$ from Equation 3.57, the equation of motion then becomes:

$$(m + A_\infty)\,\ddot{x} + D_1\dot{x} + D_2 f(\dot{x}) + Kx + \int_0^t h(t-\tau)\dot{x}(\tau)\mathrm{d}\tau = q(t, x, \dot{x}) \tag{3.61}$$

The retardation function, $h(\tau)$, is calculated by transforming the frequency-dependent added-mass and damping

$$h(\tau) = \frac{1}{2\pi}\int_{-\infty}^{\infty} c(\omega) + i\omega a(\omega)e^{i\omega t}\ \mathrm{d}\omega = \frac{1}{2\pi}\int_{-\infty}^{\infty} H(\omega)e^{i\omega t}\ \mathrm{d}\omega \tag{3.62}$$

For $\tau < 0$, the retardation function $h(\tau) = 0$, meaning that the process does not have any memory effect of the future. The two terms in Equation 3.62 must therefore be opposite for $\tau < 0$ and identical for $\tau > 0$, mathematically this becomes:

$$h(\tau) = \frac{2}{\pi}\int_0^{\infty} c(\omega)\cos(\omega\tau)\mathrm{d}\omega = -\frac{2}{\pi}\int_0^{\infty} \omega a(\omega)\sin(\omega\tau)\mathrm{d}\omega \tag{3.63}$$

for $\tau > 0$.

The frequency-dependent added mass and damping is then found from the retardation function:

$$\begin{aligned} a(\omega) &= -\frac{1}{\omega}\int_0^{\infty} h(\tau)\sin(\omega\tau)\mathrm{d}\tau \\ c(\omega) &= -\int_0^{\infty} h(\tau)\cos(\omega\tau)\mathrm{d}\tau \end{aligned} \tag{3.64}$$

To calculate the retardation function, either the frequency-dependent added mass or frequency-dependent damping and one value of the added mass is required. The relation between the frequency-dependent added mass and damping is known as the Kramers-Kronig relation. In SIMO, it is the frequency-dependent damping that is used for calculating the retardation functions.

Methods for Numerical Integration - SIMO

In SIMO there are three methods available for the numerical integration; the modified Euler method, the 3rd-order-Runga-Kutta method and the Newark-β predictor-corrector method. The modified Euler method differs from the ordinary method in that $\dot{x}_{k+1}$ is used instead of $\dot{x}_k$, this ensures stability when the method is applied to linear models where there is no damping.

3.7.2 Time-Domain Dynamic Analysis - RIFLEX

The dynamic equilibrium of a spatially discretized finite element system model in RIFLEX is described as:

$$R^I(r, \ddot{r}, t) + R^D(r, \dot{r}, t) + R^S(r, t) = R^E(r, \dot{r}, t) \tag{3.65}$$

where

- R^I is the inertia vector
- R^D is the damping vector
- R^S is the internal structural reaction force vector
- R^E external force vector
- r, $\dot{r}$, $\ddot{r}$ is the structural displacement, velocity and acceleration vectors, respectively.

The system described in Equation 3.65 is a nonlinear system of differential equations due to the displacement dependencies in the inertia and damping forces and the coupling between the external load and structural displacement and velocity. Additionally, there is a nonlinear relationship between the internal forces and the displacements.

Inertia Force

The inertia force in RIFLEX can be expressed as:

$$R^I(r, \ddot{r}, t) = \left[M^S + M^F(r) + M^H(r)\right] \ddot{r} \tag{3.66}$$

where

- M^S is the structural mass
- $M^F(r)$ is the mass matrix accounting for internal fluid flow
- $M^H(r)$ is the hydrodynamic mass matrix accounting for the structural acceleration terms in the Morison equation as added mass contributions in local directions. The hydrodynamic mass matrix is displacement-dependent.

Internal Structural Reaction Force

The internal reaction force is in general a nonlinear function of the nodal displacement vector. Numerically, static equilibrium is found by using a incremental loading procedure with equilibrium iterations at each load step. The principle in this approach is to accumulate the external loading in a number of small load increments. The static configuration is then found at each time step for the accumulated external load vector using the displacement vector from the previous load increment as the initial solution.

Damping Force

The damping force matrix is written as:

$$R^D(r, \dot{r}) = \left[C^S(r) + C^H(r) + C^D(r, \dot{r})\right] \dot{r} \tag{3.67}$$

where

- $C^S(r)$ is the internal structural damping
- $C^H(r)$ is the hydrodynamic damping matrix which account for diffraction effects for floating, partly submerged elements
- $C^D(r, \dot{r})$ is a matrix of specified discrete dampers which may be dependent on the displacement and velocity

To account for the energy dissipation in the structure itself, the internal structural damping must be included in the dynamic analysis. The structural damping is highly dependent on the cross sectional properties of the structure. In a dynamic analysis of slender marine structures, the most important nonlinear effects that must be considered are:

- Geometric stiffness
- Nonlinear material properties
- Nonlinear hydrodynamic loading, such as the generalized Morison equation expressed by relative velocities.
- Integration of loading to actual surface elevation
- Contact problems, such as bottom contact

Finite Element Analysis Techniques

In RIFLEX, two finite element analysis techniques can be used: nonlinear time-domain analysis and linearized time-domain analysis. The difference between the two methods is how the nonlinearities are treated.

The nonlinear time-domain analysis is a step-by-step numerical integration of the incremental dynamic equilibrium equations with a Newton-Raphson type of equilibrium iteration. This integration method gives a good description of the nonlinearities. However, a nonlinear dynamic analysis could be very time consuming as the mass, damping and stiffness matrices need to be reassembled for each time step during the iteration process.

The linearized time-domain analysis is also a step-by-step numerical integration of the dynamic equations. However, in this method, the mass, damping and stiffness matrices are linearized at the static equilibrium position, meaning that the system matrices are kept constant throughout the analysis. The nonlinear hydrodynamic loading is, however, included in the analysis. Therefore, this type of analysis is a good alternative when the nonlinear hydrodynamic loading is dominant. This analysis technique significantly reduces the computational time compared with the nonlinear analysis.

4 FOWT Concepts

Today, there is a wide range of floating foundation concepts for offshore wind turbines, where most of the designs are familiar to the oil and gas industry. In general, it is the geometry of the floating structure which determines the different foundation classes by considering how the platform counters the overturning moment generated by the wind turbine thrust load (Atcheson, 2016). Figure 4.1 presents today's foundation classes regarding floating offshore wind.

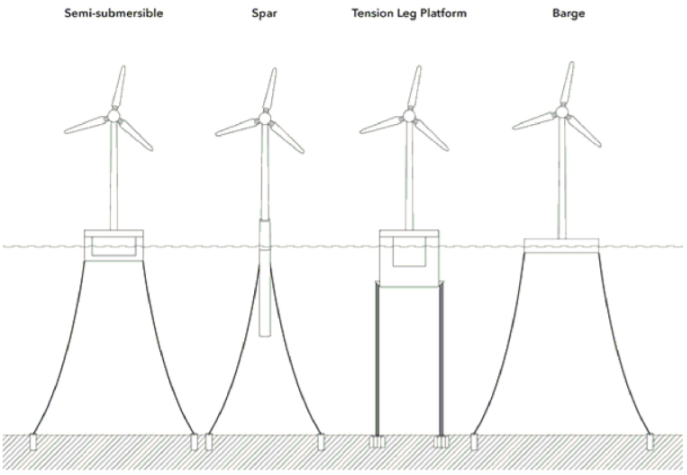

Figure 4.1: Floating foundation classes (DNV, 2018b).

Each of the floating foundation classes has different strengths and weaknesses that need to be considered when selecting a floating foundation platform, the key criteria for this selection are (Atcheson, 2016):

- Motion response and Station-keeping
- Structural loading
- Maturity of the design
- Fabrication and installation
- Safety

4.0.1 Spar-Buoy

The Spar-Buoy concept is based on a simple design consisting of a long vertical cylinder with a low waterplane area. The Spar-Buoy achieves stability by using ballast such that the centre of gravity is below the centre of buoyancy. Hence ballast stabilised. These properties provide the spar-buoy with good stability and small heave motions. As an effect of the low waterplane area, the spar-buoy experiences small wave-induced forces and low amplitudes of motions. The large hull draught needed for the spar excludes using the spar-buoy concept at locations with less than 100 m water depths. Another aspect of the large draught of the spar is the possibility of quayside assembly and towing from inshore to offshore locations. The floating foundation is held in place by three mooring lines, ensuring lower installed mooring costs. Further, the spar-buoy is inherently stable, meaning the structure will not capsize if the mooring should fail.

4.0.2 Semi-Submersible

The semi-submersible foundation concept relies on buoyancy to stabilize. This stability is due to the water plane moment of inertia, provided by the gain and loss of buoyancy from the submerged pontoons acting at large distances from the centre of gravity, thus countering the turbine thrust. The semi-submersible is the most flexible design concerning the water depth, allowing for inshore assembly and towing to installation sites. However, the structure requires a more complex fabrication method and suitable assembly facilities, leading to higher costs. Compared to the spar-buoy concept, a large part of the semi-submersible structure lies at the water's surface. Hence the semi-submersible experiences larger structural loads and amplitudes of motion, especially in heave. The floating foundation is supported by catenary mooring lines, providing lower installed mooring costs.

4.0.3 Tension Leg Platform - TLP

The TLP obtains its stability through the mooring lines, consisting of axially rigid tendons or tethers, leading to a highly loaded submerged structure. The tension system acts as a soft spring in surge, sway and yaw, corresponding to low natural frequencies, while in heave, roll and pitch, the system tension is rather stiff, providing quite high natural frequencies (DNV, 2018b). This type of floating foundation is more cost-effective than the other concepts. It also allows for lower wave-induced motions due to the low waterplane area but generally experiences horizontal wave frequency motions in the horizontal plane. The wave frequency motions will not be excited in the vertical plane as the TLP acts as a bottom fixed structure. The TLP is flexible for installation sites with intermediate water depths. However, the installation itself proves to be more challenging and time-consuming when considering tow-out operation and installation compared to the other foundation concepts.

4.0.4 Monohull Structures - Barge

A monohull structure shaped like a barge differs from the other floating foundations. The large waterplane area and its relatively small draught lead to larger structural loads and higher amplitudes of motion. The barge is designed with a moonpool to suppress wave induced loading. However, the main concern regarding this foundation is the combination of head sea and beam swell, which can form a critical condition for a monohull structure (DNV, 2018b). The barge is quite compatible with quayside assembly inshore with its small draught. Its simple shape will allow for simple fabrication techniques and towing operations to the installation site.

4.1 OO-Star and INO-WINDMOOR

The two selected floaters to be investigated in this master's thesis are the OO-Star Wind Floater and the INO-WINDMOOR base case floater. The OO-Star Wind Floater is designed by Dr. Tech. Olav Olsen AS, while the INO-WINDMOOR semi-submersible, is jointly designed by Inocean and Equinor.

OO-Star

The OO-Star concept is a semi-submersible consisting of three outer columns and a central column mounted on a three-legged, star-shaped pontoon with a bottom slab. The main material of the OO-Star is concrete. The mooring system consists of three catenary mooring lines connected to each outer column. Due to the small draft of the OO-Star, the concept does not require deep waters for assembly. The complete turbine can be fully assembled by cranes on land at the quayside before being towed out to the operational site. The OO-Star is scalable for wind turbines up to 12-15MW, without size limitations related to assembly and installation (Explorer, 2020). The concept is illustrated in Figure 4.2, while the main parameters for the OO-Star 10MW turbine are presented in Table 4.1. Lastly, the reference values of the natural periods are given in Table 4.2.

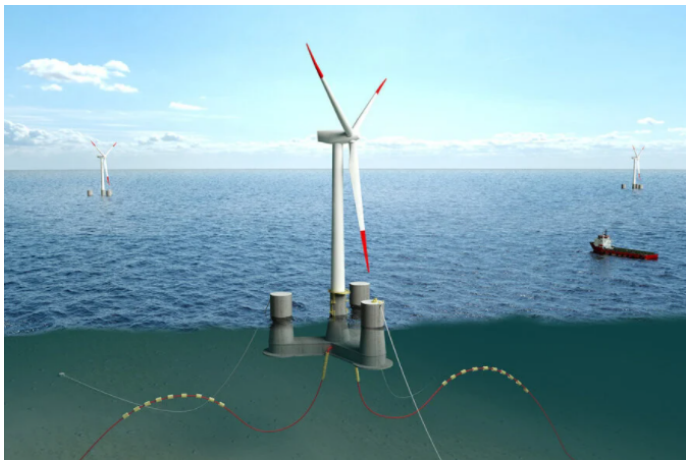

Figure 4.2: OO-Star 10 MW FWT concept (Olsen, 2020).

Table 4.1: OO-Star Wind Floater Semi 10MW platform parameters including ballast (Yu et al., 2018).

Property	Value	
Displacement	21709	[t]
Draft	22	[m]
Centre of mass below (CM) below MSL	4.23	[m]
Roll inertia about CM	9.43E+09	[kg m^2]
Pitch inertia about CM	9.43E+09	[kg m^2]
Pitch inertia about CM	1.63E+10	[kg m^2]
Tower base interface above MSL	11.0	[m]
Displaced water volume	2.3509E+04	[m^3]
Centre of buoyancy below MSL	14.23	[m]

Table 4.2: Reference values of the natural periods given in Yu et al. (2018).

DOF	Surge	Sway	Heave	Roll	Pitch	Yaw
Natural period	181.81 s	-	20.4 s	-	31.25 s	116.3 s

INO WINDMOOR 12 MW

The INO WINDMOOR 12 MW was chosen as the research candidate for the WINDMOOR project. The project started in 2019 and is a 4-year competence building project funded by the Research Council of Norway and the offshore wind industry (Inocean, 2021). The semi-submersible platform consists of three columns, connected by pontoons and deck beams. The floating platform is made of steel, and the turbine is mounted on top of one of the columns. The mooring system consists of three catenary mooring lines connected to each column. The mooring system is further described in the reference report Souza et al. (2021). Figure 4.3 illustrates the FWT concept, while the full floating wind turbine properties and main hull dimensions are presented in Table 4.3 and Table 4.4, respectively. Reference values of the natural periods are given in Table 4.5.

Figure 4.3: INO-WINDMOOR 12 MW FWT concept (Souza et al., 2021)

Table 4.3: Full floating wind turbine main properties (Souza et al., 2021).

Property	Value	
Displacement	14176.1	[t]
Draft	15.5	[m]
CG_x*	[-0.37, 0.37]	[m]
CG_y*	[-0.37, 0.37]	[m]
CG_z	4.23	[m]
R_{xx}	43.67	[m]
R_{yy}	44.18	[m]
R_{zz}	30.26	[m]
Static heel angle at rated thrust	6.4	[deg]
Still water airgap to column top	15.5	[m]
Still water airgap to deck beam bottom	12	[m]
Still water airgap to blade tip	21.7	[m]

* CG_x and CG_y are dependent on the nacelle orientation.
For 0°orientation, $CG_x = 0.37$ m and $CG_y = 0$ m.
For 90°orientation, $CG_x = 0$ m and $CG_y = 0.37$ m.

Table 4.4: Hull main dimesions and inertia properties (including ballast) (Souza et al., 2021).

Property	Value	
Column diameter	15	[m]
Column height	31	[m]
Pontoon width	10	[m]
Pontoon height	4	[m]
Center-center distance	61	[m]
Deck beam width	3.5	[m]
Deck beam height	3.5	[m]
Total substructure mass	11947	[t]
Total substructure CG_x	-5.91	[m]
Total substructure CG_z	-9.7	[m]
Total substructure R_{xx}	23.66	[m]
Total substructure R_{yy}	18.63	[m]
Total substructure R_{zz}	28.10	[m]

Table 4.5: Reference values of the natural periods given in Souza et al. (2021).

DOF	Surge	Sway	Heave	Roll	Pitch	Yaw
Natural period	97.3 s	98 s	16.3 s	29.5 s	31.4 s	88 s

4.2 The WINDMOOR 12 MW Wind Turbine

In this thesis, the WINDMOOR 12 MW is mounted on top of both the INO WINDMOOR and OO-Star floater. The WINDMOOR 12 MW turbine uses a direct-drive generator and is an upscaled version based on the design of the International Energy Agency (IEA) 10 MW turbine. Table 4.6 presents the main properties of the WINDMOOR 12 MW wind turbine, while the tower's main properties are given in Table 4.7, based on the information given by Souza et al. (2021).

Table 4.6: Main properties of the WINDMOOR 12 MW turbine (Souza et al., 2021).

Parameter	Value	
Rated power	12	[MW]
Rotor diameter	216.9	[m]
Hub diameter	5	[m]
Number of blades	3	[-]
Hub height	131.7	[m]
Cut- in/rated/cut-out wind speed	4.0/10.5/25.0	[m/s]
Nacelle mass	600 000	[kg]
Hub mass	60 000	[kg]
Blade mass	3×63 024	[kg]

Table 4.7: Tower main properties (Souza et al., 2021).

Parameter	Value	
Diameter at top	5.97	[m]
Diameter at bottom	9.90	[m]
Thickness at top	30.1	[mm]
Thickness at bottom	90.0	[mm]
Length	110.2	[m]
Mass	1181.6	[t]
CG_z from base	56.65	[m]

5 Environmental Conditions

This section will briefly introduce the selected site for Norwegian floating offshore wind development and the procedure for establishing environmental conditions. Lastly, the lumping method used for fatigue damage assessment is outlined.

5.1 Site

A suitable location for the two FOWT concepts is necessary to be defined to obtain met-ocean data, which is used to identify the operational and extreme conditions to be examined in the analyses. The best locations suitable for offshore wind turbines concerning the wind potential are Northern Europe, Japan, South Korea, South Africa, Australia, New Zealand, Chile, North America, and China's south coast. Figure 5.1 illustrates the global wind speed potential.

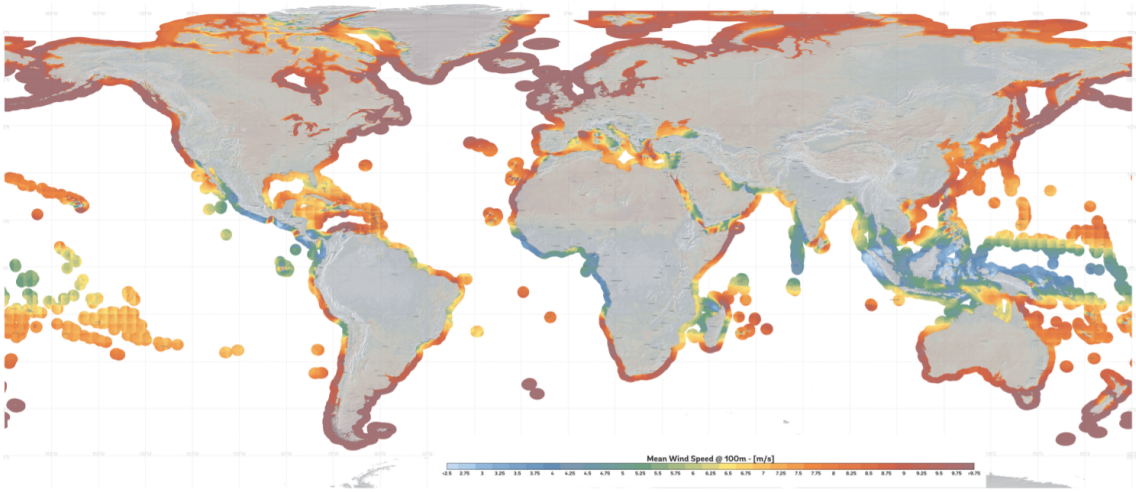

Figure 5.1: Overview of the wind speed potential globally, purple indicates a high wind potential, light blue indicates a low wind potential (Energy, 2019).

Figure 5.2 presents the electricity generation potential for countries with a high wind speed potential, including Australia, Norway, Argentina and China. These are countries with both large relative offshore areas, and high average wind speeds (Bosch et al., 2018).

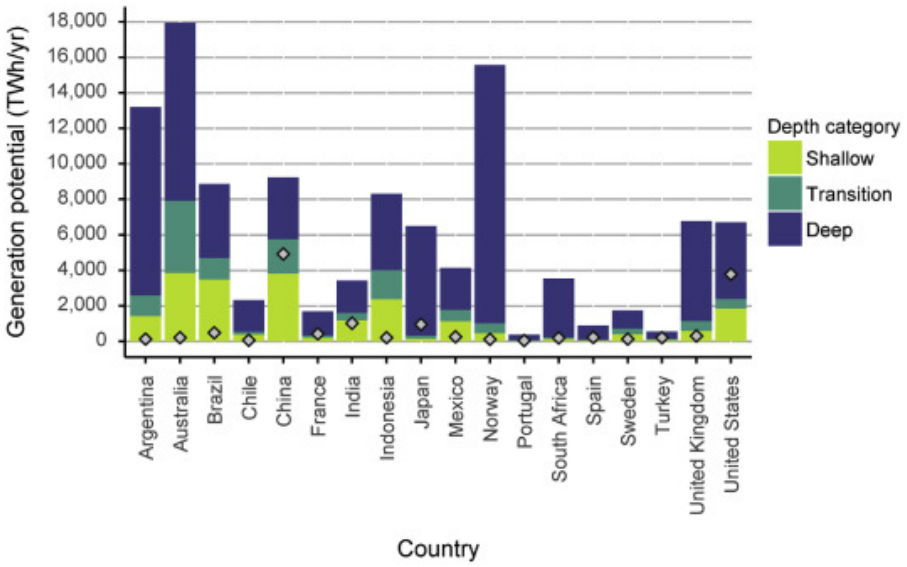

Figure 5.2: Annual energy production (AEP) of offshore wind farms for different depth categories for a selection of high producing countries. The point on each bar is the electricity demand of each country in 2015. The depth categories are Shallow (0-40 m), Transitional (40-60 m) and Deep (60-1000 m) (Bosch et al., 2018).

As Figure 5.2 illustrates, Norway has a large relative generation potential. However, almost all of Norway's potential is located over deep waters, while only 1000 TWh is available in shallow and transitional depths combined (Bosch et al., 2018). It is then necessary to investigate the availability of these deep water areas to find out if it is economically feasible to develop a wind farm at these locations. Figure 5.3 shows the generation potential of offshore wind farms for different distance categories, while Figure 5.4 shows the bathymetry of the North Sea.

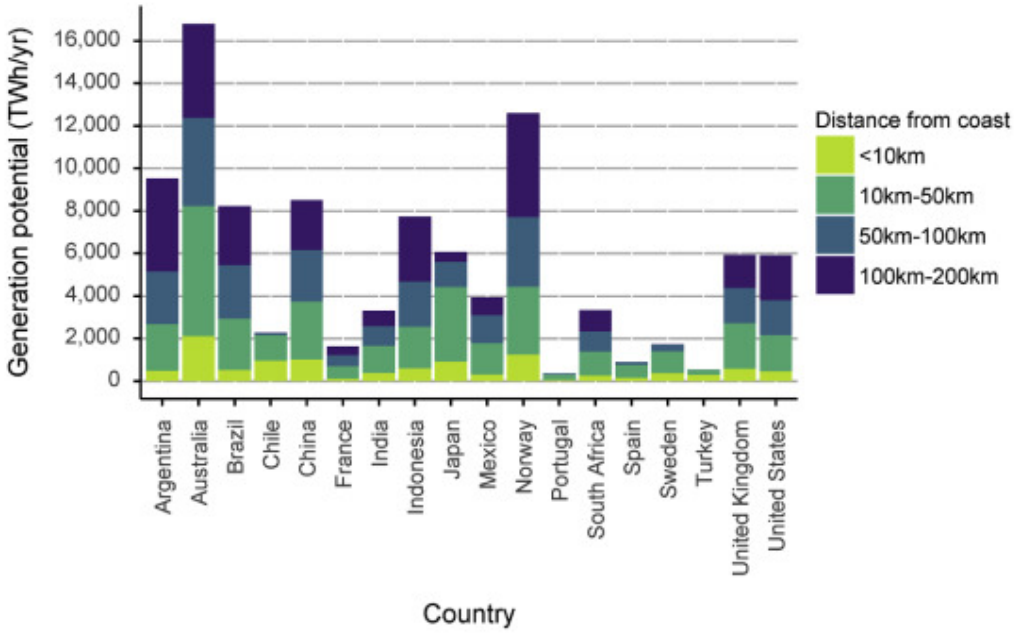

Figure 5.3: Annual average energy generation potential of offshore wind farms for different distance categories for a selection of high producing countries (Bosch et al., 2018).

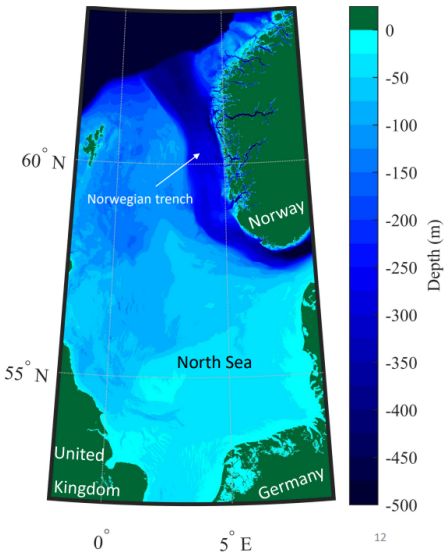

Figure 5.4: Bathymetry of the North Sea (Cheynet, 2020).

As seen from Figure 5.3, countries such as Australia, Norway, China and Japan have large relative potentials in the 10-50 km range, which indicate significant scope for economically feasible wind farm development. From Figure 5.4 it is seen that the Norwegian trench, which is an elongated depression in the seafloor off the southern coast of Norway, creates deep waters close to the Norwegian coast. This makes it possible to develop floating offshore wind farms that are economically feasible relative close to the Norwegian coast.

To harvest the potential of the global offshore wind and speed up the energy transition, governments need to approve floating offshore wind locations. In 2020 the Norwegian government opened the areas Utsira Nord and Sørlige Nordsjø II for offshore renewables, including offshore wind power. Sørlige Nordsjø II borders the Danish sector in the North sea. The area is 2591 square kilometres and has a water depth suitable for bottom-fixed wind turbines, but floating solutions are also possible (Berthelsen and Nagell, 2020).
Utsira Nord is located west of Haugesund and has a water depth of approximately 280 m, suitable for floating wind turbines. The area is 1010 square kilometres, close to shore and provides opportunities for demonstration projects but also larger projects (Berthelsen and Nagell, 2020). It will be possible to submit license applications for offshore wind projects in these two areas. Therefore, these offshore sites are highly relevant for Norwegian FOWT development. In the master's thesis, the chosen location is the Utsira Nord area as the water depth is more suitable for floating wind turbines than Sørlige Nordsjø II. Figure 5.5 shows the location of the two areas.

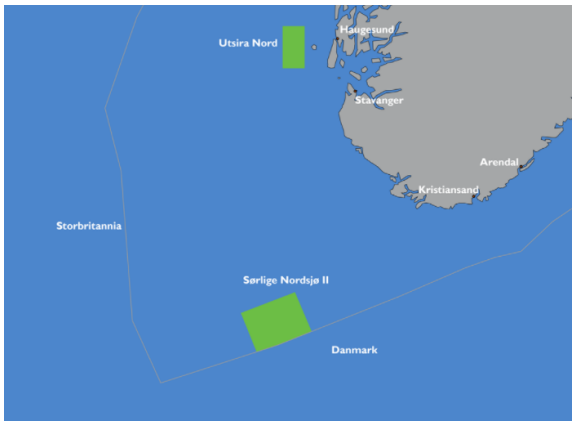

Figure 5.5: Utsira Nord and Sørlige Nordsjø II (Energidepartementet, 2020)

5.2 Establishment of Environmental Conditions

In the absence of specific environmental distribution parameters at the selected location, Utsira Nord, it was decided to determine the environmental conditions based on the findings done by L. Li et al. (2013) on a nearby site in the North Sea. For calculation of the joint distribution, the distribution parameters for site 14, as shown in Figure 5.6 are used. With the same distance to shore and approximately the same water depth, the data for site 14 is assumed to correspond fairly good with the Utsira Nord site. The hindcast data used in L. Li et al. (2013) is based on hourly samples of wind and waves from 2001 to 2010.

Figure 5.6: Location of nearby site (L. Li et al., 2013).

5.2.1 Comparison with NORA10

The met-ocean data for the Utsira Nord area was provided by Kjell Larsen from The Department of Marine Technology. This data are obtained from the NORA10 data set, a long-term hindcast for wind and waves in Norwegian areas. In the NORA10 data set, the hindcast data are based on 6-hourly samples of wind and waves from 1957 to 2021 for the geographical coordinates 59.27°N and 4.39°E.

According to DNV (2014), the most commonly used averaging times are 1 minute, 10 minutes and 1-hour. Thus an averaging time of 6-hours would be an inaccurate description of the mean wind speed, despite the number of years with hindcast data. However, the NORA10 data could indicate how the distribution parameters estimated by L. Li et al. (2013) compare with the measurements from the NORA10 file at Utsira Nord.

Figure 5.7 presents the fitted curve of the marginal distribution of the 6-hour mean wind speed U_w on the Weibull probability paper. As seen in Figure 5.7, the wind speed is well described by a two-parameter Weibull distribution as proposed in L. Li et al. (2013). A distribution fitter function in Matlab is used to obtain the distribution parameters as shown in Table 5.1. The provided parameters from the nearby site show a quite good correspondence with the estimated parameters at Utsira Nord. Hence, the parameters used in L. Li et al. (2013) are assumed to be sufficient to represent the environment at Utsira Nord.

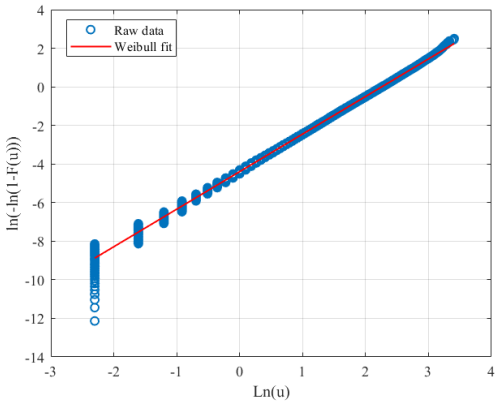

Figure 5.7: Weibull probability paper for marginal distribution of U_w.

Table 5.1: Comparison of parameters for the marginal distribution of U_w.

Parameter	NORA10 measurement	Reference site	Deviation
α_U	1.963	2.029	3.2%
β_U	9.550	9.409	1.4%

Further, when considering only the wave data, the marginal distribution of the significant wave height H_s is described in L. Li et al. (2013) to follow a hybrid lognormal and Weibull distribution - Lonowe distribution, as shown in Equation 5.1.

$$f_{Hs}(h) = \begin{cases} \frac{1}{\sqrt{2\pi}\sigma_{LHM}h} \exp\left(-\frac{1}{2}\left(\frac{\ln(h)-\mu_{LHM}}{\sigma_{LHM}}\right)^2\right) & h \leq h_0 \\ \frac{\alpha_{HM}}{\beta_{HM}}\left(\frac{h}{\beta_{HM}}\right)^{\alpha_{HM}-1} \exp\left[-\left(\frac{h}{\beta_{HM}}\right)^{\alpha_{HM}}\right] & h > h_0 \end{cases} \tag{5.1}$$

Here h_0 denotes the shifting point of the significant wave height H_s between the lognormal and Weibull distribution. The main data is best described by a lognormal distribution, while the data in the tail follow a Weibull distribution. This method of describing the significant wave height with a Lonowe distribution is seen to be in compliance with the fitting results from the NORA10 data set in Figure 5.8.

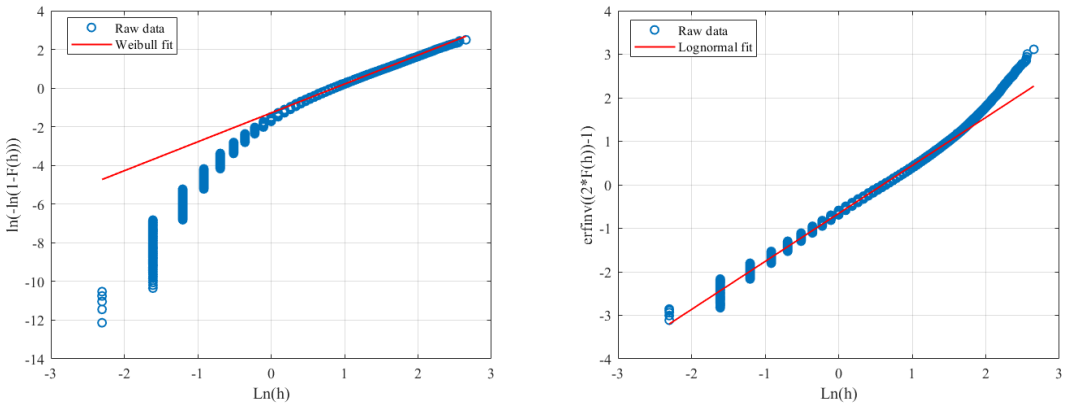

(a) (b)

Figure 5.8: Fitted curve of Weibull distribution (a) and lognormal distribution (b) on Weibull probability paper ($h_0 = 5m$).

5.2.2 Design Wind Profile

The mean wind speed varies with the height above the still water level. A wind speed profile can represent this variation. As outlined by DNV (2014), it is required to use the mean wind speed at hub height. A power law profile can be utilized for estimating the mean wind speeds at different heights, as shown in Equation 5.2:

$$U_w(z) = U_w(H)\left(\frac{z}{H}\right)^{\psi} \tag{5.2}$$

here, $U_w(H)$ denotes the 1-hour mean wind speed in the reference height $H = 10$ m, while z represents the height. The wind speed profile parameter ψ depends on the terrain roughness. According to L. Li et al. (2013), the wind speed profile parameter is set to $\psi = 0.1$ at the current site.

5.2.3 Marginal Distribution of Mean Wind Speed

As proposed by L. Li et al. (2013), the one-hour mean wind speed at the reference height of 10 m follows a tow-parameter Weibull distribution, as seen in Equation 5.3:

$$f_{Uw}(u) = \frac{\alpha_U}{\beta_U}\left(\frac{u}{\beta_U}\right)^{\alpha_U - 1} \exp\left[-\left(\frac{u}{\beta_U}\right)^{\alpha_U}\right] \tag{5.3}$$

$f_{Uw}(u)$ refers to the probability density function (PDF), α_U is the shape parameter and β_U is the scale parameter. The distribution parameters are determined by site-specific data and are given in Table 5.1.

Using the long-term statistics, the extreme value is defined by the number of sea states N over a period of time. To calculate the characteristic value for the wind speed corresponding to an annual exceedance probability of 0.02 or a return period of 50 years, the following equation yields:

$$1 - F_{Uw}(u_{,50}) = \frac{1}{N} \tag{5.4}$$

where $F_{Uw}(u)$ is the cumulative distribution function and $N = 8 \cdot 365 \cdot 50$ represents the number of 3 hour sea states for 50 years.

The expected value of the two-parameter Weibull distribution is by:

$$E[u] = \beta \cdot \Gamma\left(\frac{1}{\alpha} + 1\right) \tag{5.5}$$

where

$$\Gamma\left(\frac{1}{\alpha} + 1\right) = \int_0^{\infty} e^{-x} x^{(\frac{1}{\alpha})} dx \tag{5.6}$$

Table 5.2: Calculated hourly expected and extreme wind speed at reference height z = 10m.

$E[U_w]$	$U_{w,50}$
8.33 m/s	33.3 m/s

5.2.4 Joint Distribution of U_w, H_s and T_p

The joint distribution of wind and waves is described by L. Li et al. (2013) as shown in Equation 5.7. Where the joint distribution consists of a marginal distribution of the wind speed U_w, a conditional distribution of H_s for a given U_w and a conditional distribution of T_p for given H_s and U_w.

$$f_{Uw,Hs,Tp}(u,h,t) = f_{Uw}(u) \cdot f_{Hs|Uw}(h \mid u) \cdot f_{T_p|Uw,Hs}(t \mid u,h) \tag{5.7}$$

The conditional PDF of H_s given U_w is given as a two-parameter Weibull distribution as seen in Equation 5.8:

$$f_{Hs|Uw}(h \mid u) = \frac{\alpha_{HC}}{\beta_{HC}} \left(\frac{h}{\beta_{HC}}\right)^{\alpha_{HC}-1} \exp\left[-\left(\frac{h}{\beta_{HC}}\right)^{\alpha_{HC}}\right] \tag{5.8}$$

here α_{HC} and β_{HC} are the shape and scale parameters, respectively. The distribution parameters are expressed as power functions of the mean wind speed as shown in the following:

$$\begin{aligned} \alpha_{HC} &= a_1 + a_2 u^{a_3} \\ \beta_{HC} &= b_1 + b_2 u^{b_3} \end{aligned} \tag{5.9}$$

a_1, a_2, a_3, b_1, b_2 and b_3 are parameters estimated from the specific site, and are presented in Table 5.3. The expected value of the significant wave height H_s for a given wind speed U_w is expressed as in Equation 5.10:

$$E[h|u] = \beta_{HC} \cdot \Gamma\left(\frac{1}{\alpha_{HC}} + 1\right) \tag{5.10}$$

Table 5.3: Distribution parameters for conditional H_s for given U_w.

Parameter	a_1	a_2	a_3	b_1	b_2	b_3
Value	2.136	0.013	1.709	1.816	0.024	1.787

Further, L. Li et al. (2013) describe the conditional distribution of T_p for a given H_s and U_w to follow a lognormal distribution, shown in Equation 5.11:

$$f_{T_p|Uw,H_S}(t \mid u,h) = \frac{1}{\sqrt{2\pi}\sigma_{\ln(T_p)^t}} \exp\left(-\frac{1}{2}\left(\frac{\ln(t) - \mu_{\ln(T_p)}}{\sigma_{\ln(T_p)}}\right)^2\right) \tag{5.11}$$

The spectral peak period is seen to mainly depend on H_s, however variations in the wind speed do result in shifting of the periods. Hence, a parameterization of the spectral peak period T_p as proposed by Johannessen et al. (2002) is used, where the mean value of T_p can be modelled as seen in Equation 5.12:

$$\mu_{T_p} = \overline{T_p}(u,h) = \overline{T_p}(h) \cdot \left[1 + \theta\left(\frac{u - \overline{u}(h)}{\overline{u}(h)}\right)^{\gamma}\right] \tag{5.12}$$

where, $\overline{T_p}(h)$ and $\overline{u}(h)$ are the expected spectral peak period and mean wind speed for a given value of H_s, respectively. The two expected values are fitted as a function of H_s, as shown in Equation 5.13. Table 5.4 presents the distribution parameters used for evaluating the mean spectral peak period.

$$\begin{aligned} \overline{T_p}(h) &= e_1 + e_2 \cdot h^{e_3} \\ \bar{u}(h) &= f_1 + f_2 \cdot h^{f_3} \end{aligned} \tag{5.13}$$

Table 5.4: Distribution parameters for conditional T_p for given U_w and H_s.

Parameter	θ	γ	e_1	e_2	e_3	f_1	f_2	f_3
Value	-0.255	1.0	8	1.938	0.486	2.5	3.001	0.745

5.2.5 Design Current Profiles

In the same manner as for the wind, the variation of wind-generated current velocity can be taken as a linear profile, as shown in Equation 5.14 (DNV, 2014):

$$\mathrm{U_{c,\ wind}}\ (z) = \mathrm{U_{c,\ wind}}\ (0) \left(\frac{d_0 + z}{d_0} \right) \text{ for } -d_0 \leq z \leq 0 \tag{5.14}$$

$U_{c,wind}(0)$ is the wind-generated current velocity at the still water level, d_0 represents the wind-generated current reference depth, $d_0 = 50$ m. The distance from the still water level is denoted z, and is positive upwards.

If there are no statistical data available for a region with deep water along an open coastline, the wind-generated current velocities at still water level could be taken as shown in Equation 5.15:

$$\mathrm{U_{c,\ wind}}\ (0) = kU_{1\ \mathrm{hour,\ 10\ m}} \tag{5.15}$$

where $k = 0.015$ - 0.03 and $U_{1\ \mathrm{hour,\ 10\ m}}$ is the 1 hour mean wind speed at the reference height of 10 m above still water level. A value of $k = 0.03$ is selected as a conservative value from (DNV, 2014), in the absence of current data at the site.

5.3 Design Load Cases

The design load cases to be considered when verifying the structural integrity of floating offshore wind turbine components are described in the DNV-ST-0437 standard DNV (2016). Table 5.5 presents the design situations for power production and for parked turbines regarding the wind and marine conditions to be used at the individual design load cases. A description of acronyms used in Table 5.5 is listed in Table 5.6.

Table 5.5: Design load case table for offshore wind turbines (DNV, 2016).

Design situation	**DLC**	**Wind condition**	**Waves**	**Current**	**water level**
Power-production	1.1	NTM	NSS	NCM	MSL
Parked	6.1	EWM	ESS	ECM	MSL

Table 5.6: Description of acronyms used in Table 5.5.

DLC	Design Load Case
NTM	Normal Turbulence Model
EWM	Extreme wind speed model
NSS	Normal Sea State
ESS	Extreme Sea State
NCM	Normal Current Model
ECM	Extreme Current Model
MSL	Mean sea level

Based on the established environmental conditions, five load cases were defined for the time-domain simulations, as shown in Table 5.7. In cooperation with our co-supervisors in SEMAR AS, the design load cases LC1-LC2 were decided to mainly focus on power production cases, with the turbine parked and operational in the same environmental condition to see how the turbine and floater affect each other. For the power production cases, rated and cut-out wind speed were selected. Further, an extreme load case, LC3, was also established for investigation under an extreme condition with the turbine in parked condition. The load cases are defined as follows:

- LC 1.1: Power production at rated wind speed
- LC 1.2: Parked turbine at rated wind speed
- LC 2.1: Power production at cut-out wind speed
- LC 2.2: Parked turbine at cut-out wind speed
- LC 3: Extreme condition with a 50-year return period

Table 5.7: Established design load cases for fully coupled time domain-analysis.

		Wind condition		**Wave condition**			**Current**	**Direction**
Case	DLC	Model	$U_{w,z=10}$ [m/s]	Model	H_s [m]	T_p [s]	$U_{c,z=0}$ [m/s]	[°]
LC 1.1	1.1	NTM	8.1	NSS	2.51	11.14	0.24	0
LC 1.2 *	1.1	NTM	8.1	NSS	2.51	11.14	0.24	0
LC 2.1	1.1	NTM	19.32	NSS	5.98	11.36	0.58	0
LC 2.2 *	1.1	NTM	19.32	NSS	5.98	11.36	0.58	0
LC 3 *	6.1	EWM	33.3	ESS	13.53	13.27	1.0	0

* Indicating that the turbine is in parked condition, if no indication the turbine is in operating condtion.

5.4 Environmental Lumping Method for Fatigue Damage Assessment

The assessment of fatigue damage on floating offshore wind turbines subjected to random loading is crucial for the design, and may induce significant fatigue damage to the structure. Using time-domain analysis combined with Rainflow counting is considered the most accurate method to calculate the fatigue damage, where the time-domain analysis also considers the nonlinear effects (Katsikogiannis et al., 2022).

Conducting fully coupled dynamic analyses on every sea state within the wave scatter diagram is quite time-consuming and computationally demanding. A way of expediting the time domain computations and reducing the number of environmental conditions to investigate for fatigue assessment is to use lumping methods. According to Song et al. (2016), a common practice is to lump the individual sea states within the scatter diagram into manageable blocks, and the fatigue assessment will be represented by the sea states within the blocks. Different blocking methods

have been proposed. However, in this thesis, the blocking method developed by Sheehan et al. (2005) is used, which is based on the DNV standard (DNV, 2010b) but includes a criterion for determining the representative sea states from the blocks. Figure 5.9 and Figure 5.10 present the blocking of the sea states within the H_s-T_p scatter diagram. The sea states were divided into 12 blocks with dimensions 4x4 as proposed by Chang et al. (2014). The scatter diagrams used for the fatigue damage assessment are obtained from the NORA10 hindcast dataset, and the sea states are gathered in H_s classes of 0.5 m and T_p classes of 1 s, where each class within the scatter diagram is represented by a class midpoint (DNV, 2014).

Hs\Tp	0-1	1-2	2-3	3-4	4-5	5-6	6-7	7-8	8-9	9-10	10-11	11-12	12-13	13-14	14-15	15-16	16-17	17-18	18-19	19-20	20-21	21-22	
0-0,5	0	0	10	107	581	439	319	330	373	289	173	90	66	34	29	15	10	3	4	1	1	0	2874
0,5-1	0	0	25	739	2821	4813	4569	3552	3097	2703	2125	1405	893	424	218	141	80	22	13	1	2	0	27643
1-1,5	0	0	0	103	2297	5320	6403	5422	4609	3789	2769	2341	1730	968	469	278	144	26	17	5	5	1	36696
1,5-2	0	0	0	1	375	3651	6240	5454	3799	3278	2678	1913	1561	1117	572	339	135	53	23	3	1	1	31194
2-2,5	0	0	0	0	33	889	4487	5616	3980	2488	2112	1679	1235	886	593	330	157	39	27	1	0	0	24552
2,5-3	0	0	0	0	1	122	2013	4406	4389	2503	1457	1252	928	602	457	294	150	40	19	1	1	0	18635
3-3,5	0	0	0	0	0	9	504	2524	4076	2762	1241	786	689	420	311	227	138	39	29	1	1	0	13757
3,5-4	0	0	0	0	0	0	78	1016	2857	2736	1314	646	427	285	150	120	95	45	22	4	1	0	9796
4-4,5	0	0	0	0	0	0	1	217	1625	2267	1465	517	319	215	106	73	49	30	16	0	1	0	6901
4,5-5	0	0	0	0	0	0	0	34	579	1510	1412	634	245	131	83	54	23	19	13	1	0	0	4738
5-5,5	0	0	0	0	0	0	0	5	229	857	1109	721	179	102	70	27	15	9	7	0	0	0	3330
5,5-6	0	0	0	0	0	0	0	0	41	392	751	682	240	91	59	26	12	16	6	0	0	0	2316
6-6,5	0	0	0	0	0	0	0	0	10	154	442	495	250	74	41	24	6	7	5	0	0	0	1508
6,5-7	0	0	0	0	0	0	0	0	1	57	215	300	250	94	36	12	5	2	2	0	0	0	974
7-7,5	0	0	0	0	0	0	0	0	0	15	88	176	214	69	31	12	4	5	1	0	0	0	615
7,5-8	0	0	0	0	0	0	0	0	0	1	39	89	129	76	22	8	2	4	2	0	0	0	372
8-8,5	0	0	0	0	0	0	0	0	0	0	18	54	78	59	24	11	4	1	3	0	0	0	252
8,5-9	0	0	0	0	0	0	0	0	0	0	2	19	21	60	24	9	4	3	1	0	0	0	143
9-9,5	0	0	0	0	0	0	0	0	0	0	0	5	17	36	20	8	6	2	1	0	0	0	95
9,5-10	0	0	0	0	0	0	0	0	0	0	0	1	3	21	13	5	1	1	1	0	0	0	46
10-10,5	0	0	0	0	0	0	0	0	0	0	0	0	0	14	9	5	2	0	1	0	0	0	31
10,5-11	0	0	0	0	0	0	0	0	0	0	0	0	0	2	7	3	2	1	1	0	0	0	16
11-11,5	0	0	0	0	0	0	0	0	0	0	0	0	0	1	4	5	0	0	0	0	0	0	10
11,5-12	0	0	0	0	0	0	0	0	0	0	0	0	0	1	1	3	0	1	0	0	0	0	6
12-12,5	0	0	0	0	0	0	0	0	0	0	0	0	0	0	2	1	0	0	0	0	0	0	3
12,5-13	0	0	0	0	0	0	0	0	0	0	0	0	0	0	1	2	1	0	0	0	0	0	4
13-13,5	0	0	0	0	0	0	0	0	0	0	0	0	0	0	0	1	0	0	0	0	0	0	1
13,5-14	0	0	0	0	0	0	0	0	0	0	0	0	0	0	0	0	0	0	0	0	0	0	0
14-14,5	0	0	0	0	0	0	0	0	0	0	0	0	0	0	1	0	0	0	0	0	0	0	1
																						sum	186509

Figure 5.9: Scatter diagram divided into 8 blocks.

Hs\Tp	0-1	1-2	2-3	3-4	4-5	5-6	6-7	7-8	8-9	9-10	10-11	11-12	12-13	13-14	14-15	15-16	16-17	17-18	18-19	19-20	20-21	21-22	
0-0,5	0	0	10	107	581	439	319	330	373	289	173	90	66	34	29	15	10	3	4	1	1	0	2874
0,5-1	0	0	25	739	2821	4813	4569	3552	3097	2703	2125	1405	893	424	218	141	80	22	13	1	2	0	27643
1-1,5	0	0	0	103	2297	5320	6403	5422	4609	3789	2769	2341	1730	968	469	278	144	26	17	5	5	1	36696
1,5-2	0	0	0	1	375	3651	6240	5454	3799	3278	2678	1913	1561	1117	572	339	135	53	23	3	1	1	31194
2-2,5	0	0	0	0	33	889	4487	5616	3980	2488	2112	1679	1235	886	593	330	157	39	27	1	0	0	24552
2,5-3	0	0	0	0	1	122	2013	4406	4389	2503	1457	1252	928	602	457	294	150	40	19	1	1	0	18635
3-3,5	0	0	0	0	0	9	504	2524	4076	2762	1241	786	689	420	311	227	138	39	29	1	1	0	13757
3,5-4	0	0	0	0	0	0	78	1016	2857	2736	1314	646	427	285	150	120	95	45	22	4	1	0	9796
4-4,5	0	0	0	0	0	0	1	217	1625	2267	1465	517	319	215	106	73	49	30	16	0	1	0	6901
4,5-5	0	0	0	0	0	0	0	34	579	1510	1412	634	245	131	83	54	23	19	13	1	0	0	4738
5-5,5	0	0	0	0	0	0	0	5	229	857	1109	721	179	102	70	27	15	9	7	0	0	0	3330
5,5-6	0	0	0	0	0	0	0	0	41	392	751	682	240	91	59	26	12	16	6	0	0	0	2316
6-6,5	0	0	0	0	0	0	0	0	10	154	442	495	250	74	41	24	6	7	5	0	0	0	1508
6,5-7	0	0	0	0	0	0	0	0	1	57	215	300	250	94	36	12	5	2	2	0	0	0	974
7-7,5	0	0	0	0	0	0	0	0	0	15	88	176	214	69	31	12	4	5	1	0	0	0	615
7,5-8	0	0	0	0	0	0	0	0	0	1	39	89	129	76	22	8	2	4	2	0	0	0	372
8-8,5	0	0	0	0	0	0	0	0	0	0	18	54	78	59	24	11	4	1	3	0	0	0	252
8,5-9	0	0	0	0	0	0	0	0	0	0	2	19	21	60	24	9	4	3	1	0	0	0	143
9-9,5	0	0	0	0	0	0	0	0	0	0	0	5	17	36	20	8	6	2	1	0	0	0	95
9,5-10	0	0	0	0	0	0	0	0	0	0	0	1	3	21	13	5	1	1	1	0	0	0	46
10-10,5	0	0	0	0	0	0	0	0	0	0	0	0	0	14	9	5	2	0	1	0	0	0	31
10,5-11	0	0	0	0	0	0	0	0	0	0	0	0	0	2	7	3	2	1	1	0	0	0	16
11-11,5	0	0	0	0	0	0	0	0	0	0	0	0	0	1	4	5	0	0	0	0	0	0	10
11,5-12	0	0	0	0	0	0	0	0	0	0	0	0	0	1	1	3	0	1	0	0	0	0	6
12-12,5	0	0	0	0	0	0	0	0	0	0	0	0	0	0	2	1	0	0	0	0	0	0	3
12,5-13	0	0	0	0	0	0	0	0	0	0	0	0	0	0	1	2	1	0	0	0	0	0	4
13-13,5	0	0	0	0	0	0	0	0	0	0	0	0	0	0	0	1	0	0	0	0	0	0	1
13,5-14	0	0	0	0	0	0	0	0	0	0	0	0	0	0	0	0	0	0	0	0	0	0	0
14-14,5	0	0	0	0	0	0	0	0	0	0	0	0	0	0	1	0	0	0	0	0	0	0	1
																						sum	186509

Figure 5.10: Scatter diagram divided into 4 blocks.

According to DNV (2010b), a single sea state within each block is to be selected to represent all sea states in the block, and the probability of occurrence for all sea states within the block is to be lumped to the selected sea state. However, a criterion for using this method, as proposed by Sheehan et al. (2005) is to select the maximum significant wave height in the block to be representative for the significant wave height of the sea state. Further, the period is denoted as the weighted average of all the periods within the block. Table 5.8 and Table 5.9 presents block 1 and 8 from the wave scatter diagram, respectively to further illustrate the blocking procedure.

Table 5.8: Block 1.

H_s \ T_p	4.5	5.5	6.5	7.5	**sum**
0.25	581	439	319	330	1669
0.75	2821	4813	4569	3552	15755
1.25	2297	5320	6403	5422	19442
1.75	375	3651	6240	5454	15720
sum	6074	14223	17531	14758	**52586**

Table 5.9: Block 8.

H_s \ T_p	10.5	11.5	12.5	13.5	**sum**
2.25	2112	1679	1235	886	5912
2.75	1457	1252	928	602	4239
3.25	1241	786	689	420	3136
3.75	1314	646	427	285	2672
sum	6124	4363	3279	2193	**15959**

5.4.1 Determining Representative Wind Conditions

In order to determine the corresponding wind velocities, a simple lumping process as outlined by Koochekali and Muskulus (2019) is utilized. From the H_s - W scatter diagram, two approaches can be used to determine the averaged significant wave height and wind speed. One approach is to preserve the wind speed distribution and calculate the average significant wave height over each wind speed bin, using the formula in Equation 5.16. The latter approach is to preserve the significant wave height distribution and calculate the average wind speed over each wave height bin, using Equation 5.17:

$$H_{s,j} = \frac{\sum_{i=1}^{n} P_{i,j} \cdot H_{s_{i,j}}}{\sum_{i=1}^{n} P_{i,j}} \tag{5.16}$$

$$W_{s,i} = \frac{\sum_{j=1}^{m} P_{i,j} \cdot W_{s_{i,j}}}{\sum_{j=1}^{m} P_{i,j}} \tag{5.17}$$

here i and j denote the index of the wind speed and significant wave height bins, respectively. The number of wind speed and significant wave height bins is represented by m and n, while $P_{i,j}$ is the probability of occurrence for the combination $[H_{s_{i,j}}, W_{s_{i,j}}]$. The lumping procedure for the two approaches is shown in Figure 5.11.

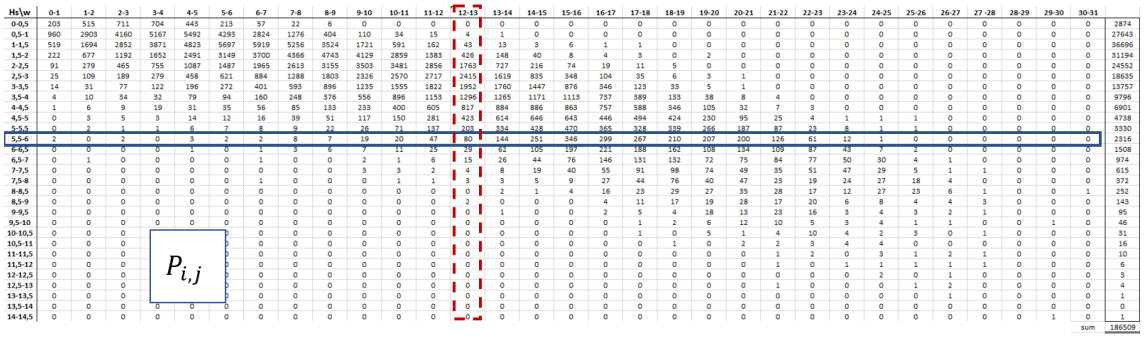

Figure 5.11: Illustration of lumping process for averaging over wind speed (blue box) and averaging over significant wave height (red box).

The significant wave height is already known from the blocking method. It was decided to preserve the significant wave height distribution and lump the wind speed, resulting in one representative wind speed for each associated class of significant wave height. In Figure 5.12, the lumped sea states using the two approaches are plotted. The averaged wind speed is illustrated in the blue curve in Figure 5.12.

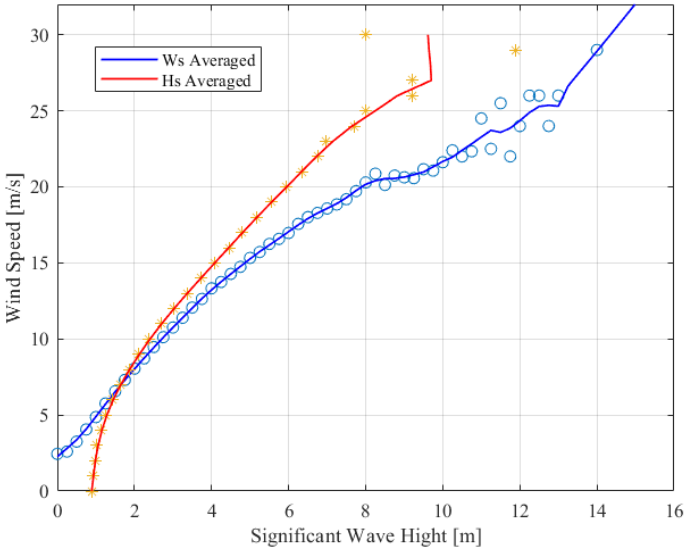

Figure 5.12: Lumped sea states.

From the environmental lumping methods as discussed above, the established load cases to be used to assess the fatigue damage in the time-domain simulations are presented in Table 5.10. In the same manner as for the design load cases in Section 5.3, the current velocity is based on the wind-generated current using Equation 5.15 and described as a linear profile using Equation 5.14. The probability of occurrence descends from the blocking method of the wave climate, and is not influenced by the wind speed.

Table 5.10: Load cases for fatigue damage assessment.

Block number	H_s [m]	T_p [s]	$U_{w,z=10m}$ [m/s]	$U_{c,z=0}$ [m/s]	Direction	Prob. of Occurrence
1	1.75	6.28	7.305	0.22	0°	0.28195
2	1.75	7.77	7.305	0.22	0°	0.29074
3	1.75	9.71	7.305	0.22	0°	0.18997
4	1.75	11.58	7.305	0.22	0°	0.10877
5	1.75	13.34	7.305	0.22	0°	0.04747
6	3.75	8.13	12.63	0.38	0°	0.24897
7	3.75	9.49	12.63	0.38	0°	0.19451
8	3.75	11.60	12.63	0.38	0°	0.08557
9	3.75	13.52	12.63	0.38	0°	0.04265
10	5.75	10.00	16.58	0.50	0°	0.07930
11	5.75	11.20	16.58	0.50	0°	0.04725
12	7.75	11.73	19.72	0.59	0°	0.01609

6 Methodology

6.1 Software

In order to perform a coupled analysis of the FWTs, a numerical model needs to be constructed by utilizing a state-of-the-art software. The numerical analysis was conducted in the steps outlined below and in Figure 6.1.

- Modelling the geometry of the floaters and generation of finite element models in GeniE
- The panel model is imported from GeniE to HydroD were frequency-domain hydrodynamic analysis is conducted by Wadam.
- Time-domain coupled aero-hydro-servo-elastic analyses are conducted in SIMA using SIMO/RIFLEX coupling. The time-domain wind data used in coupled analysis are generated in TurbSim.

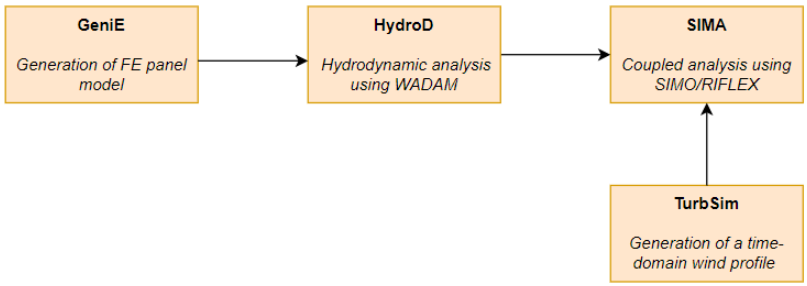

Figure 6.1: Flow diagram of the software used to construct the numerical model.

6.1.1 GeniE

GeniE is an analysis tool for structural design in the Sesam package, which supports work phases from initial concepts, such as finite element panel models, to mature design and analysis. The software can perform modelling, analysis and results presentation within the same user interface, which also allows for 3D visualization of the model and results. The software uses industry-standard technologies such as finite element mesh generation to perform hydrodynamic analyses (DNV, 2020). In this thesis, GenieE is used to create panel models of the submerged parts of the two floaters for subsequent hydrodynamic analysis in Wadam. GeniE is further used to generate a finite element panel model of the free surface. The modelling of the panel models will be described in Section 6.2.

6.1.2 HydroD

HydroD is an integrated part of the Sesam package. It works as an analysis tool for computations of hydrostatics, stability, wave loads and motion response for ships and offshore structures (DNV, 2021). HydroD uses the finite element panel models generated in GeniE as input. The frequency-domain hydrodynamic analysis is performed by Wadam, an analysis program for calculating wave-structure interaction for fixed and floating structures. Wadam uses Morison's equation for load

calculations on slender elements and first and second-order 3D potential theory for large volume structures (*SESAM USER MANUAL WADAM v8.1* 2010).

6.1.3 SIMA

SIMA is an integrated prediction tool suited for marine operations and floating systems analysis. The SIMA workbench includes numerical codes developed at MARINTEK, including SIMO and RIFLEX. SIMO is a general-purpose time-domain program for the modelling and simulation of offshore structures, while RIFLEX is a nonlinear finite element model code that is used to model the static and dynamic analyses of slender marine structures, such as risers, mooring lines and wind turbine blades (Atcheson, 2016). SIMO and RIFLEX can be coupled to determine all of the hydrodynamic and structural options in order to model floating offshore wind turbines (Atcheson, 2016). The aerodynamics are calculated in a separate module in RIFLEX using BEM theory. The connection between the different codes in the SIMA workbench is illustrated in Figure 6.2 (Bachynski, 2021a).

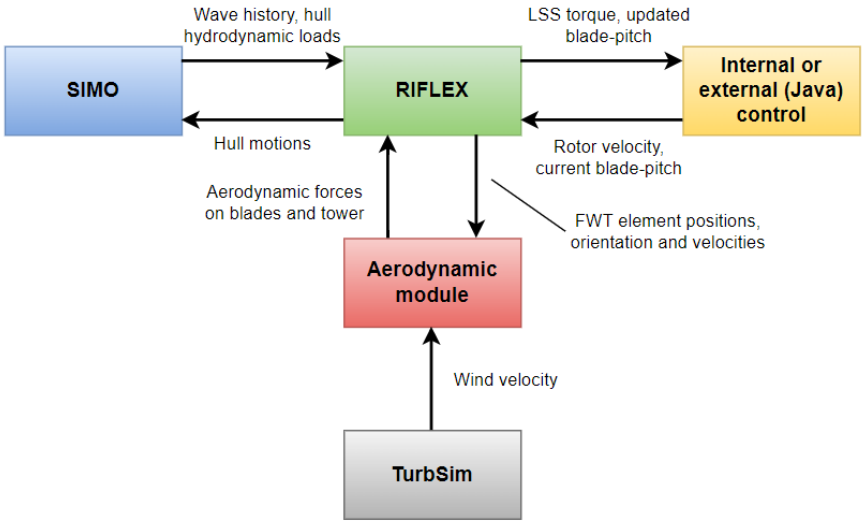

Figure 6.2: Flow chart for the coupled analysis in the SIMA workbench.

6.2 FE Panel Models in GeniE

The finite element panel models used in the hydrodynamic analysis are generated in GeniE. The OO-Star model was designed according to the structural drawings given in the D4.2 report by the LIFES50+ project (Yu et al., 2018). In the structural drawings, the pontoons are slightly tapered, which was neglected in the modelling to make a simple geometry with regards to meshing. The pontoons were instead modelled with a fixed width equal to the width of the outer column. The structural drawings of the OO-Star model are presented in Appendix H. The INO WIDNMOOR model is designed according to the structural dimensions listed in Table 4.4, provided in Souza et al. (2021), by SINTEF. For the hydrodynamic analysis, the model is simplified by excluding the top deck as it was deemed negligible during the analyses in HydroD.

In order to increase the computational efficiency in HydroD, the structures are modelled symmetrically in the xz-plane. The local coordinate system for both models is shown in Figure 6.3, and Figure 6.4. The symmetric panel models from GeniE are shown in Figure 6.5. After the floater geometry is defined, a wet surface is assigned to the body, applied with a hydro-pressure load pointing from the water onto the body. The body is then discretised into a finite element panel model that defines the wet surface. The symmetrically finite element panel models are shown in Figure 6.5.

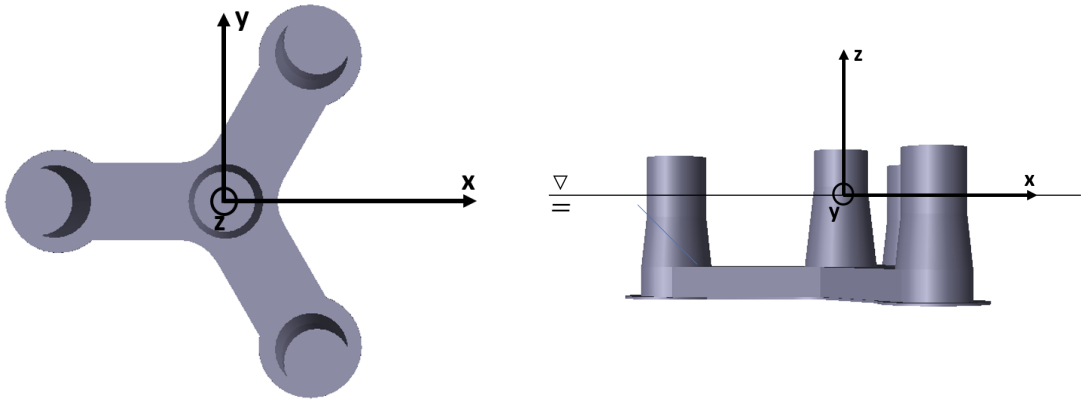

(a) (b)

Figure 6.3: Local body-fixed coordinate system for the OO-Star floater, top view (a) and side view (b).

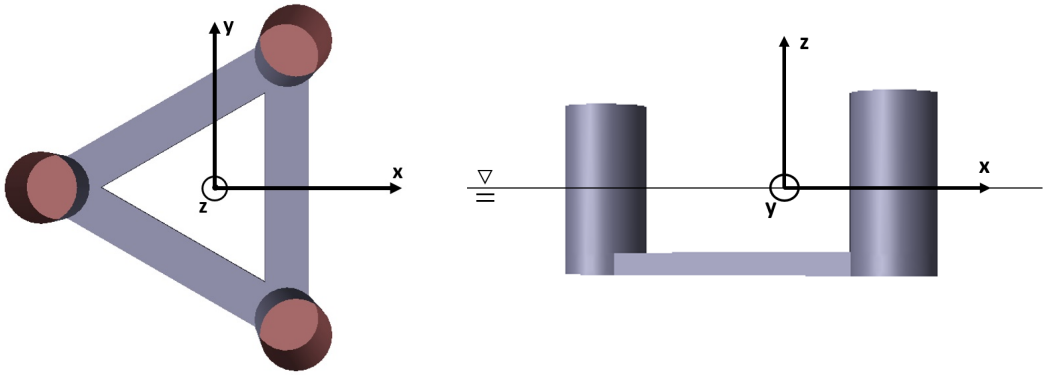

(a) (b)

Figure 6.4: Local body-fixed coordinate system for the INO WINDMOOR floater, top view (a) and side view (b).

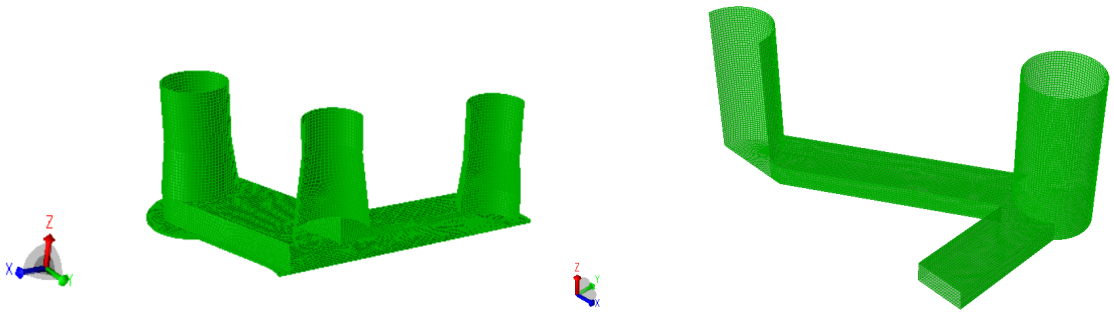

(a) (b)

Figure 6.5: Discretised FE panel models of the OO-Star (a) and INO WINDMOOR (b).

6.2.1 Free Surface FE Model

In order to perform a second-order difference-frequency analysis in HydroD, a finite element panel model of the free surface needs to be defined. The free surface is modelled and discretised in GeniE similarly to the floaters, where a wet surface with a hydro-pressure load is defined. The free surface finite element model has the same symmetry as the floaters, where the surface piercing components are cut out of the free surface. The discretised FE panel models of the free surfaces are illustrated in Figure 6.6.

The radius of the outer boundary is defined according to the decaying rate of local waves (DNV, 2017). For deep water, an appropriate approximation for the radius R is $R \sim O(\lambda)$, where λ is the longest wave involved. From the environmental conditions, it is seen that the peak period for the operational condition is $T_p = 11.13$ s which has a corresponding wavelength of approximately $\lambda = 193$ m. The outer radius is, however, set to 250 m in order to examine the second-order excitation forces for more extreme conditions and hence longer wavelengths.

The mesh configuration is divided into three zones to obtain a finer mesh close to the floater. The inner zone, which has a radius of 90 m, has a finer mesh than the outer zone. The finest mesh is found around the surface piercing columns of the floater, which has a mesh size equal to the floater panel model. When modelling the free surface, two constraints need to be considered to be able to import the panel model into HydroD. The number of free surface panels must be below 10000, and the free surface mesh should consist of four-node shell elements. The latter constrain proved to be especially difficult to fulfil because of the complex geometry of the OO-Star.

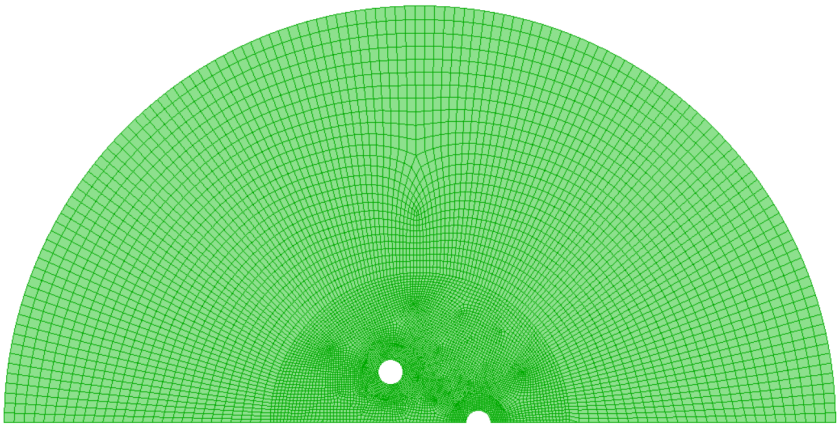

(a) INO WINDMOOR

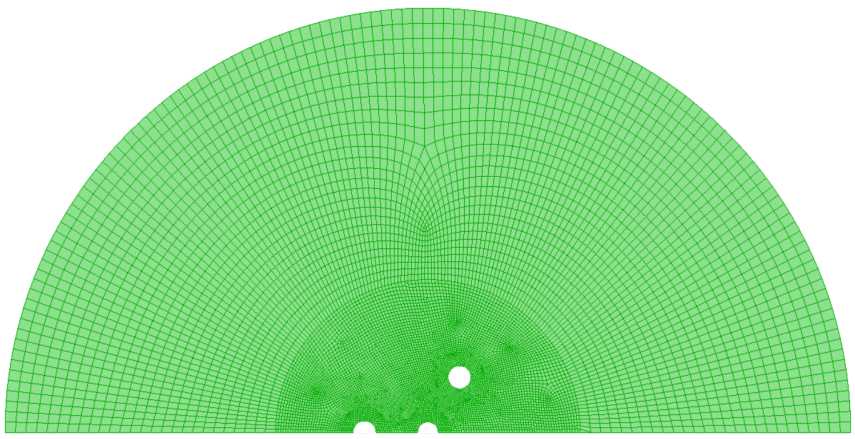

(b) OO-Star

Figure 6.6: Discretised FE panel models of the free surface for INO WINDMOOR and OO-Star.

6.2.2 Mesh Quality/Study

The maximum number of elements on the floaters and the free surface is 50000 and 10000, respectively. It was decided to apply fewer elements for the floaters due to the computational cost of having maximum number of elements. During the work done in the project thesis, a convergence study was done for the added mass coefficients in heave, pitch, and the RAOs. From this convergence study, a panel size of $\Delta x = 0.8$ m was assumed sufficient for both floaters. In this thesis, the structures' mesh is verified by calculating the mean drift force on the body surfaces using two different methods: Conservation of momentum and direct pressure integration. These results are presented in Section 7.1.2.

For the free surface mesh, it was decided to use almost the maximum number of elements as this had a small effect on the computational cost of the analysis. A mesh refinement study was performed for the free surface, using two coarser meshes to see if a lower amount of panel elements would influence the results. This showed to have no influence at all. Thus, using the maximum number of elements with no triangular elements for the discretization of the free surface is assumed to be sufficient. Table 6.1 presents the total number of panel elements on the floaters and free surfaces for the INO WINDMOOR and OO-Star.

Table 6.1: Number of elements on the floaters and the free surface models.

	Floater	Free Surface
INO WINDMOOR	7185	9350
OO-Star	11362	9964

6.3 Scaling of the OO-Star Semi-Submersible Platform

In order to compare the two different floating foundation concepts, it is convenient to have the same power capacity of the turbines. The OO-Star floating foundation, which is suited for a 10 MW turbine, is therefore needed to be upscaled to support a 12 MW turbine. Hence, the WINDMOOR 12 MW turbine will be used on the upscaled OO-Star floating platform. The two scaling parameters are calculated by Equation 6.1 and Equation 6.2, respectively.

$$S = \sqrt[3]{\frac{M_{turbine}^{upscale}}{M_{turbine}^{original}}} = \sqrt[3]{\frac{2010.672t}{1933.723t}} = 1.013 \tag{6.1}$$

$$s = \sqrt{\frac{P_{new}}{P_{initial}}} = \sqrt{\frac{12MW}{10MW}} = 1.095 \tag{6.2}$$

Since no strict rules about the type of scaling method to be used, as discussed in Section 3.5, the scaling parameter for the ratio of the turbine masses, Equation 6.1, is used in this study. The reason for choosing this scaling parameter is the small difference in the turbine masses, which leads to a smaller scaling parameter. Thus unnecessary geometric upscaling of the platform is achieved when considering material costs.

For the scaling procedure, the original model of the OO-Star semi-submersible will first be modelled and verified with existing literature to ensure a sufficient numerical model. Then, the upscaled model will be compared with the original model concerning the hydrodynamic results. By following the up-scaling procedure as proposed by Kikuchi and Ishihara (2019), the draft remains constant as an effect of construction constraints related to docking size and port depth during the upscaling. Further, the diameter of the main column depends on the tower base's diameter, where in this case, no increase in the main column is needed. Table 6.2 presents the properties of the upscaled OO-Star 12MW floater.

Table 6.2: Properties of the upscaled OO-Star floater.

Property	Value	
Substructure mass	22567	[t]
Draft	22	[m]
Centre of mass below (CM) below MSL	-15.23	[m]
Roll inertia about CM	1.0059E+10	[kg m^2]
Pitch inertia about CM	1.0059E+10	[kg m^2]
Pitch inertia about CM	1.7387E+10	[kg m^2]
Tower base interface above MSL	11.143	[m]
Displaced water volume	2.4437E+07	[m^3]
Centre of buoyancy below MSL	-14.42	[m]
Overall system mass*	25048.767	[t]

* Overall mass of the ballasted platform, tower and turbine without the mooring lines.

6.4 Frequency-Domain Analysis

The finite element panel models of the floaters and the free surface are imported into HydroD, where the wave loads and motion response are calculated by Wadam as explained in Section 6.1.2. Wadam uses first-order potential theory for large volume structures to calculate first-order radiation and diffraction effects. The second-order forces and moments are calculated by applying second-order potential theory in the presence of bi-chromatic and bi-directional waves (DNV, 2017). The output from the hydrodynamic analysis consisted of the following:

- Mass matrix and hydrostatic stiffness for the floaters
- Frequency-dependent added mass and damping
- First order excitation forces and moments
- First order response amplitude operators
- Horizontal mean drift forces
- Quadratic transfer functions for difference-frequency forces
- Retardation functions

In compliance with Souza et al. (2021), some additional linear damping was added to the hydrodynamic analysis for the INO WINDMOOR floater. By making a critical damping matrix in HydroD, approximately 5% of critical damping in heave, roll and pitch was implemented in the analysis. The additional damping is applied to obtain reasonable motion transfer functions from Wadam, as Wadam only accounts for potential flow and not viscous damping.

Defining the Total Mass, Centre of Gravity and Radius of Gyration

As the panel models from GeniE do not contain any information about the mass, radius of gyration and centre of gravity, this needs to be defined in HydroD.

The total mass and centre of gravity (COG) for the INO WINDMOOR model were defined according to the parameters in Table 4.3. The total mass given in Table 4.3 is the sum of the platform, tower and rotor mass. As the geometry of the INO WINDMOOR floater was modelled according to the structural dimensions given in Souza et al. (2021) without any simplifications, the displacement at the operational draft was equal to the displacement given in the Souza et al. (2021). The radius of gyration was defined according to the value given in Table 4.3.

For the OO-Star model, the total mass was defined as the mass corresponding to the displaced volume at the operational draft equal to 22 m, while an iterative process defined the COG by calculating the metacentric height (GM) for the floater according to the data given in Yu et al. (2018). The geometry of the panel model had some simplifications that resulted in a higher displacement compared to the reference model, and as a consequence of this, the draft became too low when applying the mass that was given in Yu et al. (2018). When defining the radius of gyration for the OO-Star model, this was done using

$$r_{\text{g axis}} = \sqrt{\frac{I_{\text{axis}}}{m}} \tag{6.3}$$

where I_{axis} is the moment of inertia and m is the total mass. The radius of gyration was calculated by using the moment of inertia values given in Table 4.1.

6.4.1 First Order Frequency-Domain

The first-order frequency domain analysis is performed for wave headings 0-360°with a step of 45°. The wave periods range from 4-35s for the INO WINDMOOR and 4-38s for the OO-Star, with a step of 1s. When deciding the range of wave periods to be used in the analysis, an emphasis was made on capturing the response at the natural periods in heave, pitch and roll. In order to capture the peak response at the natural periods, a finer step between the wave periods was applied around these natural periods. During the project thesis, the models were verified by comparing the obtained frequency-dependent added mass and damping with results from the reference articles Souza et al. (2021) and Yu et al. (2018) for the INO WINDMOOR and OO-Star, respectively. The comparison is given in Section 7.1.1.

6.4.2 Second Order Frequency-Domain

A second-order frequency domain analysis calculates the difference-frequency excitation loads in surge, heave, and pitch. The difference-frequency effect occurs due to the difference of two frequencies, meaning that all valid combinations of the frequency input were subjected to the analysis. As a consequence of this, solving the second-order difference-frequency analysis is computationally demanding. It was, therefore, decided to only perform the analysis with a wave heading of 0°. The discretized free surface radius is set to 250 m, corresponding to a wave period of $T = 12.65s$ and $\omega = 0.496rad/s$, and thus the lower frequency range limit is set to $\omega = 0.5rad/s$. The frequency range for the second-order analysis is therefore set to $0.5 - 1.5$rad/s with a frequency step of $\delta\omega = 0.025$.

Regarding the calculation methods used in Wadam, conservation of momentum (far-field integration) is used for the three horizontal degrees of freedom. This method is less dependent on the mesh quality, making it a more robust method. Therefore, the vertical motions are calculated using direct pressure integration.

The second-order frequency domain analysis is performed to check the applicability of Newman's approximation in the time-domain analysis in SIMA. The application of Newman's approximation brings a significant advantage since there is no need to solve the second-order problems. The validity of the approximation is based on that the difference frequencies are close to the main diagonal, which implies that the natural period is long. It is, therefore, usually assumed that the approach is accurate enough for moored systems in deep waters with large natural periods (Nuno Fonseca, 2018). The mean drift forces are checked against results where full QTFs are applied. The results are presented in Section 7.1.4.

6.5 Coupled Model in SIMA

The fully coupled analysis is performed in the SIMA workbench. The frequency-domain hydrodynamic output from Wadam is imported into SIMA as a SIMO-body, modelled as a nodal component in a dynamic analysis. The floating SIMO body is then connected to the tower, turbine and mooring system using the master-slave technique. The tower base and the mooring fairleads are then defined as slaves with the floating body as their master. Erin Bachynski from The Department of Marine Technology, provided the tower models and the WINDMOOR 12 MW turbine. The properties of the tower and the turbine are described in Section 4.2. Figure 6.7 presents the two FWT models in SIMA.

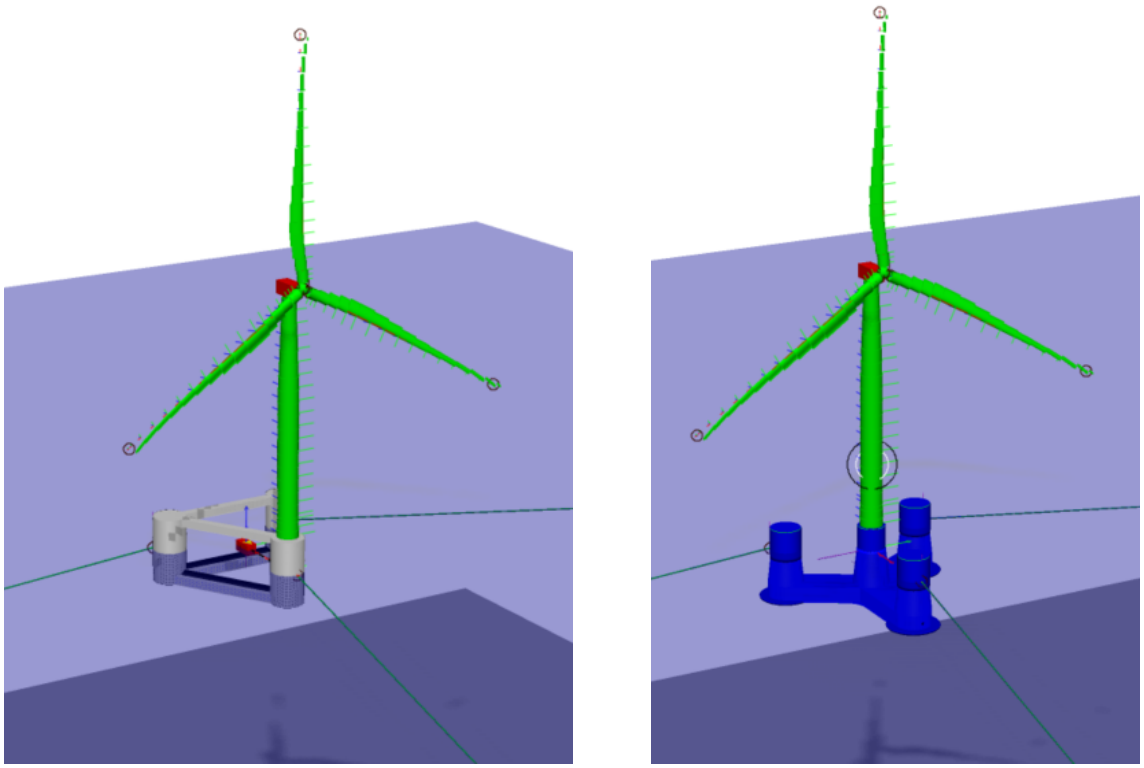

(a) (b)

Figure 6.7: Complete numerical models of the INO WINDMOOR (a) and The OO-Star (b) FWT's in SIMA.

The hydrodynamic results from the frequency domain analysis in HydroD correspond to the total weight of the FWT. In SIMA, the SIMO body only accounts for the data relevant to the floating body. Consequently, some corrections had to be made regarding the hull hydrostatic data in SIMA. The modified values of the INO WINDMOOR and OO-Star floaters concur with the properties presented in Table 4.4 and Table 6.2, respectively.

6.5.1 Hydrostatic Restoring Corrections

The restoring matrix is imported to SIMO from the frequency domain analysis. The hydrostatic stiffness in pitch and roll needs to be modified such that only the parts related to the SIMO-body are included. The restoring coefficients can be determined according to Equation 6.4

$$C_{ii} = \rho g I_{wp} + \rho g \nabla z_B - M g z_G \tag{6.4}$$

where ρ is water density, g is the gravity constant, I_{wp} is the moment of inertia of the waterplane area, ∇ is the displaced volume of water, M is the mass of the floater and z_G and z_B are the z-coordinates of the centre of gravity and centre of buoyancy, respectively. The last term on the right side of Equation 6.4 is taken into account in SIMA by choosing the option "Gravity included" for the floating platform. In contrast, the buoyancy is accounted for as a specified vertical force applied at the centre of buoyancy and pointing in a positive global z-direction. The hydrostatic restoring matrix then only contains the contribution due to the volume variation caused by small motions around equilibrium, as the weight and buoyancy at equilibrium are already considered.

The recalculated restoring coefficients C_{ii} are then given as (Faltinsen, 1993)

$$\begin{aligned} C_{33} &= \rho g A_{wp} \\ C_{44} &= \rho g \iint_{A_{wp}} y^2 ds \\ C_{55} &= \rho g \iint_{A_{wp}} x^2 ds \end{aligned} \tag{6.5}$$

where ρ is water density, g is gravity constant, A_{wp} is the waterplane area. This modelling approach ensures that the weight of the other FWT components are properly accounted for, and was originally outlined in Kvittem (2014).

6.5.2 Wind Input

The turbulent wind input used in the time-domain analysis in SIMA is generated by the stochastic, full-field, turbulence wind simulator TurbSim, developed by NREL. TurbSim generated a time-series of three-component wind speed vectors at points in a 2-dimensional vertical rectangular grid that is fixed in space (B. Jonkman, 2009). Each grid has a matrix of 40 grid points horizontally and vertically. The grid size is defined as 230 m x 230 m, and the radius of the turbine is 108.45 m. The generated wind data are based on the environmental conditions presented in Section 5.2.4. For most of the meteorological boundary conditions, the default values in TurbSim are used, meaning:

- The IEC Kaimal Model
- A Normal Turbulence Model (NTM) defined in (*Wind energy generation systems - Part 1: Design requirements* 2019), as the time-domain simulations only will be performed with wind speeds below cut-off.
- A power law wind profile, meaning that the power law exponent is used to calculate the average wind speed at height z using Equation 5.2.
- A surface roughness of 0.0003 m

6.5.3 Controller

The controller used for the INO WINDMOOR 12 MW turbine is adopted from the NREL Open-Source Controller (ROSCO). The ROSCO controller uses a variable-speed-pitch (VSVP) control approach and a peak shaving strategy near rated wind speed (Souza et al., 2021). The controllers objective is according to (Bachynski, 2021b):

- Drive-train load alleviation
- Power quality control
- Maximising energy capture
- Dynamic mode damping
- Avoidance of enhancing structural loads
- Actuator activity reduction

Below rated rotor speed, the torque is set to optimise the power capture, while the blade-pitch angle remains unchanged at zero degrees. Above rated, the rotor speed should never exceed the rated rotor speed. However, due to dynamic variations in the wind speed, fluctuations in the rotor speed can occur. Both the blade pitch controller and the generator torque in the above rated region are active. Regarding the generator torque, two options are available:

- Constant power. The generator torque is then adjusted to try to maintain a constant power output.
- Constant torque. The generator torque is kept constant as the rotor speed is above or equal to the rated speed. The constant value can be found if the rated power and the rated generator torque are known. This strategy is mostly used for floating wind turbines.

The generator torque is given as:

$$Q_{gen} = \frac{P_{\text{rated}}}{\omega_{\text{rated}}} \tag{6.6}$$

where P_{rated} is the rated power and ω_{rated} is the rated rotor speed. The controller was provided by Erin Bachynski from The Department of Marine Technology.

6.5.4 Quadratic Drag Contribution

The submerged part of the floaters were discretised into slender elements in order to account for the quadratic drag term in Morison's Equation 3.30. The INO WINDMOOR floater was discretised into six elements: three vertical circular cylinders corresponding to the surface-piercing columns and three horizontal cuboids corresponding to the pontoons. The OO-Star floater was discretised into 15 elements: 9 circular cylinders with different width and drag coefficients corresponding to the columns, three horizontal cuboids corresponding to the pontoons and three circular cylinders corresponding to the heave plates. The drag contribution on each element is calculated using strip theory. As most of the contribution to the mean wave force comes from the drag force on the members near the free surface, an approach with different drag coefficients on the upper and lower parts of the columns is applied for the OO-Star model. Using this approach makes it possible to model the mean and varying part of the wave loads more accurate.

The non-dimensional drag coefficients C_d provided in Table 6.3 follow Appendix E of DNV (2014) For the OO-Star model, the drag coefficients are obtained from Kvittem et al. (2018) where the

drag components are determined from irregular wave test in operational conditions, these values are provided in Table 6.4.

Table 6.3 and Table 6.4 present the slender elements modelled in SIMA for the INO WINDMOOR and OO-Star model, respectively. L [m] is the vertical length of the columns and heave plates, while it is the horizontal length for the pontoons, D [m] is the diameter of the columns and heave plates, W [m] is the width of the pontoons, H [m] is the height of the pontoons, z_1 and z_2 are the vertical coordinates of the elements and C_D is the quadratic drag coefficient.

Table 6.3: Slender elements in SIMA for the INO WINDMOOR floater.

INO WINDMOOR							
	L [m]	D [m]	W [m]	H [m]	z_1 [m]	z_2 [m]	C_D [-]
Columns	31	15	-	-	-15.5	15.5	1
Pontoons (z-direction)	61	-	10	4	-13.5	-13.5	1.4
Pontoons (y-direction)	61	-	10	4	-13.5	-13.5	2.35

Table 6.4: Slender elements in SIMA for the OO-Star floater.

OO-Star							
	L [m]	D [m]	W [m]	H [m]	z_1 [m]	z_2 [m]	C_D [-]
Center Column - Top	11.14	12.2	-	-	11.14	0	0.8
Center Column - Middle	4.05	13.27	-	-	0	-4.05	0.8
Center Column - Lower	11.15	15.09	-	-	-4.05	-15.2	0.35
Corner Column - Top	13.67	13.57	-	-	9.62	-4.05	0.8
Corner Column - Below	11.15	14.79	-	-	-4.05	-15.2	0.35
Heave Plate	0.51	23.1	-	-	-21.779	-22.29	12
Pontoons (z-direction)	45.48		16.2	7.09	-18.74	-18.74	0.7
Pontoons (y-direction)	45.48	-	16.2	7.09	-18.74	-18.74	0.8

As the non-dimensional drag coefficients for the INO WINDMOOR in Table 6.3 are not based on either extreme or operational conditions for the given location, an investigation of the drag coefficient is performed, taking into account the variability of the Keulegan Carpenter (KC) number for irregular sea states. According to DNV (2014), the KC number for combined wave and current in-line action is expressed as shown in Equation 6.7, under the assumption of a fixed cylinder.

$$KC = \frac{(v_m + v_c)T_z}{D} \tag{6.7}$$

v_m is the maximum horizontal wave particle velocity taken at the centre of the column, and v_c is the current velocity. T_z is the zero up-crossing period, and D is the column diameter.

From the time-domain analyses performed in SIMA with design load cases LC1 and LC3 as defined in Section 5.3, this resulted in KC numbers of 0.7863 and 4.423 for the columns of INO WINDMOOR in operational and extreme conditions, respectively. Further, the viscous drag coefficients are obtained by using the experimental results in Figure 6.8, which presents drag coefficients versus KC number for a smooth circular cylinder in planar oscillatory flow (Faltinsen, 1993).

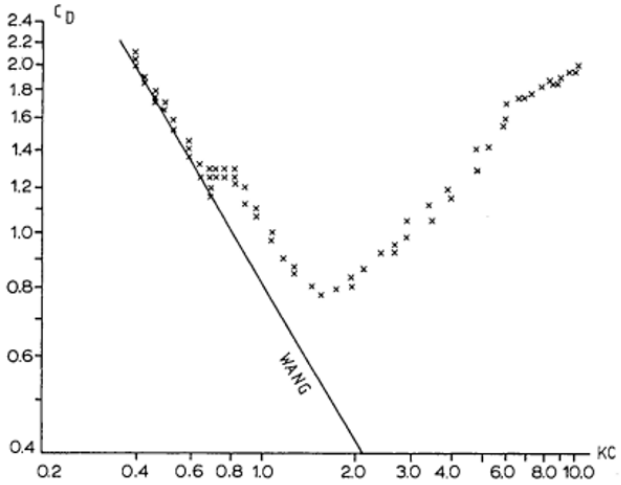

Figure 6.8: Experimental results of C_D for a circular cylinder in sub-critical conditions at small KC numbers (Faltinsen, 1993).

Drag coefficients of approximately $C_D = 1.3$ and $C_D = 1.1$ is found for operational and extreme condition, respectively. Thus, the quadratic damping is underestimated when using the coefficients given in the DNV standard. Moreover, it should be noted that the drag components regarding the OO-Star are only determined for operational conditions and thus not completely representative of extreme conditions. The calculation of the KC number is based on the assumption of a fixed cylinder, however, in this scenario the cylinder is not fixed. Thus, a rough estimate of the KC number is expected.

6.6 Design of Mooring System

For the selected location of interest, with a water depth of 280 m, a new mooring system design is needed for both FWTs. The mooring system design is based on the preliminary mooring system used in Souza et al. (2021), consisting of 3 hybrids (chain + polyester) catenary lines. As this thesis aims to compare the two different floater designs, it was decided to use the same mooring line setup for both floaters while maintaining the natural periods in surge for the respective floater designs.

6.6.1 Material

Chain is the most common component used in mooring lines in offshore mooring systems. With its simple and effective design, the offshore mooring chain is sturdy, provides added holding capacity to the anchor and exhibits excellent abrasion resistance to the seabed. Stud-link and studless chain are the two types of chain constructions that are frequently used in offshore mooring lines today, as shown in Figure 6.9. Stud-link chain differs from the studless chain by having a stud fitted inside the oval link to avoid tangling of the chain. Consequently, the stud-link chain is most common for temporary moorings, where the moorings are expected to be deployed and retrieved numerous times during their lifetime. However, for permanent moorings studless chain is most common.

The polyester rope has been increasingly favoured for deep water permanent mooring applications due to its low weight and low stiffness. Hence, the chain-polyester-chain configuration is becoming more extensively used for deep and ultradeep waters (Ma et al., 2019).

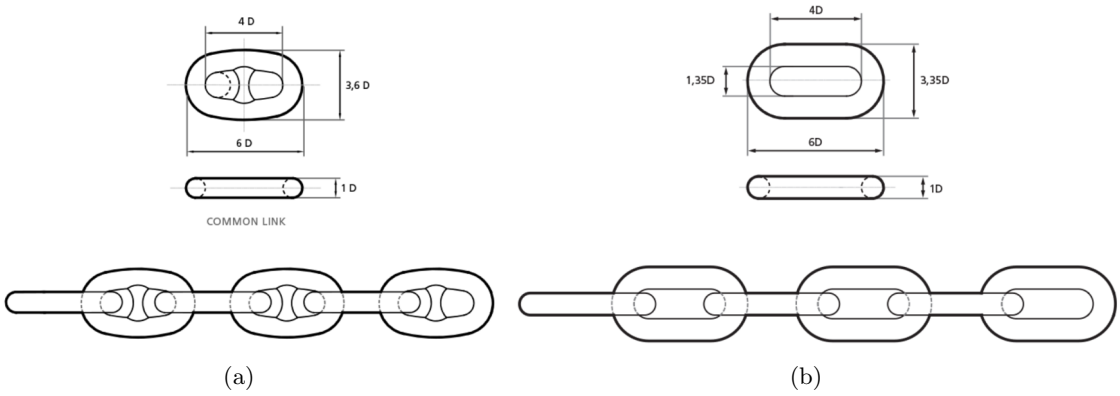

Figure 6.9: Stud-link chain (a) and studless chain (b) (Chain, 2021).

The offshore mooring chain is classified by specified minimum ultimate tensile strength and dividend into five grades: R3, R3S, R4, R4S, and R5 DNV (2015). The characteristics of the different chain grades are presented in Table 6.5

Table 6.5: Minimum mechanical properties for chain cable materials (DNV, 2015).

Steel grade	*Yield stress* R_e N/mm^2	*Tensile strength* R_m N/mm^2	*Elongation* A_5 %	*Reduction of area* Z %	*Charpy V-notch*		
					Temperature [1] °C	*Average energy* J	*Single energy* J
R3	410	690	17	50 [2]	0	60	45
					-20	40	30
R3S	490	770	15	50 [2]	0	65	49
					-20	45	34
R4	580	860	12	50 [3]	-20	50	38
R4S	700	960	12	50 [3]	-20	56	42
R5	760	1000	12	50 [3]	-20	58	44

[1] For grade R3 and R3S, testing may be carried out at either 0°C or -20°C.
[2] For cast accessories, the minimum value shall be 40%.
[3] For cast accessories, the minimum value shall be 35%.

According to DNVGL-OS-E301 DNV (2018a), the effective elastic modulus applied in the mooring analysis for preliminary design may be taken as presented in Table 6.6.

Table 6.6: Effective elastic modulus applied in mooring analysis, where d is the chain diameter in mm.

Chain grade	**Elastic modulus**
Stud chain R3/R4/R5	Not less than $5.6 \cdot 10^{10}$ N/m^2
Studless chain R3	$(5.40 - 0.0040 \cdot d) \cdot 10^{10}$ N/m^2
Studless chain R4	$(5.45 - 0.0025 \cdot d) \cdot 10^{10}$ N/m^2
Studless chain R5	$(6.0 - 0.0033 \cdot d) \cdot 10^{10}$ N/m^2

6.6.2 Design Procedure

The first step in the design procedure is to determine the anchor radius. The anchor radius is established by the ratio of anchor radius to water depth, R/D given in Ma et al. (2019), which is based on data from several existing facilities. Using the reference R/D ratio presented in Ma et al. (2019), a water depth of 280 m yields a R/D ratio of 3.4, which in turn gives an anchor radius of approximately 950 m.

Secondly, a value for the unstretched mooring line length is assumed, where in this case, the mooring line length is initially assumed to be 1020 m. Then, as mentioned previously, the mooring system is based on the design given by Souza et al. (2021). Thus the same fraction of chain-polyester-chain configuration is implemented to the assumed unstretched mooring line length.

Lastly, a free decay test is performed to check the natural period in surge while adjusting the pretension to achieve the wanted natural periods of 97.3 s and 181.81 s for the respective FWTs, given in Souza et al. (2021) and Yu et al. (2018), respectively. From the decay tests for the OO-Star, a strong surge-pitch coupling effect occurred, which led to the decision to lower the location of the fairleads down to the free surface level. This will be discussed in Section 7.2.

6.6.3 Final Mooring Line Design

The properties of each hybrid mooring line segment are presented in Table 6.7. The two first segments account for 100 mm marine growth, while the latter two segments account for 50 mm marine growth. The effect of marine growth is reflected in the mass/length and coefficients of the mooring line segments in compliance with DNV (2018a).

Table 6.7: Mooring line segment properties.

Segment	Type	Length [m]	Mass/length [kg/m]	Axial stiff [MN]	Ca,T [-]	Ca,L [-]	Cd,T [-]	Cd,L [-]
1	130 mm studless chain	36.7	377.7	1443	1	0.5	6.1	2.9
2	190 mm polyester	124.78	60.7	228	1	0	2.5	0.1
3	190 mm polyester	124.78	46	228	1	0	1.8	0.1
4	130 mm studless chain	733.7	353.6	1443	1	0.5	4.2	2

From the design procedure discussed in the previous section, the final mooring design configuration for INO WINDMOOR and OO-Star are presented in Table 6.8 and Table 6.9, respectively. Figure 6.10 illustrates a top view of the two mooring systems, while the fairlead and anchor positions are shown in Table 6.10 and Table 6.11.

Table 6.8: Mooring line configuration INO WINDMOOR.

Parameter	Value
Unstretched mooring line length	1020 m
Anchor radius from centerline	950 m
Number of mooring lines	3
Angel between adjecent lines	120°
Water depth	280 m
Pretension	2332.3 kN

Table 6.9: Mooring line configuration OO-Star.

Parameter	Value
Unstretched mooring line length	1020 m
Anchor radius from centerline	950 m
Number of mooring lines	3
Angel between adjecent lines	120°
Water depth	280 m
Pretension	1444 kN

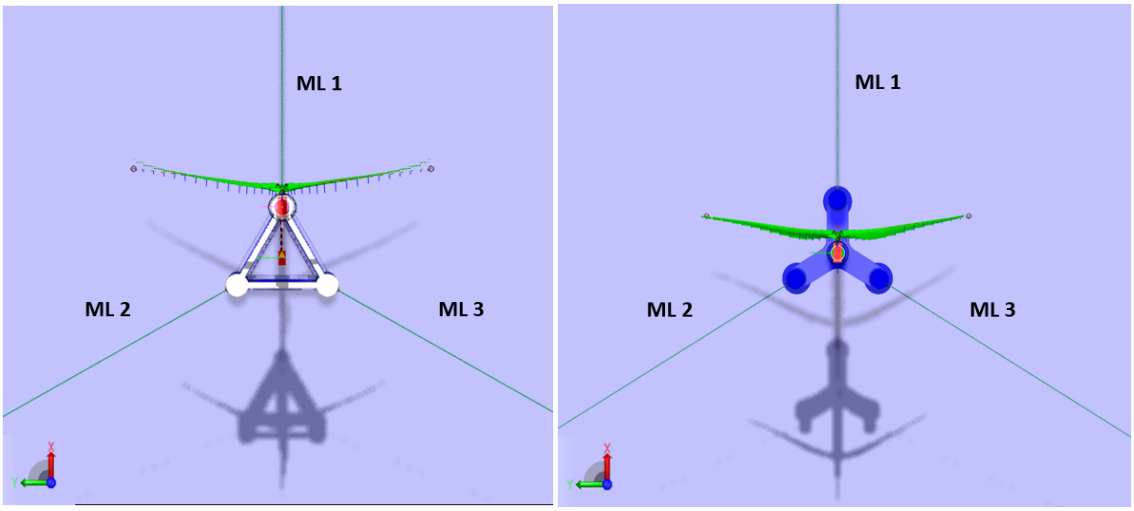

(a) (b)

Figure 6.10: Top view of mooring system for INO WINDMOOR (a) and OO-Star (b).

Table 6.10: INO WINDMOOR fairlead and anchor positions.

	Fairlead			Anchor		
Mooring line	x [m]	y [m]	z [m]	x [m]	y [m]	z [m]
ML1	42.7	0	0	992.92	0	-280
ML2	-21.4	37	0	-496.51	859.92	-280
ML3	-21.4	-37	0	-496.51	-859.92	-280

Table 6.11: OO-Star fairlead and anchor positions.

	Fairlead			Anchor		
Mooring line	x [m]	y [m]	z [m]	x [m]	y [m]	z [m]
ML1	44.268	0	0	977.67	0	-280
ML2	-22.134	38.337	0	-488.83	846.69	-280
ML3	-22.134	-38.337	0	-488.83	-846.69	-280

6.7 Fatigue Damage Estimation

The procedure of the fatigue damage analysis is illustrated in Figure 6.11. Firstly, a fully coupled time-domain analysis in SIMA is conducted with the environmental conditions determined in Section 5.4. The relevant outputs such as axial loads, flapwise and edgewise moments are then obtained in the time domain in order to calculate the axial stress in the tower base and fairlead. The number of axial stress cycles corresponding to different stress ranges is then counted by applying the rainflow counting algorithm to the time series of the axial stress. Lastly, the cumulative fatigue damage is calculated using the Miner-Palmgren's rule with the specific S-N curve, including the probability of occurrence for the specific sea state. The different steps in the fatigue damage calculation are explained more thoroughly in Section 6.7.1 to Section 6.7.4.

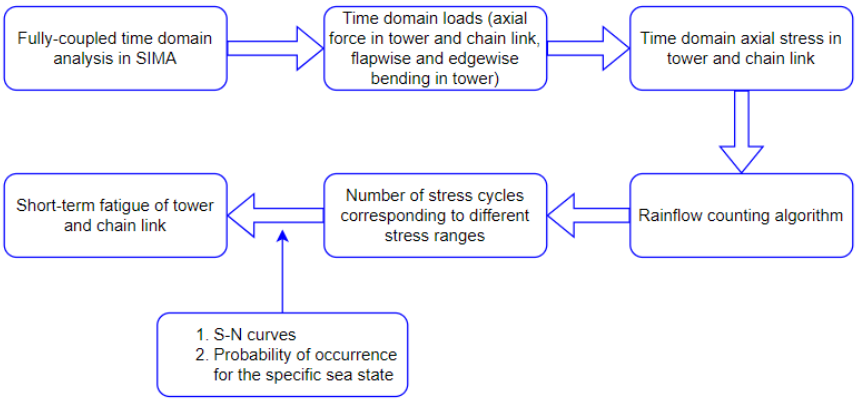

Figure 6.11: Process of the short-term fatigue damage for the tower and chain link.

6.7.1 Calculation of Axial Stress in Tower and Fairlead/Mooring Line

Tower

The tower cross-section is simplified as a thin-walled cylinder structure as illustrated in Figure 6.12 without considering welding effects and connection components between the tower and the sub-structure. The fatigue damage should be calculated considering both the axial and shear stress. However, according to Kvittem and Moan (2015), the fatigue damage from the shear stress is significantly lower than from axial stress. Thus, only the fatigue damage from the axial stress is considered.

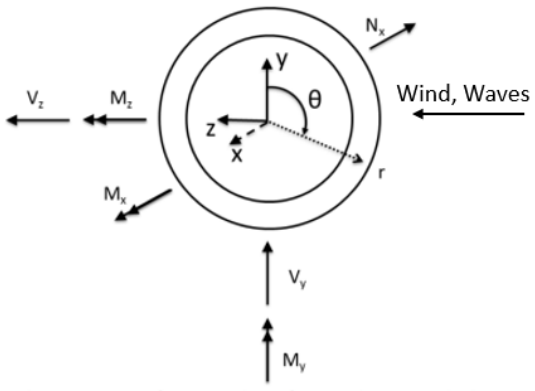

Figure 6.12: Cross-section of the tower with coordinate system for the tower fatigue damage calculation (Bachynski, 2021c).

For a location (r, θ) on the cross section, the axial stress σ can be calculated as (Bachynski, 2021c):

$$\sigma = \frac{N_x}{A} + \frac{M_y}{I_y} r \sin\theta + \frac{M_z}{I_z} r \cos\theta \tag{6.8}$$

where N_x is the axial force where the positive direction is pointing to the tower top, A is the nominal cross-section area, M_y and M_z are the flapwise and edgewise bending moment, respectively. The directions in these moments are based on the right-hand rule. I_y and I_z are the sectional moments to the area of the Y-axis and X-axis, respectively. r is the cross-sectional radius, and θ is the angle from the Y-axis to the calculated point in the clockwise direction. In general, all locations on the cross-section should be considered for the calculation of fatigue damage. In this case, with the wind and waves coming from the same direction, it is permissible only to consider a point on the outer radius of the cross-section and with an angle $\theta = 270°$.

Mooring Line

For the stress calculation in the chain links, it is assumed that the chain link is frequently located on a chain wheel with 7 pockets. Figure 6.13 illustrates three chain links on a 7 pocket fairlead. Additionally, it is assumed that the angular rotation at the fairleads due to the FWT roll and pitch motions is negligible. The nominal tensile stress in the chain link is calculated as:

$$\sigma_{nominal} = \frac{T}{A_{link}} \tag{6.9}$$

where T is the tension in the chain and A_{link} is the chain link cross-sectional area, which is equal to twice the area of a single leg of a link. In addition to the tension-tension fatigue, the fatigue caused by out of plane bending is considered. According to DNV (2018a) chain links that are frequently located on a chain wheel (fairlead) with 7 pockets shall have a stress concentration factor (SCF) of 1.15 due to out of plane bending. The correct stress range is then obtained as:

$$\Delta\sigma = |\sigma_1 - \sigma_2| \cdot SCF \tag{6.10}$$

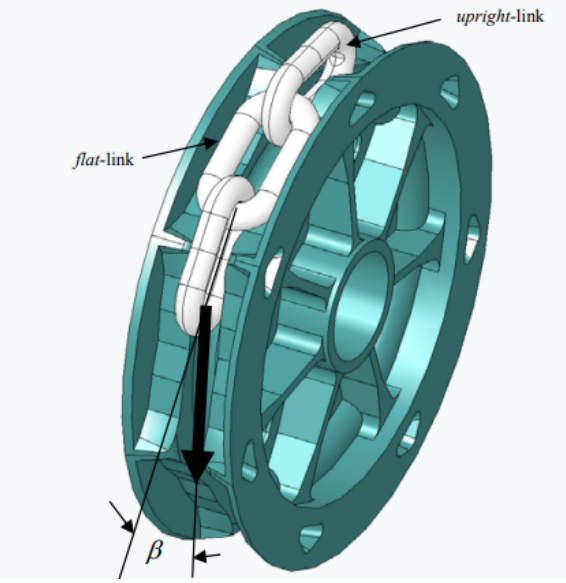

Figure 6.13: Chain links on a 7-pocket fairlead (Vargas et al., 2004).

For stress calculation in the polyester rope, the nominal tensile stress is calculated using Equation 6.9, replacing A_{link} with the cross-sectional area of the polyester rope.

6.7.2 Rainflow Counting Algorithm

The rainflow counting method is widely accepted as a reliable method for fatigue damage calculation with random signals. In a fatigue analysis, most of the fatigue damage parameters are connected with the cycles measured by hysteresis loops H. Li et al. (2017). By applying the rainflow counting method, these hysteresis loops can be obtained based on a stress time series. The principle of the rainflow counting method is illustrated in Figure 6.14. The rainflow counting method applies the following general steps to produce stress cycles (Naess and Moan, 2012):

- *The stress time series is rotated 90° such that the time axis vertically downward as illustrated in Figure 6.14.*
- *Each rainflow begins at the beginning of the time series and successively at the inside of every peak and valley.*
- *Rainflow initiating at a peak (or a valley) drops down until it reaches opposite a peak more positive (or a valley more negative) than the peak (or the valley) from which it started.*
- *Rainflow also stops when it meets the rainflow from a roof above.*
- *Rainflow must terminate at the end of the time series.*
- *The horizontal length of each rainflow is counted as a half cycle with that stress range.*

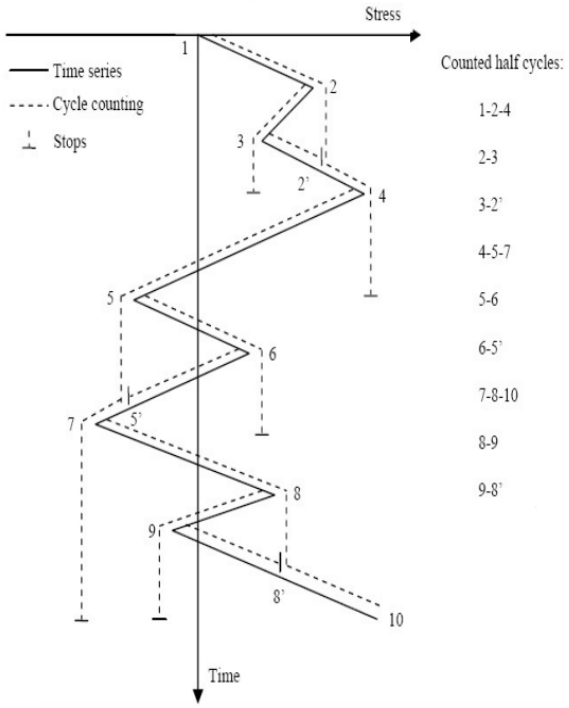

Figure 6.14: Illustration of the rainflow counting method (Naess and Moan, 2012).

The rainflow counting is performed in MATLAB using the WAFO routines *dat2tp* and *tp2rfc*. *dat2tp* extracts the value and location of the turning points from the stress time series while *tp2rfc* finds the rainflow cycles from the sequence of turning points.

6.7.3 Selection of S-N Curves

Tower

The fatigue damage on the tower was calculated by using S-N curves from DNV (2010a). The DNV S-N curve is defined as:

$$\log N = \log \bar{a} - m \log \left(\Delta\sigma \left(\frac{t}{t_{ref}} \right)^k \right) \tag{6.11}$$

where N is the predicted number of cycles to failure for the stress range $\Delta\sigma$, and t is the thickness through which a crack will most likely grow. t_{ref} is the reference thickness equal to 25 mm for welded connections, m is the negative inverse slope of the S-N curve, $\log \bar{a}$ is the intercept of $\log N$-axis by S-N curve and k is the thickness exponent. As the fatigue is assumed to occur in the welds rather than in the base material, S-N curves for girth welds is utilized. Based on the geometry of the joint, S-N curve D from Table 2-1 from DNV (2010a) is chosen. The parameters for the fatigue curve are given in Table 6.12.

The MATLAB code *cc2dam-2slope* is used to compute the fatigue damage based on a two-part S-N curve. This code is modified from the WAFO code *cc2dam* which accounts for S-N curves with a single slope. Additionally, the code is modified to account for the difference in definition between the DNV S-N curve and WAFO. The DNV curves are based on stress ranges, while WAFO is based on amplitudes.

Table 6.12: S-N curve parameters for the tower.

$N \leq 10^7$ cycles		$N > 10^7$ cycles		Fatigue limit at 10^7 cycles	k	t_{ref}
m	$\log \bar{a}$	m	$\log \bar{a}$			
3.0	12.164	5.0	15.606	52.63 MPa	0.20	25 mm

Mooring Line

The calculation of fatigue damage on the different segments of the mooring line is based on the S-N curves from DNV (2018a). The following linearized equation is used for the component capacity against tension fatigue:

$$\log\left(n_c(s)\right) = \log\left(a_D\right) - m \cdot \log(s) \tag{6.12}$$

where $n_C(s)$ is the number of stress ranges, s is the stress range, a_D is the intercept parameter of the S-N curve and m is the slope of the S-N curve. The parameters a_D are given in Table 6.13 and S-N curves in Figure 6.15

Table 6.13: S-N curve parameters for mooring lines (DNV, 2018a).

	a_D	m
Stud chain	$1.2 \cdot 10^{11}$	3.0
Studless chain (open link)	$6.0 \cdot 10^{10}$	3.0
Stranded rope	$3.4 \cdot 10^{14}$	4.0
Spiral rope	$1.7 \cdot 10^{17}$	4.8

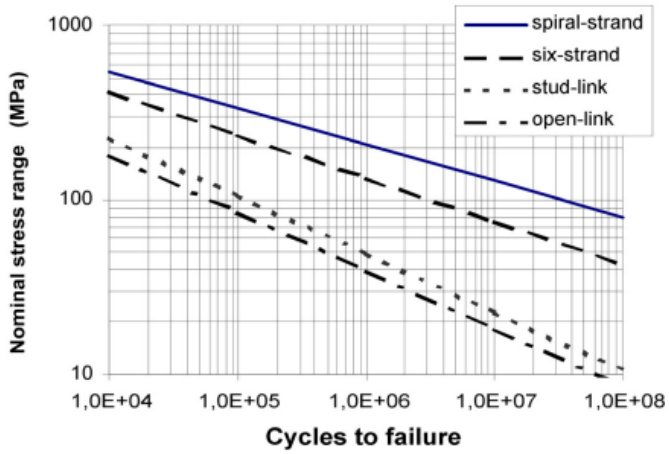

Figure 6.15: Design S-N curves for mooring lines (DNV, 2018a).

The fatigue damage for the mooring line is calculated in MATLAB using the WAFO code *cc2dam*. The fatigue damage calculation for the chain links and the polyester rope is based on the parameters for the studless chain and spiral rope, respectively, in Table 6.13.

6.7.4 Fatigue Damage Calculation

The total fatigue damage is calculated using the Palmgren Miner rule. Miner's rule is a simplified process that computes the damage increment for each stress cycle and then adds up all the damage increments (H. Li et al., 2017). The damage increment is calculated based on a specific S-N curve. The structural component will fail when the total fatigue damage equals 1.0. The accumulated fatigue damage is calculated as:

$$\Delta D_i = \frac{n_i}{N_i} \tag{6.13}$$

$$D = \sum_{i=1}^{n} \Delta D_i \tag{6.14}$$

where ΔD_i is the damage increment from the i th stress cycle, n_i is the number of cycles computed by the rainflow algorithm corresponding the i th stress cycle, N_i is the number cycles to failure for the i th stress range, n is the number of stress cycles, and D is the accumulated fatigue damage based on specific S-N curves and cycles derived from the rainflow algorithm. The accumulated fatigue damage is without considering the probability of a specific environmental condition and the simulation length. In order to find the accumulated fatigue damage in a specific environmental condition, the probability of occurrence for the specific environmental condition must be included in the calculation of the fatigue damage. The factor of simulation length can also be included to investigate the effect of simulation length. The accumulated fatigue damage is then calculated as:

$$D_{tot} = \frac{T_{tot}}{T_{sim}} \cdot D \cdot p \tag{6.15}$$

where D_{tot} is the accumulated damage, p is the probability of occurrence for a specific environmental condition, T_{tot} is the total duration in the calculation of the short-term fatigue damage, T_{sim} is the simulation length in SIMA, and D is the accumulated fatigue damage calculated in Equation 6.14.

7 Model Verification

This section presents the verification of the two numerical models prior to the fully integrated analyses in the time-domain. Firstly, a description of the hydrodynamic characteristics from the frequency domain analyses is outlined. Followed by system characteristics in the time-domain, such as natural periods, wind turbine performance, mooring system and a seed convergence study.

7.1 Hydrodynamic Analysis in HydroD

7.1.1 Added Mass and Damping Coefficients

The project thesis conducted a thorough comparison of the hydrodynamic coefficients for both models with existing literature. The added mass and damping coefficient for both models showed satisfying results with the reference values from Souza et al. (2021) and Yu et al. (2018). Figure 7.1 shows added mass and damping coefficients in heave for both the numerical models, while plots of added mass and damping in surge, pitch and yaw can be found in Appendix A.1. It should be noted that the hydrodynamic coefficients presented for the OO-Star are for the unscaled floater, which is used to verify the modelling before the up-scaling.

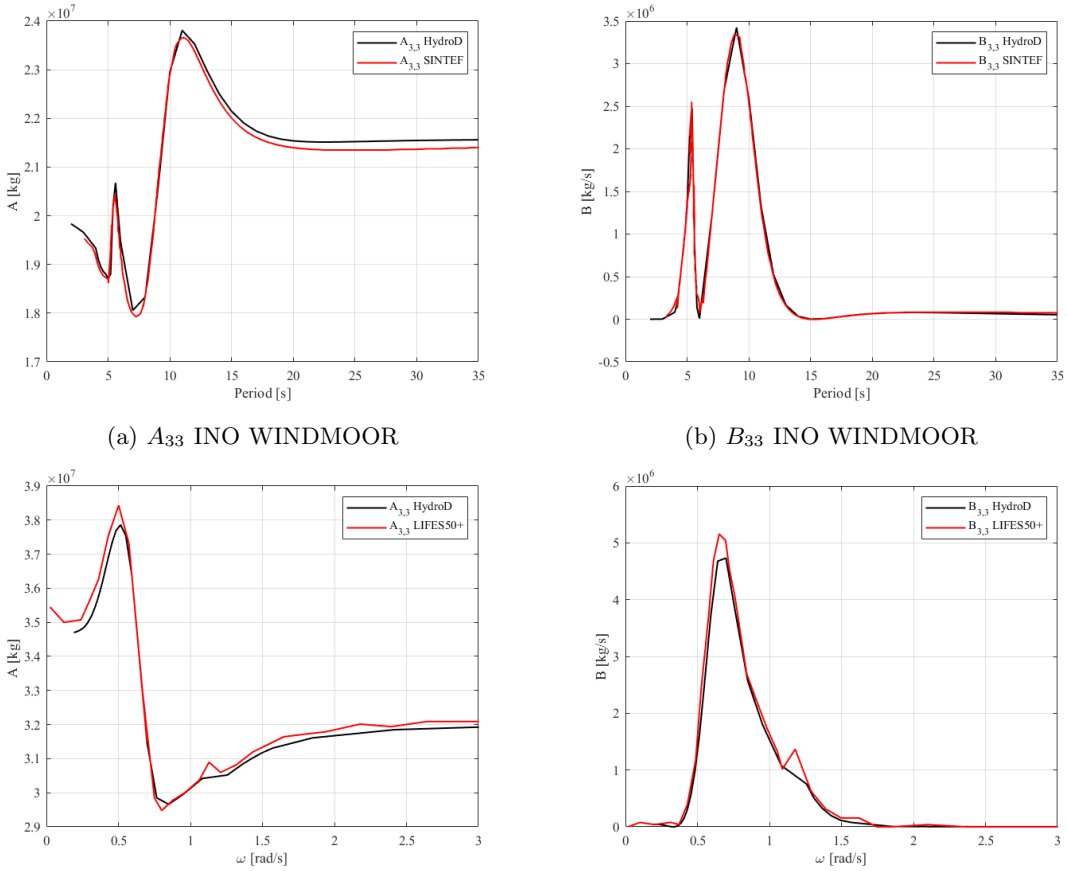

(a) A_{33} INO WINDMOOR

(b) B_{33} INO WINDMOOR

(c) A_{33} OO-Star

(d) B_{33} OO-Star

Figure 7.1: Verification of added mass and damping coefficients against existing literature.

Further, Figure 7.2 presents a convergence study on the heave added mass coefficients conducted in the project thesis for both models. From the results, it is evident that the results are converging as the number of panel elements increases. It can also be observed that the INO WINDMOOR is more sensitive to the panel size than the OO-Star.

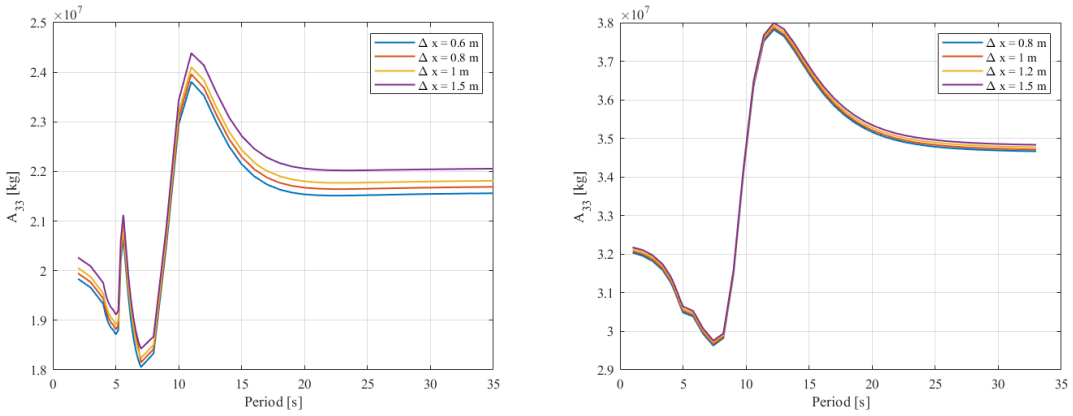

(a) (b)

Figure 7.2: Convergence of heave added mass for different panel element sizes for INO WINDMOOR (a) and OO-Star (b).

7.1.2 Mean Drift Forces

The second-order mean drift forces due to incident waves can be calculated using the momentum conservation method (far-field approach) or the pressure integration method (near-field approach) in Wadam. A way of assessing the quality of the mesh is by comparing the mean drift force from the two calculation methods, noting that according to Pan et al. (2013) the pressure integration method is largely dependent on the mesh quality. Hence, a small difference indicates that the mesh is good. Figure 7.3 illustrates the mean drift forces for both floater models calculated by the two methods. Minor differences in the mean loads are observed for the INO WINDMOOR. However, for the OO-Star, the two methods differ slightly more. The pressure integration method is more sensitive to geometrical approximations, and geometrical singularities of the body surface can be a source of numerical errors (Greco, 2019). Thus, the cone centre column of the OO-Star could explain the deviation in the mean load using pressure integration. Moreover, the selected mesh size is deemed sufficient for both numerical models.

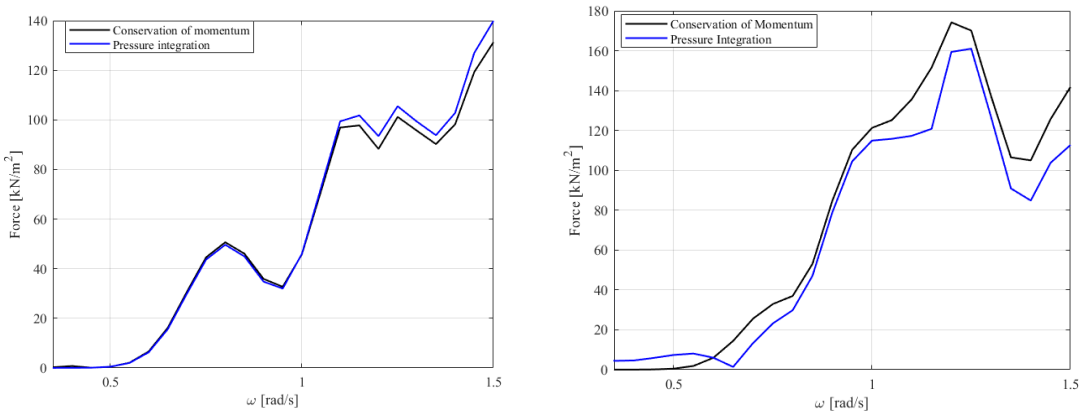

(a) (b)

Figure 7.3: Mean drift force in surge for INO WINDMOOR (a) and OO-Star (b).

7.1.3 Natural Periods from HydroD

From the frequency domain analyses in HydroD, both FWT models are modelled without any influence of the mooring system and thus no additional stiffness for the horizontal motions. Hence, only the natural periods in heave, pitch and roll are obtained from HydroD. Table 7.1 presents the natural periods for both FWT concepts.

Table 7.1: Natural periods from HydroD.

	Heave	Roll	Pitch
INO WINDMOOR	17 s	31 s	31.2 s
OO-Star	21 s	31.4 s	31.4 s

7.1.4 Quadratic Transfer Functions

Figure 7.4 presents the difference frequency excitation forces for surge, heave and pitch for both floaters. The difference frequency forces are calculated using the full quadratic transfer function (QTF) and the mean drift loads from the main diagonal. As expected, the mean drift loads provide satisfactory results for the difference frequency forces in surge, where the natural frequency of the floaters are very low compared to the wave frequency. The lower the natural frequency of the floater, the closer the difference frequencies are to the diagonal elements in the full QTF, as shown in Figure 7.5. This is reflected in the results between INO WINDMOOR and OO-Star, where the natural periods in surge are 97.3 and 181.81 s, respectively.

Further, when looking at the difference frequency force and moment in heave and pitch, respectively, it is observed that the mean drift loads underestimate the forces/moments with respect to the full QTF for both floaters. For motions in the vertical plane, the natural periods are less large and thus further away from the main diagonal where $\omega_j \neq \omega_i$. Consequently, this indicates the effect of the off-diagonal terms in the full QTF, which is not accounted for in the mean drift loads.

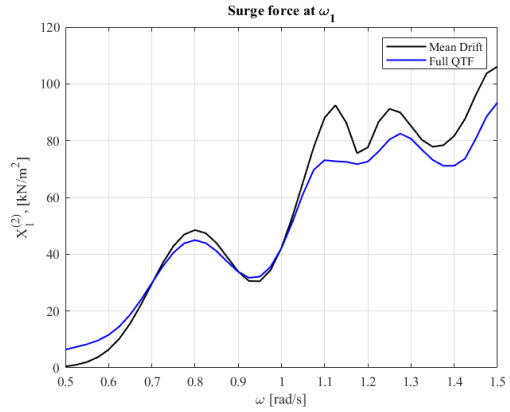

(a) INO WINDMOOR

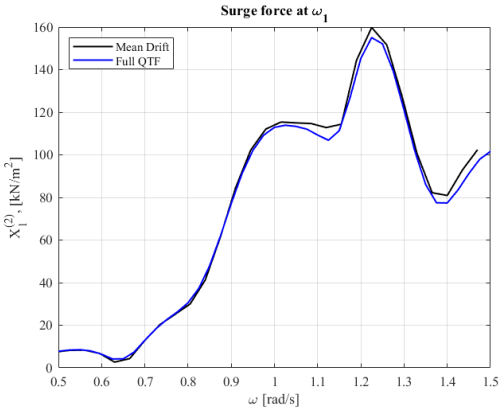

(b) OO-Star

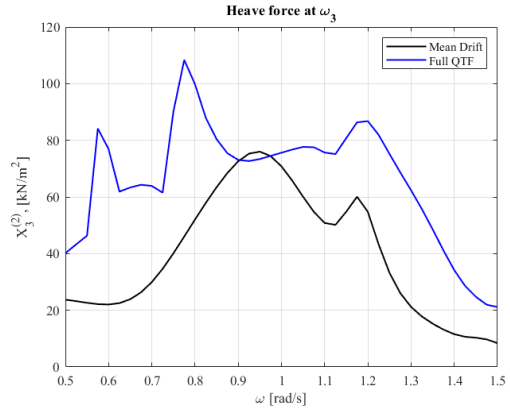

(c) INO WINDMOOR

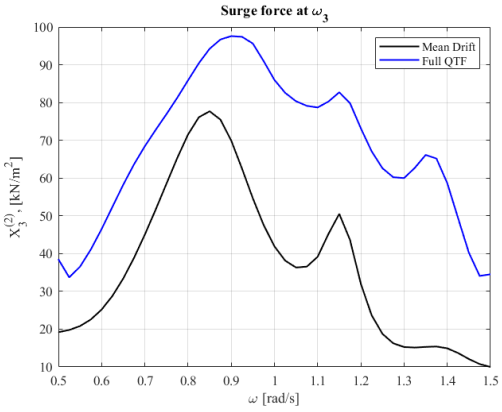

(d) OO-Star

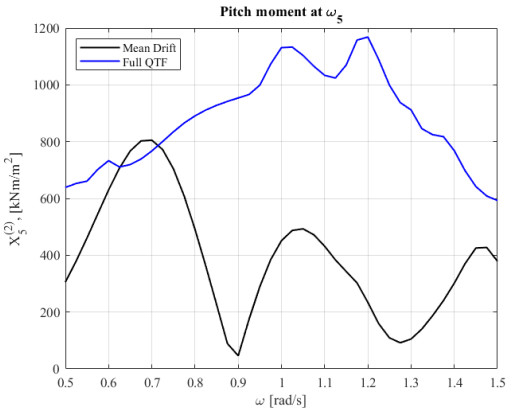

(e) INO WINDMOOR

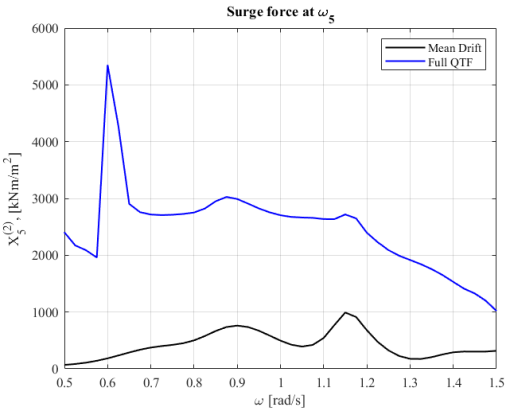

(f) OO-Star

Figure 7.4: Transfer functions for second order excitation forces at difference frequencies for both platforms.

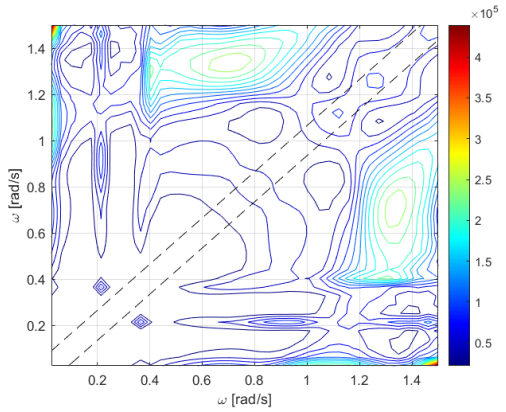

(a) INO WINDMOOR

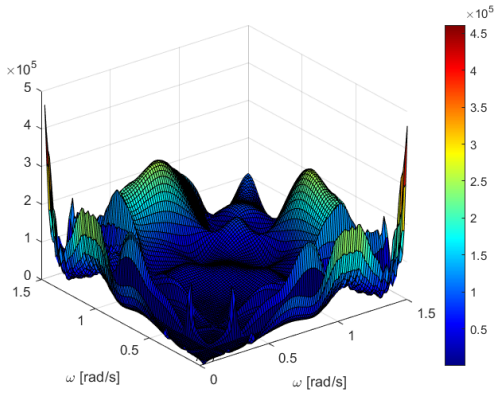

(b) INO WINDMOOR

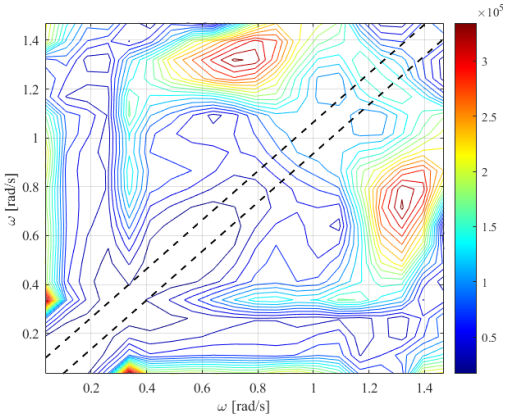

(c) OO-Star

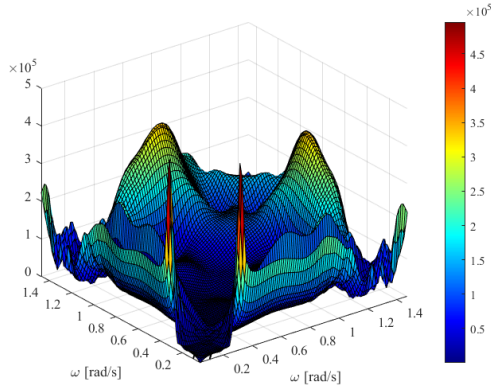

(d) OO-Star

Figure 7.5: INO WINDMOOR difference-frequency surge QTF contour (a) and surface plot (b). OO-Star difference frequency surge QTF contour (a) and surface plot (b). Dashed lines (- -) indicating the surge natural frequency of the respective floaters.

7.2 Decay Tests

In order to document the system's natural periods and damping, free decay tests are performed for the two FWT in all DOFs in SIMA. The free decay test is performed by applying a ramp force, followed by a constant force, which will then be released, as illustrated in Figure 7.6. During the decay tests, the wind turbine is in parked condition, meaning that the rotor blades are feathered 90°and fixed to the tower. For the environmental parameters used in the simulations, the constant wind speed is set to $U_w = 0.01$ m/s, whereas the wave conditions are represented by $H_s = 0.01$ m and $T_p = 20$ s. The point of application for the decay force is [0, 0, 0] and [0, 0, -12] for the INO WINDMOOR and OO-Star, respectively. Table 7.2 presents the simulation parameters used for both models, and the results from the free decay tests are shown in Figure 7.7 and Figure 7.8.

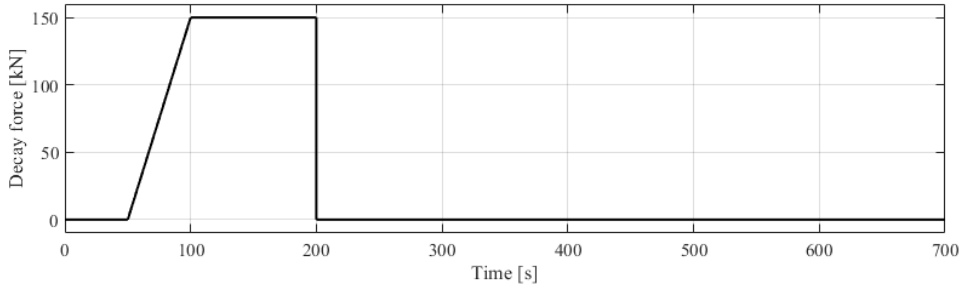

Figure 7.6: Example of decay force with ramp force of 50 s, and constant force of 100 s.

Table 7.2: Simulation parameters for the decay tests.

Vessel	DOF	Force/Moment	Simulation length	Ramp duration	Const. force duration
INO WINDMOOR	Surge	1700 kN	1400 s	100 s	200 s
	Heave	10000 kN	600 s	50 s	100 s
	Pitch	220000 kNm	800 s	100 s	100 s
	Yaw	10000 kNm	1200 s	100 s	100 s
OO-Star	Surge	1000 kN	1400 s	100 s	200 s
	Heave	10000 kN	600 s	50 s	100 s
	pitch	180000 kNm	600 s	50 s	100 s
	Yaw	17000 kNm	800 s	50 s	100 s

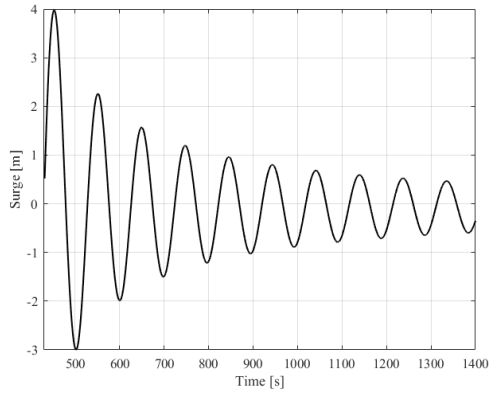

(a) Surge

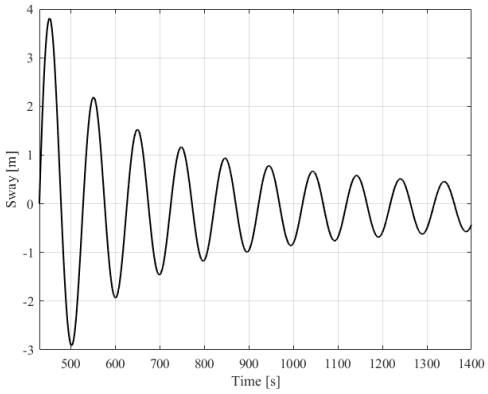

(b) Sway

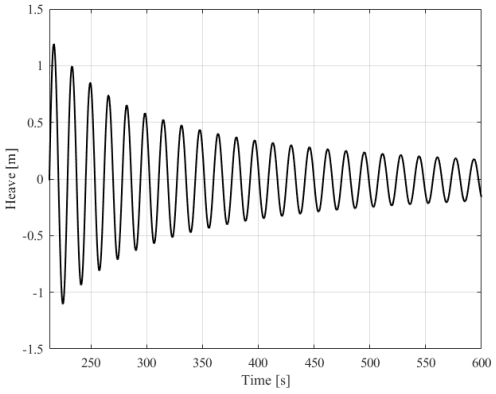

(c) Heave

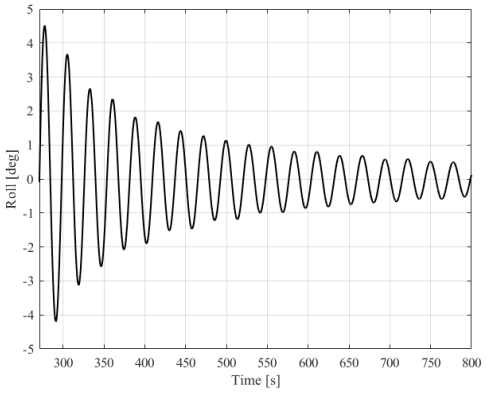

(d) Roll

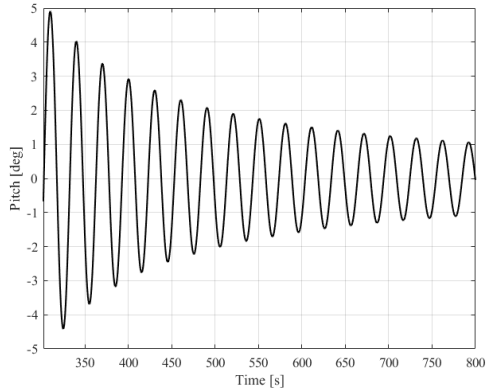

(e) Pitch

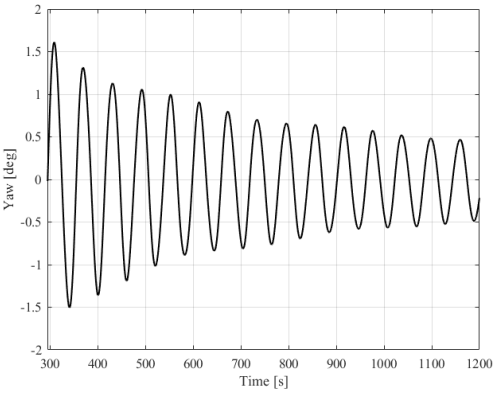

(f) Yaw

Figure 7.7: Free decay tests in all 6 DOF for INO WINDMOOR.

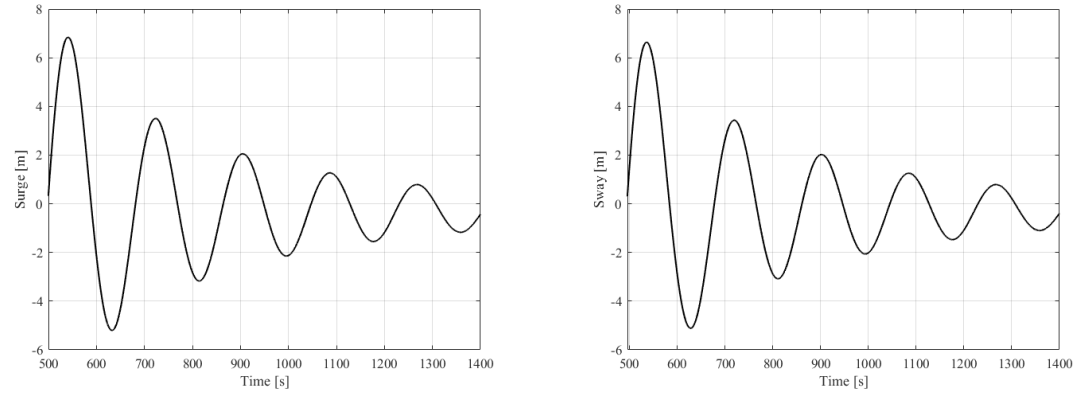

(a) Surge

(b) Sway

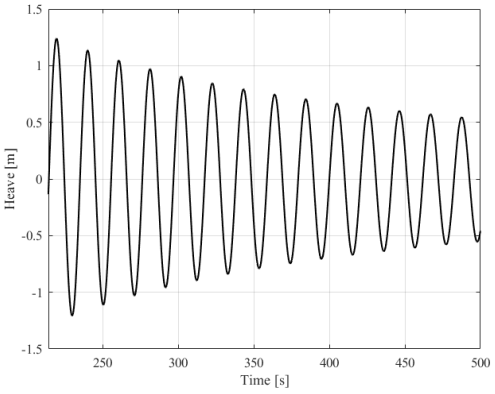

(c) Heave

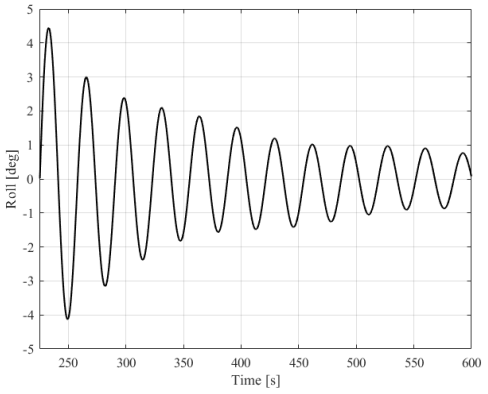

(d) Roll

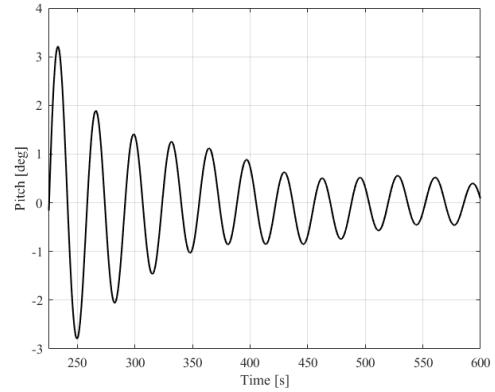

(e) Pitch

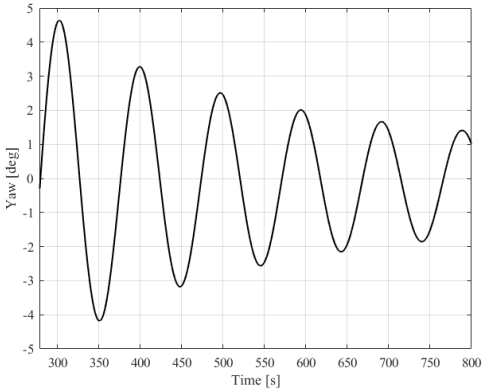

(f) Yaw

Figure 7.8: Free decay tests in all 6 DOF for OO-Star.

In Table 7.3, natural periods from the free decay tests are presented and compared with reference values for the INO WINDMOOR and OO-Star, respectively. The results from the free decay test performed with the INO WINDMOOR model in SIMA show satisfying results when compared with the corresponding natural periods given in Souza et al. (2021), where the most considerable discrepancies of 4 and 6 % are found in the pitch and roll motion, respectively. Furthermore, the large discrepancy in yaw is due to the significant increase in pretension connected to the new mooring system. Hence, a higher yaw stiffness yields a lower natural period for the FWT in yaw.

In contrast to the INO WINDMOOR model, the OO-Star FWT is an upscaled model and fitted with a new turbine compared to the reference model, which is given in Yu et al. (2018). Thus a direct comparison with the reference model would be slightly misleading. However, an increase

in the heave and pitch natural period can be observed, which is due to the increase in the total mass of the system and the moment of inertia in pitch. Moreover, in the same manner, as for the INO WINDMOOR FWT, the lower natural period in yaw is connected with the pretension of the new mooring system. From Figure 7.8e, it can be observed from the decay test in pitch that the pitch motion is coupled; in fact the pitch decay oscillates with the surge natural period, and hence coupled with surge. This surge-pitch coupling is assumed to originate from a nonlinear mooring restoring effect which is dependent on the vertical distance from the fairleads to the platform's centre of gravity (Souza and Bachynski-Polić, 2019).

Table 7.3: Natural periods from free decay tests.

	INO WINDMOOR			OO-Star		
DOF	Free decay	Reference	Deviation	Free decay	Reference	Deviation
Surge	97.7 s	97.3 s	+ 0.4 %	181.72 s	181.81 s	- 0.04 %
Sway	98.45 s	98.0 s	+ 0.4 %	182.75 s	-	-
Heave	16.36 s	16.3 s	+ 0.3 %	20.63 s	20.4 s	+ 1.1 %
Roll	27.8 s	29.5 s	- 6 %	32.68 s	-	-
Pitch	30.14 s	31.4 s	- 4 %	32.74 s	31.25 s	+ 4.7 %
Yaw	60.7 s	88.0 s	- 44 %	97.32 s	116.3 s	- 19.5 %

7.2.1 Decay Tests with Steady Incident Wind Speed

Decay tests with constant wind speeds are performed for both models in surge and pitch, as shown in Figure 7.9 and Figure 7.10. FWT are complex systems, and unexpected behaviour may occur when subjected to nonlinear and coupled loads. One such behaviour is the phenomenon of variation in the surge and pitch decay period when exposed to different wind velocities. For the surge motion, the variation in the natural period is connected to the mooring system non-linearities (Souza and Bachynski-Polić, 2019). The platform will oscillate at a new offset with a new stiffness when subjected to a mean wind speed, and hence, the nonlinear stiffness results in different periods for different wind speeds from when the platform oscillates around the neutral position. As expected, the largest offset in surge is observed at rated wind speed for both models, which corresponds to the wind speed where the turbine experiences the most significant thrust force.

For pitch, the dominating reason for variations in the natural period is, according to Souza and Bachynski-Polić (2019), an inertia/damping effect that originates from the relative phase between the nacelle velocity and the thrust induced at the turbine.

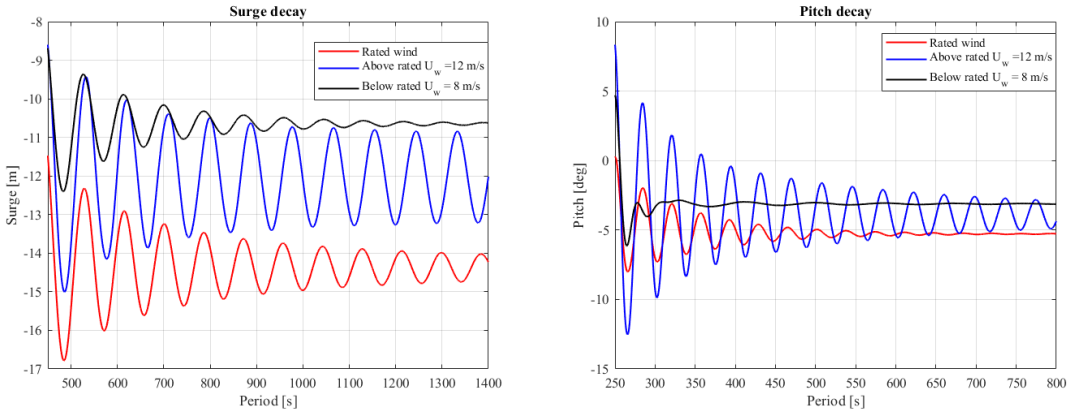

(a) (b)

Figure 7.9: INO WINDMOOR decay tests with constant wind in surge (a) and pitch (b).

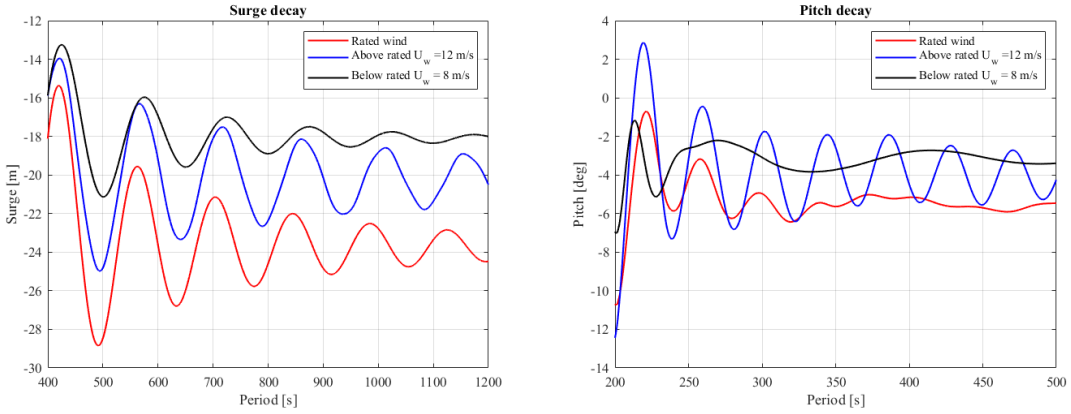

(a) (b)

Figure 7.10: OO-Star decay tests with constant wind in surge (a) and pitch (b).

7.3 Regular Wave Test

The response amplitude operators (RAOs) are obtained through a regular wave test in SIMA. During the regular wave test, the FWT is subjected to incident regular waves with an amplitude $\zeta_a = 1$ m and wave periods ranging from $T = 4$-38 s with a step of 0.5 s. Each simulation is performed with a simulation length of 1200 s, where the motion statistics are taken after the transient phase and the FWT has reached a steady state. The RAOs is then plotted as the motion response per wave amplitude as the function of wave period as seen in Figure 7.11 and Figure 7.12 for the INO WINDMOOR and OO-Star, respectively.

The RAOs for the INO WINDMOOR in surge, heave and pitch correspond well with the RAOs given in the Souza et al. (2021) report. For the OO-Star, no relevant reference data were found in the literature study regarding the RAOs. Therefore, it was found difficult to assess the RAOs of the OO-Star. However, from the heave and pitch RAOs, it is seen that the resonance period corresponds well with the natural periods obtained from the decay tests, indicating that the obtained RAOs from the regular wave test are reasonable.

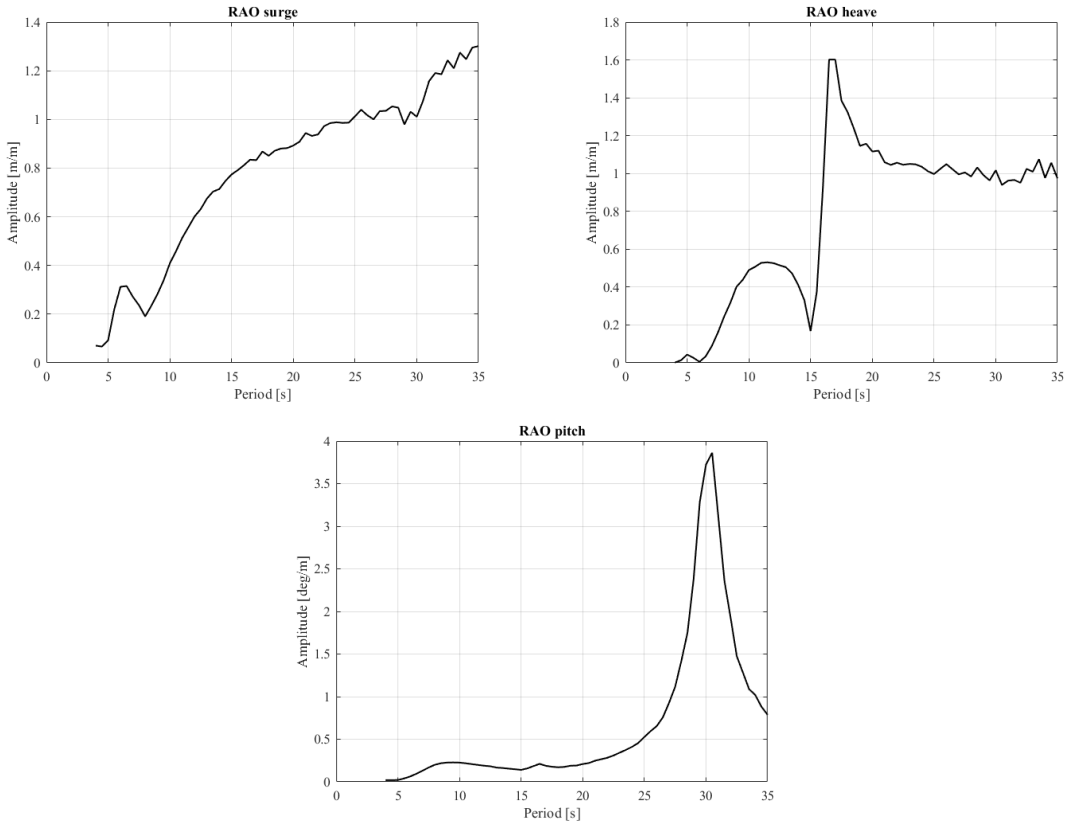

Figure 7.11: INO WINDMOOR RAOs from regular wave tests in SIMA.

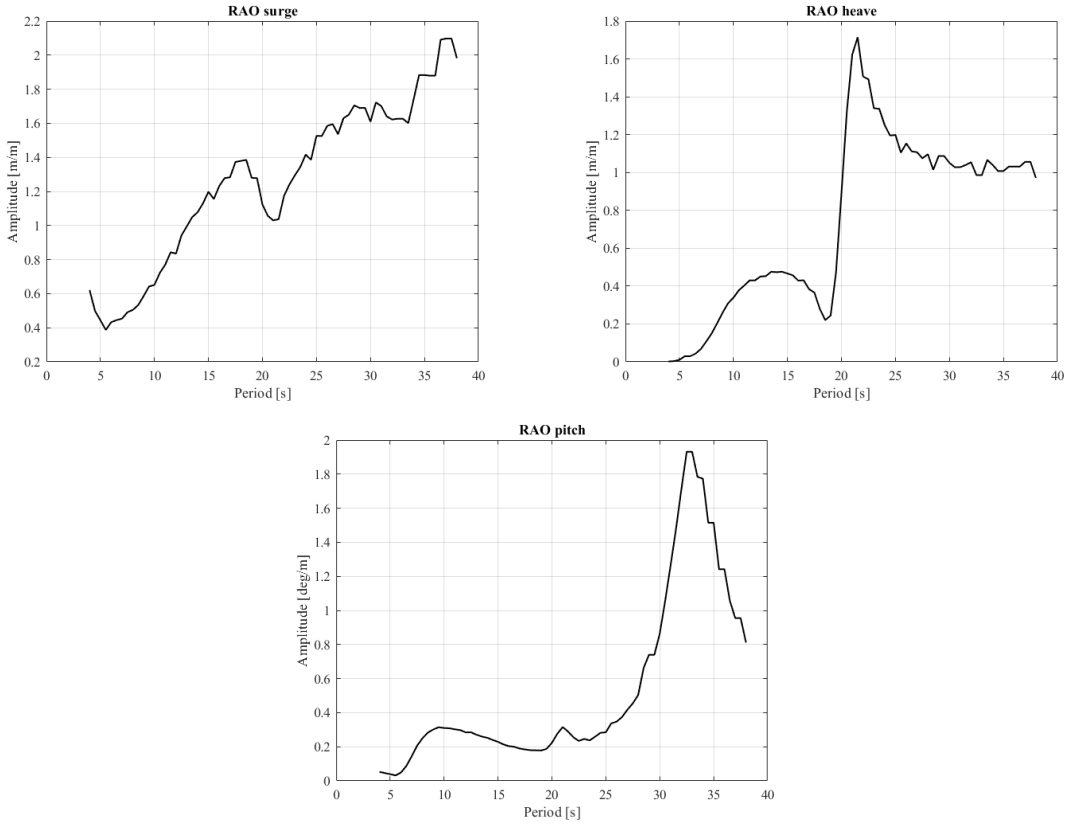

Figure 7.12: OO-Star RAOs from regular wave tests in SIMA.

7.4 Wind Turbine Performance

Constant uniform wind tests are performed to investigate the wind turbine performance and the controller. The dynamic time-domain simulation performed for the FWTs contains wind speeds ranging from 4 - 24 m/s, including the rated wind speed. The turbine is now in operational condition, while the wave parameters are set to $H_s = 0.001$ m and $T_p = 20$ s. An input file with step wind is used for the analysis, with 900 s as the duration for each wind speed. The step wind input file is illustrated in Figure 7.13. The wind turbine performance curves are the mean value of the statistics after the turbine reaches its steady-state condition.

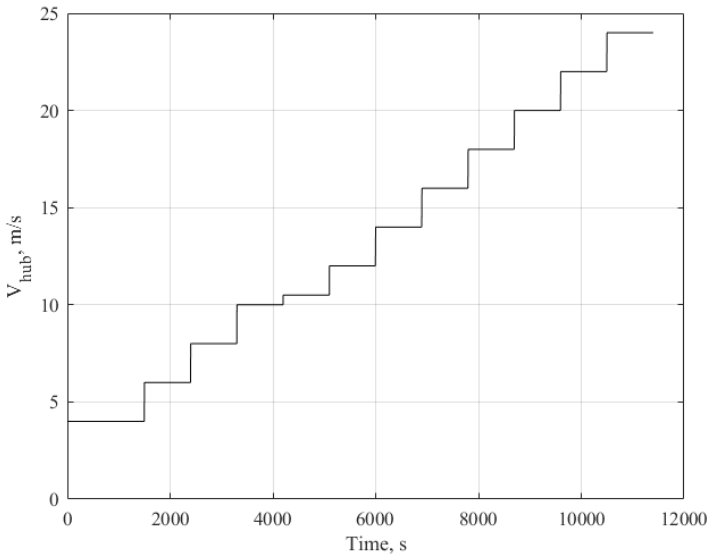

Figure 7.13: Step wind input file for the constant wind test.

Figure 7.14 presents the WINDMOOR 12 MW wind turbine performance curves. The results from the constant wind test are checked with the results given by Souza et al. (2021), and from a graphical assessment, the results correlate quite well with the reference values. Below rated wind speed, the blade pitch angle remains unchanged as the torque is set to optimize the power capture. The largest thrust is observed at rated wind speed. However, the thrust force decreases for wind speeds above rated due to the blade pitch controller as discussed in Section 6.5.3. Consequently, the fixed rotor speed above rated wind speed helps to ensure an optimal conversion efficiency of the wind energy power.

When looking at the mean offset for the platform motions, results from the INO WINDMOOR turbine is representative for both models. The most significant offset for both surge and pitch occurs at rated wind speed. This is an expected result due to the thrust force being maximum at this wind speed. Above rated wind speed, the surge and pitch offset reduce as the pitch control activates and the thrust force reduces. The roll motion during the constant wind tests is marginal. This is mainly because the forces are acting in the x-direction along the symmetry plane of the floater. The small roll motion may be explained by the torque generated by the wind, which causes a moment around the nacelle, hence resulting in a small roll motion.

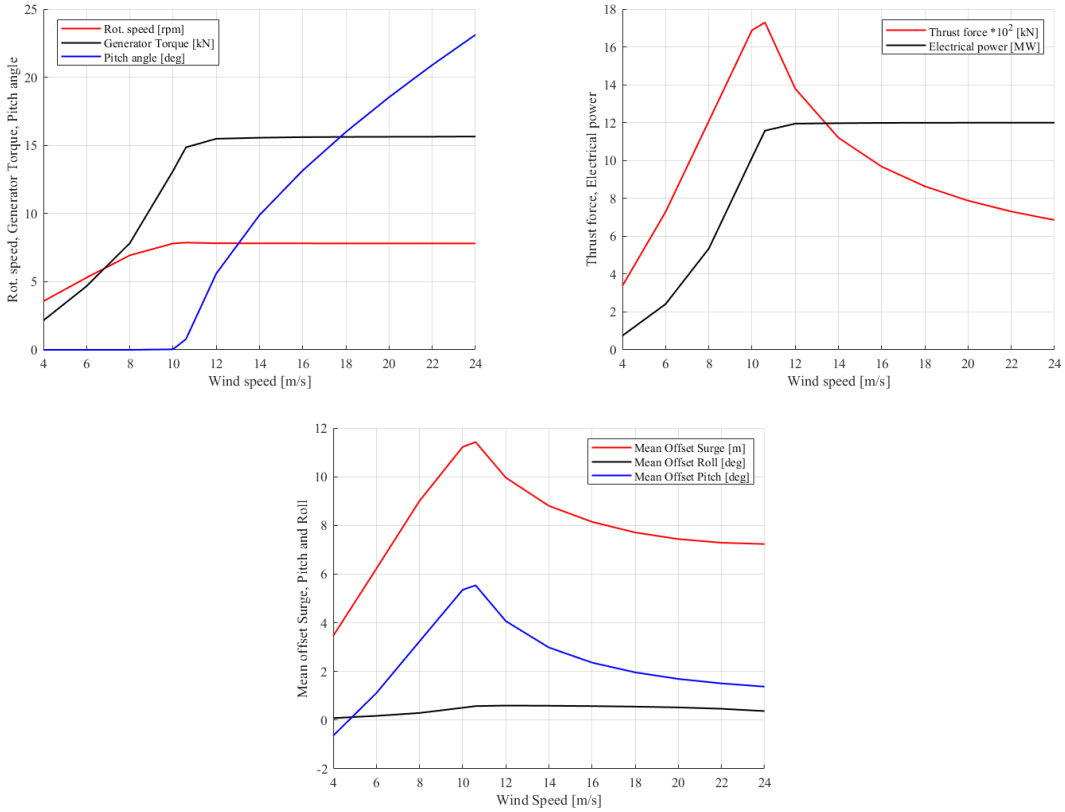

Figure 7.14: WINDMOOR 12 MW turbine performance curves.

7.5 Mooring System Characteristics

The restoring properties of the mooring system in surge were investigated by performing a load-displacement test or pull-out test in SIMA. The load-displacement test is performed similarly to the decay test, utilizing the same wave climate and the turbine in parked condition. A constant horizontal force ranging from 100 to 20000 kN is applied over time, such that the FWT reaches a new offset of oscillation. Thus the surge offset is obtained as the mean value after the FWT reaches a steady-state condition. As an effect of the mooring line arrangement, as seen in Figure 6.10, the restoring is different in 180°(in-line) when only one mooring line is responsible for the offset than for 0°(in-between). Hence, the external force was applied in the positive and negative x-direction.

The restoring force curves are presented in Figure 7.15 and Figure 7.16 for the INO WINDMOOR and OO-Star, respectively. From the restoring curves, it can be observed how the geometric stiffness contributes to the system's stiffness, as the restoring curves are non-linear. A higher restoring force is observed for in-line loading as the restoring curve is steeper, which is expected. Further, the difference in the restoring force between the FWTs as an effect of the pretension, is seen by the larger offset when subjected to a smaller force for the OO-Star.

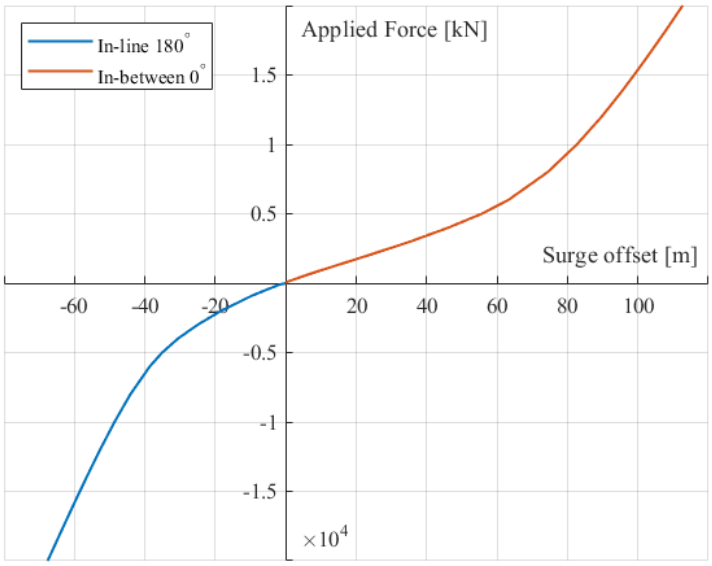

Figure 7.15: INO WINDMOOR restoring force curve from load-displacement test.

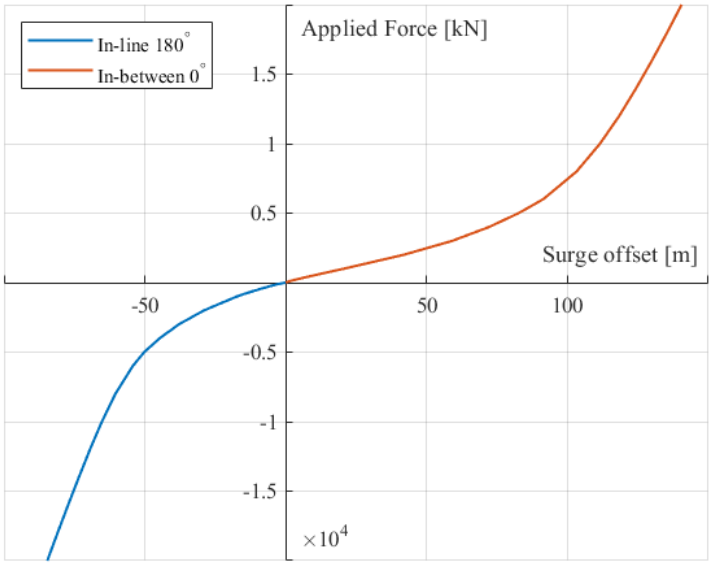

Figure 7.16: OO-Star restoring force curve from load-displacement test.

7.6 Seed Convergence Study

To establish different time series of wind and waves, seeds are used to account for stochastic variability in the simulations, where each seed number generates a random phase angle for the simulation. A seed convergence study is performed to determine the number of seeds needed to get sufficiently converged results. The convergence study is based on the maximum mooring line tension during design load case LC1.1. The convergence study is only performed using the INO WINDMOOR, assuming that the results are representative of both FWTs. According to DNV (2018a), for time-domain analyses, at least 10-20 realisations are needed so that an extreme value distribution can be fitted. The Gumbel distribution is proposed as a good statistical model for the maximum line tension, and it provides a good description of the extreme sample values as shown in Figure 7.17.

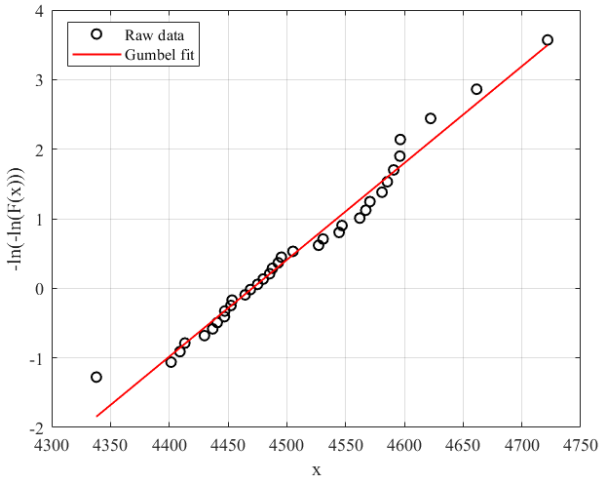

Figure 7.17: Gumbel probability paper.

Figure 7.18a presents the probability density function for the different sample sizes, while Figure 7.18b shows the most probable maximum (MPM) line tension from the Gumbel distribution. The convergence study is performed using 35 seeds. Increasing the number of seeds leads to the MPM line tension start converging after 12 seeds. The difference between the MPM line tension for seed 15 and seed 35 ranges within 1%, and thus 15 seeds are determined to provide reasonable results.

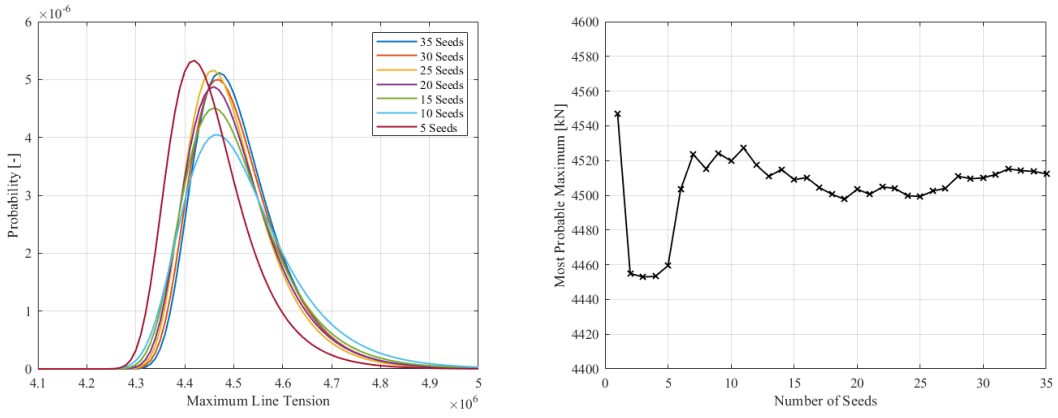

(a) (b)

Figure 7.18: Gumbel probability density function for increasing number of seeds (a) and MPM line tension convergence plot (b).

8 FOWTs Analysis: Results

8.1 Platform Motion Response

The dynamic behaviour of the two FWTs is studied under the selected load cases in which different load effects are dominating. Simulations using both Newman's approximation and the full QTF were performed to investigate the applicability of Newman's approximation compared to the full QTF. The same random seed of the irregular waves is used to investigate the discrepancy between Newman's approximations and the full QTF. The statistics are obtained by averaging 15 one-hour simulations for each load case. As the configuration of the floater is symmetric and the incoming wind and wave direction are in the symmetric plane, it is assumed that the sway and roll motion is negligible. Hence, this study selected the responses in surge, heave and pitch as critical. The main focus of this study is to highlight the difference between Newman's approximation and the full QTF regarding the motion response and how the turbine influence the floater motions of the two FWTs. Additionally, a comparative study between the two FWTs is performed to investigate how the two floaters are affected by the hydro and aerodynamic loading.

8.1.1 Comparison of Newman's Approximation and Full QTF

The mean and standard deviation for the INO WINDMOOR and OO-Star are given in Table 8.1 and Table 8.2, respectively. The standard deviation of the motion is also presented in Figure 8.1 and Figure 8.2 in terms of bar plots to illustrate better the differences in the motion response using Newman's approximation and the full QTF.

When comparing Newman's approximation and a full QTF concerning the different-frequency response, it is presumed that a full QTF will provide the most accurate results in all six degrees of freedom. Newman's approximation becomes inaccurate for motions with a low natural period, such as heave and pitch. Therefore, it is expected that Newman's approximation will underestimate the motion response in heave and pitch.

From Table 8.1 and Table 8.2 it is seen that Newman's approximation slightly underestimates the motion response in surge, heave and pitch. However, by looking at the mean motion of the INO WINDMOOR, it is observed that Newman's approximation marginally overestimates the motion response in surge at LC1.2, LC2.1 and LC.2.2 compared to the full QTF. The main diagonal of the QTF, which corresponds to the mean drift force, is identical to the mean drift calculated by the pressure integration method. In contrast, the mean drift force is calculated using the conservation of momentum method for Newman's approximation. As seen from Figure 7.3b, the pressure integration method slightly underestimates the mean drift force compared to the conservation of momentum. Hence, the full QTF will slightly underestimate the mean surge response. It should be noted that these deviations are minimal and can therefore be assumed negligible.

The deviation between the motion response using Newman's approximation and the full QTF increases as the wave condition becomes more severe, indicating that the application of Newman's approximation becomes questionable for more severe sea states. Furthermore, it is observed that the discrepancy between Newman's approximation and full QTF is more significant for the OO-Star floater. Regarding the standard deviation of the surge and pitch motion for the extreme load case, Newman's approximation underestimates the surge and pitch response by 15.2% and 8%, respectively, for the OO-Star floater.

Table 8.1: INO WINDMOOR platform motion response.

Mean FWT motion						
	Surge [m]		**Heave** [m]		**Pitch** [deg]	
	Newman	Full QTF	Newman	Full QTF	Newman	Full QTF
LC1.1	14.01	14.01	0.06	0.06	3.93	3.93
LC1.2	0.90	0.89	0.08	0.07	1.98	1.98
LC2.1	11.37	11.32	0.01	0.01	0.95	0.96
LC2.2	5.86	5.81	0.04	0.04	1.70	1.69
LC3	16.38	16.49	0.17	0.16	0.96	0.99

Standard deviation FWT motion						
	Surge [m]		**Heave** [m]		**Pitch** [deg]	
	Newman	Full QTF	Newman	Full QTF	Newman	Full QTF
LC1.1	1.37	1.38	0.27	0.29	1.02	1.02
LC1.2	0.42	0.42	0.28	0.28	0.15	0.15
LC2.1	1.14	1.15	0.69	0.70	0.92	0.92
LC2.2	1.24	1.24	0.68	0.69	0.49	0.5
LC3	2.83	2.85	1.74	1.75	1.33	1.36

Table 8.2: OO-Star platform motion response.

Mean FWT motion						
	Surge [m]		**Heave** [m]		**Pitch** [deg]	
	Newman	Full QTF	Newman	Full QTF	Newman	Full QTF
LC1.1	21.11	21.14	-0.07	-0.07	4.13	4.13
LC1.2	2.65	2.70	0.01	0.01	2.13	2.14
LC2.1	17.62	17.84	0.01	0.01	0.94	0.93
LC2.2	10.09	10.36	0.04	0.04	1.92	1.93
LC3	23.60	24.75	0.14	0.14	1.71	1.77

Standard deviation of FWT motion						
	Surge [m]		**Heave** [m]		**Pitch** [deg]	
	Newman	Full QTF	Newman	Full QTF	Newman	Full QTF
LC1.1	1.52	1.53	0.22	0.22	1.08	1.08
LC1.2	0.50	0.55	0.22	0.22	0.17	0.18
LC2.1	1.40	1.43	0.53	0.54	0.80	0.80
LC2.2	1.57	1.64	0.53	0.54	0.49	0.52
LC3	2.84	3.35	1.42	1.43	1.15	1.25

8.1.2 Turbine Influence on Floater Motion

In order to analyse how the turbine influences the floater response, simulations with both operational and parked turbine are performed for the same environmental conditions. Figure 8.1 and Figure 8.2 illustrate the standard deviation of the INO WINDMOOR and OO-Star, respectively, in surge, heave and pitch for each load case. The time series of the pitch motion for the INO WINDMOOR at rated and cut-out wind speed is given in Figure 8.3a and Figure 8.3b, respectively, to better illustrate the dynamics of the motion response when the turbine is operational versus parked. The time series in Figure 8.3 presents both the total motion, including the mean offset and the dynamic motion where the mean offset is excluded. The main trend of the motion response of the INO WINDMOOR is representative of both the floaters. Therefore, only the motion response for the INO WINDMOOR will be explained in this section. A direct comparison of the motion response between the two floaters is given in Section 8.1.3.

In operational conditions, the surge and pitch motion of the floaters is dominated by the wind, while the incoming waves mainly dominate the heave motion. The mean values of the surge and pitch motion are non-zero due to the mean wind and waves. The mean and standard deviation are highest at rated wind speed in LC1.1 and thereafter decrease as the wind speed increases to cut-out wind speed in LC2.1. As the wind speed increases above rated wind speed, the control system starts to pitch the blades, leading to a decreasing thrust force. Consequently, the mean value of the surge and pitch motion decreases until around cut-out wind speed. This is clearly seen in Figure 8.3, where the mean value of the pitch response at rated wind speed is significantly larger than at cut-out wind speed due to the large thrust force. The mean value of the heave response is close to zero for all load cases as the wave-induced loads govern the heave response while the standard deviation increases with the severity of the sea state. Further, it is observed from Figure 8.1 and Figure 8.2 that the deviation between operational and parked condition concerning the heave response is marginal.

As the waves govern the pitch and surge response when the turbine is parked, the dynamic response increases as the waves become more severe. However, in operational conditions, the dynamic surge and pitch response slightly decrease from LC1.1 to LC2.1. As the wind dominates the surge and pitch motion in operational conditions, the dynamic response is governed by the fluctuations in the incoming wind speed, leading to an inconsistent thrust force and dynamic motions. Figure 8.3 shows that the dynamic response at cut-out wind speed is slightly smaller than at rated wind speed. This is because the thrust force at cut-out wind speed is less dominant than at rated wind speed, hence, smaller variations in the pitch response. At LC.3, the surge and pitch response is governed by the wave-induced response as the turbine is in parked condition.

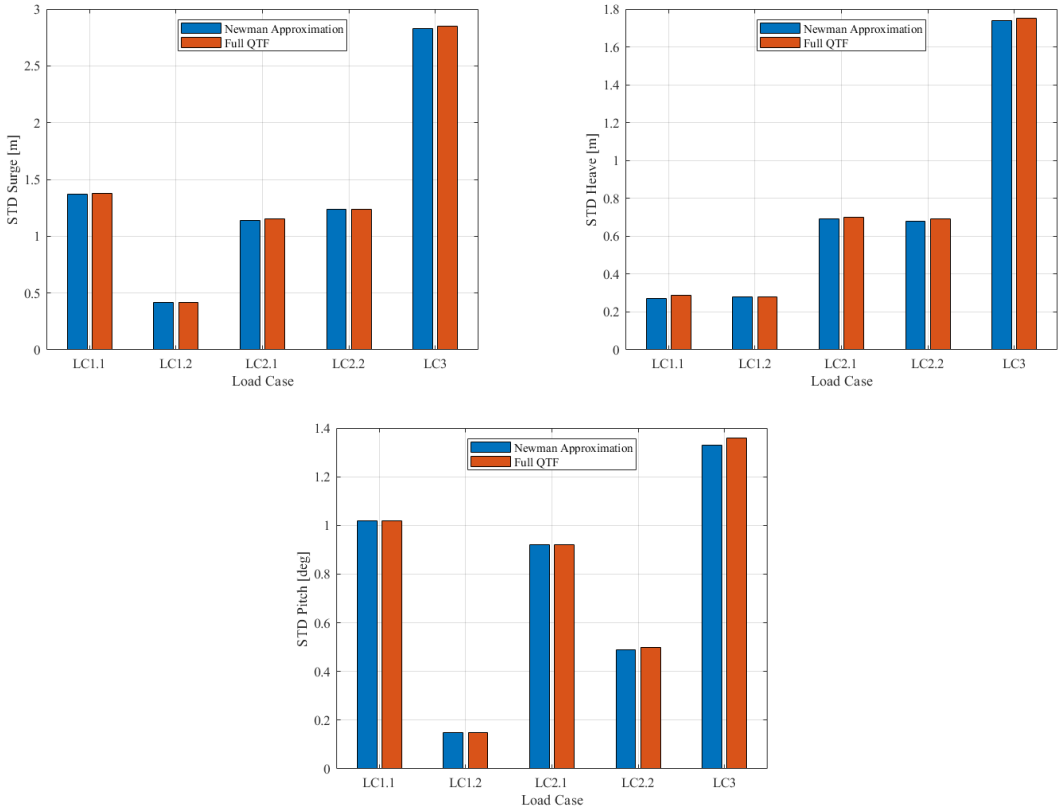

Figure 8.1: Standard deviation of platform motion response - INO WINDMOOR.

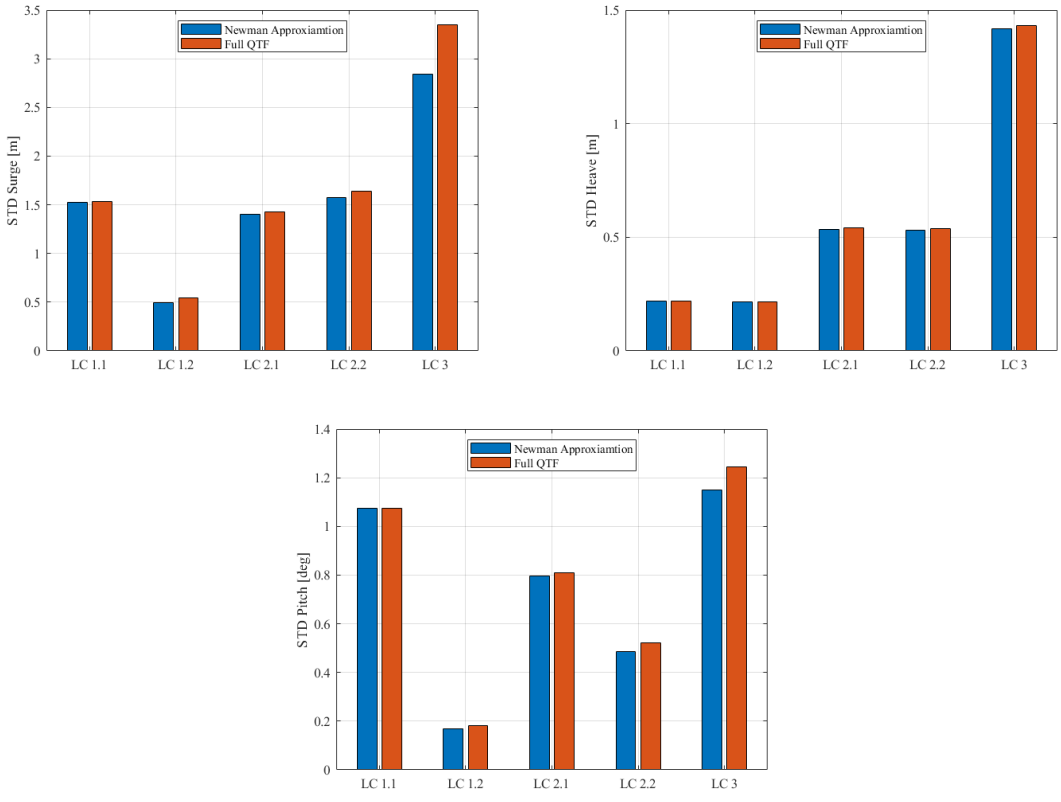

Figure 8.2: Standard deviation of platform motion response - OO-Star.

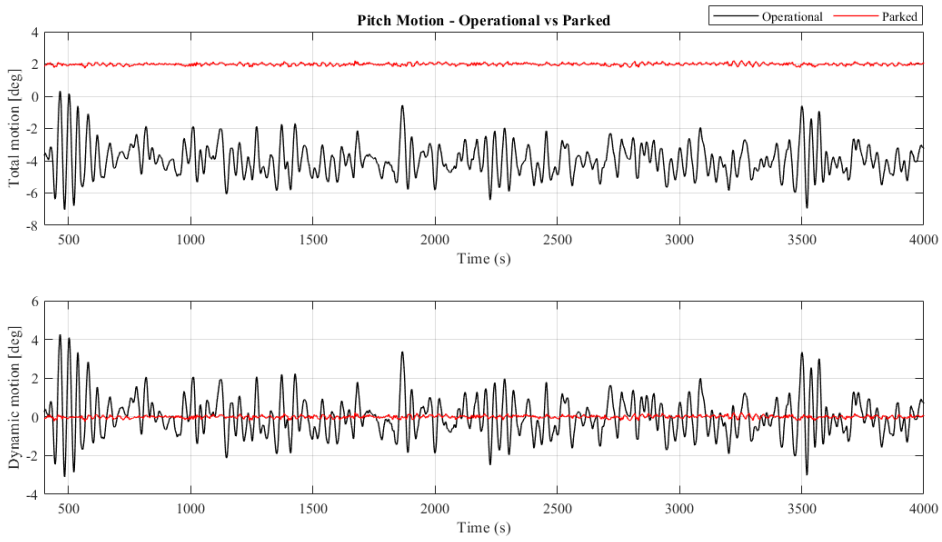

(a)

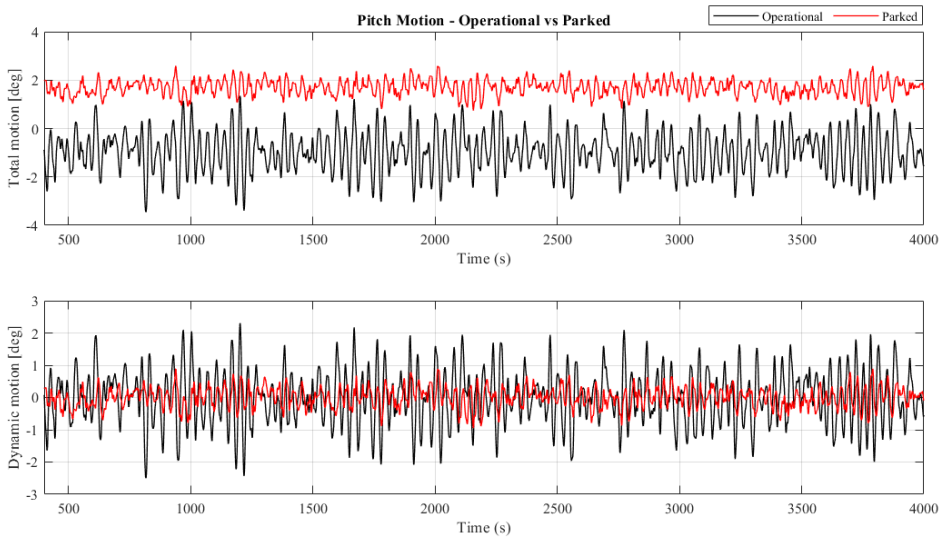

(b)

Figure 8.3: Time series of the pitch motion at rated (a) and cut-out (b) wind speed for the INO WINDMOOR.

8.1.3 Comparison of Motion Response Between the Two FWTs

A comparative study is carried out concerning the motion response of the two FWTs in order to analyse how the two different floater designs are affected by the aero and hydrodynamic loading. The results presented in this section are performed with the full QTF. Figure 8.4 presents the standard deviation of the motion response of the two FWTs for each design load case. To better illustrate the dynamic motion, the time series of the surge and pitch motion at the cut-out wind speed in the operational and parked condition are given in Figure 8.5 and Figure 8.6, respectively. Additionally, the time series of the pitch response in extreme conditions is presented in Figure 8.7. Time series at rated wind speed are given in Appendix C.1.

From Figure 8.4a, it is observed that the OO-Star experiences a more significant surge response for all load cases. The surge response is affected by the pretension of the mooring system. As the pretension of the OO-Star is significantly smaller than for the INO WINDMMOR, the mean offset will increase accordingly. The mean offset is clearly seen in Figure 8.5a and Figure 8.5b where the OO-Star experiences a significantly larger mean offset in both operational and parked conditions. Furthermore, it is observed that the dynamic surge response of the two FWTs deviates as well. The differences in the dynamic surge response are significant for all load cases. In operational conditions, the dynamic surge response is approximately 10% larger for the OO-Star for rated wind speed than the INO WINDMOOR, while at cut-out wind speed, the dynamic surge response is approximately 20% larger.

For the heave motion, it is observed from Figure 8.4b that the INO WINDMOOR experiences a larger response for all load cases, indicating that the hydrodynamic damping in heave is larger for the OO-Star. A study of the hydrodynamic damping of the two floaters is not performed in this thesis. However, it is assumed that the heave plates on the OO-Star floater generate more significant vertical damping than the pontoons on the INO WINDMOOR floater. From Table 8.7 in Section 8.3.5, it is seen that the first-order wave load in heave is larger for the OO-Star floater for all load cases, supporting the assumption that the vertical damping is more significant for the OO-Star floater. The discrepancy in the heave response between the two FWTs is quite similar for all the load cases. In general, the INO WINDMOOR experience a 20-25% larger heave response.

For the pitch motion, it is distinguished between the mean and dynamic response. For the mean pitch response, it is seen from Table 8.1 and Table 8.2 that the OO-Star floater experiences a more significant mean pitch response for all load cases except for LC2.1. The difference in the mean pitch response is connected to the fact that the hydrostatic restoring coefficient of the INO WINDMOOR floater is higher than the OO-Star. The FWTs is exposed to a large quasi-static thrust force that governs the mean pitch response at rated wind speed. Therefore, the response will be smaller for the INO WINDMOOR as this floater is more resistant to quasi-static forces. However, for LC2.1, the mean pitch response is marginally larger for the INO WINDMOOR floater. In LC2.1, the thrust force is significantly smaller than in LC1.1, and hence, the mean offset in pitch will reduce accordingly. Consequently, the deviation in mean pitch response between the two floaters is mainly connected with the dynamic response, and as seen in Figure 8.6a, the INO WINDMOOR floater experiences a slightly larger dynamic pitch response. In general, the discrepancy in the mean pitch response between the two FWTs is quite small. In LC1.1, the mean pitch response is 5% higher for the OO-Star, while in LC2.1, the pitch response is approximately equal. When parked, the differences between the two floaters are slightly larger. In LC1.2 and LC2.2, the mean pitch response for the OO-Star is 7% and 12% larger, respectively.

There is no clear trend between the load cases for the dynamic pitch response. First of all, it is seen from Figure 8.4c that the OO-Star floater experiences a larger dynamic pitch response at rated wind speed in both operational and parked condition of 6% and 16%, respectively. In operational conditions, the difference in the dynamic pitch response can be explained by considering the power spectra of the pitch response in Section 8.2.1. From the pitch response spectra at rated wind speed in operational conditions, it is observed that the OO-Star floater is more sensitive to the low-frequency wind-induced response compared to the INO WINDMOOR floater. Consequently, the OO-Star floater will experience a larger dynamic pitch response at rated wind speed as the wind governs the loading. In parked conditions, where the FWTs are less affected by the wind-

induced response, the OO-Star experience a slightly larger dynamic pitch response than the INO WINDMOOR. Furthermore, it is observed that the INO WINDMOOR experiences approximately 13% and 23% larger dynamic pitch response at LC2.1 and LC3, respectively. Again, this can be explained by considering the pitch response spectra. For cut-out wind speed, both in operational and parked conditions, the pitch resonant frequency response is significantly larger for the INO WINDMOOR, indicating that the INO WINDMOOR will experience more significant dynamic motions compared to the OO-Star. The dynamic motions in LC2.1 and LC3 can also be seen from Figure 8.6a and Figure 8.7 where larger extremes for the dynamic motion of the INO WINDMORR floater are observed. The response spectra are discussed in more detail in Section 8.2.
Lastly, it is observed from Figure 8.4c that the OO-Star has a marginally larger dynamic pitch response at LC2.2. By considering Figure 8.6b, it is seen that the OO-Star floater experiences a more significant mean pitch response due to the wind. However, when considering only the dynamic motion, it is seen that response is more or less the same.

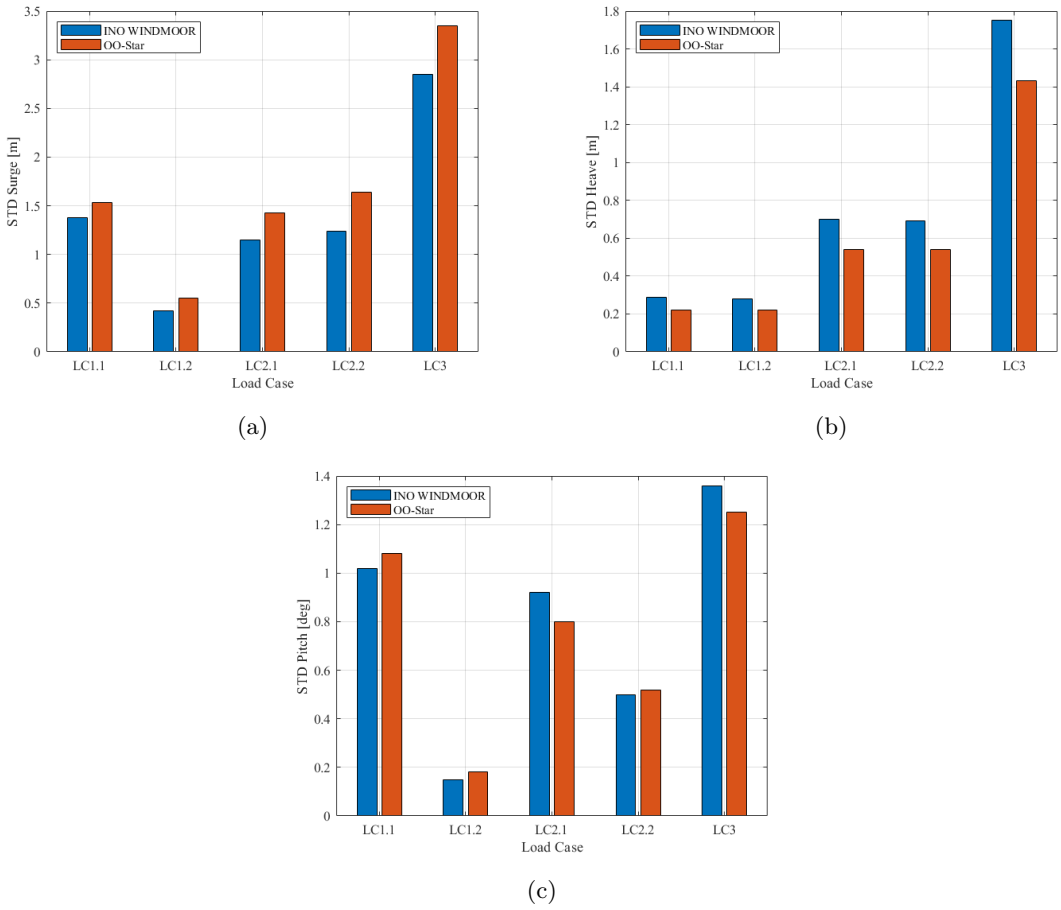

Figure 8.4: Comparison of the standard deviation between the INO WINDMOOR and the OO-Star.

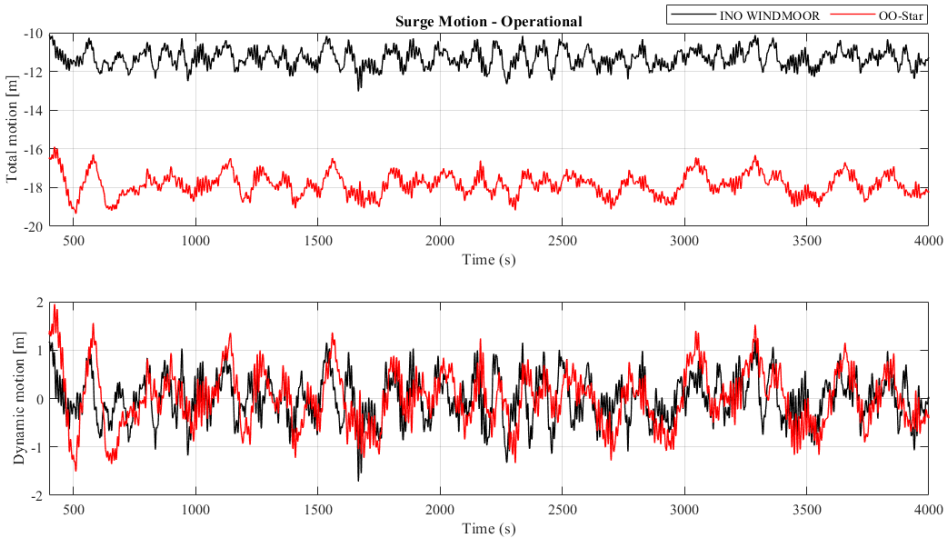

(a)

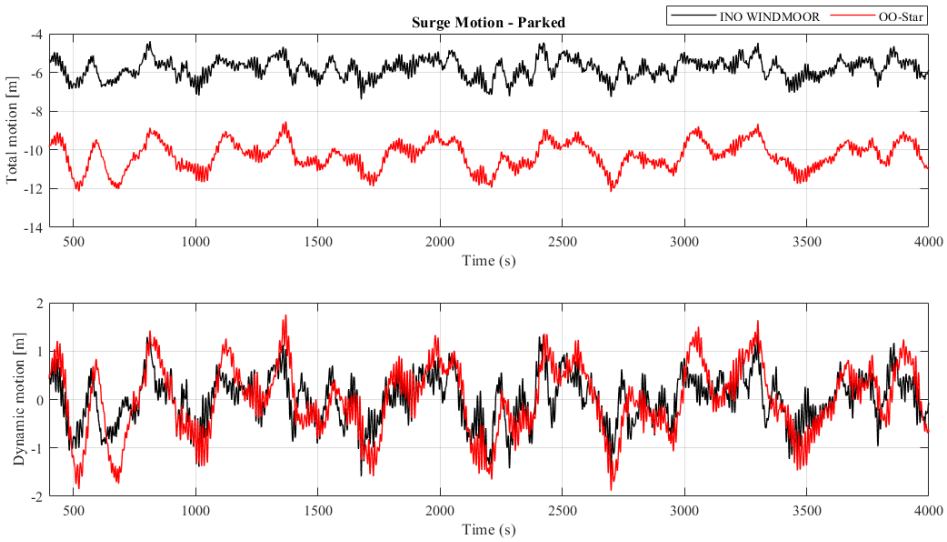

(b)

Figure 8.5: Time series of the surge response at cut-out wind speed for operational (a) and parked (b) condition.

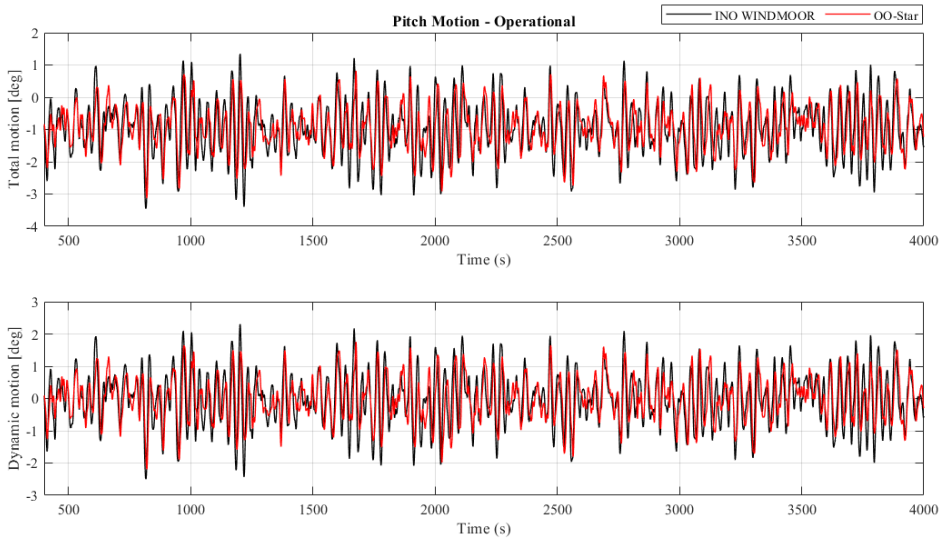

(a)

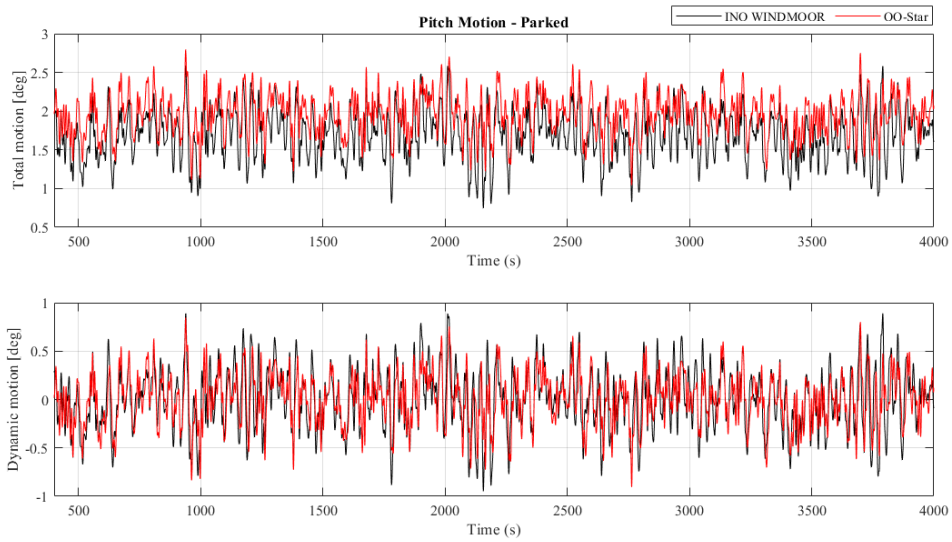

(b)

Figure 8.6: Time series of the pitch response at cut-out wind speed for operational (a) and parked (b) condition.

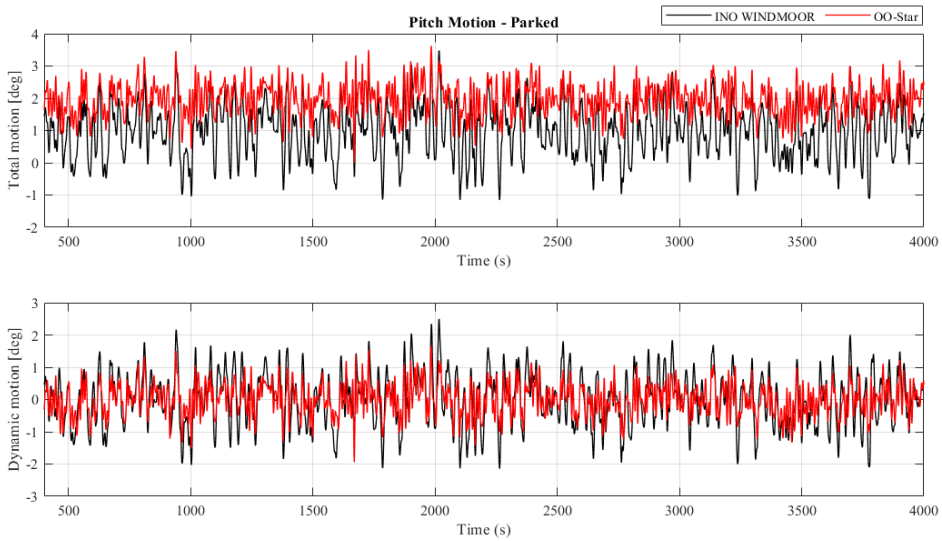

Figure 8.7: Time series of the pitch response in extreme conditions LC3.

8.2 Response Spectra

This section presents the power spectral analysis of the floater motions. A power spectral analysis points out the contribution of different frequency components. Spectral analysis is performed for all load cases to analyse how the contribution of the different frequency components changes concerning operational and parked turbine and with increasingly severe sea states. The spectral analysis is performed using Newman's approximation and full QTF. The power spectra presented in this section are the average of the 15 seeds used for each load case. The power spectra showing the variations between the different seeds are given in Appendix E.

8.2.1 Load Case 1.1 and 1.2

The power spectra of the floater motions at rated wind speed for surge, heave and pitch in both operational and parked condition is given in Figure 8.8 and Figure 8.9 for the INO WINDMOOR and OO-Star floater, respectively.

In operational conditions, the surge resonance response governs the surge motion with minimal contribution from the wave frequency response. Therefore, only the low-frequency contribution is shown in the spectra for the surge motion in Figure 8.8a and Figure 8.9a. The contribution from slowly-varying wind-induced loads is significant for the total surge response in operational conditions. Furthermore, it is observed from Figure 8.8a and Figure 8.9a that the surge resonant frequency in operational conditions does not correspond with the natural surge frequency obtained from the decay tests. The natural surge frequency is connected with the non-linearities of the mooring system as the large thrust force at rated wind speed will force the floater to oscillate at a new offset with higher stiffness, and hence, the FWTs experience a higher resonance frequency.
In parked conditions, the response amplitude is significantly smaller than for operational conditions due to the absence of the thrust force. The surge resonant frequency still dominates the surge response. However, the wave frequency response is more prominent when the turbine is parked.
By comparing the response amplitude in surge between the two FWTs, it is observed that OO-Star experiences a larger response both in operational and parked condition, especially at the surge resonance frequency. As discussed in Section 8.1.3, this is due to the lower pretension of the mooring system of the OO-Star floater. Concerning the resonant response in surge, it is observed that the deviation between Newman's approximation and a full QTF is significantly larger for the OO-Star compared to the INO WINDMOOR in parked condition, where Newman's approximation underestimates the surge response.

The wave frequency response governs the heave motions both in operational and parked condition with a small contribution from the heave resonant frequency. Unlike surge and pitch, the response amplitude of the heave motion between an operational and parked turbine is approximately the same as the thrust force mainly acts in the horizontal direction. Further, it is observed that the contribution from the heave resonant frequency is considerably smaller for the OO-Star compared to the INO WINDMOOOR floater. Newman's approximation underestimates both FWTs heave response at the heave resonant frequency. However, it should be noted that this will have a negligible impact on the total heave motion as the wave frequency response is the dominating component.

The main contribution to the pitch response when the turbine is operational, is the pitch resonance and low-frequency wind-induced response. The wave frequency response is insignificant for the pitch response in operational condition and is therefore not shown in the spectra in Figure 8.8e and Figure 8.9e. The pitch resonance occurs at a lower frequency than the pitch resonance obtained from the decay tests. As discussed in Section 7.2.1, the shift in resonance frequency is due to an inertia/damping effect which origins from the relative phase between the nacelle velocity and the thrust induced at the turbine.
In parked condition, the low-frequency wind-induced response decreases while the response from the wave frequency increases. For the OO-Star floater, the wave frequency response is the dominating contribution to the pitch response, while for the INO WINDMOOR, it is the pitch resonance response that is the dominating contribution. It should be noted that the response amplitude for the parked turbine is significantly smaller than for the operational condition. Newman's approximation underestimates the pitch resonant response for both FWTs. However, the difference between Newman's approximation and a full QTF is more prominent for the OO-Star.

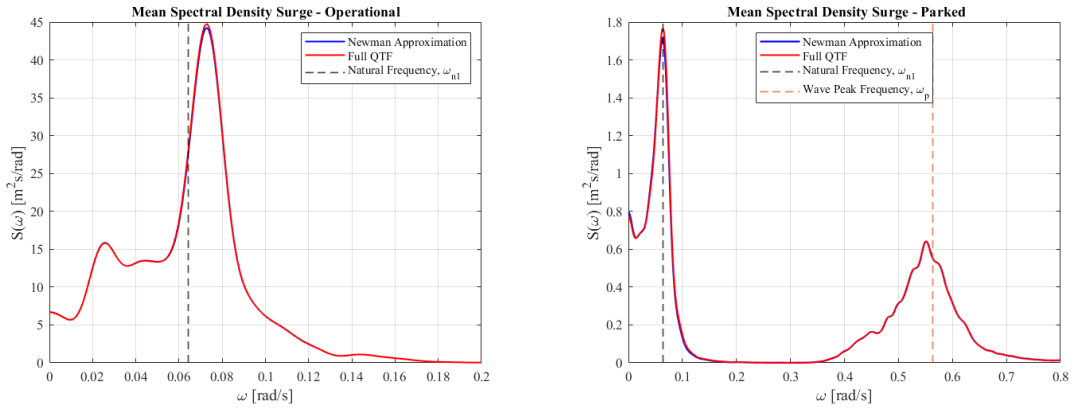

(a)

(b)

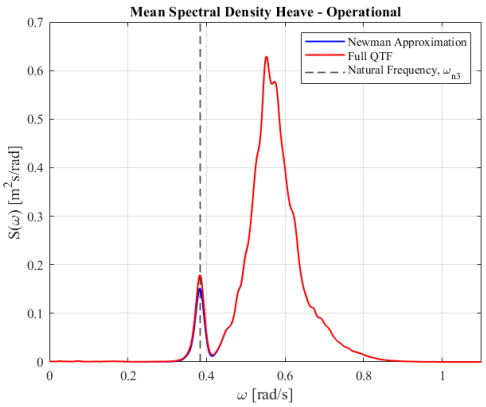

(c)

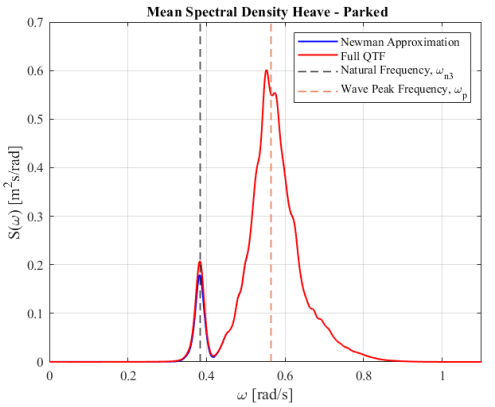

(d)

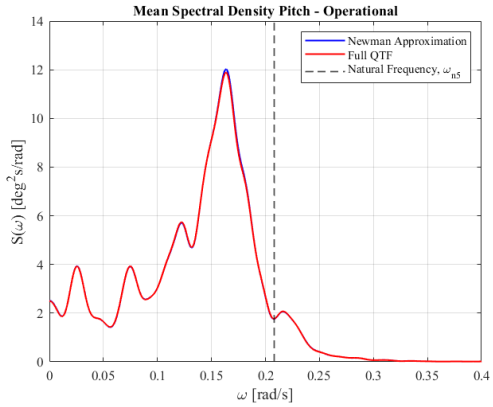

(e)

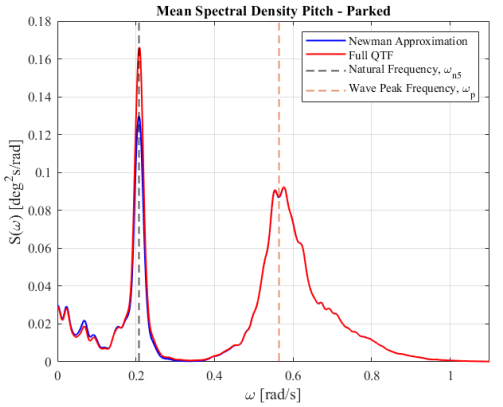

(f)

Figure 8.8: Spectra for floater motions at LC1.1 and LC1.2 for the INO WINDMOOR.

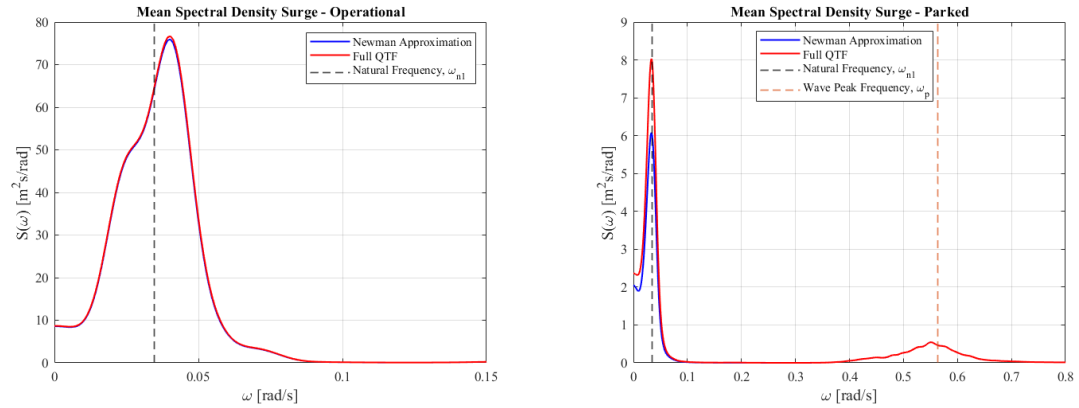

(a)

(b)

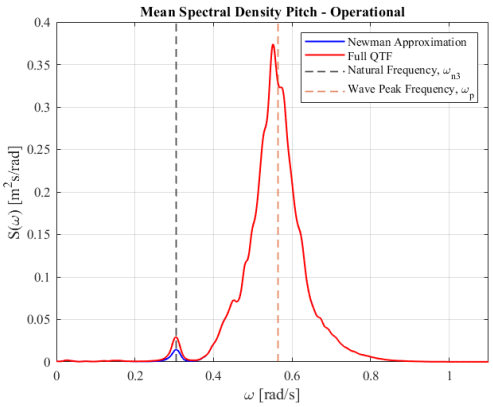

(c)

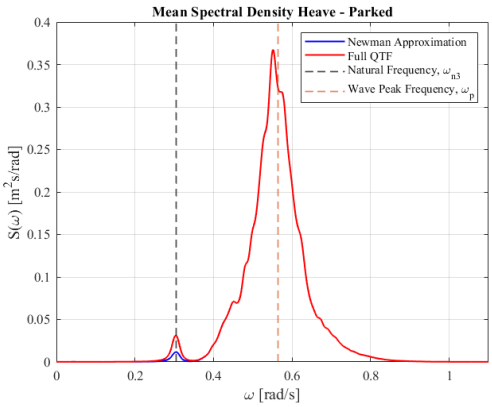

(d)

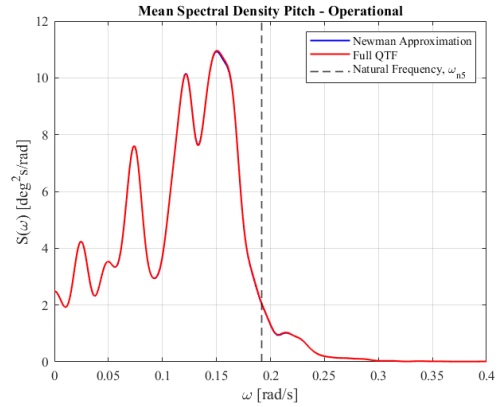

(e)

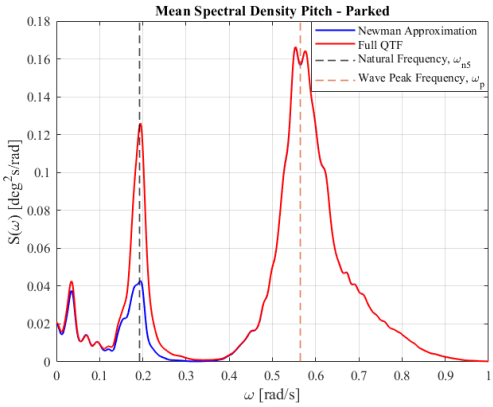

(f)

Figure 8.9: Spectra for FWT motions at LC1.1 and LC1.2 for the OO-Star.

8.2.2 Load Case 2.1 and 2.2

The power spectra of the FWT motions at cut-out wind speed for surge, heave and pitch in the operational and parked condition are given in Figure 8.10 and Figure 8.11 for the INO WINDMOOR and OO-Star, respectively.

First of all, the response amplitude in surge is significantly smaller in operational conditions for both models compared to the surge response at rated wind speed due to the reduction in the thrust force. The surge resonant response also dominates the surge response at cut-out wind speed. However, the contribution from the wave frequency response is now noticeable as the surge resonant response is smaller than at rated wind speed, and the sea state is more severe than at rated wind speed. As the mean offset is significantly lower at cut-out wind speed, the surge resonance frequency in operational conditions coincides well with the surge resonance frequency obtained from the decay test.
Contrary to the surge response at rated wind speed, the response in parked condition is larger than the response in operational condition at cut-out wind speed. From Figure 8.10b and Figure 8.11b, it is evident that the surge resonant response is significantly more prominent for the OO-Star compared to the INO WINDMOOR, making the wave-frequency induced response less critical for the OO-Star.

The wave frequency component dominates the heave motion for both operational and parked turbine at cut-out wind speed. Like the surge motion, the INO WINDMOOR is more sensitive to the wave frequency response than the OO-Star floater. Newman's approximation underestimates both FWTs heave response at the heave resonant frequency.

For the pitch motion in operational conditions, the low-frequency wind-induced response decreases compared to the rated wind speed, while the response from the wave frequency is still insignificant for the total pitch response. The pitch response is twice as high for the INO WINDMOOR compared to the OO-Star, contrary to the pitch response at rated wind speed, where the response was approximately equal for the two floaters.
Large differences between the two FWTs in pitch response are observed when the turbine is parked. For the INO WINDMOOR, the pitch response is mainly governed by the pitch resonance frequency response with a small contribution from the wave frequency response, while for the OO-Star, the pitch resonant component contributes equally as the wave frequency component to the total pitch response. Further, Newman's approximation underestimates the response at the resonance frequency for the OO-Star, while for the INO WINDMOOR, Newman's approximation is quite accurate.

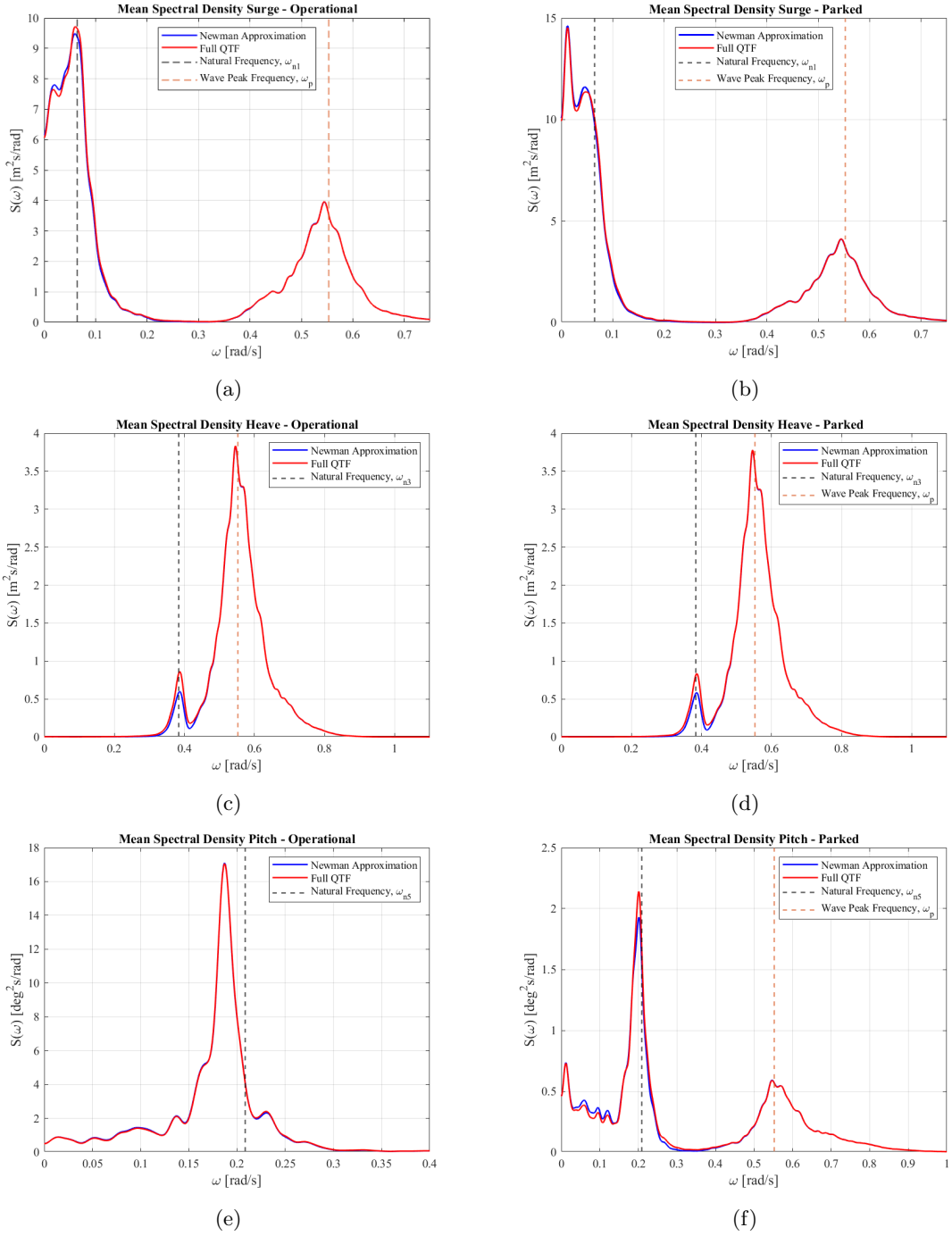

Figure 8.10: Spectra for FWT motions at LC2.1 and LC2.2 for the INO WINDMOOR.

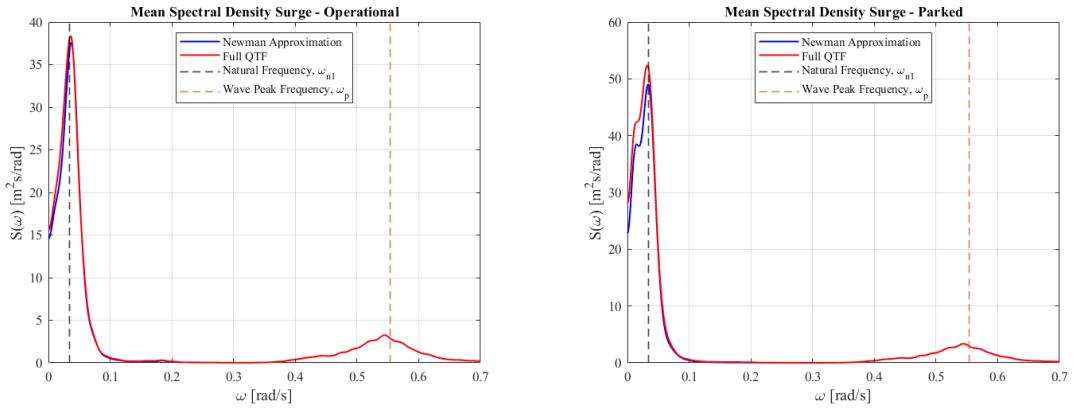

(a)

(b)

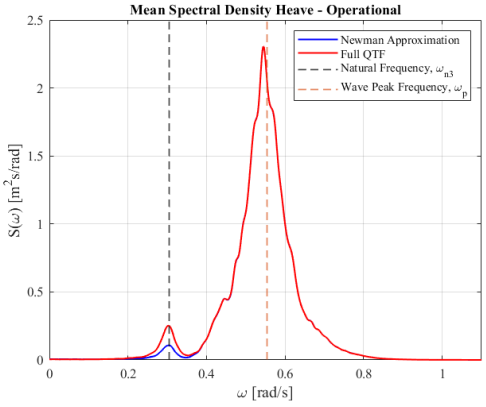

(c)

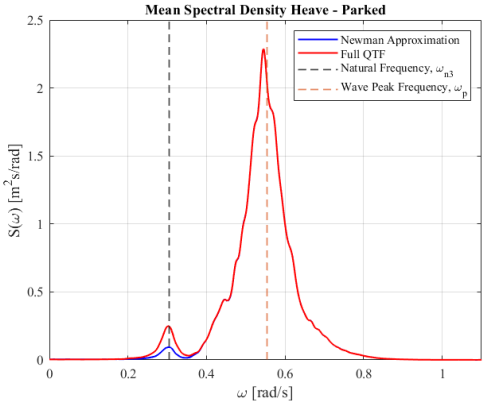

(d)

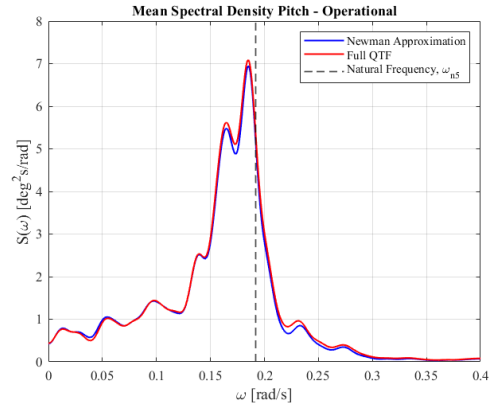

(e)

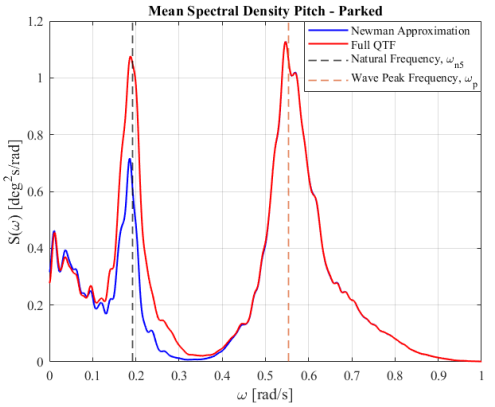

(f)

Figure 8.11: Spectra for FWT motions at LC2.1 and LC2.2 for the OO-Star.

8.2.3 Load Case 3

Figure 8.12 and Figure 8.13 present the power spectral of the FWT response in extreme conditions for the INO WINDMOOR and OO-Star floater, respectively.

For the INO WINDMOOR, the pitch resonant response is the dominant contribution to the total pitch response, with a significant contribution from the low-frequency wind-induced and wave-frequency induced responses. For the OO-Star floater, it is the low-frequency response, including both the wind-induced and surge resonant response, that mainly contributes to the total surge motion, while the contribution from the wave frequency response is significantly smaller. Further, a large discrepancy in the surge response between Newman's approximation and full QTF is observed in the low-frequency range for the OO-Star floater.

For the heave response, the distribution of the frequency components contributing to the heave motion is quite different for the two floaters. The wave frequency response is the dominant component of both FWTs total heave response. However, for the INO WINDMOOR, the heave resonant frequency response contribution is quite prominent in contrast to the OO-Star, where the heave resonant frequency response is insignificant for the total heave response.

Also for the pitch motion, the distribution of the frequency components is different for the two FWTs. For the INO WINDMOOR, the pitch resonant response dominates the pitch motion, while for the OO-Star, the wave frequency response is the dominating component. Further, Newman's approximation underestimates the pitch resonant response, while for the INO WINDMOOR floater, Newman's approximation is less underestimating.

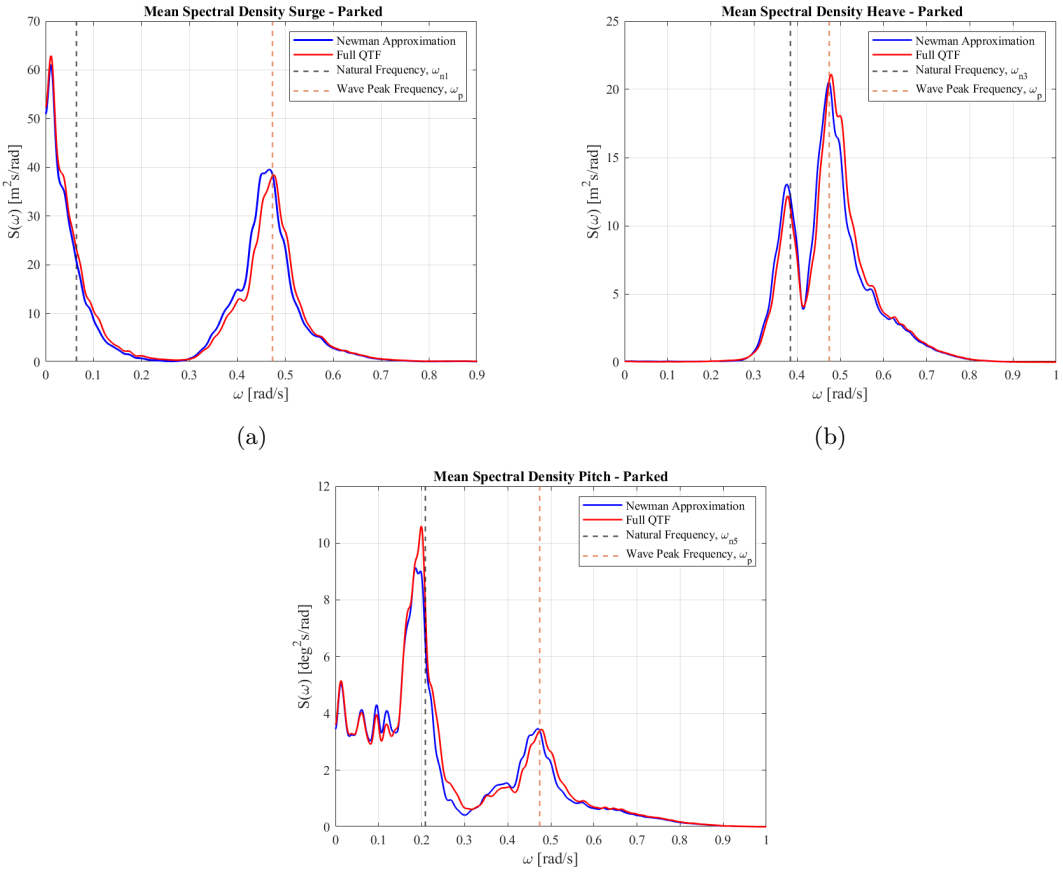

Figure 8.12: Spectra for FWT motions at LC3 for the INO WINDMOOR.

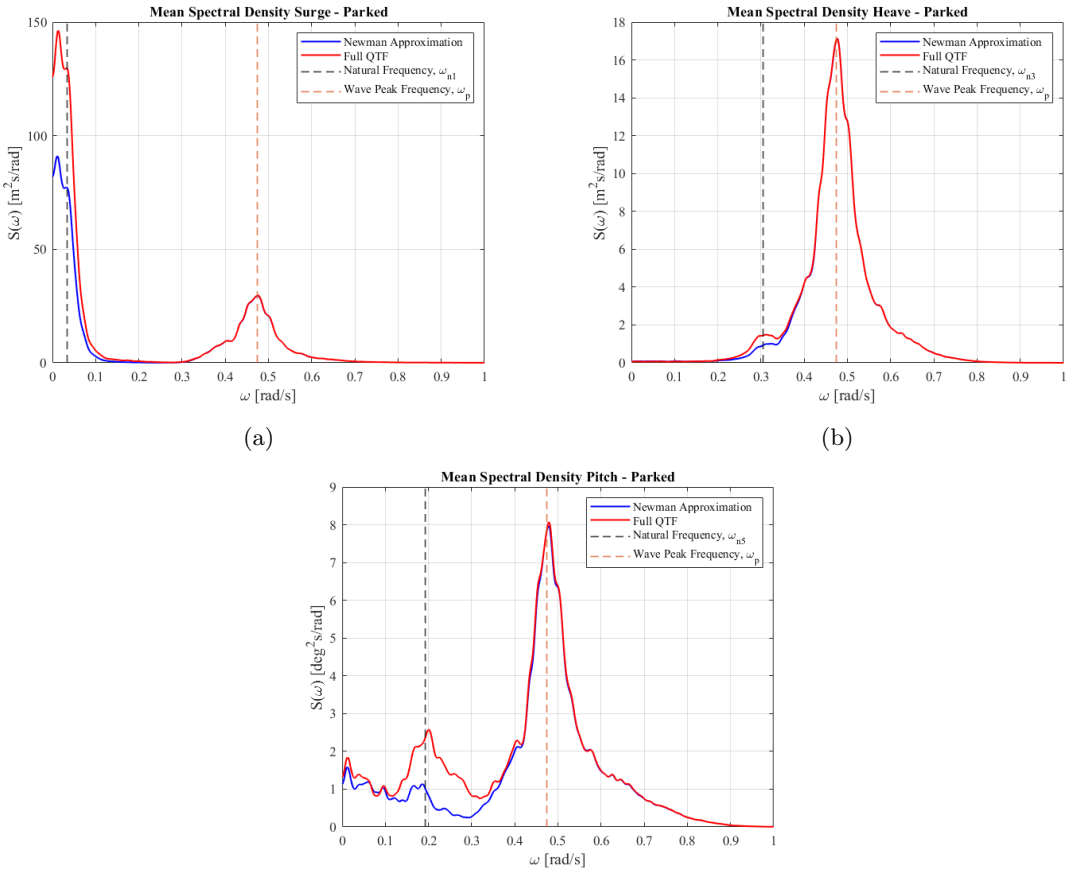

Figure 8.13: Spectra for FWTs motions in extreme conditions for the OO-Star.

8.2.4 Comparison between parked and operating turbine

To better illustrate the response differences between an operational and parked turbine in the response spectra, a direct comparison for both floaters is given in Figure 8.14 and Figure 8.15 for rated and cut-out wind speed, respectively.

Generally speaking, the response amplitude with an operational turbine is significantly larger at rated wind speed for both floaters. The only exception is the heave response, where the response amplitude is approximately equal for both conditions. As previously discussed, the wave-induced response governs the heave motion and is not influenced by the thrust force as this mainly acts in the horizontal direction.
The same trend is apparent at cut-out wind speed for the heave and pitch motion as for the rated wind speed. For the surge motion, however, both floaters experience a more significant response in the low-frequency range when parked, indicating that the wind-induced response is more critical at cut-out wind speed. For both floaters, the wave frequency response is approximately equal in operational and parked condition.

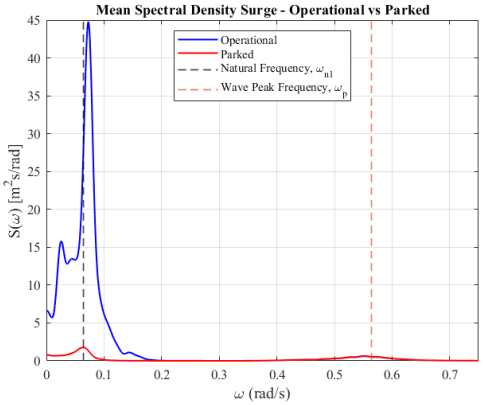

(a) INO WINDMOOR

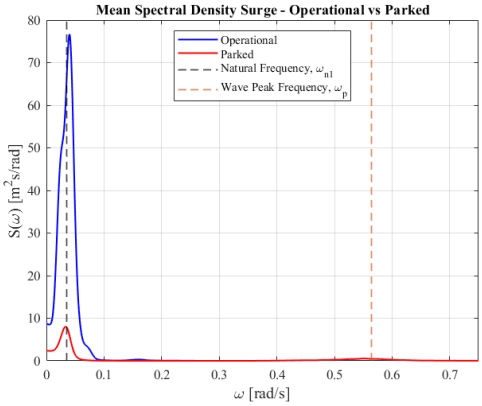

(b) OO-Star

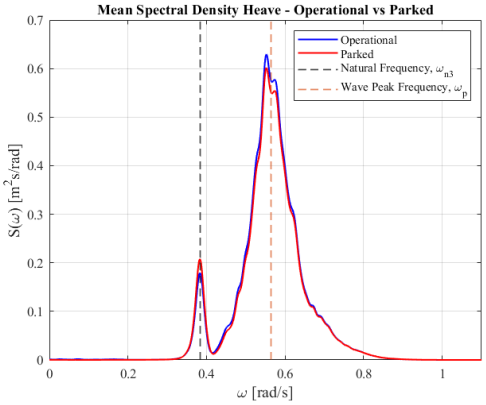

(c) INO WINDMOOR

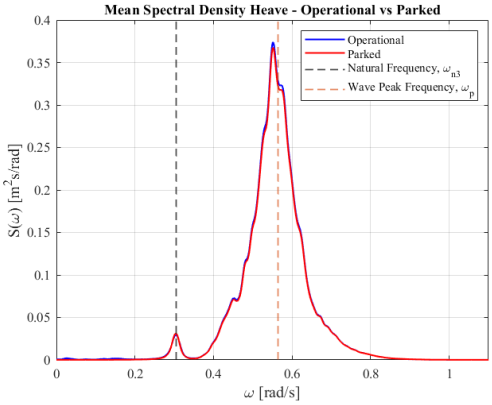

(d) OO-Star

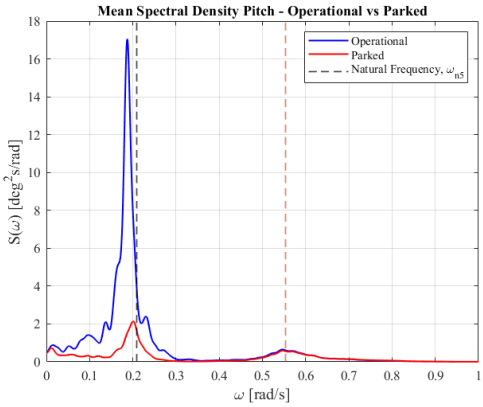

(e) INO WINDMOOR

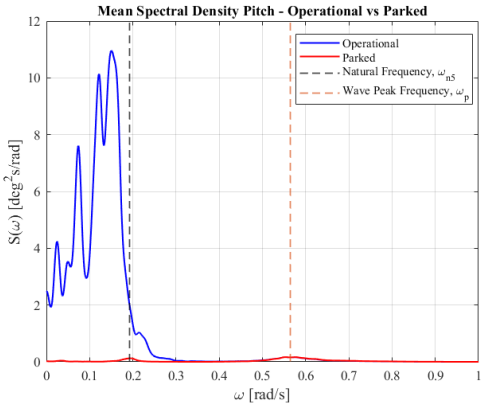

(f) OO-Star

Figure 8.14: Comparison between operational and parked turbine at LC1.1 and LC1.2.

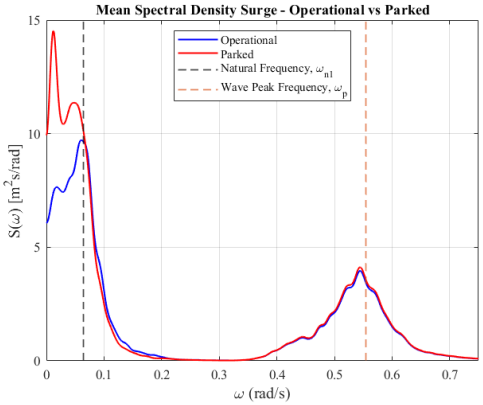

(a) INO WINDMOOR

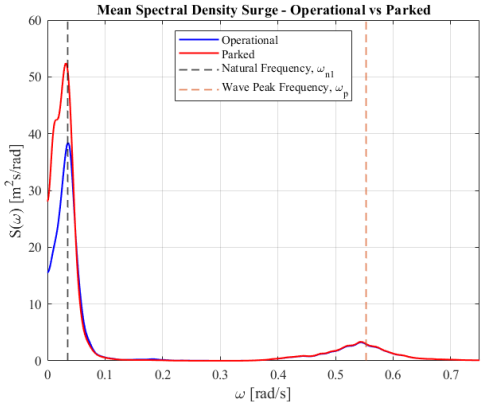

(b) OO-Star

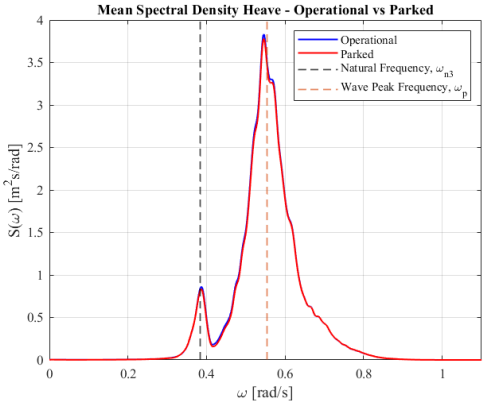

(c) INO WINDMOOR

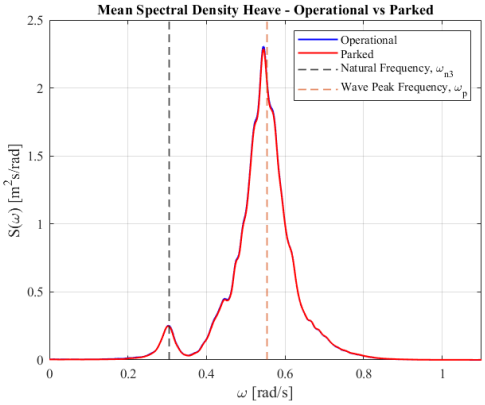

(d) OO-Star

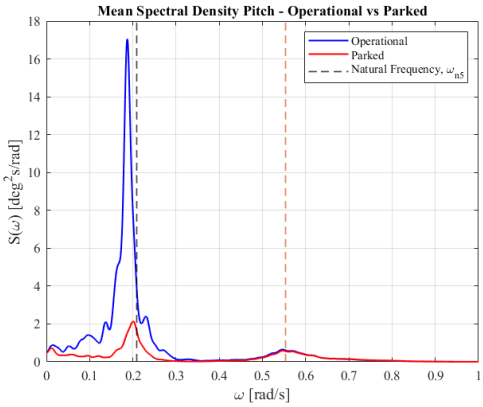

(e) INO WINDMOOR

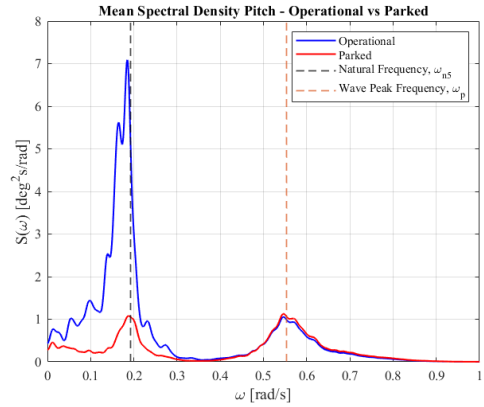

(f) OO-Star

Figure 8.15: Comparison between operational and parked turbine at LC2.1 and LC2.2.

8.3 Loads on the FWTs

This section will investigate how the structural loads in the tower are affected by the two different floater designs. The axial force and fore-aft bending moment (about the local y-axis) at the tower base and tower top are presented, including the effect of using Newman's approximation and the full QTF. Furthermore, the time series of the axial loads and fore-aft bending moment at the tower base for LC2.1 and LC2.2 are presented for both floaters, along with time series that compare the two floaters directly. The time series of the tower loads and bending moments in LC1.1, LC1.2 and LC3 are given in Appendix D. Section 8.4 presents the power spectra of the tower loads and fore-aft moment. Lastly, the hydrodynamic wave loads acting on the two floaters using first-order wave force and second-order difference frequency wave forces will be presented.

8.3.1 Axial Loads

Table 8.3 and Table 8.4 present the statistical values of the axial force in the tower base and tower top for the INO WNDMOOR and OO-Star, respectively. The accuracy of the axial force in the tower is observed to be ensured using Newman's approximation, as the deviation of the axial force values using the two methods is negligible. Furthermore, the maximum axial force for all load cases is more than twice as large in the tower base compared to the top of the tower, for both FWTs. The axial force at the tower increases with an increasingly severe sea state.

For both FWTs, a slightly higher axial force at both the tower base and tower top occurs when the turbine is operational. Furthermore, it is observed that the axial loads in the tower top are more sensitive to whether the turbine is operational or parked than at the tower base. The influence of the turbine on the tower base axial loads is further illustrated in the time series for design load cases LC2.1 and LC2.2 in Figure 8.16 and Figure 8.17 for the INO WINDMOOR and OO-Star, respectively.

Table 8.3: Maximum and standard deviation of axial force in the tower - INO WINDMOOR.

	Tower Base				**Tower top**			
	MAX [MN]		STD [kN]		MAX [MN]		STD [kN]	
	Newman	Full QTF	Newman	Full QTF	Newman	Full QTF	Newman	Full QTF
LC1.1	20.43	20.43	252.33	252.45	9.09	9.09	121.08	121.13
LC1.2	20.16	20.16	236.25	236.03	8.83	8.83	105.82	105.44
LC2.1	21.58	21.60	580.08	581.34	9.60	9.61	278.55	279.05
LC2.2	21.33	21.36	573.16	574.38	9.35	9.37	260.51	261.00
LC3	23.14	23.45	1149.50	1179.80	10.27	10.39	556.63	568.77

Table 8.4: Maximum and standard deviation of axial force in the tower - OO-Star.

	Tower Base				**Tower top**			
	MAX [MN]		STD [kN]		MAX [MN]		STD [kN]	
	Newman	Full QTF	Newman	Full QTF	Newman	Full QTF	Newman	Full QTF
LC1.1	19.98	19.99	144.74	144.82	8.90	8.90	76.44	76.47
LC1.2	19.81	19.80	142.75	142.84	8.67	8.67	63.63	63.67
LC2.1	20.68	20.67	354.82	355.37	9.24	9.23	190.03	190.24
LC2.2	20.43	20.43	344.59	345.16	8.94	8.94	158.31	158.60
LC3	21.70	21.70	753.26	755.85	9.51	9.56	363.97	365.91

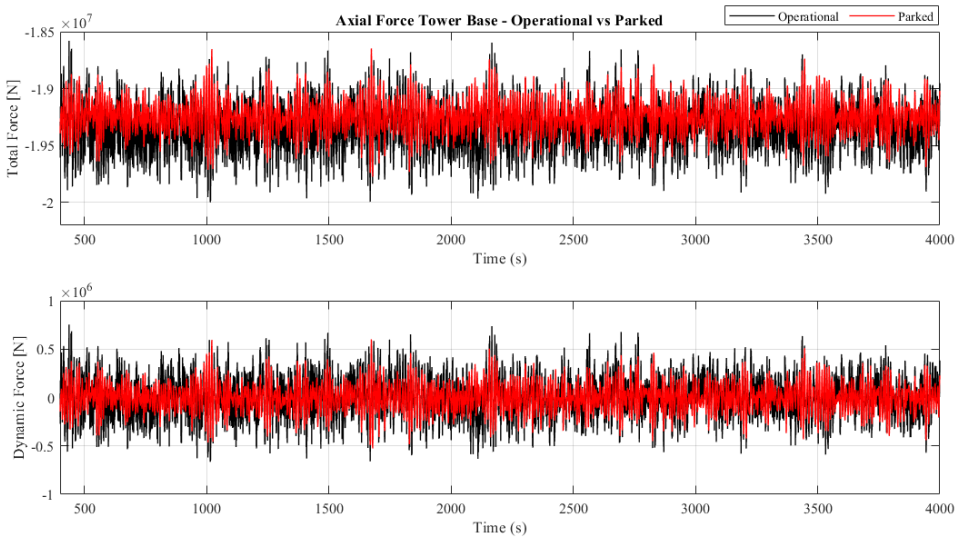

Figure 8.16: Time series of axial force at tower base for INO WINDMOOR at load case LC2.1 and LC2.2.

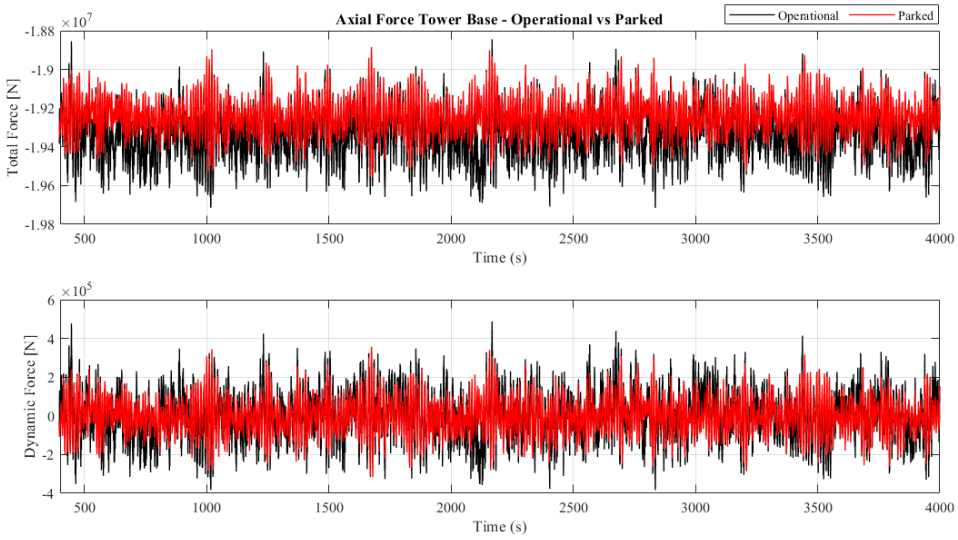

Figure 8.17: Time series of axial force at tower base for OO-Star at load case LC2.1 and LC2.2.

8.3.2 Floater Influence on Axial Loads

A comparison of the axial loads in the tower base and top between the two FWTs is presented in Figure 8.18, while Figure 8.19 and Figure 8.20 present the time series of the axial loads in the tower base in LC2.1 and LC2.2, respectively.

The results indicate that the INO WINDMOOR experiences a significantly larger dynamic axial force in the tower base and top for all design load cases. In LC1.1 and LC2.2, the standard deviation of the axial loads in the tower base and tower top for the INO WINDMOOR is approximately 40 % and 30 % larger than for the OO-Star, respectively. In the extreme load case, the INO WINDMOOR experience a 36 % higher axial force in both tower base and top than the OO-Star. The same trend is seen for the maximum axial force, where the INO WINDMOOR experiences the largest forces in all load cases.

As the tower is located off-centre on one of the columns in the INO WINDMOOR, the tower will experience a higher vertical motion due to the pitch response. Additionally, the rigid body motion in heave is also seen from Section 8.1 to be more significant for the INO WINDMOOR. Hence the magnitude of the axial force increases. The time series in Figure 8.19 and Figure 8.20 highlight the difference in the dynamic axial tower force between the two FWTs.

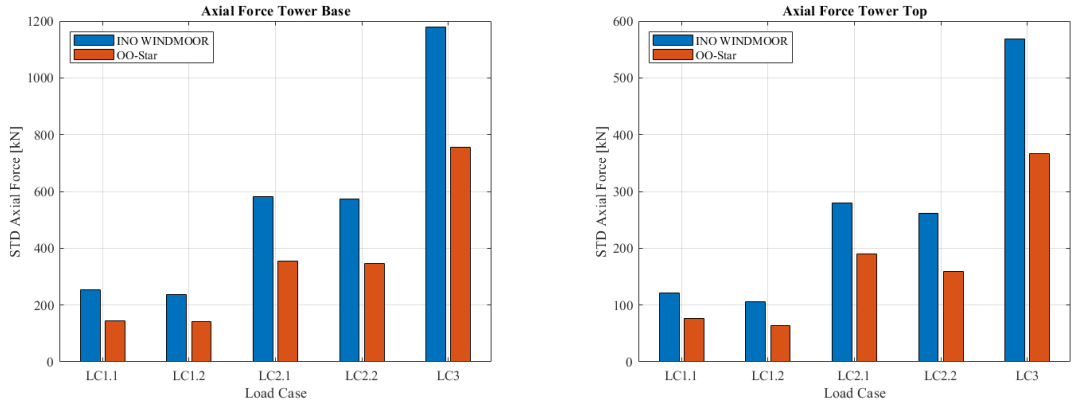

Figure 8.18: Comparison of standard deviation of axial force in the tower base and tower top with the QTF.

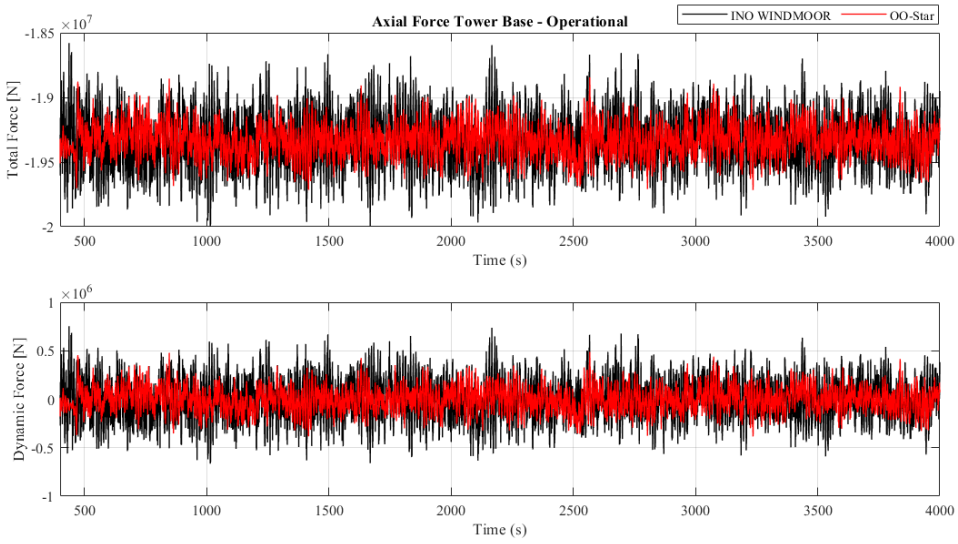

Figure 8.19: Time series of axial force at tower base between INO WINDMOOR and OO-Star in LC2.1.

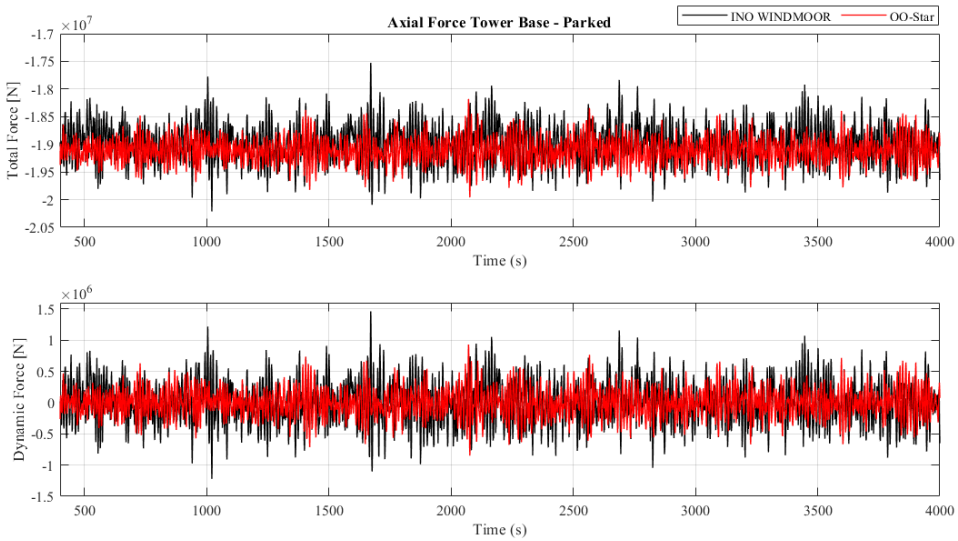

Figure 8.20: Time series of axial force at tower base between INO WINDMOOR and OO-Star in LC2.2.

8.3.3 Fore-Aft Bending Moment

The fore-aft bending moment at the tower base and tower top is presented in terms of the standard deviation and maximum values for the INO WINDMOOR and OO-Star in Table 8.5 and Table 8.6, respectively. The time series of the fore-aft bending moment in LC2.1 and LC2.2 is presented in Figure 8.21 and Figure 8.22 for the INO WINDMOOR and OO-Star.

The moment arm is significantly larger for the tower base than for the tower top, and hence the most extensive bending moments occur in the base of the tower for both FWTs. Similarly, as for the axial forces in the tower, the effect of Newman's approximation and full QTF is of minor concern regarding the tower bending moments. The fore-aft bending moment is parallel to the incoming wind and wave direction. Thus the tower fore-aft bending moment is primarily due to the thrust force induced by the rotor and the wave excitation forces on the floater. In addition, the rotor moment will lead to a fore-aft bending moment caused by the rotor's weight and wind shear. In LC1.1, where the thrust force is at its maximum, the tower base dynamic bending moment is approximately 70 % larger when the turbine is operational compared to parked. This is valid for both FWTs. However, for the tower top, the bending moment at operational and parked conditions is more similar. Furthermore, the standard deviation indicates a higher dynamic bending moment in operational conditions for both FWTs.

At the cut-out wind speed in LC2.1, the thrust force is significantly smaller, and the waves have increased. Still, the maximum bending moment is larger in LC1.1, indicating the severity of the thrust force on the fore-aft bending moment. From the time series, an opposite sign in the bending moment between the operational and parked conditions is observed, indicating that the turbine is leaning forward when not subjected to a thrust force. Furthermore, the largest total and dynamic bending moments are found in LC3 for both FWTs, showing that the wave excitation contribution to the fore-aft bending moment can be significant as well.

Table 8.5: Maximum and standard deviation of bending moment INO-WINDMOOR.

	Tower Base				**Tower top**			
	MAX [MNm]		STD [kNm]		MAX [MNm]		STD [kNm]	
	Newman	Full QTF	Newman	Full QTF	Newman	Full QTF	Newman	Full QTF
LC1.1	363.45	363.13	48.66	48.62	58.90	58.87	5.24	5.24
LC1.2	158.26	158.14	15.12	15.18	57.17	57.16	1.15	1.14
LC2.1	269.47	271.42	55.70	55.79	73.37	73.16	9.03	9.03
LC2.2	236.48	237.91	41.11	41.36	62.79	63.29	3.05	3.05
LC3	448.20	450.71	105.72	106.92	77.40	79.79	8.12	8.23

Table 8.6: Maximum and standard deviation of bending moment OO-star.

	Tower Base				**Tower top**			
	MAX [MNm]		STD [MNm]		MAX [MNm]		STD [MNm]	
	Newman	Full QTF	Newman	Full QTF	Newman	Full QTF	Newman	Full QTF
LC1.1	366.88	366.55	48.91	48.92	59.44	59.42	5.21	5.22
LC1.2	157.72	160.64	13.80	13.99	55.82	55.86	0.76	0.76
LC2.1	251.62	248.66	48.00	48.52	70.51	70.34	8.57	8.58
LC2.2	227.81	245.35	35.81	36.65	60.14	60.75	2.11	2.13
LC3	415.58	459.79	83.65	87.04	71.95	74.88	5.60	5.75

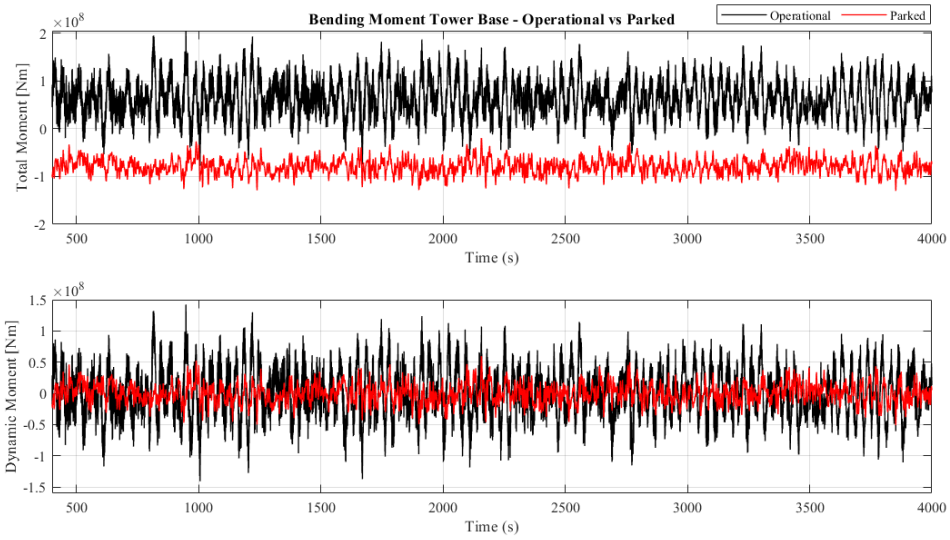

Figure 8.21: Time series of bending moment at tower base for INO WINDMOOR in operational and parked condition at LC2.1 and LC2.2.

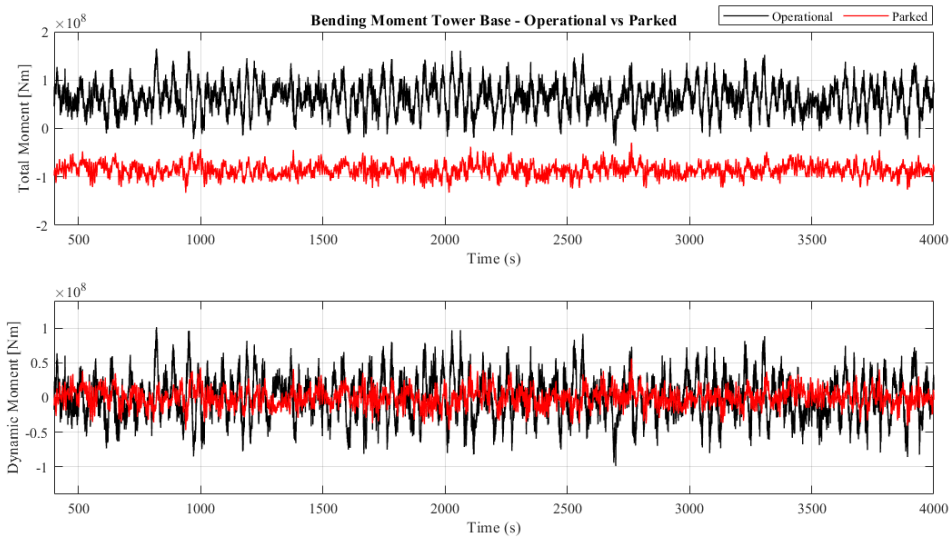

Figure 8.22: Time series of bending moment at tower base for OO-Star in operational and parked condition at LC2.1 and LC2.2.

8.3.4 Floater Influence on Fore-Aft Bending Moment

In Figure 8.23 and Figure 8.24, a comparison of the tower fore-aft bending moment at base and top is presented in terms of the standard deviation and maximum value for the INO WINDMOOR and OO-Star, respectively. Figure 8.25 and Figure 8.26 illustrate the time series of the tower base bending moment for the two FWTs in LC2.1 and LC2.2, respectively.

At the tower base, the maximum bending moments occur for the OO-star in all conditions, except for LC2.1. The larger maximum bending moment in LC2.1 for the INO WINDMOOR is due to the larger dynamic motions, as seen from Figure 8.25. Furthermore, as seen from Figure 8.26 the OO-Star experiences a larger mean bending moment when parked and hence, a larger maximum value. The OO-Star's larger mean bending moment in the parked condition is due to the slightly larger static pitch angle. In operational conditions, the tower base fore-aft bending moment is mainly governed by the thrust force and the pitch motion of the FWT. At rated wind speed in LC1.1, where the waves are quite small, the bending moment is mainly dominated by the thrust force, while in LC2.1, the bending moment is mainly governed by the wave-induced response as the thrust force is significantly smaller.

When considering the standard deviation of the bending moment, which is relevant for the fatigue damage at the tower, it is seen that the INO WINDMOOR experience a larger dynamic bending moment for all load cases. This is seen in the time series shown in Figure 8.25 and Figure 8.26. These results indicate that the dynamic tower base bending for the INO WINDMOOR is more affected by the wave excitation forces than the OO-Star.

Moreover, the maximum tower top bending moment is seen from the results to be the largest for the INO WINDMOOR, except for LC1.1. In operational conditions, the wind dominates the tower top bending moments, and the response of the floaters have a relatively small influence on the tower top moments when operating. This will be discussed more thoroughly in Section 8.4. Furthermore, the results also reveal that the INO WINDMOOR experiences the largest dynamic tower top bending moments. When the turbine is operating, LC2.1 is the dominating condition for the dynamic tower top bending moment, where the tower top is subjected to a combination of the thrust force and increased wind speed. Regarding the standard deviation, larger fluctuations in the bending moment are observed in operational conditions, which is connected with the fluctuations in the incoming wind.

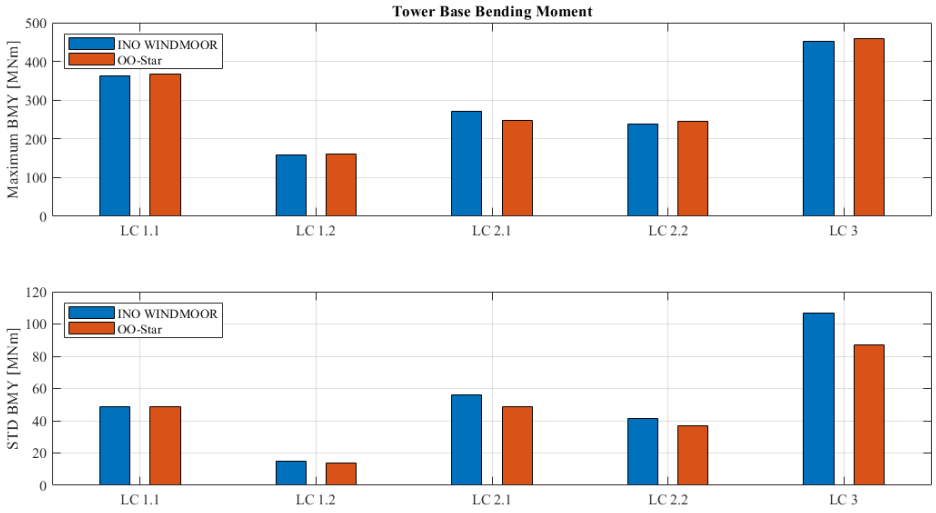

Figure 8.23: Maximum and standard deviation of tower base bending moment between INO WINDMOOR and OO-Star.

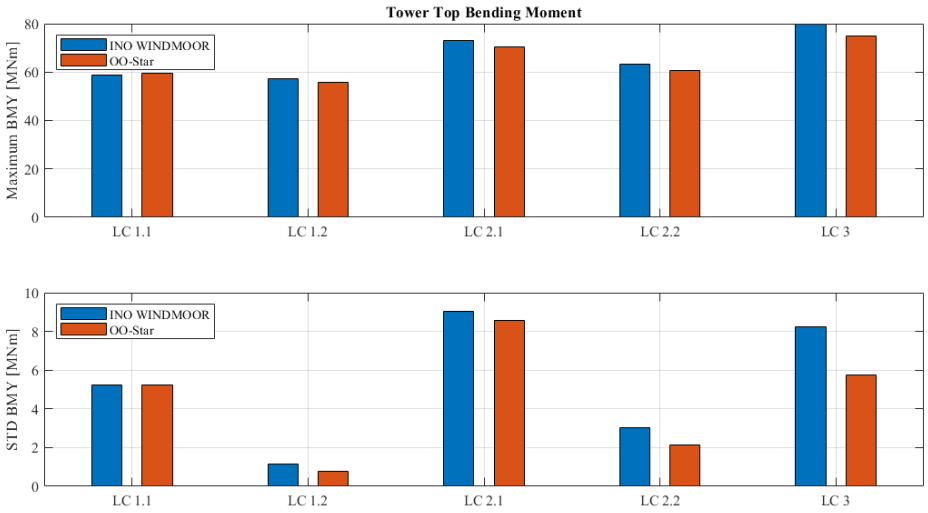

Figure 8.24: Maximum and standard deviation of tower top bending moment between INO WINDMOOR and OO-Star.

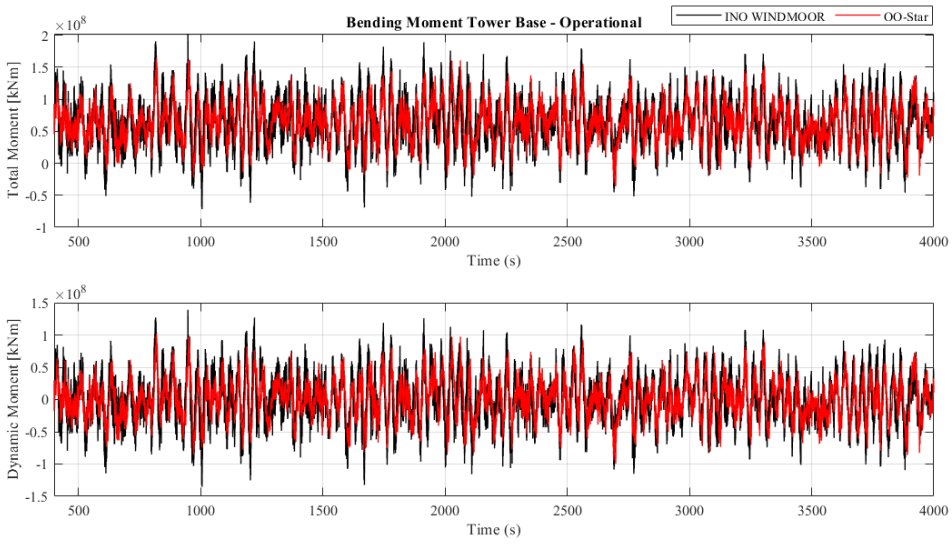

Figure 8.25: Time series of tower base bending moment between INO WINDMOOR and OO-Star in LC2.1.

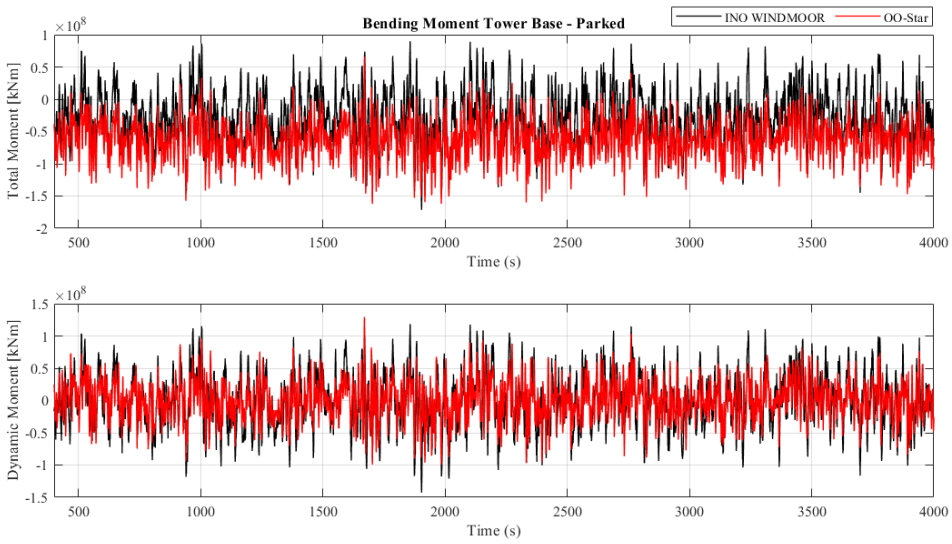

Figure 8.26: Time series of tower base bending moment between INO WINDMOOR and OO-Star in LC2.2.

8.3.5 Hydrodynamic Wave Loads

This section presents the excitation forces computed with first-order wave and second-order wave forces using Newman's approximation and the full QTF in surge, heave and pitch. As the wave forces are not influenced by the turbine being in operational or parked condition, only one load case is presented for rated and cutout wind speed, denoted LC1 and LC2, respectively.

In Table 8.7, hydrodynamic wave loads acting on the two floaters are presented as the standard deviation in surge, heave and pitch. The results show that the first-order wave forces are significantly larger than the wave drift forces for both FWTs. For LC1 and LC2, the second-order wave forces are 1-3% the magnitude of the first-order loads. However, even if the second-order loads are much smaller than the first-order loads, the second-order response could be larger than the first-order response if excited at resonance. For the pitch loads in LC3, the difference-frequency wave loads estimated using a full QTF are 17.8% and 7.7% the magnitude of the first-order wave load for the INO WINDMOOR and OO-Star, respectively, resulting in a considerable contribution to the total load. Both the first and second-order wave forces increase accordingly for increasing sea states. Consequently, the discrepancy between the difference-frequency loads using Newman's approximation and the full QTF increases. The most considerable discrepancy is observed in pitch at LC3, where the loads using the full QTF are 60% and 90% larger than the loads calculated with Newman's approximation for the INO WINDMOOR and OO-Star, respectively. It can be observed that Newman's approximation underestimates the second-order difference-frequency wave loads compared to a full QTF method for both FWTs in surge, heave and pitch. The smallest deviation between the two methods is seen for the heave force in both the INO WINDMOOR and OO-Star.

Table 8.7: Standard deviation of first and second order wave loads in surge, heave and pitch for INO WINDMOOR and OO-Star.

Surge

	INO WINDMOOR [kN]			**OO-Star [kN]**		
	First-order	Newman	Full QTF	First-order	Newman	Full QTF
LC1	2420.97	15.28	38.67	4193.47	20.41	49.80
LC2	5732.65	80.71	211.74	9982.06	107.76	273.20
LC3	11699.92	217.06	809.89	21688.86	309.47	1055.20

Heave

	INO WINDMOOR [kN]			**OO-Star [kN]**		
	First-order	Newman	Full QTF	First-order	Newman	Full QTF
LC1	2134.62	23.86	35.81	3240.38	27.15	37.14
LC2	4954.30	134.19	197.84	7643.06	149.79	203.59
LC3	8250.39	687.65	848.11	14875.35	626.02	810.84

Pitch

	INO WINDMOOR [kNm]			**OO-Star [kNm]**		
	First-order	Newman	Full QTF	First-order	Newman	Full QTF
LC1	26228.16	368.74	737.70	73288.94	135.49	1181.99
LC2	60467.55	2027.65	4088.36	172796.87	733.78	6537.98
LC3	99422.03	7128.63	17728.44	346302.34	2694.44	26908.28

A direct comparison of the first-order excitation forces in surge, heave, and pitch between the INO WINDMOOR and OO-Star is presented in Figure 8.27. The graphs show that the OO-Star is subjected to larger wave forces than the INO WINDMOOR for all load cases in surge, heave, and pitch. However, the OO-Star is designed with an extra column and heave plates compared to the INO WINDMOOR. Hence the different geometry between two floaters will influence the magnitude of the forces.

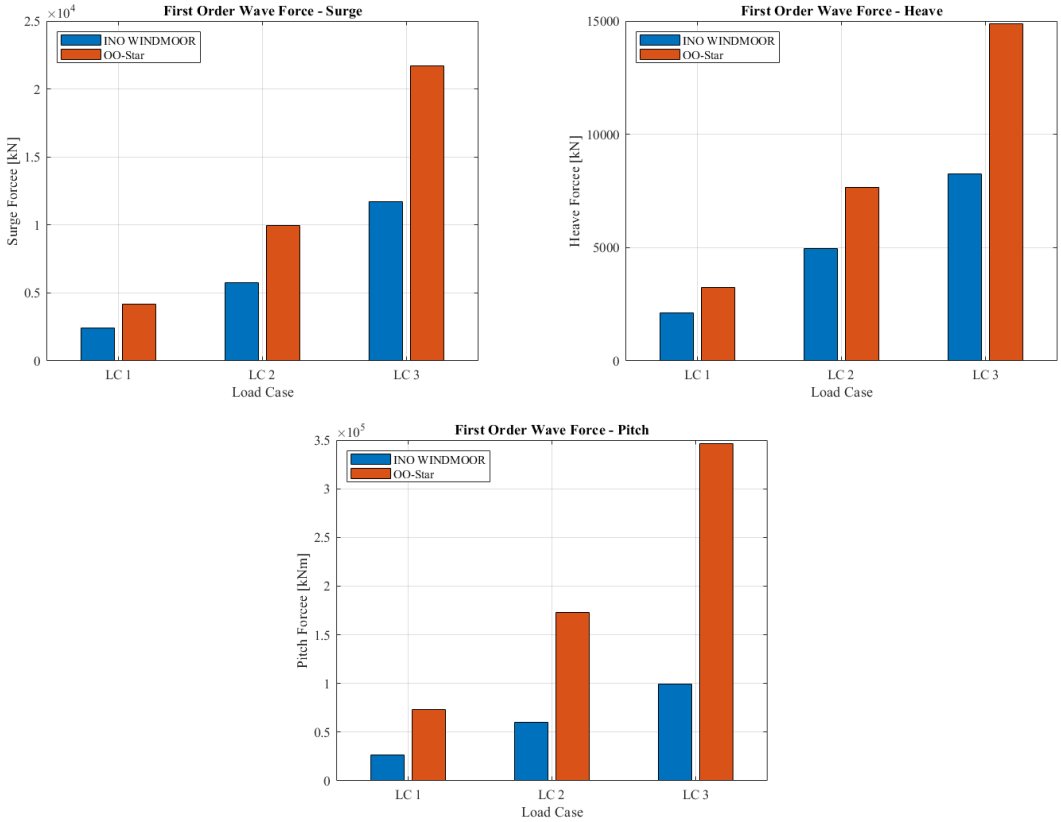

Figure 8.27: Comparison of first-order wave force for INO WINDMOOR and OO-Star in surge, heave, and pitch.

8.4 Tower Loads Spectra

This section presents the power spectra of the tower base axial force, the tower base bending moment and the bending moment at the tower top. The spectral analysis is performed with a full QTF representing the second-order difference-frequency forces.

8.4.1 Axial Force Tower Base

The power spectra of the tower base axial loads for LC1.1 and LC1.2 are presented in Figure 8.28 and Figure 8.29 for the INO WINDMOOR and OO-Star, respectively. The power spectra of tower base axial loads for LC2.1, LC2.2, and LC3 are given in Appendix E.2 because the power spectra at rated wind speed are representative of the other load cases.

As illustrated in Figure 8.28 and Figure 8.29, the axial force at the tower base is dominated by the wave-induced response for both FWTs. Consequently, the axial loads at the tower base are approximate of the same magnitude in operational and parked conditions. For the INO WINDMOOR, a small contribution from the pitch and heave resonant response is observed when the turbine is operational. In contrast, only a small contribution from the resonant heave response is apparent in

parked conditions. For the OO-Star, the contribution from the heave and pitch resonant response is negligible.

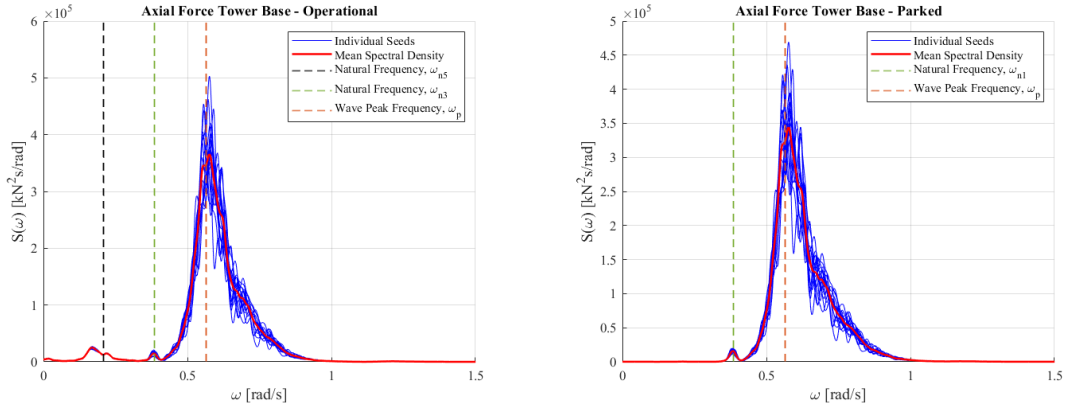

Figure 8.28: Spectra for axial force at tower base for LC1.1 and 1.2 for the INO WINDMOOR FWT.

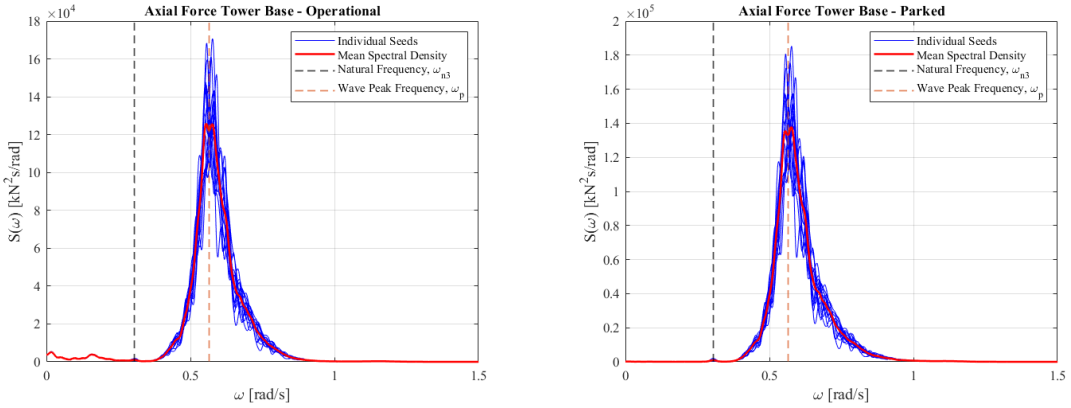

Figure 8.29: Spectra for axial force at tower base for LC1.1 and LC1.2 for the OO-Star FWT.

8.4.2 Axial Force Tower Top

Figure 8.30 and Figure 8.31 illustrate the power spectra of the tower top axial loads in LC1.1 and LC1.2 for the INO WINDMOOR and OO-Star, respectively. As for the axial loads at the tower base, the power spectra of tower top axial loads for LC2.1, LC2.2 and LC3 are given in Appendix E.3 because the power spectra at rated wind speed are representative of the other load cases as well.

As for the tower base, the wave-induced response is the dominating contribution to the axial force at the tower top. However, a slightly larger contribution from the low-frequency wind-induced response is observed compared to the axial force at the tower base under operational conditions. Consequently, the tower top will experience a slightly larger axial force when the turbine is operating. Comparing the two FWTs, the INO WINDMOOR is slightly more sensitive to the resonant heave response than the OO-Star.

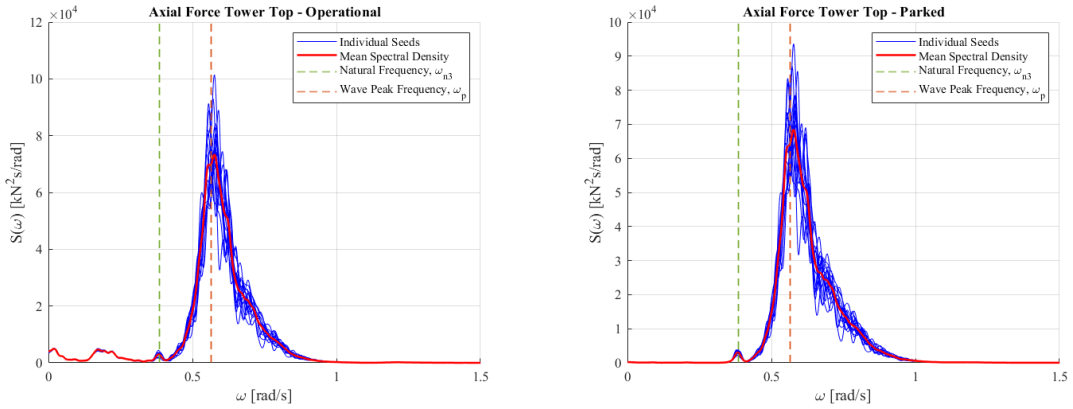

Figure 8.30: Spectra for axial force at tower top for LC1.1 and 1.2 for the INO WINDMOOR.

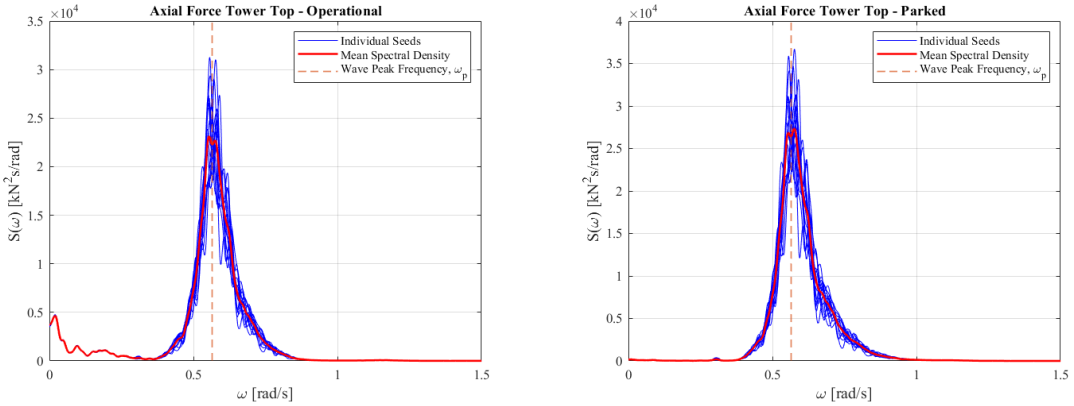

Figure 8.31: Spectra for axial force at tower top for LC1.1 and 1.2 for the OO-Star.

8.4.3 Fore-Aft Bending Moment Tower Base

This section presents the power spectra for the fore-aft tower base bending. In contrast to the tower base axial force, the distribution of the different frequency components of the fore-aft bending spectra is highly dependent on the load case. Therefore, the tower base bending spectra are presented for each load case. The spectral analysis is performed with a full QTF.

LC1.1 and LC1.2

Figure 8.32 and Figure 8.33 present the power spectra of the tower base bending moment at rated wind speed in operational and parked condition for the INO WINDMOOR and OO-Star, respectively.

In operational conditions, the low-frequency wind-induced response and the pitch resonant frequency response dominate the fore-aft bending moment with a marginal contribution from the wave frequency response. However, in parked conditions, the wave frequency response governs the fore-aft bending moment. Additionally, a significant contribution from the pitch resonant response is seen. The power spectra in parked conditions indicate that the wave-induced response is quite different for the two FWTs. For the INO WINDMOOR, the peak response corresponds well with the wave peak frequency. However, for the OO-Star, the peak response in the wave frequency range occurs at a slightly higher frequency than the wave peak frequency at approximately $\omega = 0.8$ rad/s. This is connected with the fore-aft bending moment response amplitude operators (RAOs) of the two FWTs. By considering the bending moment RAO of the two FWTs in the wave frequency

range, it is seen that the OO-Star has a quite high response amplification of the bending moment at $\omega = 0.8$ rad/s, which is close to the wave peak frequency. Consequently, the dominating bending moment contribution for the OO-Star will occur at this frequency. For the INO WINDMOOR, it is seen from the bending moment RAO that the response amplification is at a higher frequency than for the OO-Star, and hence, the peak at $\omega = 0.8$ rad/s becomes less prominent. The RAOs of the fore-aft bending moment for the two FWTs are given in Appendix F.

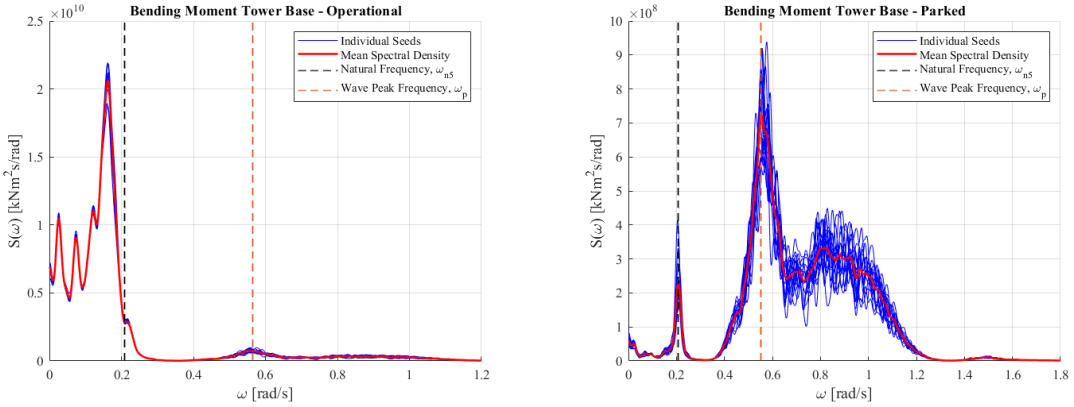

Figure 8.32: Spectra for the tower base bending moment at LC1.1 and LC1.2 for the INO WINDMOOR.

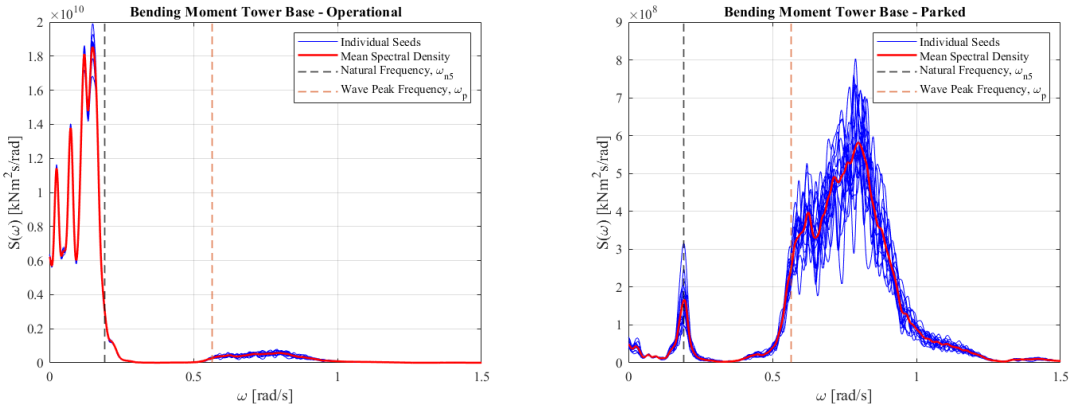

Figure 8.33: Spectra for the tower base bending moment at LC1.1 and LC1.2 for the OO-Star.

LC2.1 and LC2.2

Figure 8.34 and Figure 8.35 illustrate the power spectra of the tower base bending moment at cut-out wind speed in operational and parked conditions for the INO WINDMOOR and OO-Star, respectively.

In operational conditions, the pitch resonant response dominates the fore-aft bending moment. Compared to LC1.1, it is seen that the low-frequency wind-induced response decreases while the response from the wave frequency increases. When parked, the response from the wave frequency is still dominating with a significant contribution from the pitch resonant response as well. Furthermore, a small contribution from the low-frequency wind-induced response becomes more prominent as the wind speed increases. The same tendency as for LC1.2 is observed, where INO WINDMOOR experiences the largest wave-induced response at the wave peak frequency while the OO-Star experiences the most extensive response at approximately $\omega = 0.8$ rad/s.

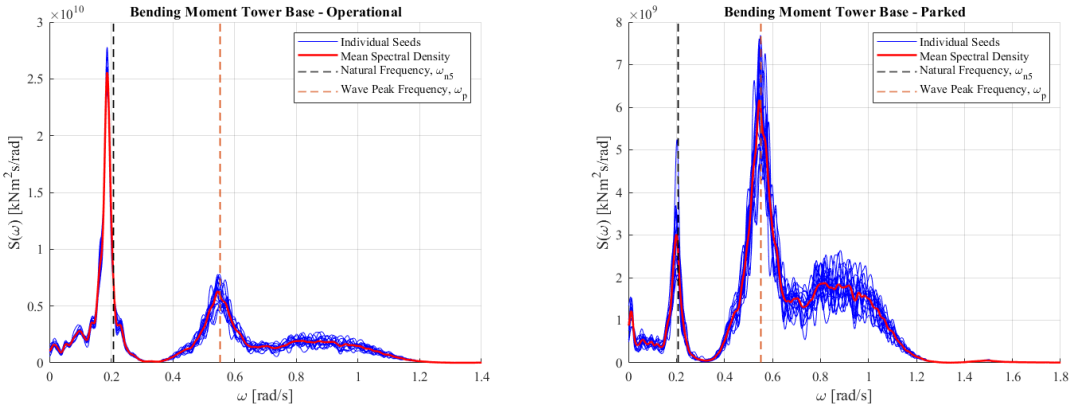

Figure 8.34: Spectra for the tower base bending moment at LC2.1 and LC2.2 for the INO WINDMOOR.

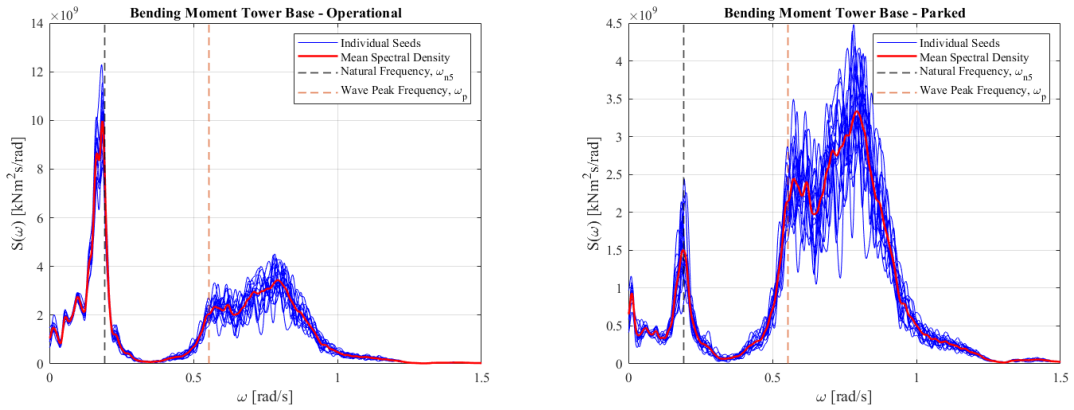

Figure 8.35: Spectra for the tower base bending moment at LC2.1 and LC2.2 for the OO-Star.

LC3

Figure 8.36a and Figure 8.36b present the power spectra of the tower base bending moment at LC3 for the INO WINDMOOR and OO-Star, respectively.

When the wave height increases as in LC3, the contribution from the wave frequency response becomes more prominent than for LC1.2 and LC2.2. The power spectra of the two FWTs indicate that the contribution from the pitch resonant response is more significant for the INO WINDMOOR. Moreover, the wave frequency response is also sufficiently larger for the INO WINDMOOR. For the OO-Star, it is seen that the largest wave-induced response occurs at the wave peak frequency, unlike in LC1 and LC2, where the largest response contribution occurred at $\omega = 0.8$ rad/s.

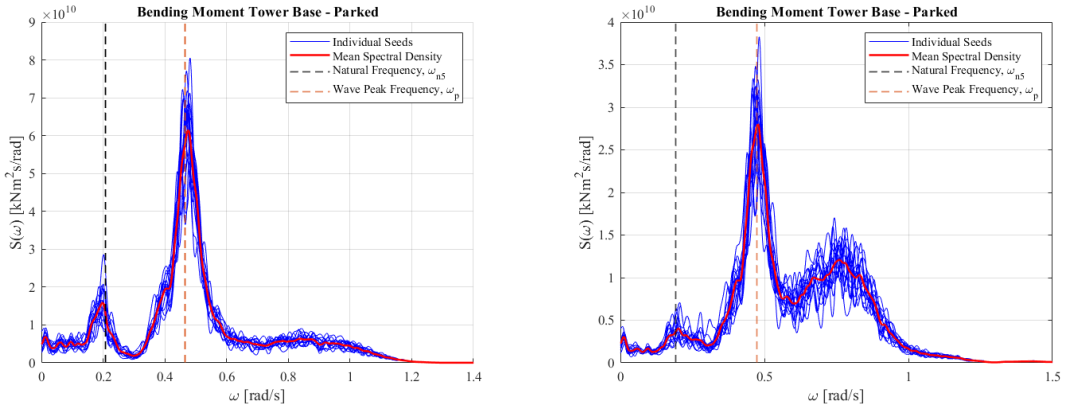

(a) (b)

Figure 8.36: Spectra for the tower base bending moment at LC3 for the INO WINDMOOR (a) and OO-Star (b).

8.4.4 Fore-Aft Bending Moment Tower Top

The power spectra for the tower top bending moment at LC1.1 and LC1.2 is presented in Figure 8.37 and Figure 8.38 for the INO WINDMOOR and OO-Star, respectively. As the same tendency is observed for the other load cases as well, the power spectra at LC1.1 and LC1.2 are representative of the load cases. The power spectra of the tower top bending at LC2.1, LC2.2, and LC3 are given in Appendix E.4.

When the turbine is operational, the tower top fore-aft bending is dominated by the low-frequency wind-induced response with an insignificant contribution from the wave frequency. As the wave height increases in LC2.1, the contribution from both the wave frequency response and the pitch resonant response to the tower top bending becomes more prominent. However, the low frequency induced response is still the dominating contribution to the tower top bending. By comparing the power spectra of the tower top bending between the two FWTs in operational conditions, it is seen that the energy distribution in the power spectra is approximately the same, which indicates that the floaters have a small influence on the tower top bending when the turbine is operating.
When parked, the wave frequency response dominates the tower top bending with a minimal contribution from the heave and pitch resonant response. In LC2.2, the response from the heave and pitch resonant frequencies become more prominent, while at LC3, the low-frequency wind-induced response becomes more significant to the tower top bending, as seen in Appendix E.4.

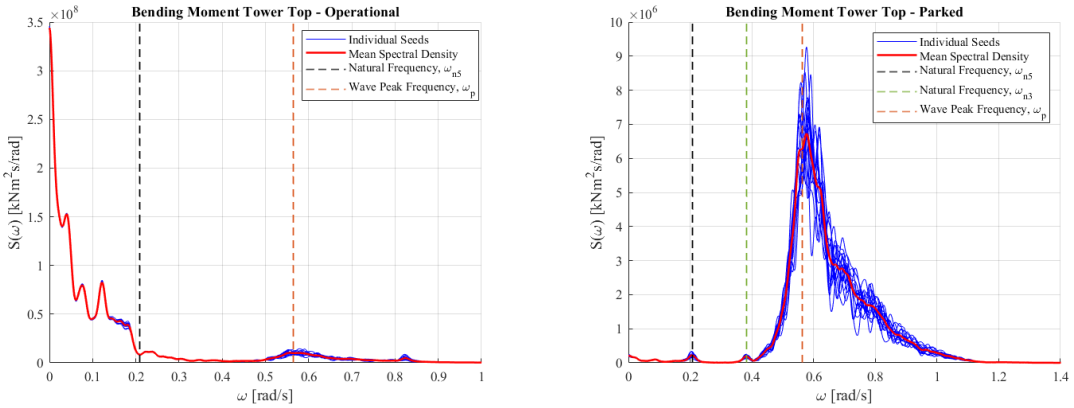

Figure 8.37: Spectra for tower top bending moment at LC1.1 and 1.2 for the INO WINDMOOR FWT.

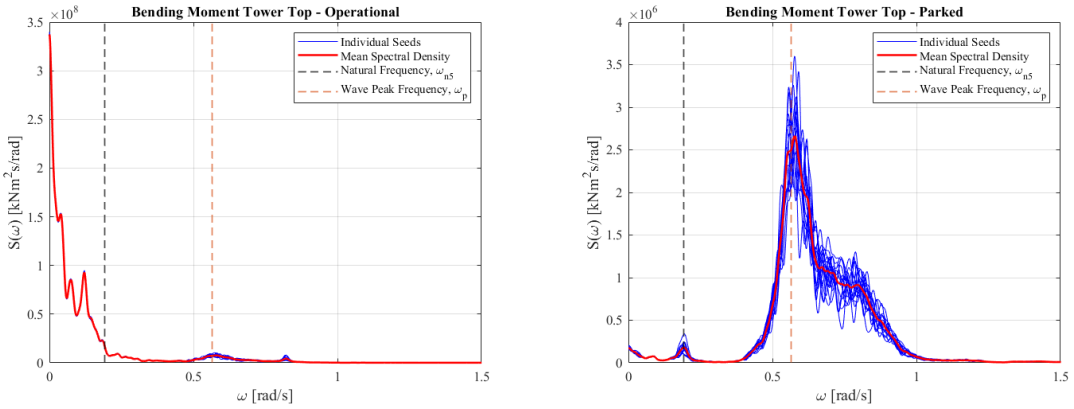

Figure 8.38: Spectra for tower top bending moment at LC1.1 and 1.2 for the OO-Star.

8.5 Mooring Line Tension

For the mooring line tension, the upwind mooring line 1 (ML1), as shown in Figure 6.10 is selected for further investigation among the three mooring lines for both the FWTs. The reason for selecting mooring line 1 is its alignment with the incoming wind and waves, thus experiencing the most considerable tension. Table 8.8 and Table 8.9 present the maximum and standard deviation of the mooring line tension for the INO WINDMOOR and OO-Star, respectively. A comparison of the mooring line tension using Newman's approximation and a full QTF is presented in Figure 8.39.

The mooring line tension is directly influenced by the FWTs surge motion. As discussed in Section 8.1, the most significant maximum and standard deviation of the surge motion occurs in LC3 for both FWTs. In LC1, which is considered a mild sea state, the effect of the thrust force at rated wind speed is observed to yield a 58% and 77.5% higher dynamic mooring line tension in operational conditions than in parked conditions for the INO WINDMOOR and OO-Star, respectively. In general, the mooring line tension increases with increasing significant wave height, as seen from Figure 8.39. The INO WINDMOOR is seen to experience a higher mooring line tension than the OO-Star in all design load cases, as indicated by the standard deviation and maximum values. In LC3, the INO WINDMOOR experiences approximately a 32.8% higher dynmaic mooring line tension and 21.7% higher maximum mooring line tension than the OO-Star. However, the pretension used for the INO WINDMOOR is significantly larger than for the OO-Star. Hence a larger tension is expected. The time series in Figure 8.40 illustrate the effect of the pretension as the mean offset on the total tension between the two floaters. In contrast, the dynamic tension reflects the standard deviation.

Looking at the maximum mooring line tension from Table 8.8 at the extreme condition in LC3, both the INO WINDMOOR and OO-Star FWTs are well below the MBL (Minimum Breaking Load) of 12660 kN and 11400 kN for the chain and polyester, respectively.

The mooring line tension calculated using Newman's approximation and the full QTF are shown to follow the same trend as for the surge motion as seen in Section 8.1. Newman's approximation slightly underestimates the standard deviation of the line tension for both FWTs in LC1.1 and LC2.2. However, the deviation is more prominent for the OO-Star. The most significant deviations in the mooring line tensions are found in LC3, where Newman's approximation underestimates the line tension by 11.6 % for the OO-Star.

Table 8.8: Maximum mooring line tension for ML1.

	INO WINDMOOR [kN]		**OO-Star [kN]**	
Newman	Full QTF	Newman	Full QTF	
LC1.1	4213.70	4208.30	3112.40	3120.60
LC1.2	2671.20	2664.30	1658.20	1668.20
LC2.1	4682.10	4661.90	3181.10	3303.80
LC2.2	4076.90	4043.00	2524.80	2628.70
LC3	8757.90	8271.40	5793.80	6468.00

Table 8.9: Standard deviation for mooring line tension for ML1.

	INO WINDMOOR [kN]		**OO-Star [kN]**	
	Newman	Full QTF	Newman	Full QTF
LC1.1	191.00	191.35	134.47	135.17
LC1.2	80.36	80.52	28.97	30.40
LC2.1	347.10	348.98	190.32	194.95
LC2.2	314.58	315.79	148.07	153.30
LC3	1291.90	1262.50	800.56	848.09

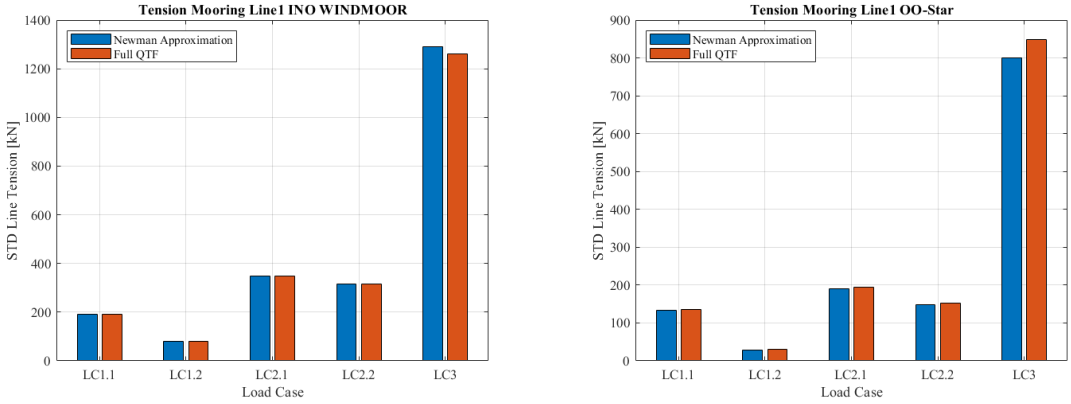

Figure 8.39: Standard deviation of tension in ML1 using Newman's approximation and full QTF.

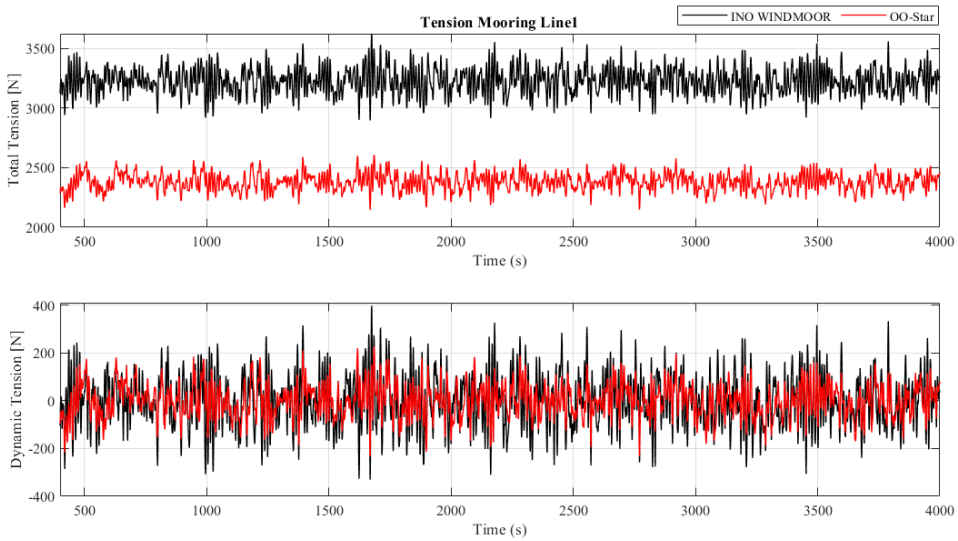

Figure 8.40: Time series of mooring line 1 tension between INO WINDMOOR and OO-Star at LC2.1

The power spectra of the mooring line tension at LC2.1 and LC2.2 are presented in Figure 8.41 for the INO WINDMOOR and OO-Star, respectively. Only the power spectra of LC2.1 and LC2.2 are shown, as these spectra are representative of the other load cases.

It is apparent from the power spectra that the wave frequency is the dominating contribution to the mooring line tension for both FWTs. Furthermore, the mooring line tension of the INO WINDMOOR is less affected by the low-frequency response than the OO-Star. Consequently, the contribution of low-frequency responses is of higher importance to the total response for the OO-Star in both operational and parked conditions. The contribution from the pitch resonance response to the mooring line tension is observed to be insignificant.

In general, it is observed that Newman's approximation slightly underestimates the mooring line tension in the low-frequency range. When comparing Newman's approximation and the full QTF, the most considerable deviations are seen in the low-frequency area, especially at surge resonance. However, it is found that the deviations in the mooring line tension between Newman's approximation and the full QTF are marginal for the milder sea states, especially for the INO WINDMOOR.

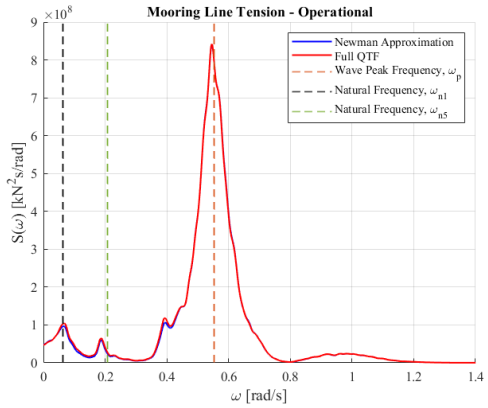

(a) INO WINDMOOR

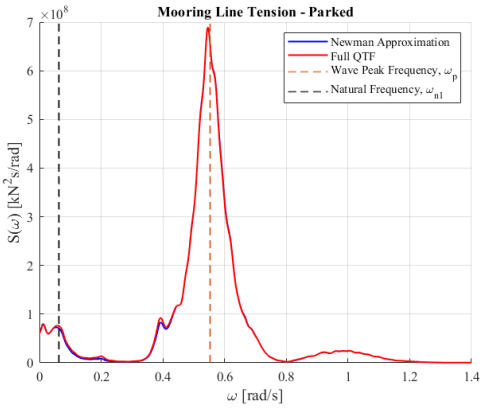

(b) INO WINDMOOR

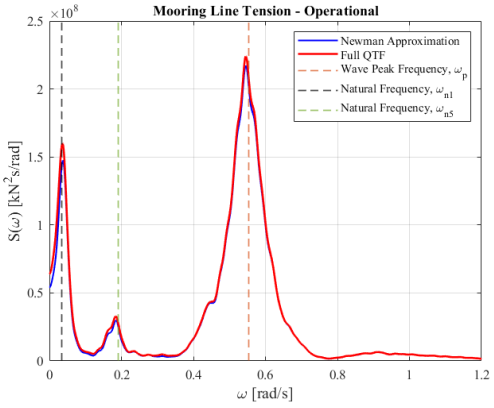

(c) OO-Star

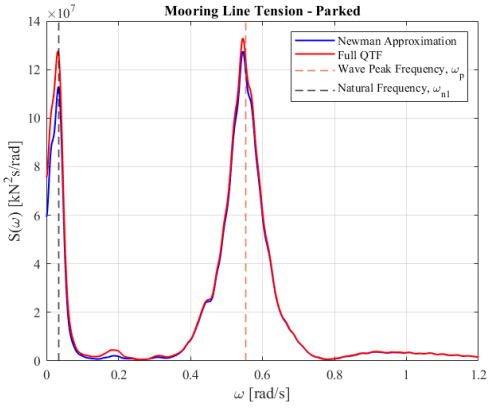

(d) OO-Star

Figure 8.41: Spectra of mooring line tension at LC2.1 and LC2.2.

8.6 Floater Influence on Power Production

An investigation of how the two floaters affect the turbine electrical generator output is performed for load cases LC1.1 and LC2.1. Table 8.10 presents the mean and standard deviation of the electrical generator output. Time series of the power production for INO WINDMOOR and OO-Star are presented in Figure 8.42 to illustrate the fluctuations in the generator output at rated and cut-out wind speed.

The results indicate that the mean electrical generator output for the INO WINDMOOR is larger at rated wind speed in LC1.1, while the opposite is observed for cut-out wind speed in LC2.1. These results suggest that the power output is correlated with the pitch motion of the FWTs. As seen in Figure 8.4, the pitch motion is more significant for the OO-Star in LC1.1 and smaller for the INO WINDMOOR in LC2.1. Hence, the electrical generator output is influenced by the pitch motion of the FWT, although for LC2.1, the difference is minuscule. As the turbulence intensity decreases with increasing wind speeds, the standard deviation is seen to be significantly smaller in LC2.1. Consequently, the mean electrical generator output difference between the two floaters is more negligible as the wind speed increases.

At rated wind speed in LC1.1, the difference between the INO WINDMOOR and OO-Star concerning the mean electrical generator output is 0.45 %. However, this marginal difference is equivalent to 412 MW during 1-year of power production to put this into perspective.

Table 8.10: Comparison of electrical generator output between INO WINDMOOR and OO-Star in LC1.1 and LC2.1.

	INO WINDMOOR		**OO-Star**	
	Mean	STD	Mean	STD
LC1.1	10.370 MW	1.704 MW	10.323 MW	1.710 MW
LC2.1	11.817 MW	0.309 MW	11.819 MW	0.303 MW

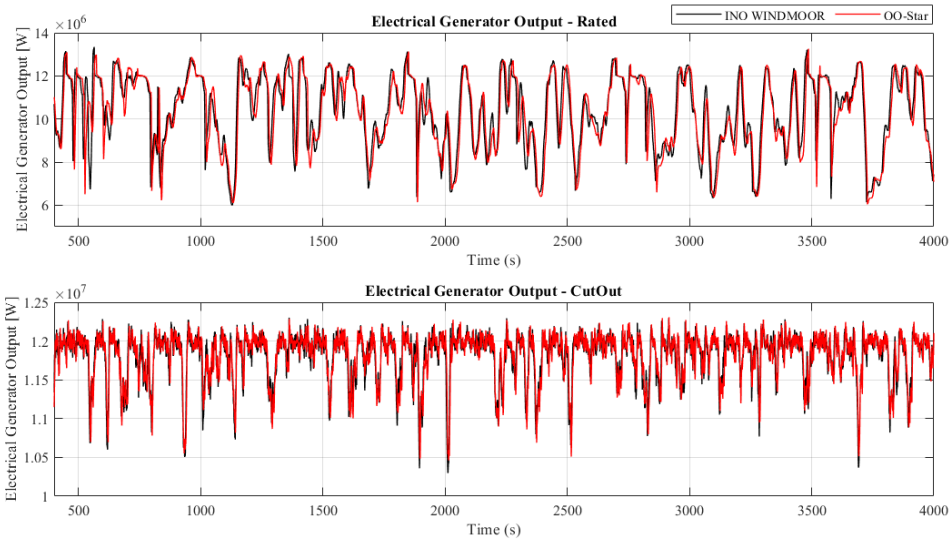

Figure 8.42: Time series of electrical generator output between INO WINDMOOR and OO-Star in LC1.1 and LC2.1.

8.7 Fatigue

In this section, a long term fatigue damage assessment is performed for both FWT models, using the established load cases defined in Table 5.10. The selected areas of investigation are along the tower, at the fairlead and segments of the mooring line. For the tower, three locations (tower base z=0m, z1=27.67 m, z2 = 51.23 m) from the tower bottom to approximately half of the tower are chosen. For the mooring line, consisting of the hybrid chain-polyester-chain configuration, the upper part of both the polyester rope and bottom chain are included in addition to the fairlead. In this work, 2-h fatigue damage estimates are obtained from load histories at various cross-sections, where the fatigue is estimated due to axial stress. Short-term fatigue damage is investigated for varying wave periods, followed by a study on the necessary simulation length and which wave/wind components influence the axial stress at the tower base in operational conditions. Lastly, the accumulated damage ratio and long-term fatigue damage are compared between the FWTs.

8.7.1 Short-Term Fatigue Damage for Varying Wave Periods

The short-term fatigue damage at the tower base and fairlead for the INO WINDMOOR and OO-Star are presented in Figure 8.43 and Figure 8.44, respectively. The figures show that the short-term fatigue damage increases with increasing wind and waves for both FWTs, where the most extensive fatigue damage occurs at the highest wind speed for both models. For the tower base fatigue damage, the varying wave periods provide coherent results for both FWTs. The lowest wave period yields the most considerable short term damage for the given wind and wave conditions. The same pattern is seen for the two other locations along the tower, z1 and z2, both models in Appendix G.1. The OO-Star is observed to be more sensitive to the wave periods, as seen

for wind speed 12.63 m/s and 16.58 m/s, where a more distinct variation in the fatigue damage is found.

The short-term fatigue damage at the fairlead increases with increasing sea states for both FWTs, similarly to the tower base. From the detailed view in Figure 8.43 and Figure 8.44, the largest fatigue damage is found for the lower wave periods. For the given wind speed of 7.31 m/s, the results indicate a good correspondence with the findings in Thies et al. (2014), where the fatigue damage, in general, tends to increase with increasing wave height and decreasing wave period. Above rated wind speed, the highest short-term fatigue damage is governed by the longest wave periods for increasing wind and wave conditions. This is also the case for the short-term fatigue damage of the polyester and bottom chain for both FWTs, as seen in Appendix G.1.

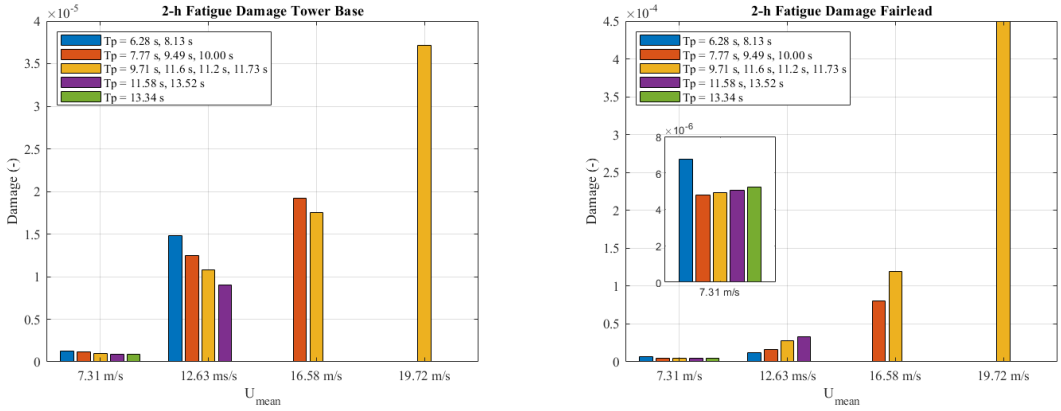

Figure 8.43: 2-h short term fatigue damage at tower base and fairlead for varying wave period for the INO WINDMOOR. Detailed view of wind speed 7.31 m/s is shown for fairlead.

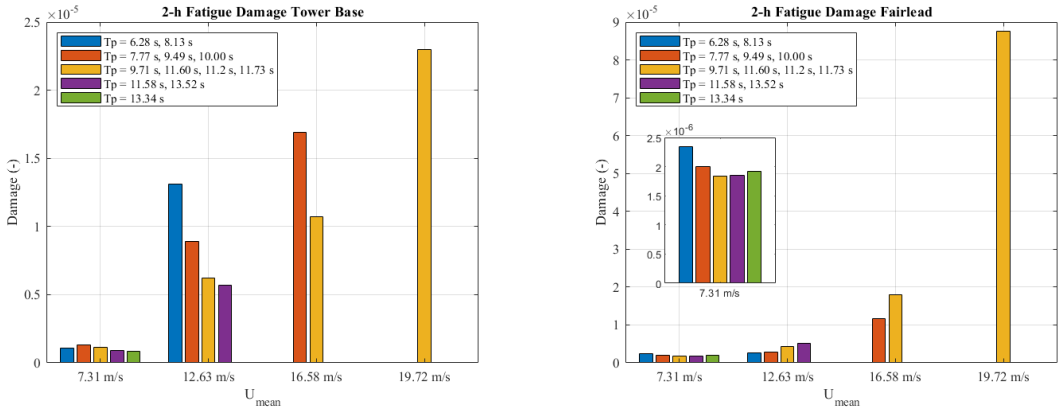

Figure 8.44: 2-h short term fatigue damage at tower base and fairlead for varying wave period for the OO-Star. Detailed view of wind speed 7.31 m/s is shown for fairlead.

8.7.2 Influence of Simulation Length

The 20-year total fatigue damage calculated from simulation lengths of 10 min, 30 min, 1 hour and 2 hours are presented in Figure 8.45 and Figure 8.46, as the relative difference to the 2-hour simulation for the INO WINDMOOR and OO-Star, respectively. The 10 min to 1-h simulations were obtained by sampling stress histories from the 2-h steady-state simulation.

The relative error of the total damage calculated based on 10 min, 30 min and 1-h simulations for the tower at all segments follows a consistent reduction in relative error for both FWTs. The total damage for the tower base is underestimated by more than twice as much for the OO-Star compared to the INO WINDMOOR when using a simulation length of 10 min. Furthermore, all the tower segments underestimated the total damage by approximately 2 % for both FWT when using 1-hour simulations, which is a significant improvement compared to the 10 and 30 min simulations. Hence, a simulation length of at least 1-h is recommended for estimating the total 20-year fatigue damage for the tower segments.

The 10-minutes simulations underestimate the total 20-year fatigue damage for all the segments of the mooring line for both FWTs, where the fatigue damage of the polyester is observed to have the largest discrepancy. In contrast to the tower base, the total damage is overestimated when using 30 minutes and 1-hour simulations for all the mooring line segments. Furthermore, the fatigue damage for the fairlead and bottom chain appears to be less affected by the simulation length than the polyester rope. The mooring line segments do not have an apparent convergence using 1-hour simulation. Hence, in compliance with Kvittem and Moan (2015), a 3-hour simulation length is recommended for the mooring line segments to capture the slowly-varying response of wave and wind loads.

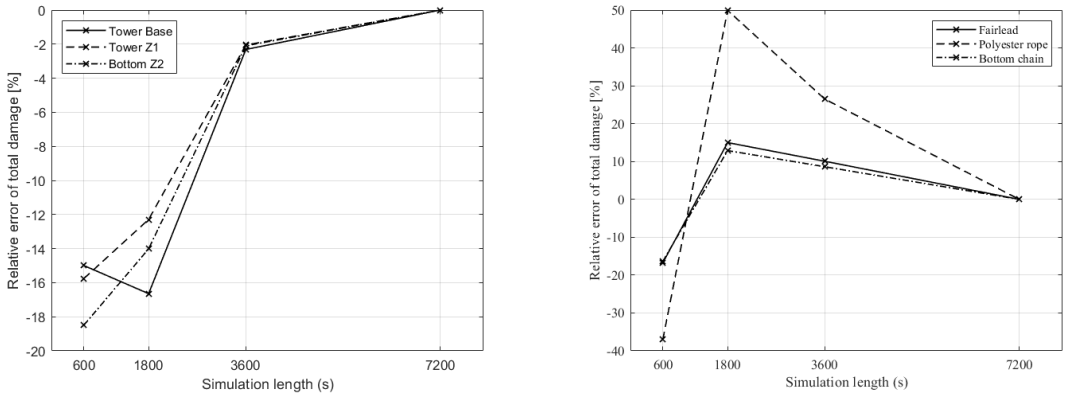

Figure 8.45: INO WINDMOOR relative discrepancy to 2-hour simulations in 20 year total damage.

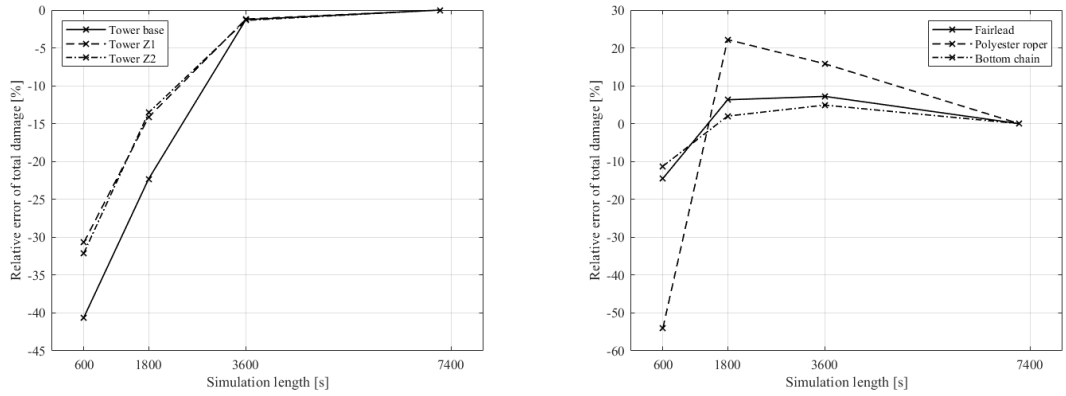

Figure 8.46: OO-Star relative discrepancy to 2-hour simulations in 20 year total damage.

8.7.3 Influence of Wind and Waves on Axial Stress

Figure 8.47 presents the power spectra of the axial stress at the tower base at block No.4, 8 and 12 for both the INO-WINDMOOR and OO-Star, respectively. Block No.4, 8, and 12 are selected to have approximately the same peak period, such that only the wind speed and corresponding significant wave height varies. Three operational cases have been selected; below rated wind speed, close to rated wind speed and above rated wind speed. As the fatigue damage at the tower base is dependent on the axial stress, these three cases are investigated to point out the dominating contributions to the axial stress and hence the corresponding fatigue damage.

The axial stress for wind speeds below rated in block No.4 is seen to be mainly dominated by the low frequency induced response by the wind and is the case for both FWTs. For block No.1-5 where the wind speed is below rated, The contribution from the wave frequency to the axial stress is almost negligible for both FWTs. Near rated wind speed in block No.8, which corresponds to the most significant thrust force, it is evident to see that the pitch resonant response is the dominating contribution to the axial stress response. Further, it is also observed that the INO WINDMOOR experiences a slightly larger response at pitch resonance and is slightly more influenced by the wave frequency than the OO-Star. However, the wave frequency contribution to the axial stress is marginal and is of little concern to the axial stress at rated wind speed.

Moreover, in block No.12, the axial stress response is still dominated by pitch resonance for above-rated wind speed. However, an increase in the wave frequency response is seen for both FWTs. Consequently, the contribution from the wave frequency response increases for increasing sea states. Furthermore, in block No.12, a marginal contribution from the tower's first fore-aft bending frequency also influences the axial stress at the tower base for both FWTs.

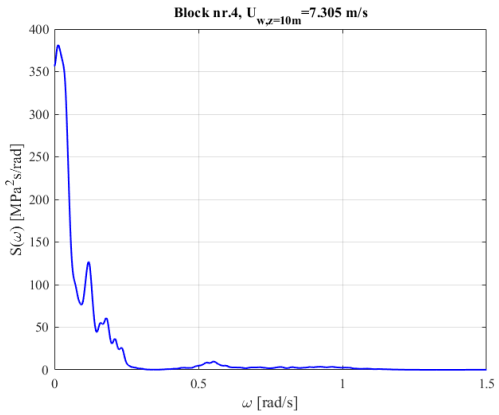

(a) INO WINDMOOR

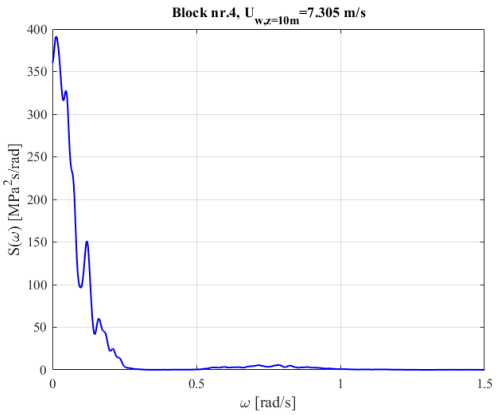

(b) OO-Star

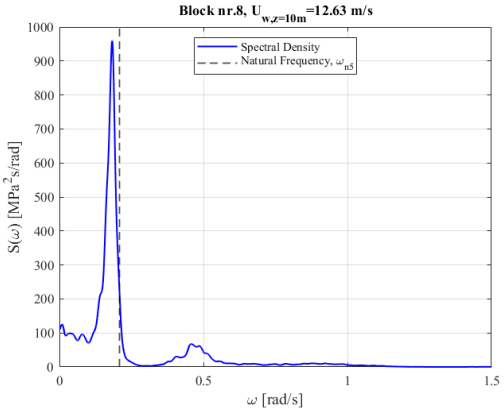

(c) INO WINDMOOR

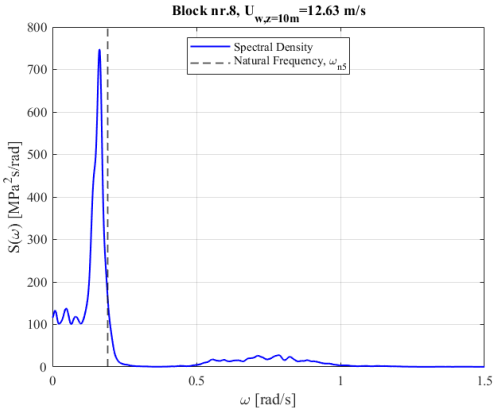

(d) OO-Star

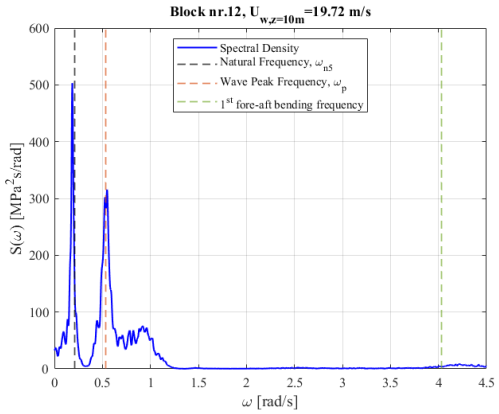

(e) INO WINDMOOR

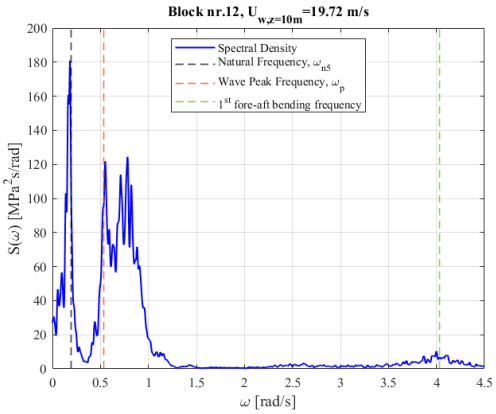

(f) OO-Star

Figure 8.47: Spectra of axial stress in block No.4, 8, 12.

8.7.4 Accumulated Fatigue Damage

Figure 8.48 presents the accumulated 20-year fatigue damage ratio for all the tower and mooring line segments for both FWTs, plotted against the environmental block numbers. The accumulated 20-year damage for the tower follows the same trend for both FWTs, with the lowest contribution of 1% coming from block No.5 and the most considerable contribution of more than 30% coming from block No.6 for all tower segments. Block No.6 is seen from Section 8.7.1 to be a condition that yields significant short-term fatigue damage and has a relatively large probability of occurrence, hence the governing fatigue damage condition. The most significant short-term tower fatigue damage is found from block No.12. However, this block has the lowest probability of occurrence and thus a little contribution to the total accumulated 20-year damage.

From the accumulated 20-year fatigue damage ratio of the mooring line segments, more variation is observed between the two FWTs and the different mooring line segments. In the milder sea states region represented by block No.1-5, the most considerable contribution of the accumulated 20-year damage is in the bottom chain for both the INO WINDMOOR and OO-Star. For increasing sea states, it is evident from the results that block No.10-12 are the highest contributors to the total 20-year damage for all mooring line segments. The polyester rope fatigue damage depends on increasing wave height, where more than 40 % of the accumulated total damage is found in block No.12 for both FWTs. Further, it is also seen that the increasing sea states, in general, leads to a higher contribution of fatigue damage at the fairlead, bottom chain and polyester for the INO WINDMOOR FWT compared to the OO-Star.

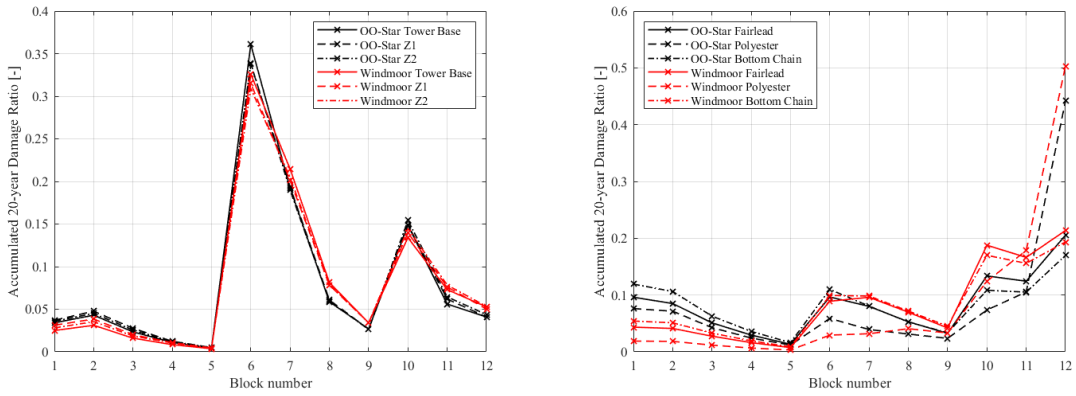

Figure 8.48: Accumulated 20-year fatigue damage ratio for tower segments (a) and mooring line segments (b).

The total 20-year fatigue damage based on 2-hour simulations is presented in Table 8.11 for both the INO WINDMOOR and OO-Star tower and mooring line segments. If the accumulated fatigue damage is larger than 1, this indicates failure, which is highlighted in red boxes in Table 8.11. For the tower segments, the most extensive fatigue damage is found in tower z1, located at approximately a quarter of the tower height in the positive z-direction from the tower base. This is suggested to be connected with the tower eigenmode deformed shape, yielding the largest stress concentrations in this area. The lowest 20-year damage is found in the tower base. Moreover, the INO WINDMOOR experiences more significant fatigue damage at all tower segments than the OO-Star. The differences are 20.3 %, 14.3 %, and 15.7 % higher in the tower base, z1 and z2, respectively. Failure occurs for both FWT at the tower z1 and z2 segments, whilst the tower base remains intact.

Considering the fact that the same turbine with the same tower properties is used for both the INO WINDMOOR and OO-Star, the total 20-year accumulated fatigue damage is sufficiently higher on the INO WINDMOOR. This is due to the findings in Section 8.3, where the INO WINDMOOR experienced, in general, a higher amplitude of oscillation as indicated by the standard deviation in both the axial force and fore-aft bending moment at the tower base in all load cases.

A significant difference in the 20-year damage at the fairlead can be observed for between the models, where the INO WINDMOOR fairlead suffers extensive fatigue damage and leads to failure during 20-years. The high fairlead fatigue damage is due to the considerable pretension needed to obtain the wanted natural period in surge. For the OO-Star, almost half of the pretension is used compared with the INO WINDMOOR. However, the required pretension for the INO WINDMOOR is seen from the results to cause extensive fatigue damage at the fairlead for the given chain-polyester-chain mooring system at the given water depth. Furthermore, the total 20-year fatigue damage of the polyester rope is almost negligible compared to the fairlead damage for both FWTs. On the other hand, the bottom chain experiences greater fatigue damage for the OO-Star than the INO WINDMOOR.

Table 8.11: Total 20-year fatigue damage based on 2-hour simulations.

	Tower [-]			**Mooring line [-]**		
	Base	z1	z2	Fairlead	Polyester	Bottom Chain
INO WINDMOOR	0.994	1.852	1.230	2.971	$5.548 \cdot 10^{-5}$	0.161
OO-Star	0.792	1.586	1.037	0.647	$1.645 \cdot 10^{-5}$	0.337

9 Discussion of Major Findings

9.1 The Applicability of Newman's Approximation

This section will discuss the most important findings regarding the applicability of Newman's approximation.

In general, the standard deviation of the low-frequency surge response calculated by Newman's approximation corresponds well with the standard deviation calculated using the full QTF. The largest difference between the two methods occurs in the extreme load case. For the INO WINDMOOR, the largest difference is 1%, corresponding to 0.02 m, while for the OO-Star, the largest difference is approximately 15%, corresponding to 0.51 m. According to these findings, Newman's approximation gives a good agreement with the full QTF for the INO WINDMOOR in all conditions. In contrast, for the OO-Star, Newman's approximation significantly underestimates the surge motion in extreme conditions. However, in the other load cases, Newman's approximation is seen to provide satisfactory results with respect to the surge response of the OO-Star.

The standard deviation of the heave motion using Newman's approximation agrees well with the values using the full QTF. The largest difference between the two methods is only 0.02 m for the INO WINDMOOR and 0.01 m for the OO-Star. Based on these findings, the accuracy of Newman's approximation is satisfactory for the heave motion.

The differences between Newman's approximation and the full QTF regarding the pitch response are generally insignificant. The largest differences are again seen for the more severe sea states where the wave-induced response is governing. For the INO WINDMOOR, the most significant difference in the standard deviation is approximately 2%, corresponding to 0.03 degrees. The most significant difference for the OO-Star is 8%, corresponding to 0.1 degrees. Even though Newman's approximation significantly underestimates the pitch resonant response for the OO-Star in extreme conditions, it has a negligible effect on the total pitch response as the wave frequency response and the low-frequency induced wind response is the dominating contribution to the total pitch response.

9.2 Aspects of the Motion Response

This section will discuss the importance of the motion response concerning the tower loads, mooring line tension and fatigue damage.

The surge response is larger for the OO-Star floater for all load cases. As previously discussed, this is mainly due to the lower pretension of the mooring system. A larger surge response does not necessarily need to have a negative effect on the system. The maximum mooring line tension and fatigue damage of the different mooring line segments are dependent on the surge response. Therefore, it is important to consider how the surge response affects these aspects. As previously discussed, it is advantageous with a low pretension of the mooring system as a high pretension result in larger maximum mooring line tension. The mooring line tension is also directly connected with the fatigue damage of the fairlead and the different mooring line segments. Therefore, the pretension of the mooring lines and the corresponding mean offset of the OO-Star is beneficial concerning the discussed aspects.

The standard deviation of the heave motion is found to be 20-25% larger for the INO WINDMOOR for the different load cases. As previously discussed, this significantly impacts the axial loads in the tower base and tower top. In operational condition at rated wind speed, the axial loads at the tower base for the INO WINDMOOR are approximately 43% larger compared to the OO-Star. The significant difference in the axial loads is also connected with the tower's location on an off-centre column in the INO WINDMOOR floater, which results in larger axial forces due to the pitch motion. The larger heave motion of the INO WINDMOOR combined with the tower's location shows that the OO-Star floater is favourable concerning the tower axial loads and hence, the fatigue damage of the tower. Furthermore, it is found that the heave motion has an insignificant impact

on the mooring line tension of the two FWTs.

In contrast to surge and heave, there is no clear trend in the dynamic pitch response between the different load cases. The largest difference between the two FWTs concerning the dynamic pitch response is 13% in operational conditions at cut-out wind speed. As the pitch response is the governing contribution to the tower fore-aft bending moment, it is important to consider how the pitch motion of the two FWTs affects the bending moment of the tower base. It is found that the OO-Star floater experiences a lower bending moment at both the tower base and top for all load cases, except for LC1.1, where the pitch response between the two FWTs is approximately equal. This indicates that the fore-aft bending moment does not necessarily follow the same trend as the pitch response. This is again connected with the fact that the tower on the INO WINDMOOR is located on an off-centre column, resulting in larger local motions of the tower even though the global rigid body pitch response is equal for the FWTs. Based on these findings, it is found that placing the tower on a centre column is advantageous for the tower fore-aft bending.
Considering the electrical generator output of the two FWTs, it is found that the mean electrical generator output is 0.45% larger for the INO WINDMOOR at rated wind speed. As previously discussed, the electrical power output is dependent on the pitch motion of the FWTs. Therefore, the INO WINDMOOR is beneficial with respect to the power production as the pitch response is smaller for rated wind speed. It should be noted that the OO-Star has a larger electrical power output at cut-out wind speed. However, the probability of occurrence for this wind condition is significantly smaller than for the rated wind speed, making it irrelevant during 1-year of power production.

9.3 Uncertainties in Fatigue Assessment of FWTs

This section will discuss the approach used for long term fatigue damage assessment in this master's thesis.

First of all, it should be noted that the primary purpose of the fatigue damage assessment is to compare and investigate differences in the expected lifetime of different components between the two FWT concepts. Therefore, the traditional fatigue analysis method as proposed by DNV, where the wave-scatter diagram is divided into blocks, is used. Generally, this method is regarded as a conservative method, where only a single sea state is to be representative of all sea states within the block. Additionally, the probability of occurrence for all sea states in the block is lumped to the selected sea state, leading to overestimating the fatigue damage. Another aspect is that this method does not consider the effect of wind. However, this thesis used a simple lumping process to determine the corresponding wind velocities. With this in mind, uncertainties in the accuracy of the fatigue damage are expected. Moreover, the method used is assumed adequate for a comparative study on fatigue damage between the two FWTs.

Today, several different lumping methods have been proposed for fatigue damage assessment of offshore wind turbines. However, a common practice for all these methods is that they inherit both advantages and disadvantages for specific areas. Such as fatigue damage assessment by using block lumping methods for FOWTs, where the main challenge is to account for wind-wave correlation, while other methods do not consider the structural dynamics. Furthermore, in the absence of recommendations and guidelines from design standards, there are still uncertainties connected with how to assess the fatigue damage of FWTs properly.

10 Conclusion and Recommendations for Further Work

10.1 Conclusion

This master's thesis had the overall target to provide insight to the influence of semi-submersible features on a selected wind turbine's operation and extreme-weather behaviour and evaluate the applicability of Newman's approximation compared to a full QTF. The two selected floaters were the INO WINDMOOR and OO-Star, both supporting the 12 MW WINDMOOR turbine. The upscaled OO-Star floater gave satisfactory results concerning system behaviour and performance. The numerical models have been successfully verified through results obtained from the frequency-domain analysis, wind turbine performance tests and free decay tests in SIMA.

The main findings in the master's thesis are summarised in the following:

- Newman's approximation generally underestimates the surge, heave, and pitch resonant response with respect to the full QTF. The deviations between the two methods increase as the sea state increases. The most significant difference in the standard deviation is found in the extreme load case in surge and pitch for the OO-Star, where Newman's approximation underestimates the surge and pitch response by approximately 15% and 8%, respectively. In general, the largest deviations between Newman's approximation and the full QTF is seen for the OO-Star.
- The OO-Star experiences the most significant motions in surge, which is due to the low pretension of the mooring lines. In heave, the INO WINDMOOR experiences a 20-25% higher response, and the deviation of the heave response between the two FWTs is quite consistent for all the load cases. The OO-Star is subjected to the largest mean pitch offset for all load cases, except for the cut-out wind speed with operational turbine. For the dynamic pitch motion, the OO-Star experiences the most significant response at rated wind speed in both operational and parked conditions. This also applies for the parked condition at cut-out wind speed, while the INO WINDMOOR experiences a larger pitch response in operational conditions at cut-out wind speed and in extreme conditions.
- The results showed that the FWTs experience larger axial loads and bending moments when the turbine is operational. The tower loads were generally most significant for the INO WINDMOOR. In operational conditions at rated wind speed, which is the load case where the deviation of the axial force in the tower base is most significant, the axial loads at the tower base for the INO WINDMOOR are approximately 43% larger compared to the OO-Star. The largest differences in the fore-aft bending moment are found in the extreme load case where the INO WINDMOOR experiences a 19% larger tower base bending moment than the OO-Star.
- The mooring line tension is directly related to the FWTs surge motion. In general, the mooring line tension increases with increasing significant wave height. In all loads cases, the INO WINDMOOR experiences higher mooring line tension than the OO-Star, with a 32.8% higher dynamic mooring line tension in extreme conditions. The pretension used for the INO WINDMOOR is significantly larger than for the OO-Star, hence the larger mooring line tension for the INO WINDMOOR.
- The electrical generator output is larger for the INO WINDMOOR at rated wind speed, while the OO-Star has the largest electrical generator output for cut-out wind speed. As the probability of occurrence for a condition with rated wind speed is significantly larger for a condition with cut-out wind speed, the INO WINDMOOR is advantageous concerning the power output. However, the electrical generator output difference between the INO WINDMOOR and OO-Star is only 412 MW during 1-year power production.
- The short term fatigue damage increases with increasing wind and waves for both FWTs. In general, the fatigue damage tends to increase with increasing wave height and decreasing wave period. However, the highest fatigue damage is governed by the longest wave periods for the mooring line segments at wind speeds above rated wind speed. For the fatigue damage

estimation of the tower, a simulation length of 1-h was found sufficient. A 3-h simulation length is recommended for the mooring line segments to capture the slowly-varying response. The tower base fatigue damage is dependent on the axial stress, where below rated wind speed the greatest contribution is from the low frequency induced response, while for above rated wind speed the pitch resonance is dominating the axial stress, and hence the fatigue damage. The INO WINDMOOR experiences higher 20-year fatigue damage at all tower segments, fairlead and the polyester line, while the OO-Star experiences more significant fatigue damage in the bottom chain. For the fairlead, the 20-year fatigue damage is 78% larger for the INO WINDMOOR.

10.2 Further Work

Based on the master's thesis work and results from the numerical simulations, suggestions and improvements for further work are presented.

- Simulations considering wind-wave misalignment should be performed to further complete the comparative study between the two FWTs, where this can have an important influence on the responses. Additionally, this should also be implemented in the fatigue damage assessment.
- For each H_s in the design load cases, one should perform simulations by selecting two or three T_p values to understand the sensitivity towards the wave period for the two FWT concepts.
- The fatigue damage should be assessed using different methods such as the equivalent damage method (EDM) or spectral method and compared with the method proposed by DNV. Additionally, it could be interesting to see the sensitivity of the block lumping strategy by selecting larger and smaller block dimensions.
- To further increase the accuracy of the fatigue damage results, running multiple seeds should be implemented for each condition. To obtain a more converging behaviour, it is also advised to calculate the fatigue damage using 3-hour simulations. Additionally, one should also include multiple seeds for the incoming wind as well.
- For floating offshore wind development in the North Sea, it would be interesting to investigate the possibility of setting up a two-peaked power spectrum to account for both wind and swell, as proposed by Torsethaugen.
- One should perform the time-domain simulations only considering first-order wave loads and then compare with the results using Newman's approximation and a full QTF to see the effect of implementing second-order contributions to the analyses.
- One should investigate the effect of using the power scaling rule for the up-scaling procedure of the OO-Star. It could be interesting to see how this scaling factor would affect the FWT compared to using the ratio of the turbine masses to obtain the scaling parameter, as was done in this thesis.

Bibliography

4Coffshore (2021). *WindFloat 1 prototype*. URL: https://www.4coffshore.com/windfarms/portugal/windfloat-1-prototype-(wf1)-portugal-pt01.html.

Atcheson, Mairéad (2016). *Floating Offshore Wind Energy : The Next Generation of Wind Energy*. eng. Cham.

Bachynski, Erin (2021a). 'Basic aerodynamics for wind turbines'. In: *Lecture notes NTNU*.

— (2021b). *Basic Concepts in Wind Turbine Controller*. Lecture note, Integrated Dynamic analyses of Wind Turbines , NTNU.

— (2021c). 'Course Project: Integrated Dynamic Analysis of Wind Turbines Fall 2021'. Unpublished.

— (2021d). *Lecture 3*. Lecture slide, Integrated Dynamic analyses of Wind Turbines , NTNU.

Berthelsen, Ole and Trude Christine Nagell (June 2020). *Norway opens offshore areas for wind power*. URL: https://www.regjeringen.no/en/aktuelt/norway-opens-offshore-areas-for-wind-power/id2705986/.

Borg, Michael and Henrik Bredmose (2015). *D4.4 – Overview of the numerical models used in the consortium and their qualification*.

Bosch, Jonathan, Iain Staffell and Adam D. Hawkes (2018). 'Temporally explicit and spatially resolved global offshore wind energy potentials'. In: *Energy* 163, pp. 766–781. ISSN: 0360-5442. DOI: https://doi.org/10.1016/j.energy.2018.08.153. URL: https://www.sciencedirect.com/science/article/pii/S036054421831689X.

Bussemakers, Pieter Jaime Matthijs (July 2020). *Validation of aero-hydro-servo-elastic load and motion simulations in BHawC/OrcaFlex for the Hywind Scotland floating offshore wind farm*. URL: file:///C:/Users/stian/Downloads/Thesis_Report_Final_PJMB_handin.pdf.

Cao, Qun et al. (2020). 'Second-order responses of a conceptual semi-submersible 10 MW wind turbine using full quadratic transfer functions'. In: *Renewable Energy* 153, pp. 653–668. ISSN: 0960-1481. DOI: https://doi.org/10.1016/j.renene.2020.02.030. URL: https://www.sciencedirect.com/science/article/pii/S0960148120302160.

Chain, Sotra Anchor & (2021). *Sotra Anchor & Chain Handbook*. URL: https://www.sotra.net/wp-content/uploads/2021/11/Catalouge-8.pdf.

Chakrabarti, SK. (1987). *Hydrodynamics of offshore structures*. Springer Verlag.

Chang, A. et al. (Jan. 2014). 'Wave-scatter lumping strategies for fatigue damage assessment'. In: *Proceedings of the 11th (2014) Pacific/Asia Offshore Mechanics Symposium, PACOMS 2014*, pp. 83–89.

Cheynet, Etienne (2020). *Offshore wind potential in Norway and the North Sea*. URL: https://www.uib.no/sites/w3.uib.no/files/attachments/presentation_cheynet_brazil.pdf.

Commission, European (May 2022). *REPowerEU: A plan to rapidly reduce dependence on Russian fossil fuels and fast forward the green transition*. URL: https://ec.europa.eu/commission/presscorner/detail/en/IP_22_3131.

Cordle, A. and J. Jonkman (Oct. 2011). 'State of the Art in Floating Wind Turbine Design Tools'. In: *NREL/CP-5000-50543*. National Renewable energy laboratory.

CORPORATION, TODA (2021). *Sakiyama 2 MW Floating Offshore Wind Turbine*. URL: https://www.toda.co.jp/business/ecology/special/pdf/sakiyama2mw_e.pdf.

Davey, Keith et al. (2020). 'The breaking of geometric similarity'. In: *International Journal of Mechanical Sciences* 187, p. 105925. ISSN: 0020-7403. DOI: https://doi.org/10.1016/j.ijmecsci.2020.105925. URL: https://www.sciencedirect.com/science/article/pii/S0020740320312558.

DNV (Apr. 2010a). *DNV-RP-C203: Fatigue Design of Offshore Steel Structures*.

— (Oct. 2010b). *DNV-RP-F204 Riser Fatigue*.

— (Oct. 2010c). *DNV-RP-F205 Global Performance Analysis of Deepwater Floating Structures*.

— (Apr. 2014). 'Environmental conditions and environmental loads'. In: *Recommended practice DNV-RP-C205*.

— (July 2015). *DNVGL-OS-E302 Offshore mooring chain*.

— (Nov. 2016). 'Loads and site conditions for wind turbines'. In: *DNVGL-ST-0437*.

— (Jan. 2017). *SESAM USER MANUAL WADAM v9.3*.

— (July 2018a). *DNVGL-OS-E301 Position mooring*.

— (July 2018b). 'Floating wind turbine structures'. In: *DNVGL-ST-0119*.

— (Dec. 2020). *GeniE V8.0-21 User Documentation*.

DNV (Oct. 2021). *HydroD D5.4.0 User Manual*.

— (Apr. 2022). *The Ukraine War Will NOT Derail Europe's Energy Transition*. URL: https://www.dnv.com/feature/the-ukraine-war-will-not-derail-europes-energy-transition.html.

EDP, Energias de Portugal (2018). *WindFloat Atlantic*. URL: https://www.edp.com/en/innovation/windfloat.

Energidepartementet, Olje- og (2020). *Opner områder for havvind i Noreg*. URL: https://www.regjeringen.no/no/dokumentarkiv/regjeringen-solberg/aktuelt-regjeringen-solberg/oed/pressemeldinger/2020/opner-omrader/id2705986/.

Energy, DTU Wind (2019). *Offshore wind resource map*. URL: https://s3-eu-west-1.amazonaws.com/globalwindatlas3/HR_posters/ws_OFFSHORE.pdf.

Engebretsen, Espen, Zhiyuan Pan and Nuno Fonseca (Aug. 2020). 'Second-Order Difference-Frequency Loads on FPSOs by Full QTF and Relevant Approximations'. In: DOI: 10.1115/OMAE2020-18132.

Equinor (2021a). *Hywind Demo*. URL: https://www.equinor.com/en/what-we-do/floating-wind.html.

— (2021b). *Hywind Scotland*. URL: https://www.equinor.com/en/what-we-do/floating-wind.html.

Explorer, The (2020). *Floating offshore wind turbines*. URL: https://www.theexplorer.no/solutions/offshore-floating-wind-turbines/.

Faltinsen, O. M. (1993). *Sea Loads on Ships and Offshore Structures*. Cambridge University Press.

Friis-Møller, Mikkel (2021). *Structural formulation*. DTU Wind Energy.

Greco, Marilena (May 2019). *TMR 4215: Sea Loads*.

Hanssen, Finn-Christian Wickmann, Roberto Bruschi and E. Pettersen (Jan. 2013). 'Aspects of the mean surge drift force for single-point moored vessel'. In: *Proceedings of the International Offshore and Polar Engineering Conference*, pp. 984–991.

Hauteclocque, Guillaume de et al. (July 2012). 'Review of Approximations to Evaluate Second-Order Low-Frequency Load'. In: vol. 1. DOI: 10.1115/OMAE2012-83407.

Havvind, Norsk (May 2022). *Kraftfull satsing på havvind*. URL: https://norskhavvind.no/kraftfull-satsing-pa-havvind/.

Inocean (Oct. 2021). *INO 12MW Floating Offshore Wind Turbine*.

IRENA (2019). *Offshore Renewables: An action agenda for deployment*. Tech. rep. The International Renewable Energy Agency, Abu Dhabi.

— (2022). *Energy Transition*. URL: https://www.irena.org/energytransition.

Jamieson, Peter (2011). 'Upscaling of Wind Turbine Systems'. In: *Innovation in Wind Turbine Design*. Chap. 4, pp. 75–104. ISBN: 9781119975441. DOI: https://doi.org/10.1002/9781119975441.ch4. eprint: https://onlinelibrary.wiley.com/doi/pdf/10.1002/9781119975441.ch4. URL: https://onlinelibrary.wiley.com/doi/abs/10.1002/9781119975441.ch4.

Johannessen, Kenneth, Trond Stokka Meling and Sverre K. Haver (2002). 'Joint Distribution For Wind And Waves In the Northern North Sea'. In: *International Journal of Offshore and Polar Engineering* 12.

Jonkman, B.J. (Aug. 2009). *TurbSim User's Guide: Version 1.50*. NREL.

Katsikogiannis, George, John Marius Hegseth and Erin E. Bachynski-Polić (2022). 'Application of a lumping method for fatigue design of monopile-based wind turbines using fully coupled and simplified models'. In: *Applied Ocean Research* 120, p. 102998. ISSN: 0141-1187. DOI: https://doi.org/10.1016/j.apor.2021.102998. URL: https://www.sciencedirect.com/science/article/pii/S0141118721004600.

Kikuchi, Yuka and Takeshi Ishihara (Oct. 2019). 'Upscaling and levelized cost of energy for offshore wind turbines supported by semi-submersible floating platforms'. In: *Journal of Physics: Conference Series* 1356, p. 012033. DOI: 10.1088/1742-6596/1356/1/012033.

Koochekali, Alahyar and Michael Muskulus (Oct. 2019). 'Spatial met-ocean data analysis for the North Sea using copulas: application in lumping of offshore wind turbine fatigue load cases'. In: *Journal of Physics: Conference Series* 1356, p. 012042. DOI: 10.1088/1742-6596/1356/1/012042.

Kristiansen, Mette Bischoff (July 2018). *Aerodynamic models*. URL: https://www.hawc2.dk/hawc2-info/aerodynamic-model.

— (2021). *Welcome to HAWC2*. URL: https://www.hawc2.dk/hawc2-info.

Kvittem, Marit I. (2014). 'Modelling and response analysis for fatigue design of a semi-submersible wind turbine'. In.

Kvittem, Marit I. and Torgeir Moan (2015). 'Time domain analysis procedures for fatigue assessment of a semi-submersible wind turbine'. In: *Marine Structures* 40, pp. 38–59. ISSN: 0951-8339.

DOI: https://doi.org/10.1016/j.marstruc.2014.10.009. URL: https://www.sciencedirect.com/science/article/pii/S0951833914000756.

Kvittem, Marit I. et al. (June 2018). 'CALIBRATION OF HYDRODYNAMIC COEFFICIENTS FOR A SEMI-SUBMERSIBLE 10 MW WIND TURBINE'. In: *Proceedings of the ASME 2018 37th International Conference on Ocean, Offshore and Arctic Engineering*.

Laboratory, National Renewable Energy (2021). *Introduction*. URL: https://openfast-wave-stretching.readthedocs.io/en/f-wave_stretching/source/user/hydrodyn/introduction.html.

Larsen, C.M (2015). *Marine Dynamics*. Department of Marine Technology.

Lee, Joyce and Feng Zhao (Sept. 2021). *Global offshore wind report 2021*. URL: https://gwec.net/wp-content/uploads/2021/09/GWEC-offshore-wind-2021-updated-1.pdf.

Leimeister, Mareike et al. (2016). 'Rational Upscaling of a Semi-submersible Floating Platform Supporting a Wind Turbine'. In: *Energy Procedia* 94. 13th Deep Sea Offshore Wind RD Conference, EERA DeepWind'2016, pp. 434–442. ISSN: 1876-6102. DOI: https://doi.org/10.1016/j.egypro.2016.09.212. URL: https://www.sciencedirect.com/science/article/pii/S1876610216308815.

Li, Haoran et al. (June 2017). 'Short-term fatigue analysis for tower base of a spar-type wind turbine under stochastic wind-wave loads'. In: *International Journal of Naval Architecture and Ocean Engineering* 10. DOI: 10.1016/j.ijnaoe.2017.05.003.

Li, Lin, Zhen Gao and Torgeir Moan (June 2013). 'Joint Environmental Data at Five European Offshore Sites for Design of Combined Wind and Wave Energy Devices'. In: *Journal of Offshore Mechanics and Arctic Engineering* 137.

Ma, Kai-Tung et al. (2019). *Mooring System Engineering for Offshore Structures*. eng. San Diego: Elsevier Science Technology. ISBN: 9780128185513.

Manwell, J. F., J. G. McGowan and A. L. Rogers (2009). 'Aerodynamics of Wind Turbines'. In: *Wind Energy Explained*. John Wiley & Sons, Ltd. Chap. 3, pp. 91–155. ISBN: 9781119994367. DOI: https://doi.org/10.1002/9781119994367.ch3. eprint: https://onlinelibrary.wiley.com/doi/pdf/10.1002/9781119994367.ch3. URL: https://onlinelibrary.wiley.com/doi/abs/10.1002/9781119994367.ch3.

MARINTEK and Det Norske Veritas (2010). *Sesam User Manual, DeepC Theory*.

Møller, Mikkel F. (July 2018). *Hydrodynamic model*. URL: https://www.hawc2.dk/hawc2-info/hydrodynamic-model.

Naess, Arvid and Torgeir Moan (2012). 'Dynamic Load Effects for Design Checks'. In: *Stochastic Dynamics of Marine Structures*. Cambridge University Press, pp. 287–319. DOI: 10.1017/CBO9781139021364.014.

Newman, John Nicklas (1974). *Second-order, Slowly-varying Forces on Vessels in Irregular Waves*.

NREL, National Renewable Energy Laboratory (2021). *Introduction*. URL: https://openfast.readthedocs.io/en/main/source/user/aerodyn/introduction.html.

Nuno Fonseca, Erin Bachynski (Nov. 2018). *LFCS Review report – Environmental loads*. SINTEF.

Olsen, Dr.techn. Olav (Apr. 2020). *Breakthrough for OO-Star Wind Floater*. URL: https://www.olavolsen.no/no/forretningsomrader/fornybar-energi.

Orcina (2021a). *Line theory: Overview*.

— (2021b). *Modelling introduction*.

— (2021c). *Turbines*.

Pan, Zhiyuan, Torgeir Vada and Finn-Christian Wickmann Hanssen (June 2013). 'A Mesh Dependency Study for the Mean Drift Forces by Pressure Integration'. In: *Proceedings of the International Conference on Offshore Mechanics and Arctic Engineering - OMAE*.

Regjeringen.no (May 2022). *Kraftfull satsing på havvind*. URL: https://www.regjeringen.no/no/aktuelt/kraftfull-satsing-pa-havvind/id2912297/.

SESAM USER MANUAL WADAM v8.1 (Jan. 2010). DNV.

Sheehan, John M. et al. (Nov. 2005). 'Characterizing the Wave Environment in the Fatigue Analysis of Flexible Risers'. In: *Journal of Offshore Mechanics and Arctic Engineering* 128.2, pp. 108–118. ISSN: 0892-7219. DOI: 10.1115/1.2185129. URL: https://doi.org/10.1115/1.2185129.

Sieros, Georgios et al. (Jan. 2012). 'Upscaling wind turbines: Theoretical and practical aspects and their impact on the cost of energy'. In: *Wind Energy* 15, pp. 3–17. DOI: 10.1002/we.527.

SINTEF-Ocean (Apr. 2021a). *RIFLEX 4.20.2 Theory Manual*. Version 4.20.2.

— (Apr. 2021b). *SIMO Theory Manual*. Version 4.20.2. SINTEF Ocean.

Song, Xiancang et al. (2016). 'An innovative block partition and equivalence method of the wave scatter diagram for offshore structural fatigue assessment'. English. In: *Applied Ocean Research* 60.C, pp. 12–28. DOI: 10.1016/j.apor.2016.08.005.

Souza, Carlos Eduardo and Erin Bachynski-Polić (May 2019). 'Changes in surge and pitch decay periods of floating wind turbines for varying wind speed'. In: *Ocean Engineering* 180, pp. 223–237. DOI: 10.1016/j.oceaneng.2019.02.075.

Souza, Carlos Eduardo et al. (Jan. 2021). *Definition of the INO WINDMOOR 12 MW base case floating wind turbine*. Tech. rep. DOI: 10.13140/RG.2.2.32947.25121.

Thies, Philipp R. et al. (2014). 'Mooring line fatigue damage evaluation for floating marine energy converters: Field measurements and prediction'. In: *Renewable Energy* 63, pp. 133–144. ISSN: 0960-1481. DOI: https://doi.org/10.1016/j.renene.2013.08.050. URL: https://www.sciencedirect.com/science/article/pii/S0960148113004667.

Tian, Jinfang et al. (2022). 'Global low-carbon energy transition in the post-COVID-19 era'. In: *Applied Energy* 307, p. 118205. ISSN: 0306-2619. DOI: https://doi.org/10.1016/j.apenergy.2021.118205. URL: https://www.sciencedirect.com/science/article/pii/S0306261921014720.

Tony Burton Nick Jenkins, David Sharpe and Ervin Bossanyi (2011). 'Aerodynamics of Horizontal Axis Wind Turbines'. In: *Wind Energy Handbook*. Chap. 3, pp. 39–136. ISBN: 9781119992714. DOI: https://doi.org/10.1002/9781119992714.ch3. eprint: https://onlinelibrary.wiley.com/doi/pdf/10.1002/9781119992714.ch3. URL: https://onlinelibrary.wiley.com/doi/abs/10.1002/9781119992714.ch3.

Vargas, Pedro, Teh-Min Hsu and Wai Lee (Jan. 2004). 'Stress Concentration Factors for Stud-Less Mooring Chain Links in Fairleads'. In: DOI: 10.1115/OMAE2004-51376.

Viselli, Anthony M., Andrew J. Goupee and Habib J. Dagher (May 2015). 'Model Test of a 1:8-Scale Floating Wind Turbine Offshore in the Gulf of Maine1'. In: *Journal of Offshore Mechanics and Arctic Engineering* 137.4. 041901. ISSN: 0892-7219. DOI: 10.1115/1.4030381. eprint: https://asmedigitalcollection.asme.org/offshoremechanics/article-pdf/137/4/041901/6402654/omae_137_04_041901.pdf. URL: https://doi.org/10.1115/1.4030381.

Wind energy generation systems - Part 1: Design requirements (Jan. 2019). IEC - International Electrotechnical Commission.

Xu, Kun et al. (2019). 'Effect of wave nonlinearity on fatigue damage and extreme responses of a semi-submersible floating wind turbine'. In: *Applied Ocean Research* 91, p. 101879. ISSN: 0141-1187. DOI: https://doi.org/10.1016/j.apor.2019.101879. URL: https://www.sciencedirect.com/science/article/pii/S0141118719303773.

Yu, Wei, Kolja Muller and Frank Lemmer (Apr. 2018). *Qualification of innovative floating substructures for 10MW wind turbines and water depths greater than 50m*. URL: http://lifes50plus.eu/wp-content/uploads/2018/04/GA_640741_LIFES50_D4.2.pdf?fbclid=IwAR03azT5GosLoouOokDez-2OXCMs2ZQnmA56mH9A0Nyak9Yctt5Qqx1cMf8.

Zhang, Lixian et al. (2020). 'Second-order hydrodynamic effects on the response of three semisubmersible floating offshore wind turbines'. In: *Ocean Engineering* 207, p. 107371. ISSN: 0029-8018. DOI: https://doi.org/10.1016/j.oceaneng.2020.107371. URL: https://www.sciencedirect.com/science/article/pii/S0029801820304029.

Appendix

A Frequency Domain

A.1 Added Mass and Damping Coefficients

A.1.1 INO WINDMOOR

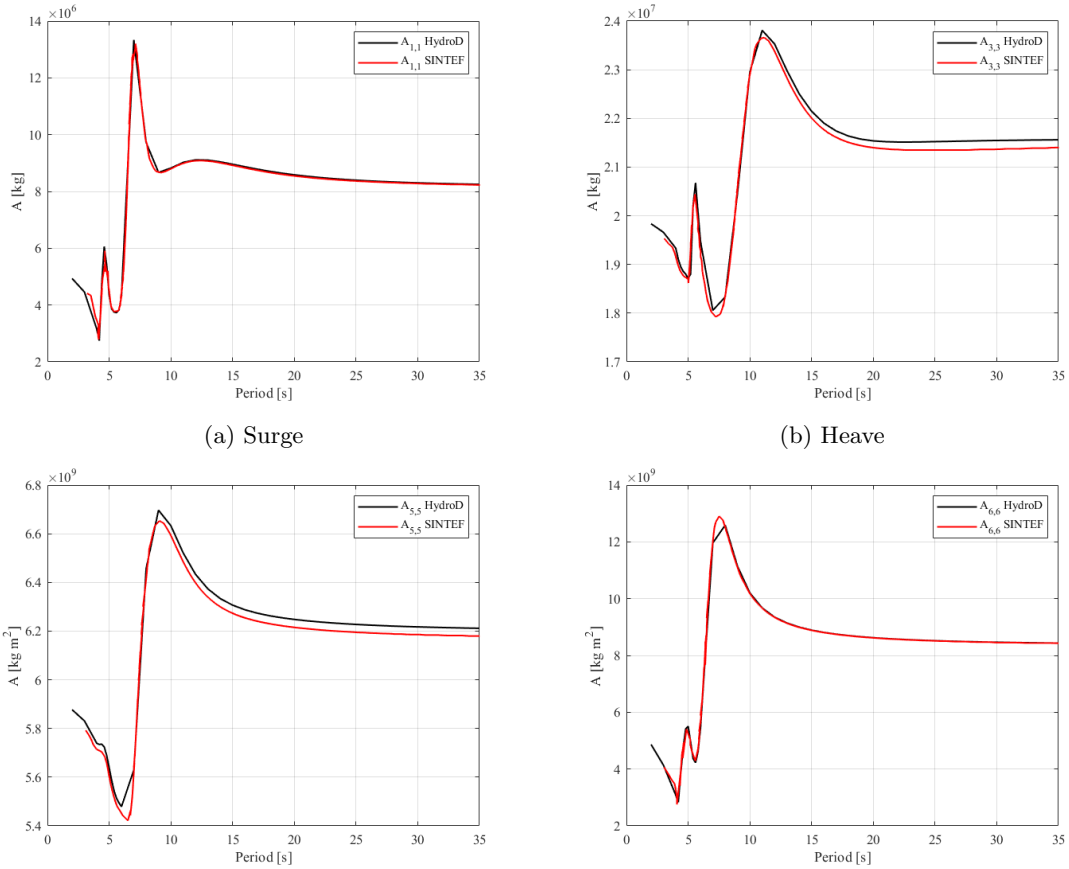

(a) Surge

(b) Heave

(c) Pitch

(d) Yaw

Figure A.1: Validation of added mass coefficients from HydroD against SINTEF.

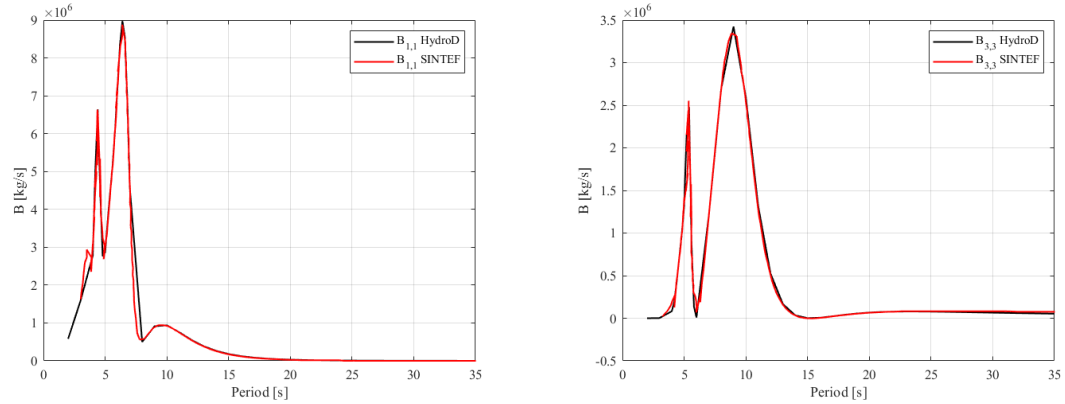

(a) Surge

(b) Heave

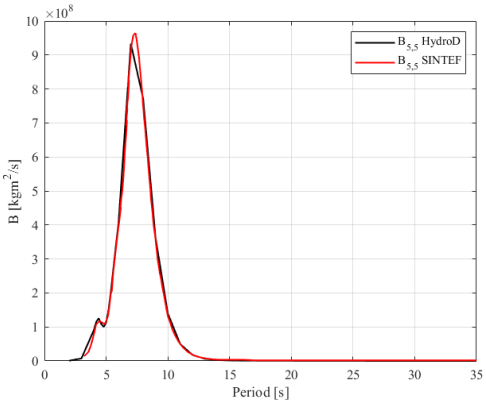

(c) Pitch

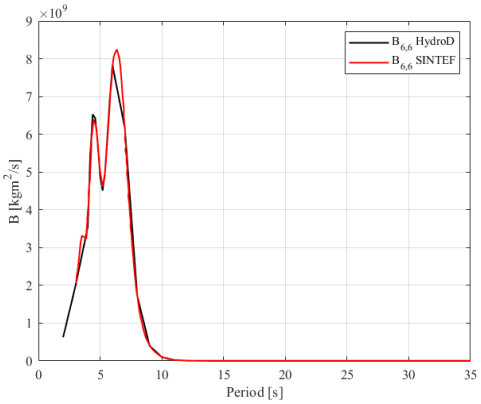

(d) Yaw

Figure A.2: Validation of damping coefficients from HydroD against SINTEF.

A.1.2 OO-Star

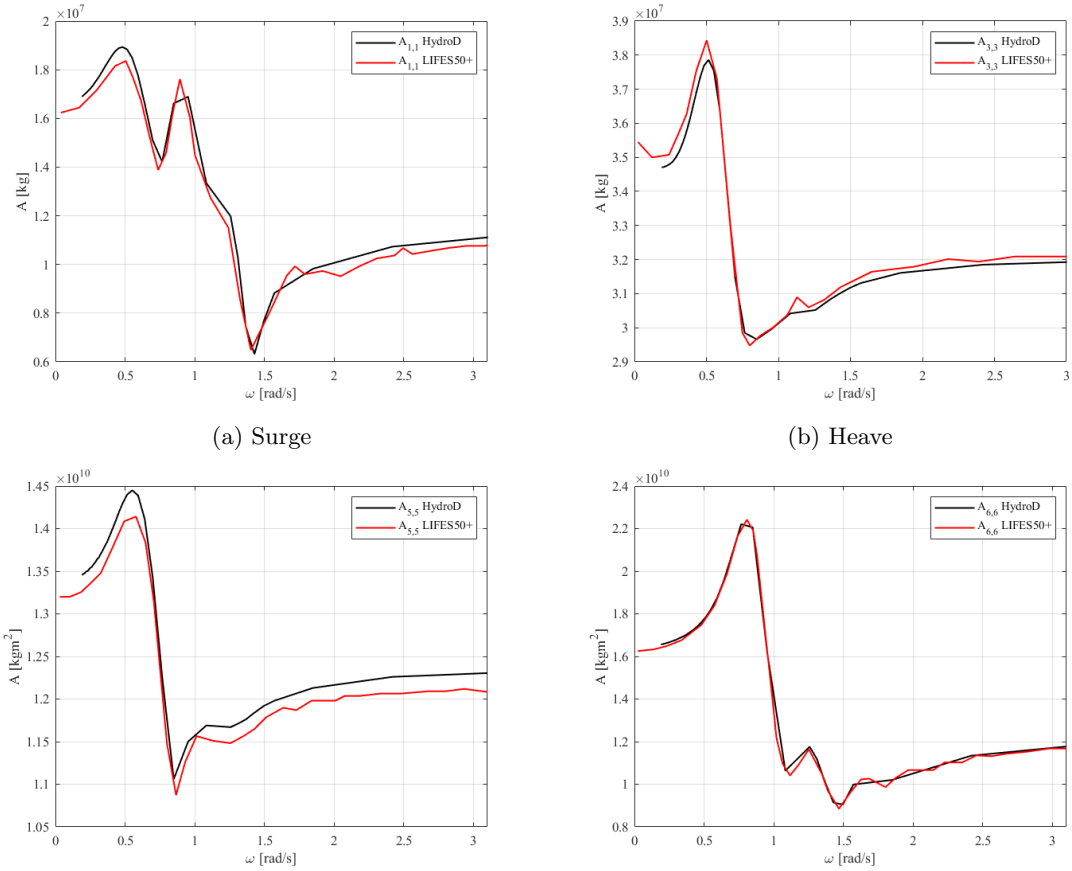

(a) Surge

(b) Heave

(c) Pitch

(d) Yaw

Figure A.3: Verification of added mass coefficients from HydroD against LIFES50+.

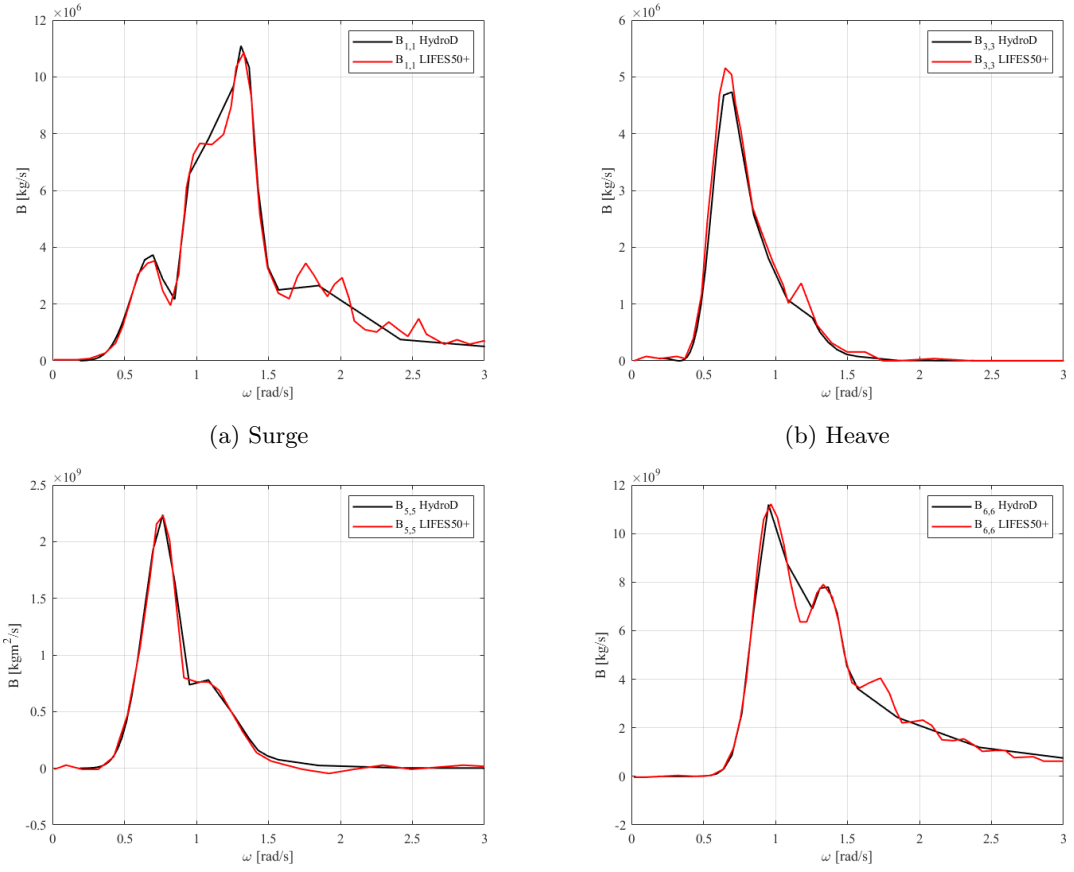

(a) Surge

(b) Heave

(c) Pitch

(d) Yaw

Figure A.4: Verification of damping coefficients from HydroD against LIFES50+.

A.2 Difference-Frequency QTF Contour

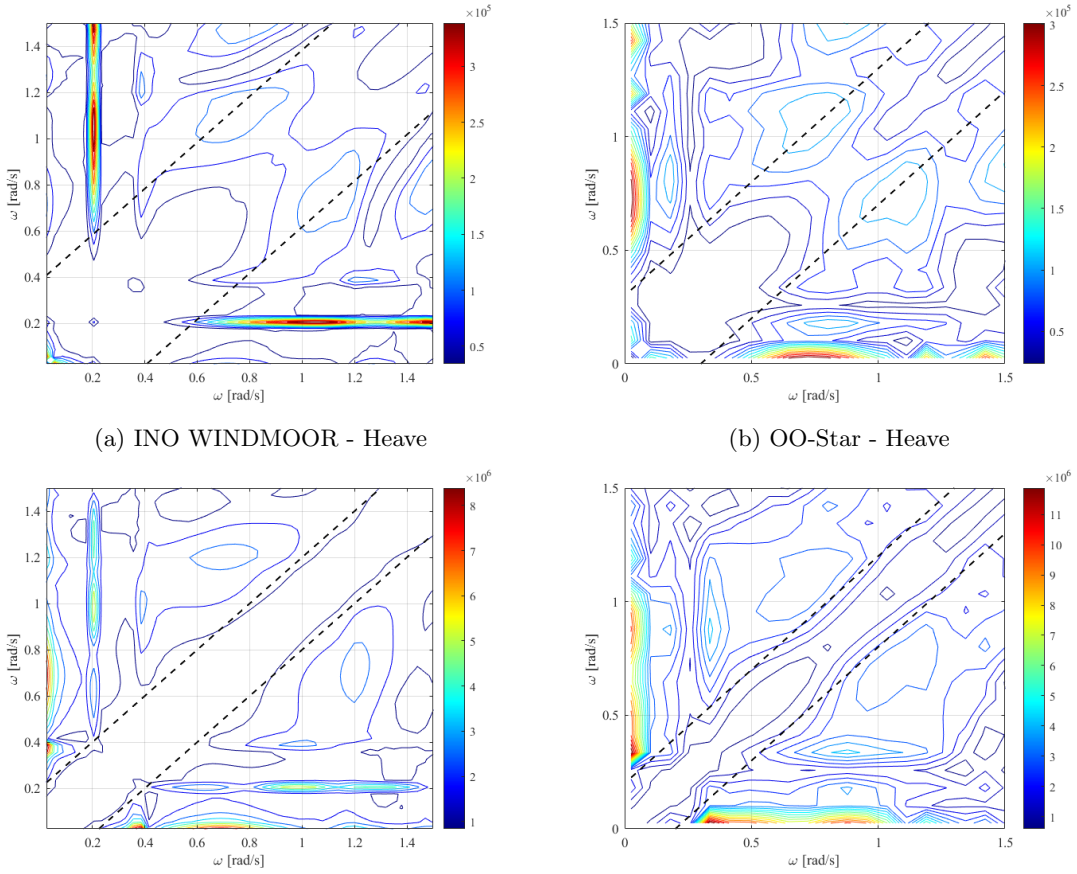

(a) INO WINDMOOR - Heave

(b) OO-Star - Heave

(c) INO WINDMOOR- Pitch

(d) OO-Star - Pitch

Figure A.5: Difference-Frequency QTF Contour in Heave and Pitch.

B Scatter diagram for Utsira Nord

Hs\Tp	0-1	1-2	2-3	3-4	4-5	5-6	6-7	7-8	8-9	9-10	10-11	11-12	12-13	13-14	14-15	15-16	16-17	17-18	18-19	19-20	20-21	21-22	
0-0,5	0	0	10	107	581	439	319	330	373	289	173	90	66	34	29	15	10	3	4	1	1	0	2874
0,5-1	0	0	25	739	2821	4813	4569	3552	3097	2703	2125	1405	893	424	218	141	80	22	13	1	2	0	27643
1-1,5	0	0	0	103	2297	5320	6403	5422	4609	3789	2769	2341	1730	968	469	278	144	26	17	5	5	1	36696
1,5-2	0	0	0	1	375	3651	6240	5454	3799	3278	2678	1913	1561	1117	572	339	135	53	23	3	1	1	31194
2-2,5	0	0	0	0	33	889	4487	5616	3980	2488	2112	1679	1235	886	593	330	157	39	27	1	0	0	24552
2,5-3	0	0	0	0	1	122	2013	4406	4389	2503	1457	1252	928	602	457	294	150	40	19	1	1	0	18635
3-3,5	0	0	0	0	0	9	504	2524	4076	2762	1241	786	689	420	311	227	138	39	29	1	1	0	13757
3,5-4	0	0	0	0	0	0	78	1016	2857	2736	1314	646	427	285	150	120	95	45	22	4	1	0	9796
4-4,5	0	0	0	0	0	0	1	217	1625	2267	1465	517	319	215	106	73	49	30	16	0	1	0	6901
4,5-5	0	0	0	0	0	0	0	34	579	1510	1412	634	245	131	83	54	23	19	13	1	0	0	4738
5-5,5	0	0	0	0	0	0	0	5	229	857	1109	721	179	102	70	27	15	9	7	0	0	0	3330
5,5-6	0	0	0	0	0	0	0	0	41	392	751	682	240	91	59	26	12	16	6	0	0	0	2316
6-6,5	0	0	0	0	0	0	0	0	10	154	442	495	250	74	41	24	6	7	5	0	0	0	1508
6,5-7	0	0	0	0	0	0	0	0	1	57	215	300	250	94	36	12	5	2	2	0	0	0	974
7-7,5	0	0	0	0	0	0	0	0	0	15	88	176	214	69	31	12	4	5	1	0	0	0	615
7,5-8	0	0	0	0	0	0	0	0	0	1	39	89	129	76	22	8	2	4	2	0	0	0	372
8-8,5	0	0	0	0	0	0	0	0	0	0	18	54	78	59	24	11	4	1	3	0	0	0	252
8,5-9	0	0	0	0	0	0	0	0	0	0	2	19	21	60	24	9	4	3	1	0	0	0	143
9-9,5	0	0	0	0	0	0	0	0	0	0	0	5	17	36	20	8	6	2	1	0	0	0	95
9,5-10	0	0	0	0	0	0	0	0	0	0	0	1	3	21	13	5	1	1	1	0	0	0	46
10-10,5	0	0	0	0	0	0	0	0	0	0	0	0	0	14	9	5	2	0	1	0	0	0	31
10,5-11	0	0	0	0	0	0	0	0	0	0	0	0	0	2	7	3	2	1	1	0	0	0	16
11-11,5	0	0	0	0	0	0	0	0	0	0	0	0	0	1	4	5	0	0	0	0	0	0	10
11,5-12	0	0	0	0	0	0	0	0	0	0	0	0	0	1	1	3	0	1	0	0	0	0	6
12-12,5	0	0	0	0	0	0	0	0	0	0	0	0	0	0	2	1	0	0	0	0	0	0	3
12,5-13	0	0	0	0	0	0	0	0	0	0	0	0	0	0	1	2	1	0	0	0	0	0	4
13-13,5	0	0	0	0	0	0	0	0	0	0	0	0	0	0	0	1	0	0	0	0	0	0	1
13,5-14	0	0	0	0	0	0	0	0	0	0	0	0	0	0	0	0	0	0	0	0	0	0	0
14-14,5	0	0	0	0	0	0	0	0	0	0	0	0	0	0	1	0	0	0	0	0	0	0	1
																						sum	186509

Figure B.1: Hs-Tp scatter diagram.

Hs\w	0-1	1-2	2-3	3-4	4-5	5-6	6-7	7-8	8-9	9-10	10-11	11-12	12-13	13-14	14-15	15-16	16-17	17-18	18-19	19-20	20-21	21-22	22-23	23-24	24-25	25-26	26-27	27 -28	28-29	29-30	30-31	
0-0,5	208	515	711	704	443	213	57	22	6	0	0	0	0	0	0	0	0	0	0	0	0	0	0	0	0	0	0	0	0	0	0	2874
0,5-1	960	2903	4160	5167	5492	4293	2824	1276	404	110	34	15	4	1	0	0	0	0	0	0	0	0	0	0	0	0	0	0	0	0	0	27643
1-1,5	519	1694	2852	3871	4823	5697	5919	5256	3524	1721	591	162	43	13	3	6	1	1	0	0	0	0	0	0	0	0	0	0	0	0	0	36696
1,5-2	222	677	1192	1652	2491	3149	3700	4366	4743	4129	2859	1383	426	148	40	8	4	3	0	2	0	0	0	0	0	0	0	0	0	0	0	31194
2-2,5	91	279	465	755	1087	1487	1965	2613	3155	3503	3481	2856	1763	727	216	74	19	11	5	0	0	0	0	0	0	0	0	0	0	0	0	24552
2,5-3	25	109	189	279	458	621	884	1288	1803	2326	2570	2717	2415	1619	835	348	104	35	6	3	1	0	0	0	0	0	0	0	0	0	0	18635
3-3,5	14	31	77	122	196	272	401	593	896	1235	1555	1822	1952	1760	1447	876	346	123	33	5	1	0	0	0	0	0	0	0	0	0	0	13757
3,5-4	4	10	34	32	79	94	160	248	376	556	896	1153	1296	1265	1171	1113	737	389	133	38	8	4	0	0	0	0	0	0	0	0	0	9796
4-4,5	1	6	9	19	31	35	56	85	133	233	400	605	817	884	886	863	757	588	346	105	32	7	3	0	0	0	0	0	0	0	0	6901
4,5-5	0	3	5	3	14	12	16	39	51	117	150	281	423	614	646	643	446	494	424	230	95	25	4	1	1	1	0	0	0	0	0	4738
5-5,5	0	2	1	1	6	7	8	9	22	26	71	137	203	334	428	470	365	328	339	266	187	87	23	8	1	1	0	0	0	0	0	3330
5,5-6	2	0	2	0	3	2	2	8	7	19	20	47	80	144	251	346	299	267	210	207	200	126	61	12	1	0	0	0	0	0	0	2316
6-6,5	0	0	0	0	1	0	1	3	6	7	11	25	29	62	105	197	221	188	162	108	134	109	87	43	7	2	0	0	0	0	0	1508
6,5-7	0	1	0	0	0	0	1	0	0	2	1	6	15	26	44	76	146	131	132	72	75	84	77	50	30	4	1	0	0	0	0	974
7-7,5	0	0	0	0	0	0	0	0	0	3	3	2	4	8	19	40	55	91	98	74	49	35	51	47	29	5	1	1	0	0	0	615
7,5-8	0	0	0	0	0	0	1	0	0	0	1	1	3	3	5	9	27	44	76	40	47	23	19	24	27	18	4	0	0	0	0	372
8-8,5	0	0	0	0	0	0	0	0	0	0	0	0	0	2	1	4	16	23	29	27	35	28	17	12	27	23	6	1	0	0	1	252
8,5-9	0	0	0	0	0	0	0	0	0	0	0	0	2	0	0	0	4	11	17	19	28	17	20	6	8	4	4	3	0	0	0	143
9-9,5	0	0	0	0	0	0	0	0	0	0	0	0	0	1	0	0	2	5	4	18	13	23	16	3	4	3	2	1	0	0	0	95
9,5-10	0	0	0	0	0	0	0	0	0	0	0	0	0	0	0	0	0	1	2	6	12	10	5	3	4	1	1	0	0	1	0	46
10-10,5	0	0	0	0	0	0	0	0	0	0	0	0	0	0	0	0	0	1	0	5	1	4	10	4	2	3	0	1	0	0	0	31
10,5-11	0	0	0	0	0	0	0	0	0	0	0	0	0	0	0	0	0	0	1	0	2	2	3	4	4	0	0	0	0	0	0	16
11-11,5	0	0	0	0	0	0	0	0	0	0	0	0	0	0	0	0	0	0	0	0	0	1	2	0	3	1	2	1	0	0	0	10
11,5-12	0	0	0	0	0	0	0	0	0	0	0	0	0	0	0	0	0	0	0	0	0	1	0	1	1	1	1	1	0	0	0	6
12-12,5	0	0	0	0	0	0	0	0	0	0	0	0	0	0	0	0	0	0	0	0	0	0	0	0	2	0	1	0	0	0	0	3
12,5-13	0	0	0	0	0	0	0	0	0	0	0	0	0	0	0	0	0	0	0	0	0	1	0	0	0	1	2	0	0	0	0	4
13-13,5	0	0	0	0	0	0	0	0	0	0	0	0	0	0	0	0	0	0	0	0	0	0	0	0	0	0	1	0	0	0	0	1
13,5-14	0	0	0	0	0	0	0	0	0	0	0	0	0	0	0	0	0	0	0	0	0	0	0	0	0	0	0	0	0	0	0	0
14-14,5	0	0	0	0	0	0	0	0	0	0	0	0	0	0	0	0	0	0	0	0	0	0	0	0	0	0	0	0	0	0	1	1
																														sum		186509

Figure B.2: Hs-w scatter diagram.

C Platform Motion Response

C.1 Time Series of Motion Response Between the two FWTs

C.1.1 LC1.1

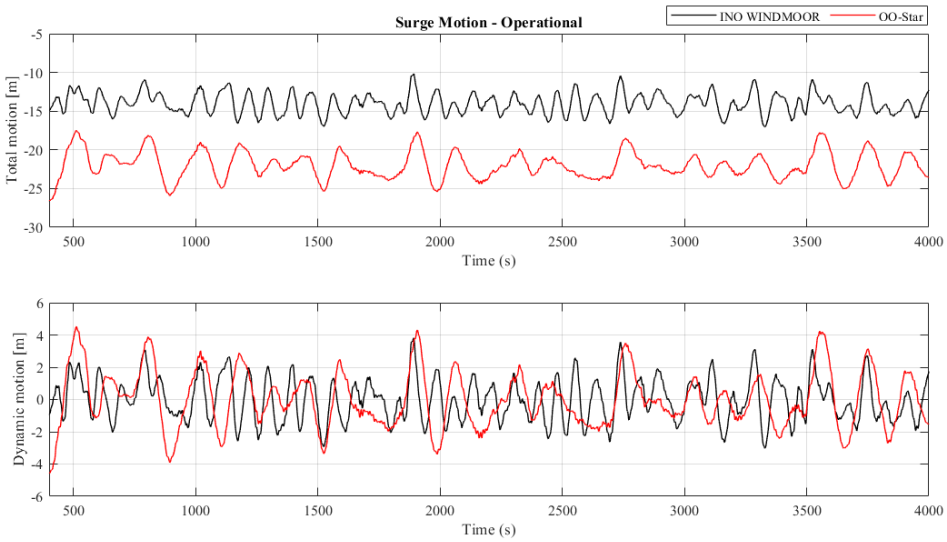

(a)

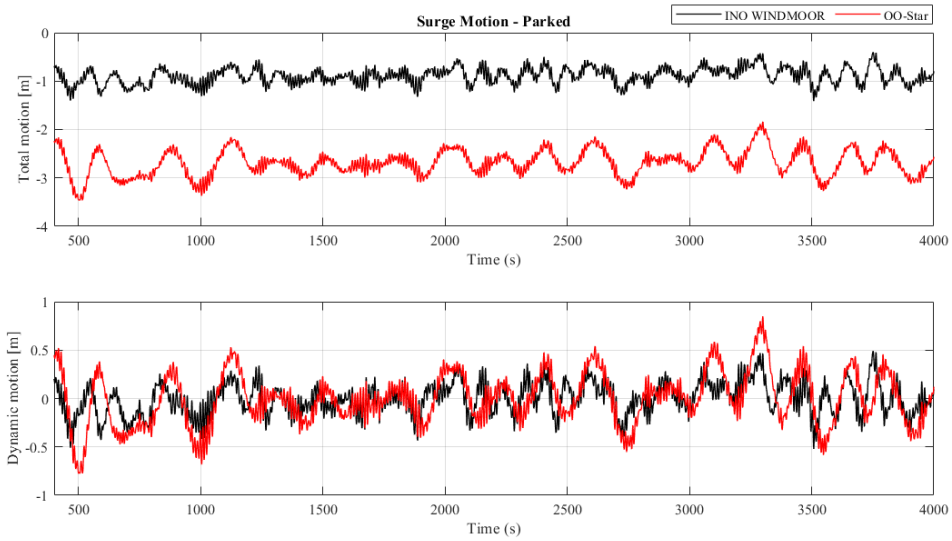

(b)

Figure C.1: Time series of the surge response at rated wind speed for operational (a) and parked (b) condition between INO WINDMOOR and OO-Star.

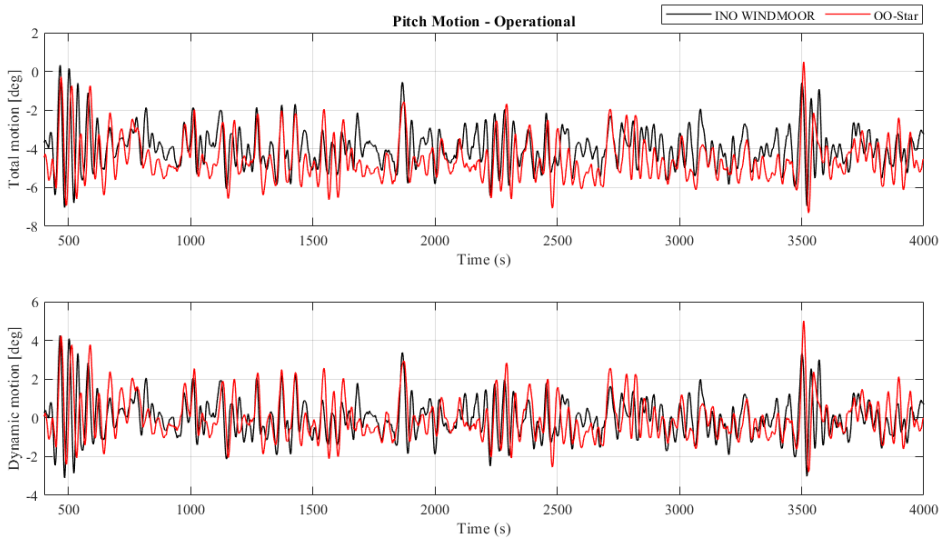

(a)

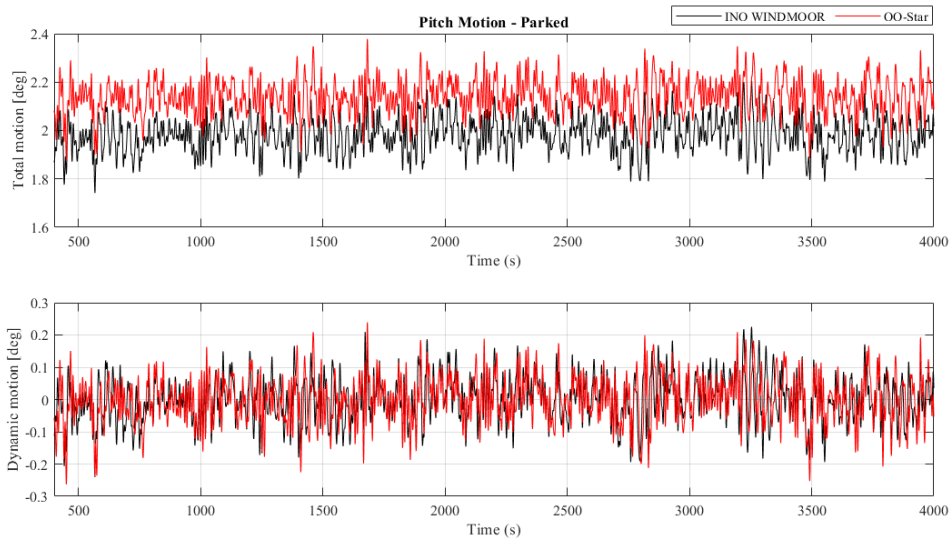

(b)

Figure C.2: Time series of the pitch response at rated wind speed for operational (a) and parked (b) condition between INO WINDMOOR and OO-Star.

C.1.2 LC3

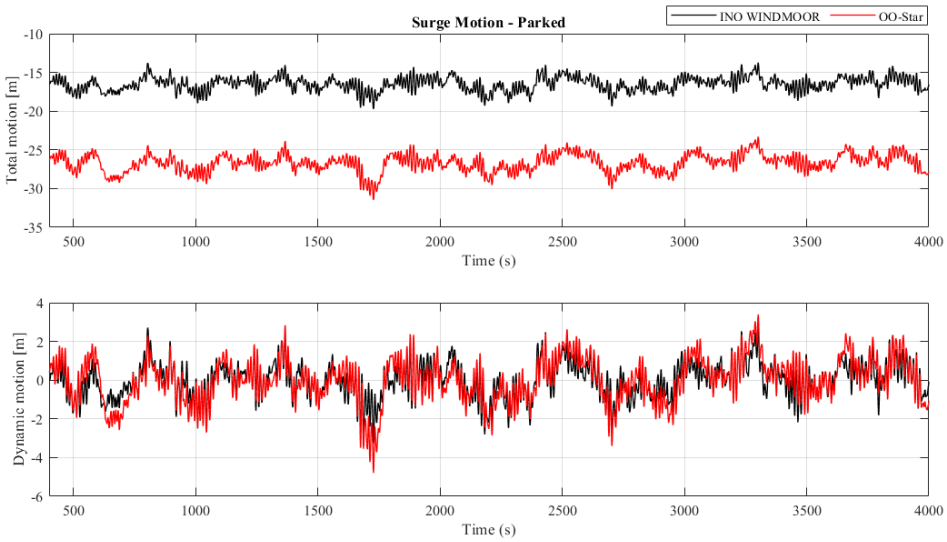

Figure C.3: Time series of the surge response in extreme condition between INO WINDMOOR and OO-Star.

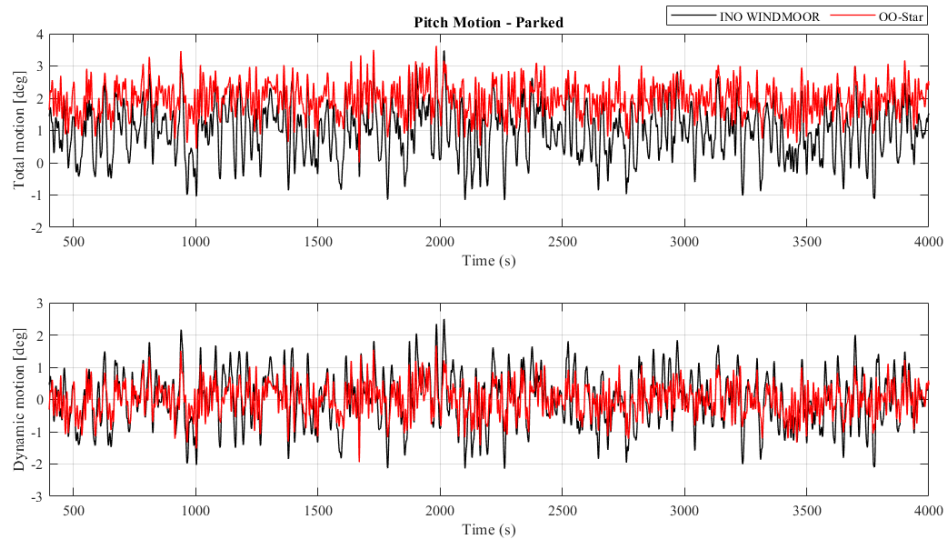

Figure C.4: Time series of the pitch response in extreme condition between INO WINDMOOR and OO-Star.

D Loads on the FWTs

D.1 Time Series of Tower Base Axial Force

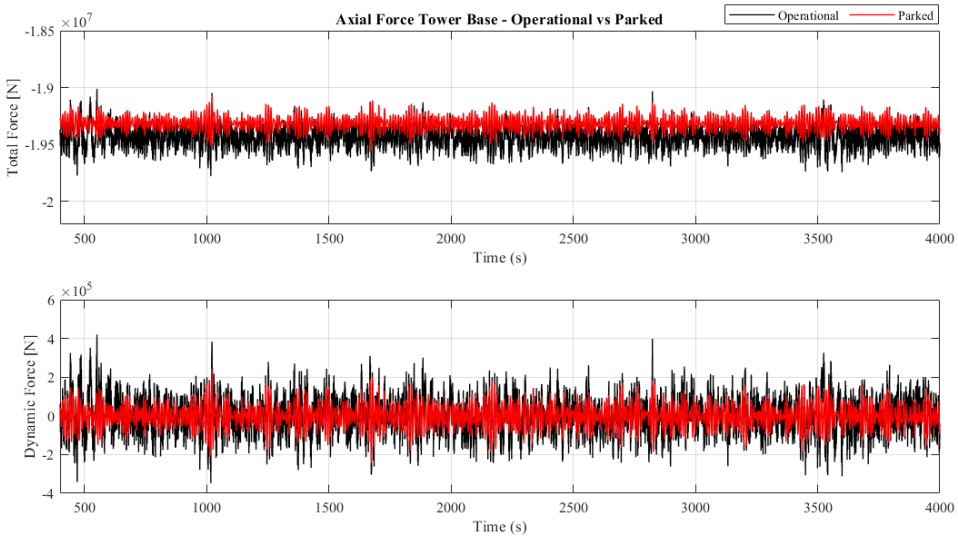

Figure D.1: Time series of axial force at tower base for INO WINDMOOR at design load case LC1.1 and LC1.2.

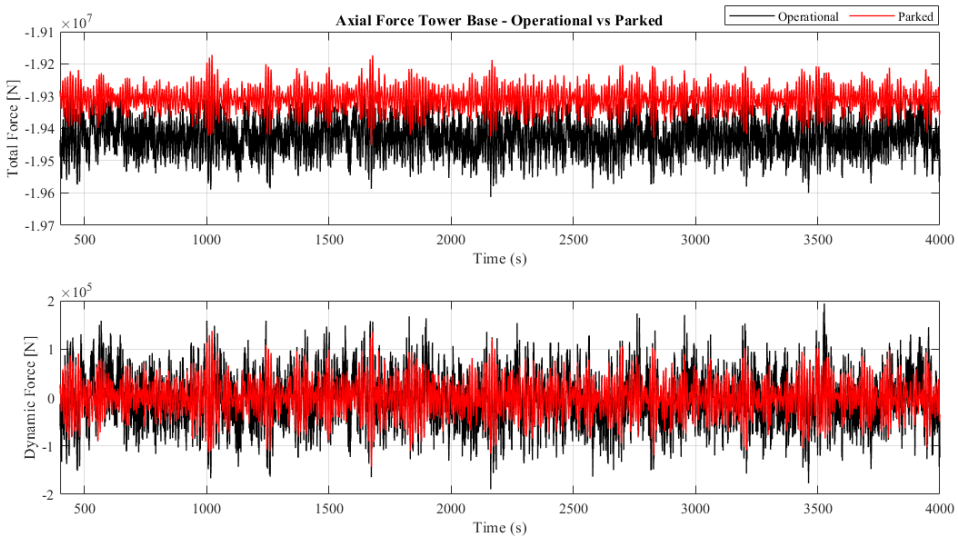

Figure D.2: Time series of axial force at tower base for OO-Star at design load case LC1.1 and LC1.2.

D.2 Time Series of Tower Base Fore-Aft Bending Moment

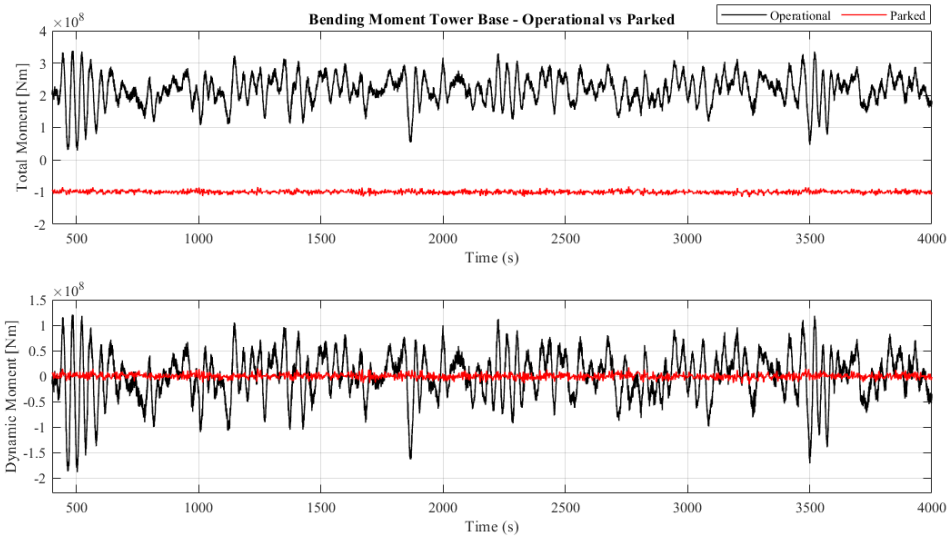

Figure D.3: Time series of bending moment at tower base for INO WINDMOOR at design load case LC1.1 and LC1.2.

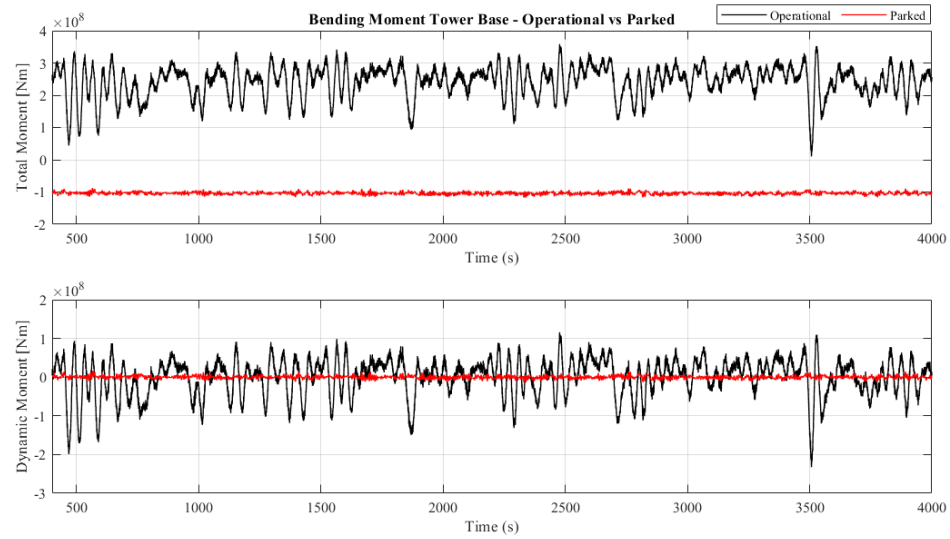

Figure D.4: Time series of bending moment at tower base for OO-Star at design load case LC1.1 and LC1.2.

E Power Spectral Density

E.1 Response Spectra

E.1.1 LC1.1 and LC1.2

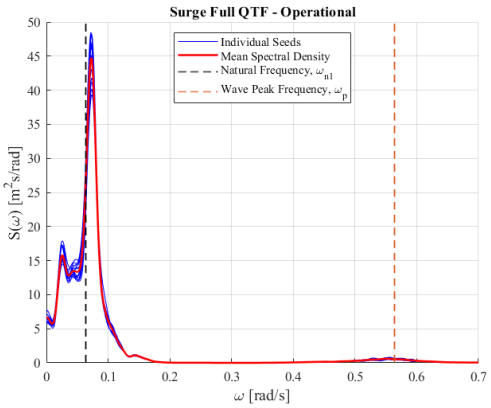

(a) INO WINDMOOR

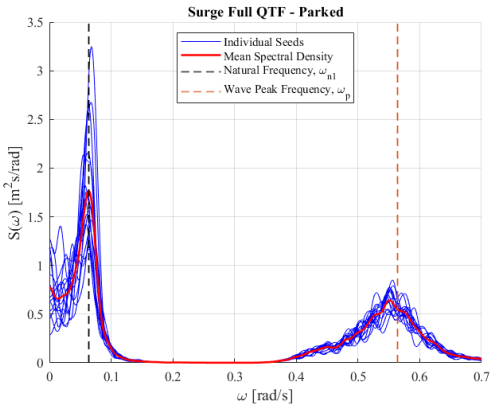

(b) INO WINDMOOR

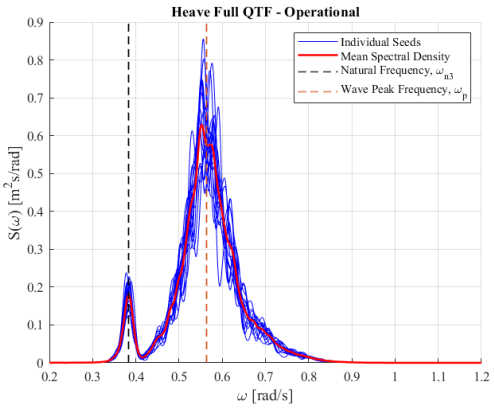

(c) INO WINDMOOR

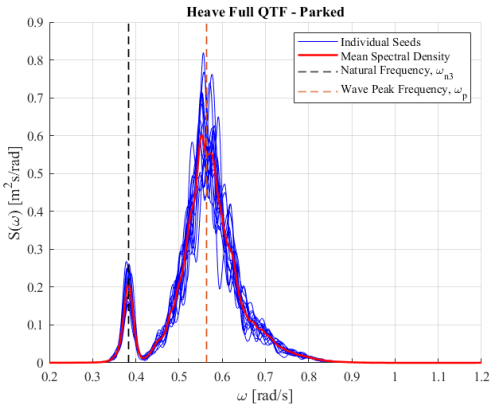

(d) INO WINDMOOR

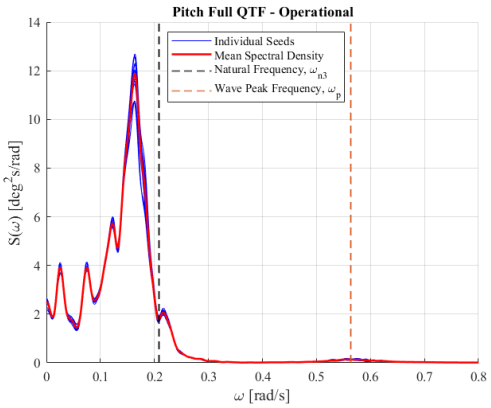

(e) INO WINDMOOR

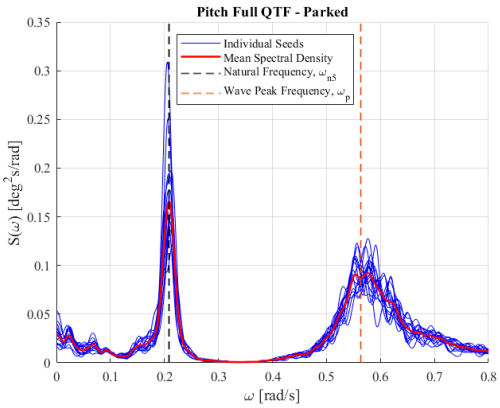

(f) INO WINDMOOR

Figure E.1: Spectra for FWT motions at LC1.1 and LC1.2 for the INO WINDMOOR floater.

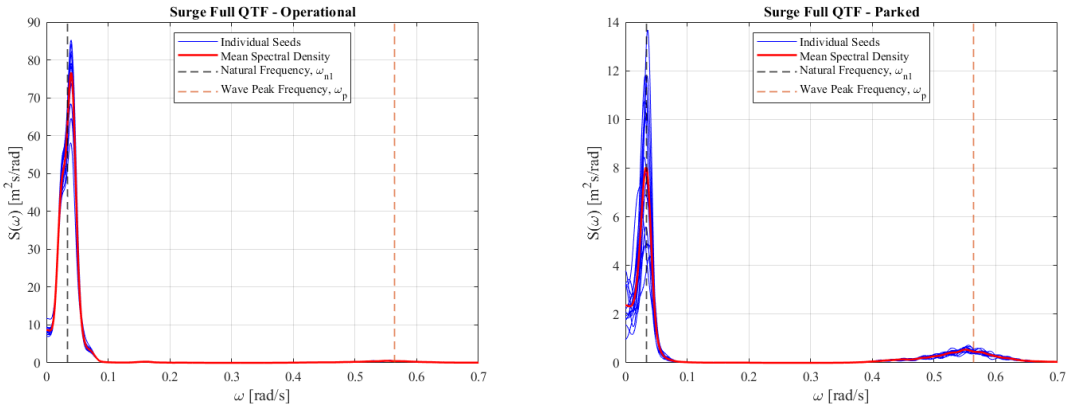

(a)

(b)

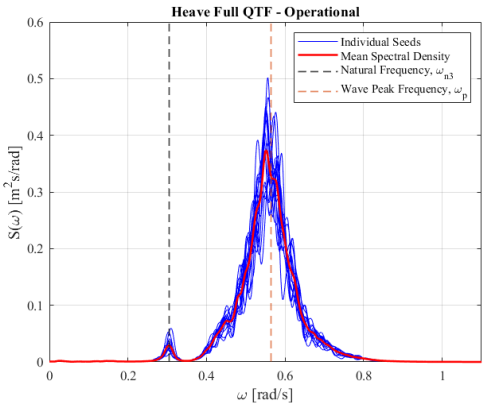

(c)

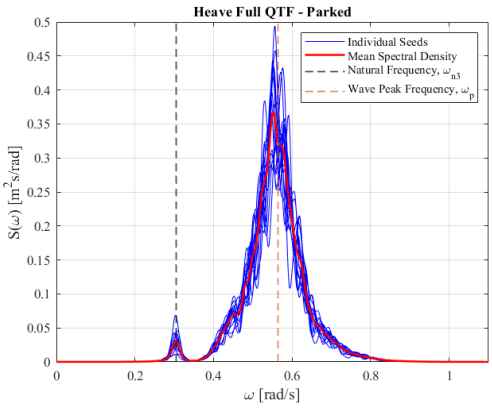

(d)

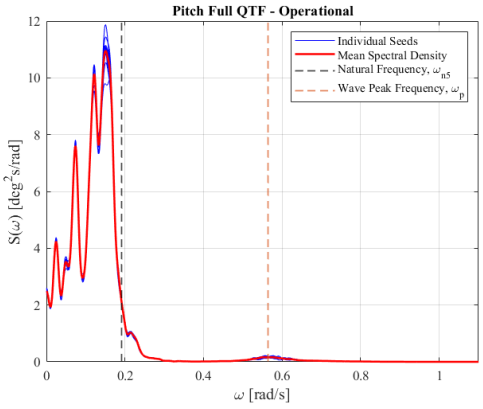

(e)

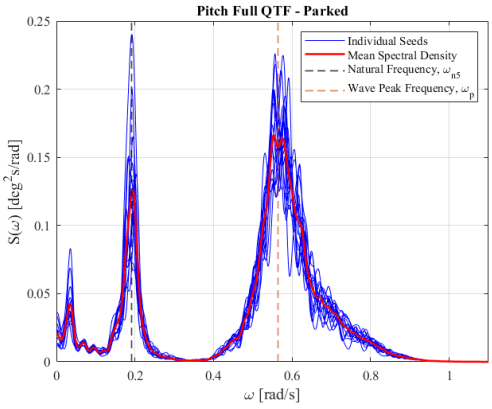

(f)

Figure E.2: Spectra for FWT motions at LC1.1 and LC1.2 for the OO-Star floater.

E.1.2 LC2.1 and LC2.2

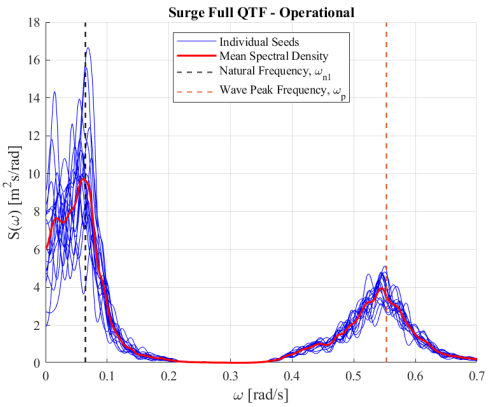

(a) INO WINDMOOR

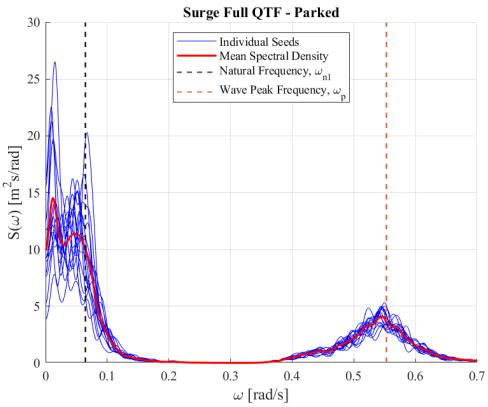

(b) INO WINDMOOR

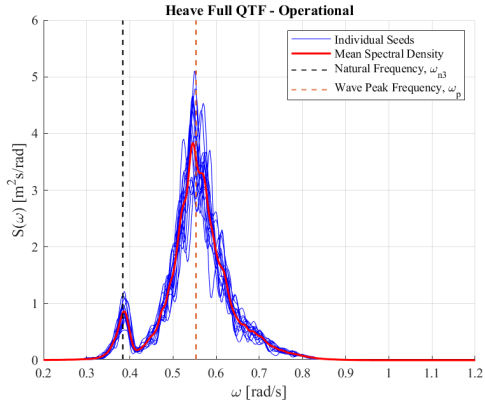

(c) INO WINDMOOR

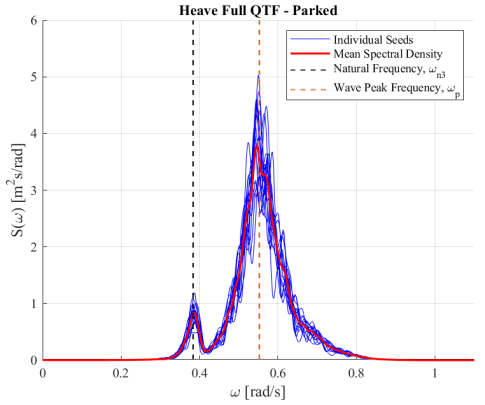

(d) INO WINDMOOR

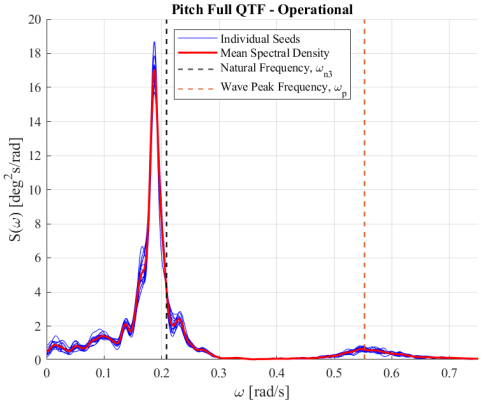

(e) INO WINDMOOR

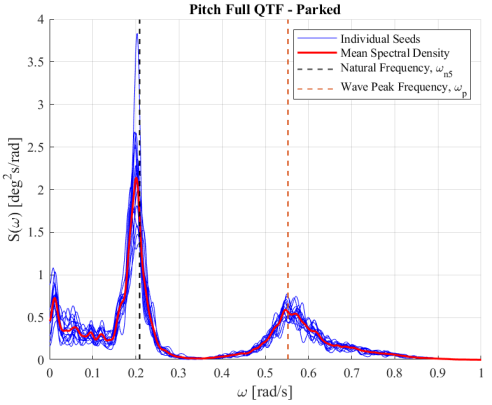

(f) INO WINDMOOR

Figure E.3: Spectra for floater motions at LC2.1 and LC2.2 for the INO WINDMOOR floater.

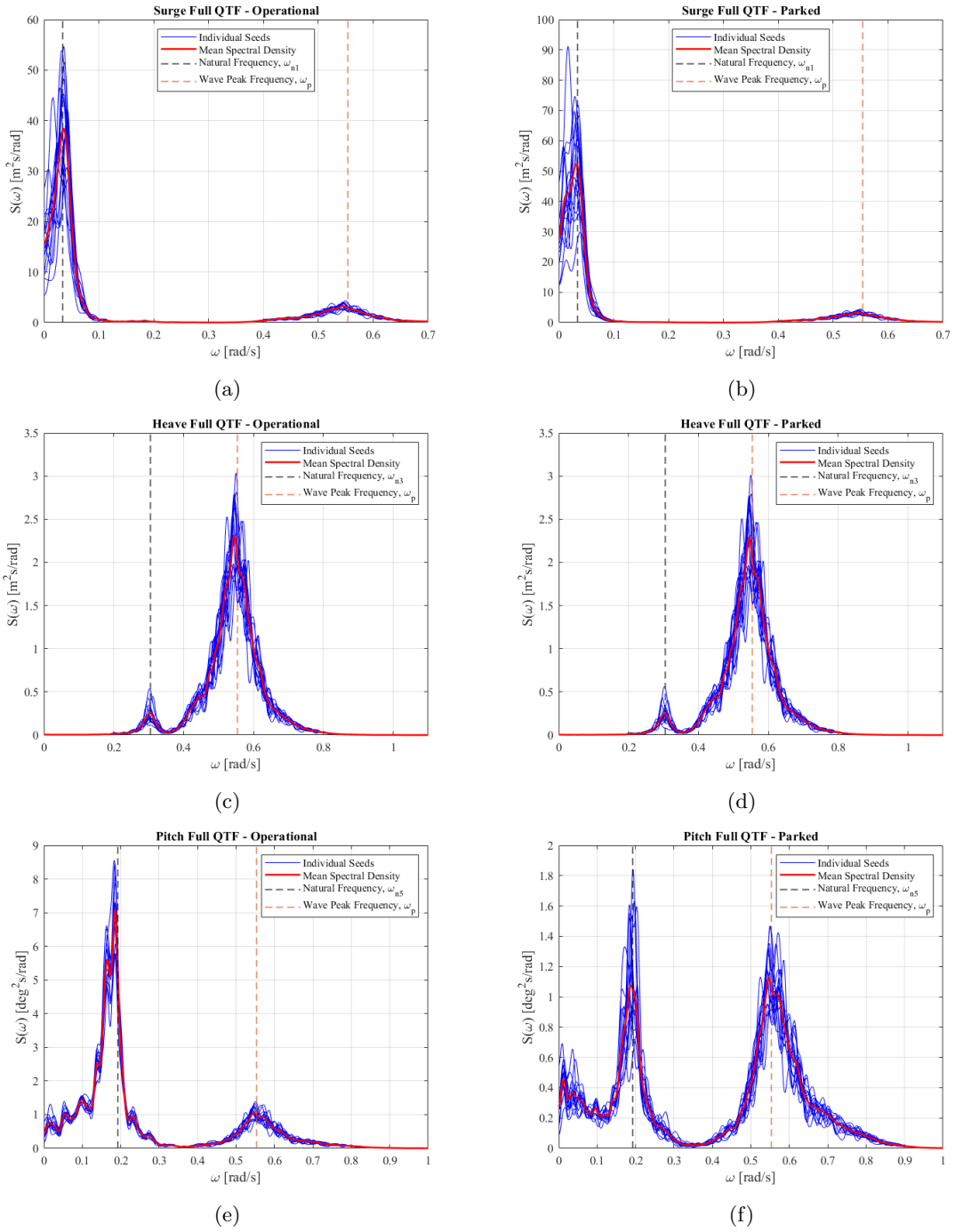

Figure E.4: Spectra for floater motions at LC2.1 and LC2.2 for the OO-Star floater.

E.1.3 LC3

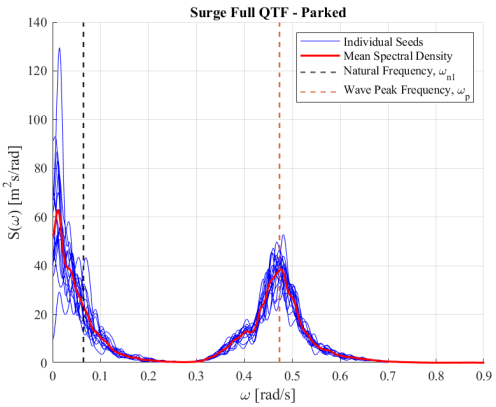

(a) INO WINDMOOR

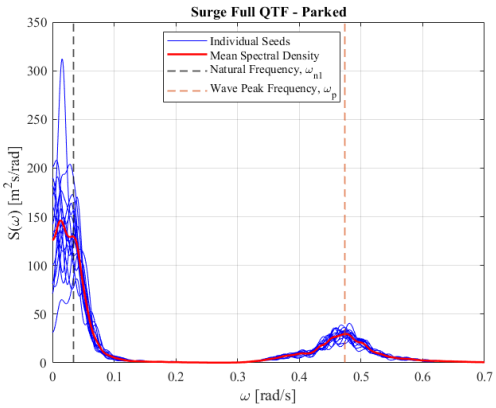

(b) OO-Star

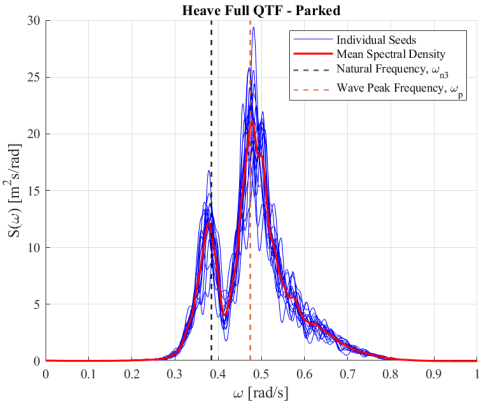

(c) INO WINDMOOR

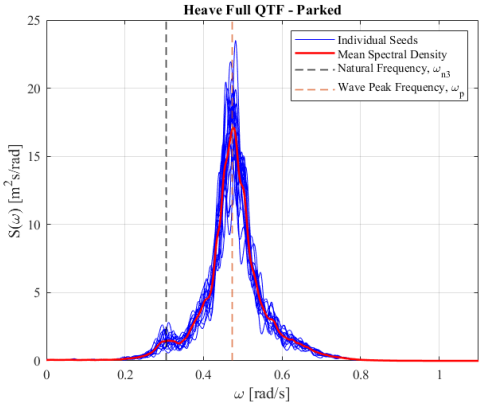

(d) OO-Star

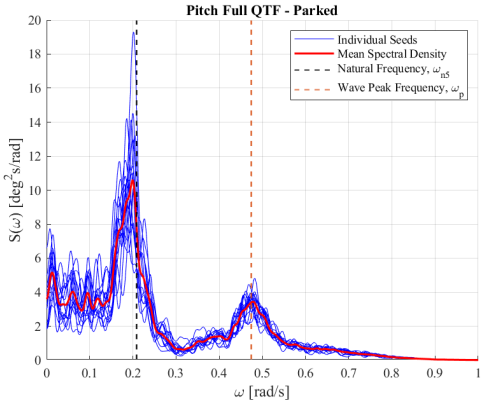

(e) INO WINDMOOR

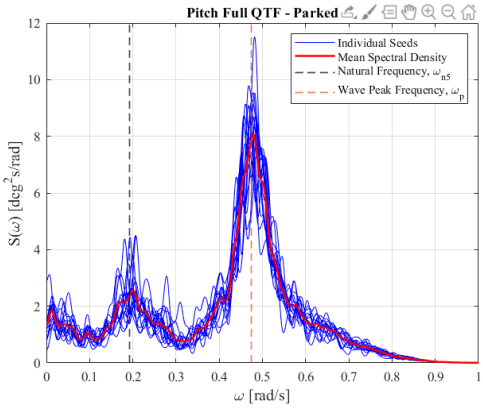

(f) OO-Star

Figure E.5: Spectra for floater motions at LC3 for the INO WINDMOOR and OO-Star floater.

E.2 Axial Force Spectra Tower Base

E.2.1 LC2.1 and LC2.2

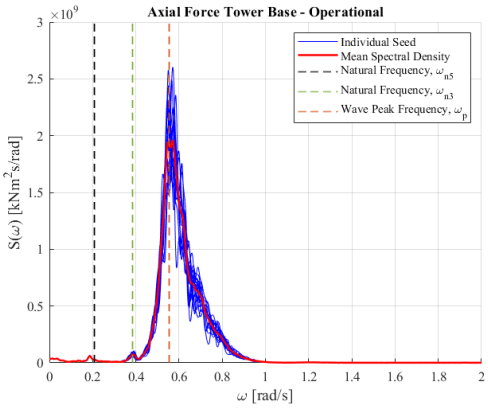

(a) INO WINDMOOR

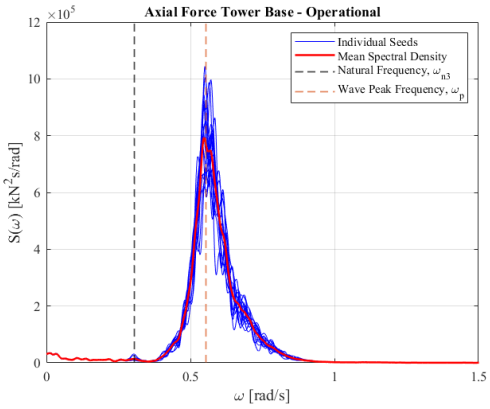

(b) OO-Star

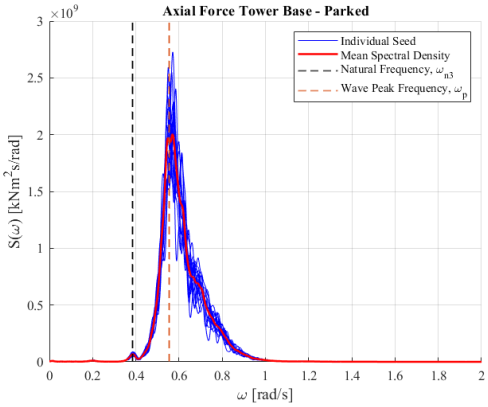

(c) INO WINDMOOR

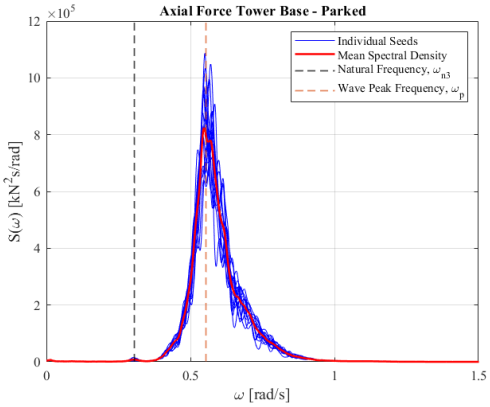

(d) OO-Star

Figure E.6: Spectra for axial force at tower base in LC2.1 and 2.2 for INO WINDMOOR and OO-Star.

E.2.2 LC3

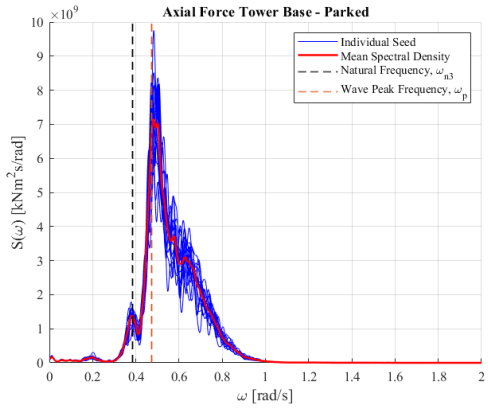

(a) INO WINDMOOR

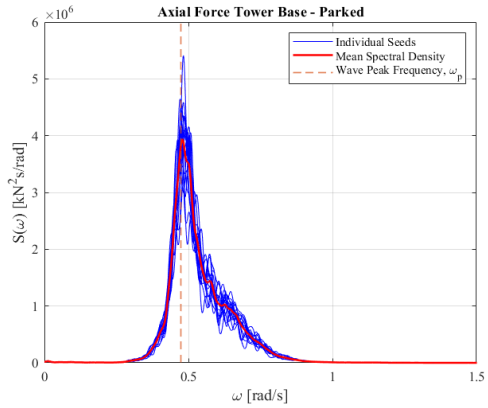

(b) OO-Star

Figure E.7: Spectra for axial force at tower base in LC3 for INO WINDMOOR and OO-Star.

E.3 Axial Force Spectra Tower Top

E.3.1 LC2.1 and LC2.2

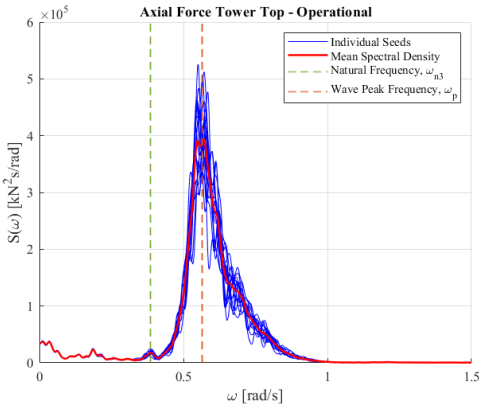

(a) INO WINDMOOR

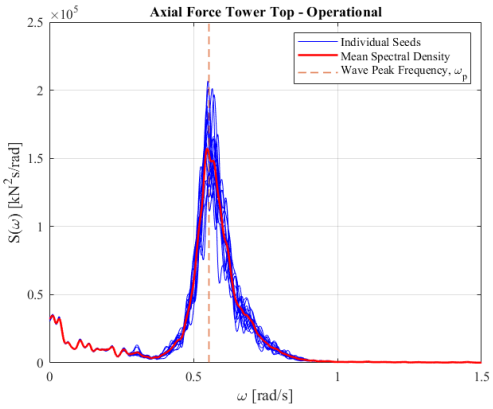

(b) OO-Star

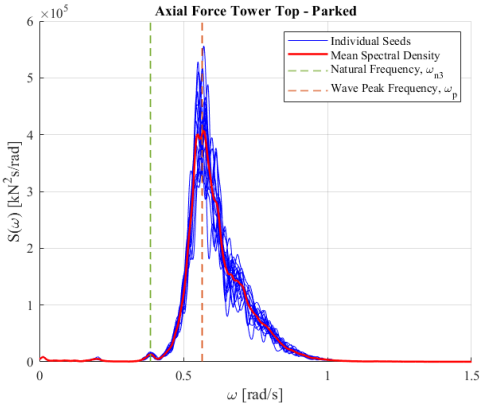

(c) INO WINDMOOR

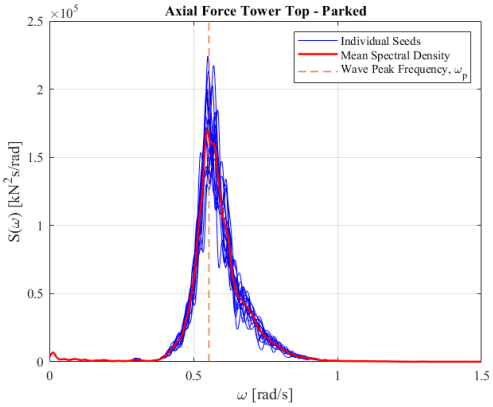

(d) OO-Star

Figure E.8: Spectra for axial force at tower top in LC2.1 and 2.2 for INO WINDMOOR and OO-Star.

E.3.2 LC3

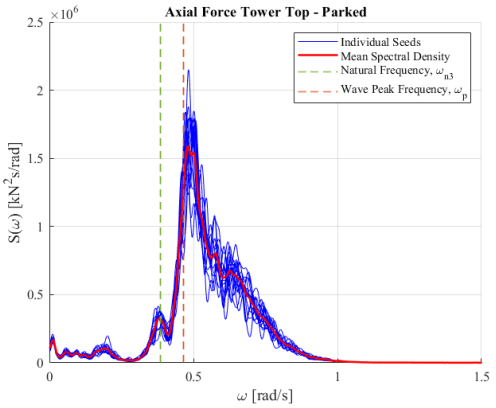

(a) INO WINDMOOR

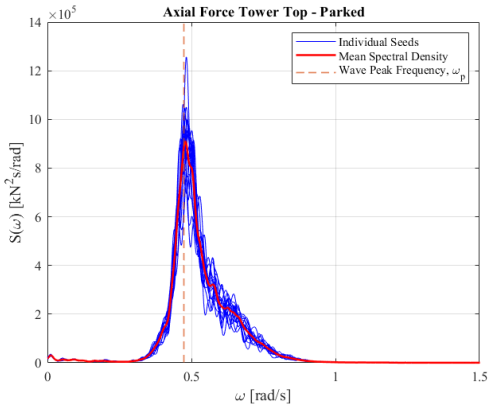

(b) OO-Star

Figure E.9: Spectra for axial force at tower top in LC3 for INO WINDMOOR and OO-Star.

E.4 Fore-Aft Bending Moment Spectra Tower Top

E.4.1 LC2.1 and LC2.2

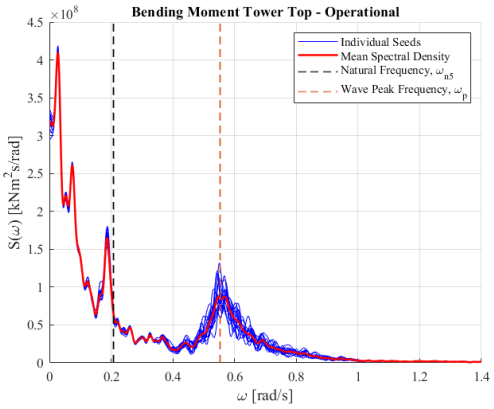

(a) INO WINDMOOR

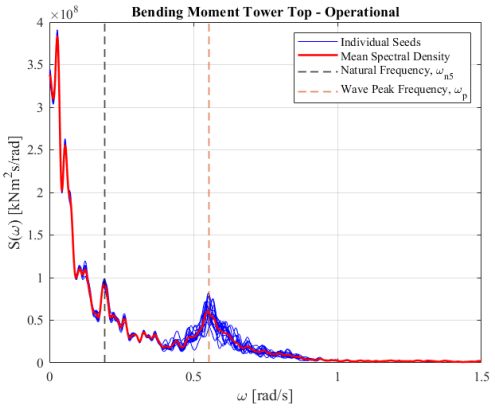

(b) OO-Star

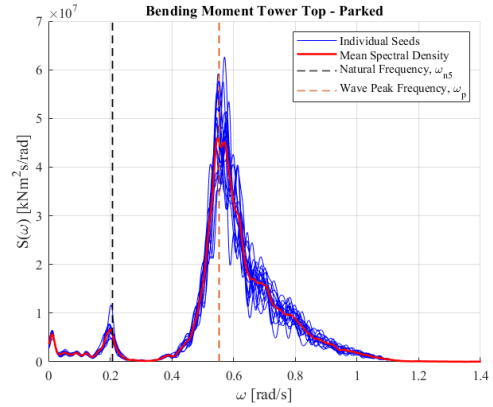

(c) INO WINDMOOR

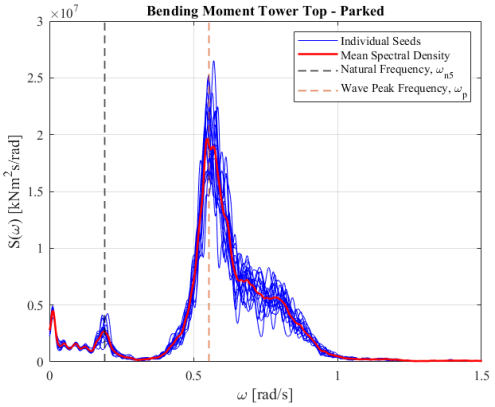

(d) OO-Star

Figure E.10: Spectra for the tower top bending moment in LC2.1 and LC2.2 for INO WINDMOOR and OO-Star.

E.4.2 LC3

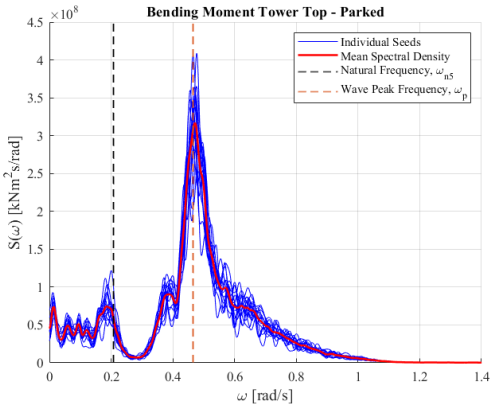

(a) INO WINDMOOR

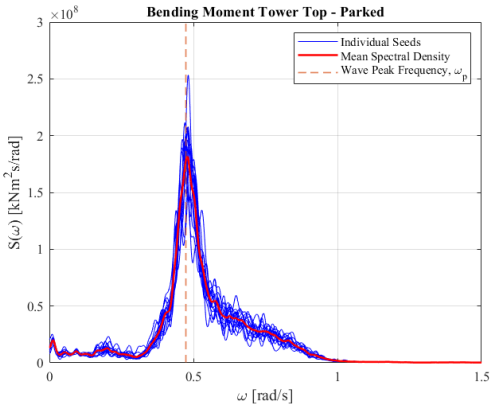

(b) OO-Star

Figure E.11: Spectra for the tower top bending moment in LC3 for INO WINDMOOR and OO-Star.

F Bending Moment RAO

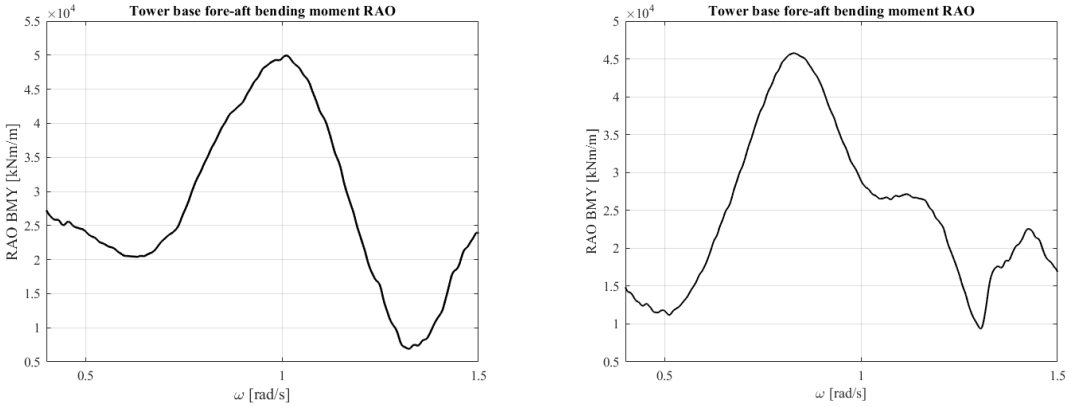

(a) (b)

Figure F.1: Bending moment RAO for INO WINDMOOR (a) and OO-Star (b).

G Fatigue

G.1 2-hour Fatigue Damage Segments

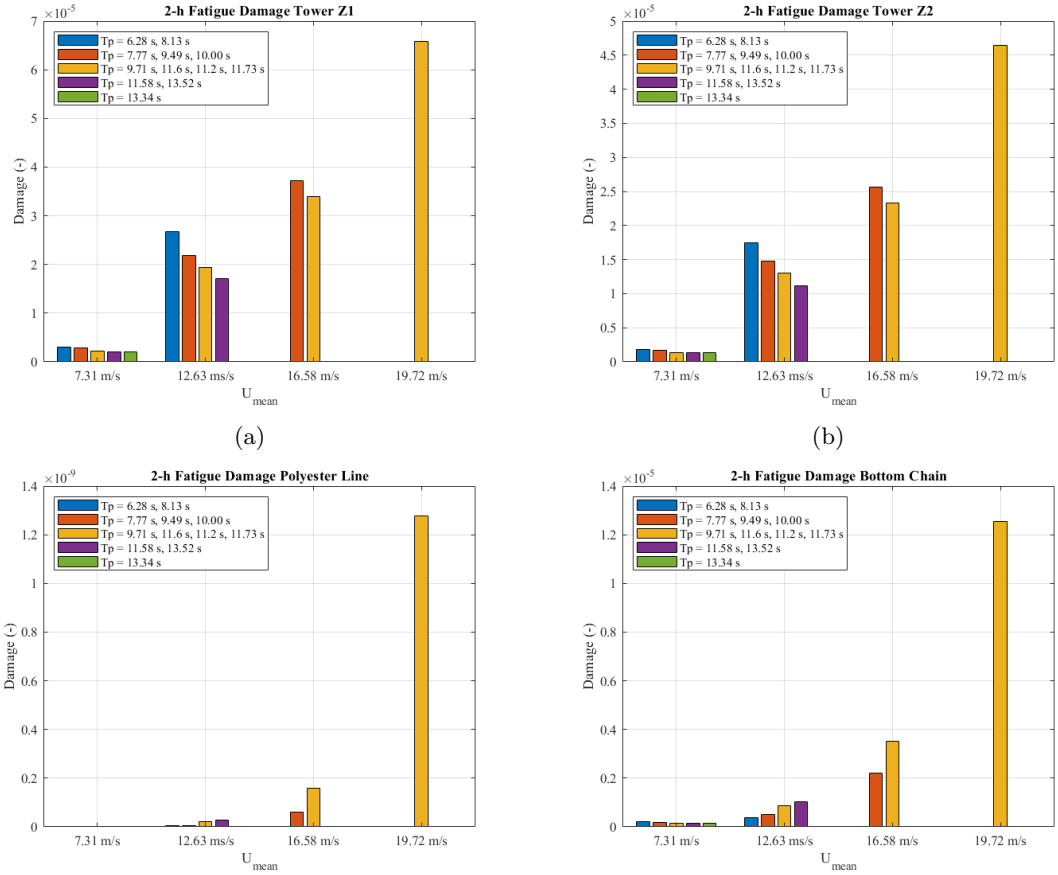

Figure G.1: 2-hour short term fatigue damage at tower $z1$ (a) and $z2$, polyester (c) and bottom chain (d) for varying wave periods for the INO WINDMOOR.

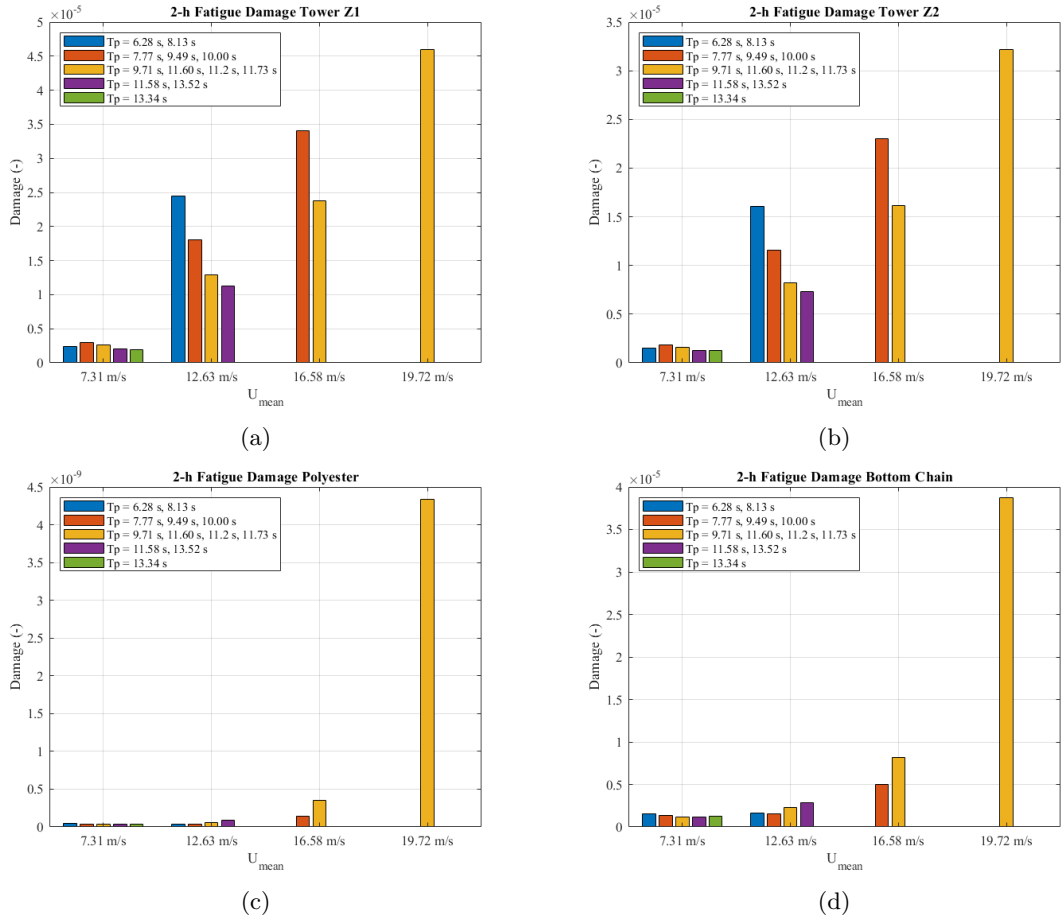

Figure G.2: 2-hour short term fatigue damage at tower $z1$ (a) and $z2$ (b), polyester (c) and bottom chain (d) for varying wave periods for the OO-Star.

H Structural drawings of OO-Star

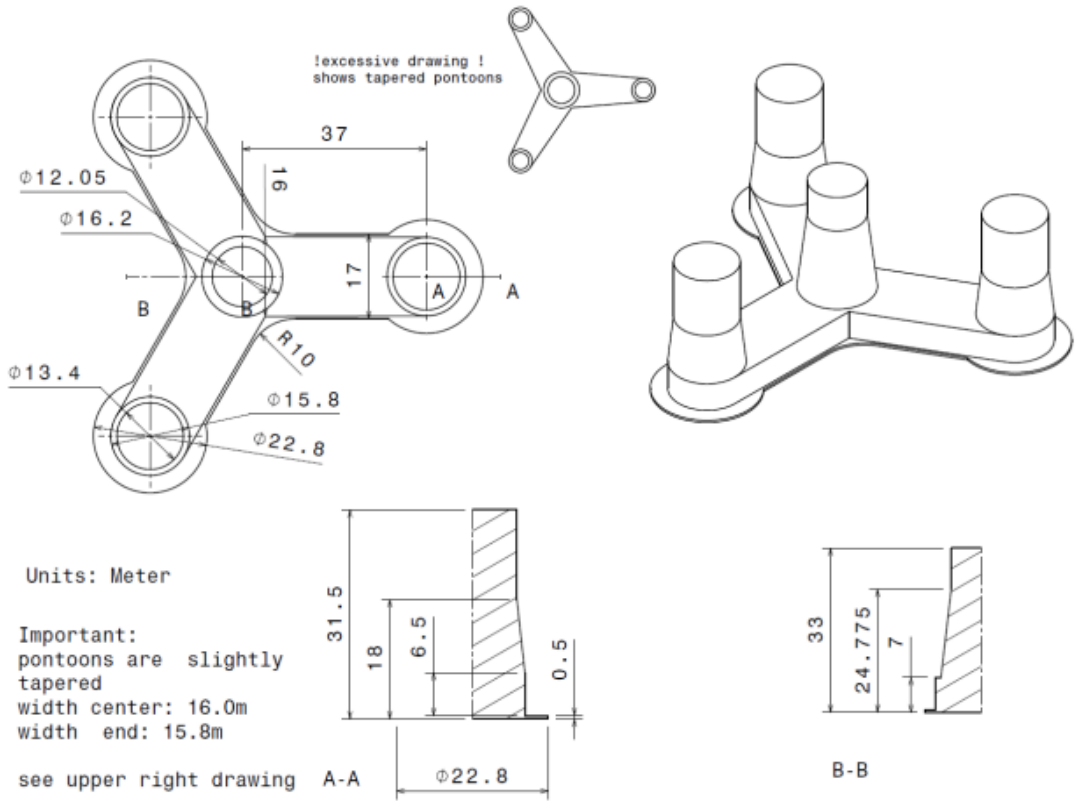

Figure H.1: Structural drawings of OO-Star.

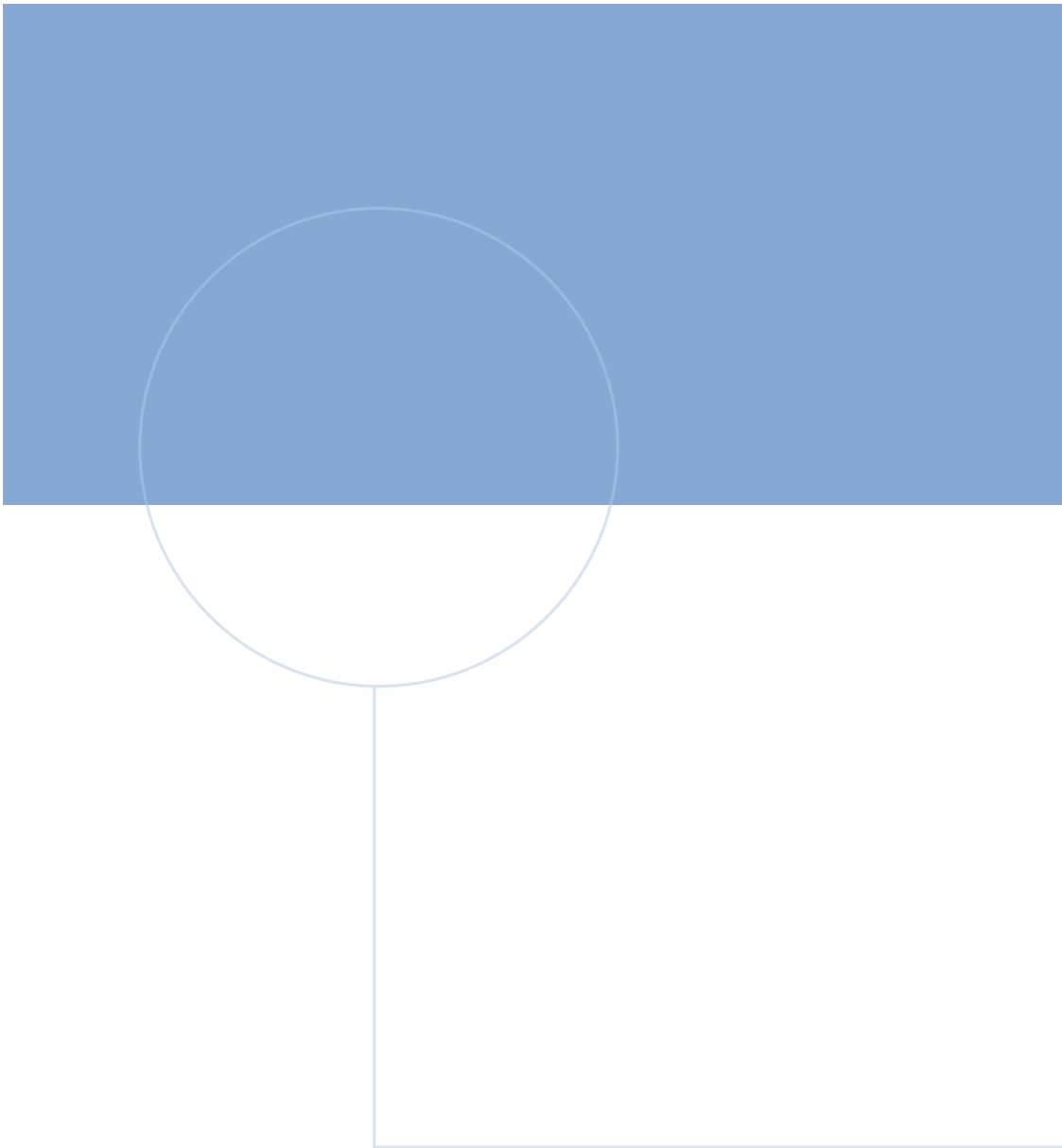

NTNU

Norwegian University of
Science and Technology